Institut de Physique du Globe de Paris, Université de Paris

Manuscrit

Habilitation à Diriger des Recherches
présenté par

Pierre DUBLANCHET

MINES ParisTech - Centre de Géosciences

Quantification and mechanical control of fault slip events : insights from physics based models.
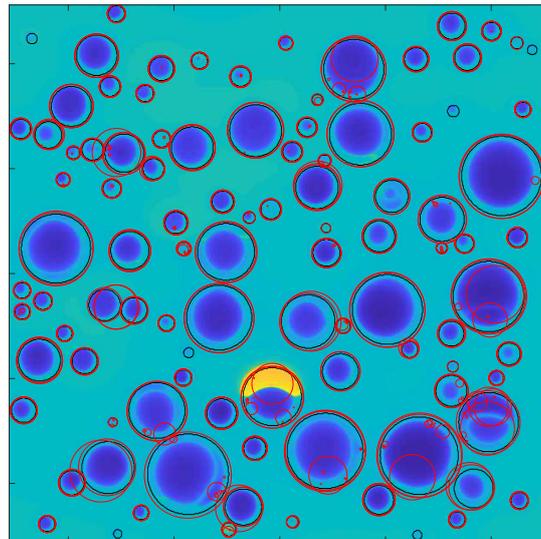
Soutenue le 18 mai 2021 devant le jury composé de :

M. Jean-Philippe AVOUAC . . . . Professeur CalTech (Rapporteur)
M. Sebastian HAINZL . . . . Senior Scientist GFZ (Rapporteur)
M. Jean-Pierre VILOTTE . . . . Physicien IPGP (Rapporteur)
Mme. Kate Huihsuan CHEN . . Professeure National Taïwan Normal University (Examinatrice)
M. Michel CAMPILLO . . . . Professeur Université Joseph Fourier (Examinateur)
M. Harsha Suresh BHAT . . . . Chargé de recherche HDR CNRS (Examinateur)
M. Hervé CHAURIS . . . . Professeur MINES ParisTech (Examinateur)

Abstract

Tectonic faults release elastic energy supplied by plate motion by a large spectrum of slip phenomena, ranging from continuous slow (cm/yr) creep to fast (m/s) slip events known as earthquakes. Decades of geodetical and seismological monitoring of fault slip have revealed in many active areas complex succesions of interacting fault slip events at different scales. Despite this apparent complexity, fault slip seems to obey rather simple scalings and statistical laws (Gutenberg-Richter magnitude-frequency distribution, Omori law, moment-duration scaling). Another important discovery about fault slip events is the ubiquitous imbrication between slow aseismic slip, radiative events and fluid flow. The important role of fluids in fault slip processes is in particular suggested by the numerous examples of seismicity induced by reservoir exploitation. Despite the considerable amount and the high quality of observations, we currently lack important aspects of the mechanical control on fault slip. First, because the mechanisms triggering fault slip (tectonic stress accumulation, deep pore pressure variations, stress redistributions between faults, aseismic slip) are poorly quantified. Then, because of our partial knowledge of the physical laws controlling fault slip, generally upscaled from laboratory experiments.

My research activities aim at improving our understanding of the mechanical control of slip by the use of fault models coupling elasticity, friction and fluids. In this manuscript, I present how such models could help to address the unresolved issues about fault slip. The first part is dedicated to the question of what mechanical parameters control the scaling and statistical relationships characterizing slip events at the scale of a planar fault undergoing slow tectonic loading. The crucial role played by prestress and frictional heterogeneity in controlling magnitude distribution, Omori decay, moment duration scaling and slip acceleration are discussed. In a second chapter, I present several studies dedicated to the quantification of the deep processes trigerring fault slip events, in particular aseismic slip and fluid flow. Two approaches are presented, one relying on the direct modeling of particular swarms, with two examples from the Corinth rift (Greece), the second one based on the derivation of general relationships between mechanical loading and fault slip properties.

The specificity of my research probably resides in the systematic search for relationships between observed quantities and well defined mechanical parameters, that is physical properties of geological material that could be measured in a laboratory. For that purpose, the results of my numerical models are always confronted to observations, and supported by asymptotic theoretical developments as far as possible.

In the final chapter, some perspectives are presented to extend and improve the study of fault slip mechanical control. The projects discussed all aim at developing the use of mechanical models for fault slip data interpretation. I propose to pursue the modeling of seismological data initiated in the Corinth rift, and to develop the modeling of laboratory fault slip experiments. In the perspective of connecting laboratory and natural observations, my research projects also involve the study of effective frictional properties. The common objective of these projects is to develop a strong theoretical background for mechanical interpretation of fault slip phenomena, and for the quantification of the deep mechanisms driving fault slip.

Contents

List of Figures

List of Symbols

α : ratio a/b of rate-and-state frictional parameters [n.d.]

β : rate of pressure increase [Pa.s^{-1}]

$\Delta\tau$: static stress drop [Pa]

$\Delta\tau_d$: dynamic stress drop [Pa]

Δv : slip rate perturbation [m.s^{-1}]

δ, δ_0 : fault slip [m]

δ_s : seismic slip [m]

$\dot{\tau}_0$: effective stressing rate (Dieterich's model) [Pa.s^{-1}]

$\dot{\tau}_c$: effective stressing rate (creep mediated transfers) [Pa.s^{-1}]

$\dot{\tau}_s$: effective stressing rate (static redistribution) [Pa.s^{-1}]

Γ : aseismic fracture energy density [Pa]

λ : wavelength of frictional heterogeneity [m]

λ_c : critical wavelength of frictional heterogeneity [m]

λ_t, λ_s : bare and dressed kernels of interaction for seismic activity [day^{-1}]

μ : shear modulus [Pa]

Π_m : fault pressurization [Pa.s^{-1}]

ψ_0 : normalizing factor for crack-like solutions [n.d.]

ρ, ρ_a : asperity density [n.d.]

ρ_c, ρ^* : critical asperity density [n.d.]

σ, σ_n : normal stress [Pa]

σ_0 : reference normal stress [Pa]

σ_1, σ_3 : maximum and minimum principal stresses [Pa]

τ_0 : initial shear stress [Pa]

τ_b : far field tectonic shear stress [Pa]

τ_r : residual shear stress [Pa]

τ_v : visco-elastic time scale [s]

τ_{ss}^0 : reference steady state frictional stress [Pa]

θ : state variable (rate-and-state friction) [s]

$\tilde{\lambda}$: normalized wavelength of frictional heterogeneity [n.d.]

ξ : power exponent for self-similar solutions [n.d.]

a, a_{rns} : first rate-and-state parameter (direct effect) [n.d.]

a_0 : spatial average of the rate-and-state parameter a [n.d.]

a_s : velocity strengthening rate-and-state a parameter [n.d.]

b : b-value (Gutenberg-Richter law) [n.d.]

b, b_{rns} : second rate-and-state parameter (state) [n.d.]

b_0 : spatial average of the rate-and-state parameter b [n.d.]

b_s : velocity strengthening rate-and-state b parameter [n.d.]

c : function of frictional parameters [n.d.]

c_a : onset time of power-law decay (Omori law) [s]

COV : covariance in recurrence time of repeating earthquakes [n.d.]

D : hydraulic diffusivity [$m^2.s.^{-1}$]

D_0 : reference hydraulic diffusivity [$m^2.s.^{-1}$]

d_c : critical slip for rate-and-state friction [m]

d_c^0 : reference critical slip for rate-and-state friction [m]

f : relative amplitude of rate-and-state friction heterogeneity [n.d.]

f_0 : reference friction coefficient [n.d.]

f_c : corner frequency [Hz]

f_d : dynamic friction coefficient (slip-weakening law) [n.d.]

f_f : friction coefficient [n.d.]

f_s : static friction coefficient (slip-weakening law) [n.d.]

f_{ss} : steady state rate-and-state friction coefficient [n.d.]

H : elastic slab thickness [m]

K : stress intensity factor [$Pa.m^{1/2}$]

k : productivity of Gutenberg-Richter law [n.d.]

K_a : aftershocks productivity (Omori law) [n.d.]

K_c : critical stress intensity factor [$Pa.m^{1/2}$]

L : fault length [m]

L_b : characteristic length associated with rate-and-state friction ($L_b = \mu d_c / b\sigma$) [n.d.]

L_c : critical nucleation length [m]

M_0, m_0 : seismic moment [N.m]

M_w, M, m : moment magnitude [n.d.]

m_{max}, m_f : maximum magnitude [n.d.]

m_{min} : minimum magnitude [n.d.]

$N(m)$: number of earthquakes exceeding magnitude m (Gutenberg-Richter law) [n.d.]

n_a : cumulative number of earthquakes [n.d.]

n_f : number of foreshocks [n.d.]

n_f^{max} : maximum number of foreshocks [n.d.]

N_{max} : maximum number of earthquakes in a sequence [n.d.]

p : power law exponent (moment-duration scaling, moment-recurrence scaling, asperity size distribution, LFE interaction kernels) [n.d.]

P, P_f : pore fluid pressure [Pa]

p_a : decay exponent (Omori law) [n.d.]

P_c : confining pressure [Pa]

p_{inj}^E : experimental injection pressure [Pa]

P_{max} : maximum pore pressure [Pa]

p_{obs}^E : experimental measured pressure [Pa]

q : pore pressure gradient at injection point [Pa.m^{-1}]

R : asperity size [m]

r : seismicity rate [s^{-1}]

r_0 : reference seismicity rate [s^{-1}]

R_a : aftershocks rate (Omori law) [s.$^{-1}$]

R_f : foreshocks rate [s^{-1}]

R_{max} : maximum asperity size [m]

r_{max} : maximum seismicity rate [s^{-1}]

R_{min}, R_1 : minimum asperity size [m]

S_0 : initial understress (relative distance to steady state frictional stress) [n.d.]

T : slip event duration [s.]

t_f : characteristic time for foreshock acceleration [s]

t_I, t_s : characteristic times for fluid induced aseismic slip acceleration [s.]

T_r : recurrence time of repeating earthquakes [s.]

t_r, t_{r0} : relaxation times for Omori decay of repeating earthquakes [s]

v : fault slip rate [m.s^{-1}]

v^* : reference slip rate for rate-and-state friction [m.s^{-1}]

v_0 : initial slip rate [m.s^{-1}]

v_b, v_p : far field relative tectonic plate velocity [m.s^{-1}]

v_c : creep rate [m.s^{-1}]

V_m : earthquake migration speed [m.s^{-1}]

v_m : maximum slip rate [m.s^{-1}]

v_r : rupture/expansion speed [m.s^{-1}]

Chapter 1

Introduction

1.1 Fault slip observations

1.1.1 Scaling and statistical laws

Tectonic faults release accumulated energy through slip events, either fast (slip rate of the order of m.s^{-1}) or slow (slip rate of the order of several cm.yr^{-1} to several m.yr^{-1}). The monitoring of active tectonic faults has allowed to detect, to locate and analyze a wide range of such events: regular earthquakes, postseismic slip (Langbein, 1990; Schaff et $al.$, 1998), aseismic creep (Wesson, 1988), slow slip events (SSE) (Dragert et $al.$, 2001), tectonic tremor (Obara, 2002; Nadeau & Dolenc, 2005), episodic tremor and slip (Rogers & Dragert, 2003; Obara et $al.$, 2004), low frequency earthquakes (LFE) (Shelly et $al.$, 2006; Ide et $al.$, 2007a), very low frequency earthquakes (VLFE) (Obara & Ito, 2005). All these events were originally detected as deformation signals at the earth surface, having different amplitudes, durations, and characteristic frequencies. Later they have been recognized as resulting from shear slip on preexisting faults (Shelly et $al.$, 2006; Ide et $al.$, 2007a; Peng & Gomberg, 2010).

What mechanics governs the evolution of fault slip, and leads to either fast or slow events, is a major question that is not yet fully addressed. To answer this question, the geophysical community has analyzed the deformation and the elastic waves generated by faults to determine different parameters characterizing the slip process: fault orientation and size, seismic moment released, stress drop, slip rate, amount of slip, expansion (rupture) speed and duration. This approach is facilitated when the slip events are large enough, or enough impulsive to generate significant deformation and wave radiation. The most impulsive ones (regular earthquakes) have been the first to be considered. Slow events (SSE, LFE and VLFE) have only been discovered and analyzed in the past twenty years.

The main outcomes resulting from source process analysis are characteristic scaling laws. First, the stress drop $\Delta\tau$ of earthquakes is to the first order constant (Abercrombie, 1995; Ide & Beroza, 2001; Allmann & Shearer, 2009; Baltay et $al.$, 2010) over a wide range of magnitudes (figure 1.1). Some observations also report a constant stress drop for slow slip events, but over a much limited range of magnitudes (Schmidt & Gao, 2010). The stress drop associated with slow events is also generally smaller than for regular earthquakes (100 times smaller in the case of Cascadia SSEs). Recent observations and models suggest that the stress drop may increase with magnitude for slow slip events (Dal Zilio et $al.$, 2020).

Then, all slip events are characterized by a power law relationship between the seismic moment M_0 and the duration T (figure 1.2). For regular earthquakes, the seismic moment increases as T^3, which could be understood as a signature of quasi constant rupture speed v_r if stress drop is scale invariant. Concerning slow events, they have first been claimed to follow a linear moment-duration scaling (Ide et $al.$, 2007b; Peng & Gomberg, 2010) (figure 1.2). But several recent studies suggest the same scaling as regular earthquakes, both from observations (Gomberg et $al.$, 2016; Michel et $al.$, 2019), and from mechanical fault models (Dal Zilio et $al.$, 2020).
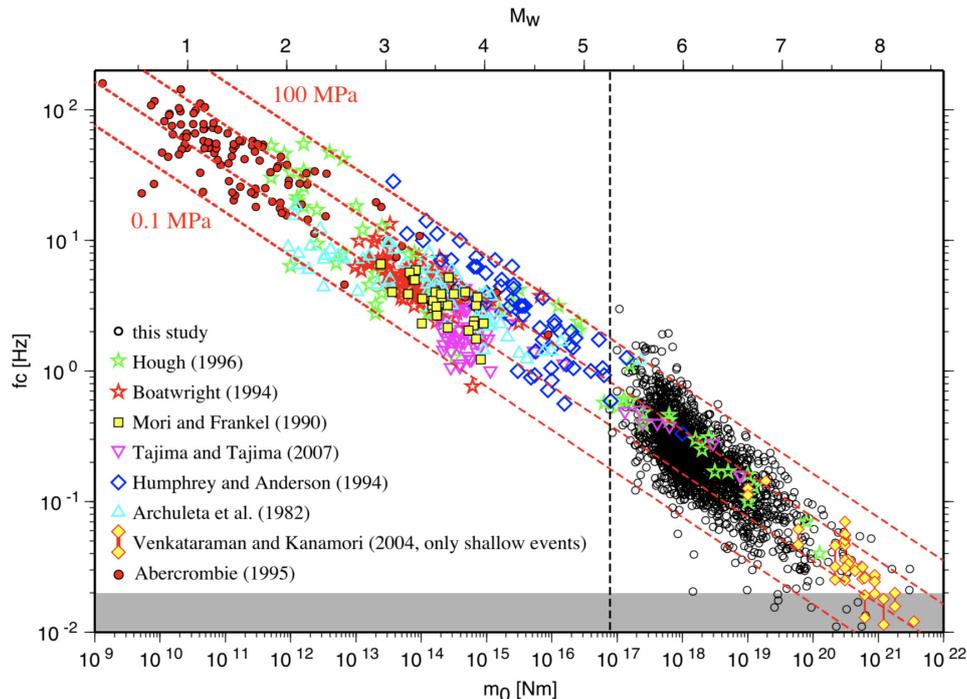
Figure 1.1: *Earthquake self-similarity over a wide range of magnitudes. m_0, M_w and f_c are the seismic moment, the moment magnitude and the corner frequency. Corner frequency is a proxy for inverse rupture duration. Red dashed lines indicate m_0, f_c relationship assuming constant stress drop. From Allmann & Shearer (2009)*

The main difficulties arising when analyzing moment duration scaling of slow slip events are the observational gaps and the limitations in the magnitude range covered by individual studies.

Another interesting scaling law characterizes a particular type of earthquakes called repeating earthquakes. Such events are observed on many tectonic faults and subduction zones all over the world, and correspond to the repetitive activation of the same fault patch (Poupinet *et al.* , 1984; Nadeau *et al.* , 1995; Nadeau & McEvilly, 1997; Nadeau & Johnson, 1998; Bürgmann *et al.* , 2000; Chen *et al.* , 2007). The recurrence time of failure T_r is typically observed to scale as $M_0^{1/6}$, M_0 being the seismic moment (figure 1.3).

Beyond the analysis of individual source processes, the interactions occurring between different slip events have received lots of attention. One of the most simple example is the occurrence of main shock-aftershock sequences, where a large earthquake triggers other smaller events, each of them generating its own sequence in a cascading process. This issue is commonly analyzed using statistical approaches, aiming at decrypting the spatio temporal structure of sequences of slip events, and the structure of the associated energy release. In the case of regular earthquakes, the statistical approach has allowed to define four empirical laws.

The first one illustrated in figure 1.4 is named Gutenberg-Richter law (Gutenberg & Richter, 1944). It states that the magnitudes of earthquakes occurring in a bounded spatio temporal region follow a power law distribution of the form:

$$N(m) = 10^{k-bm}, \tag{1.1}$$

where $N(m)$ is the number of events with magnitude exceeding m, k is a constant depending on the catalog analyzed, and b a decay exponent, typically ranging from 0.5 to 2 (El-Isa & Eaton, 2014).
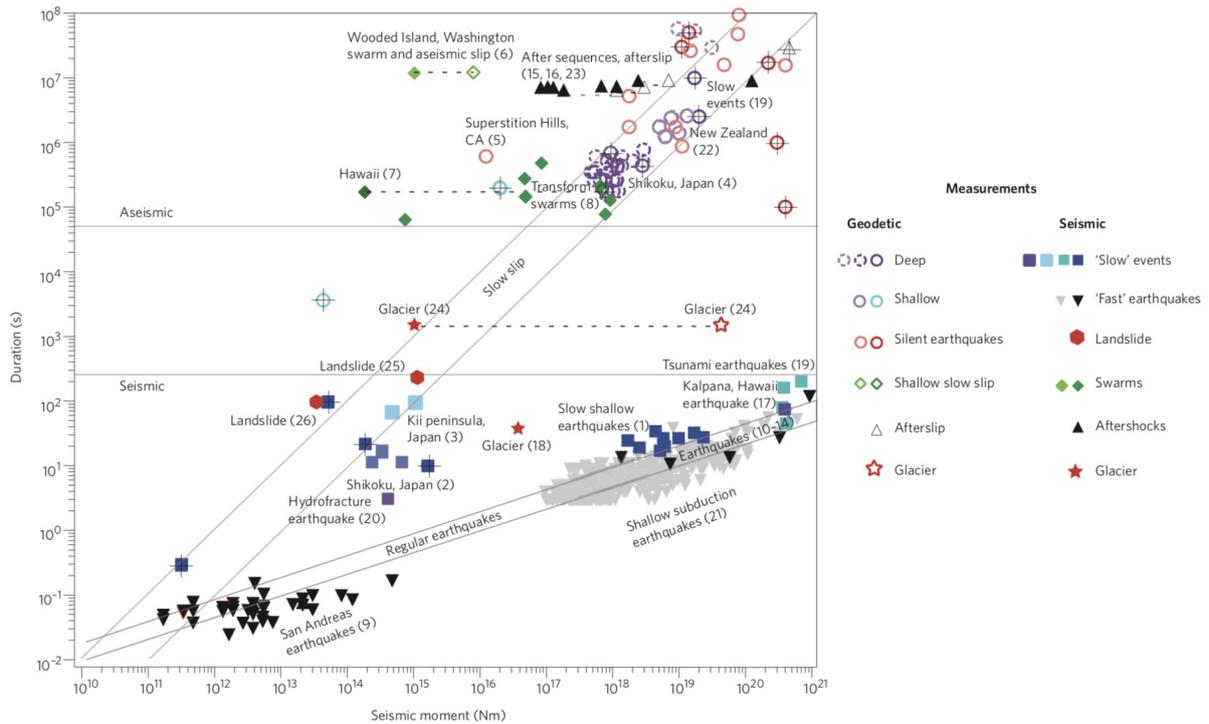
Figure 1.2: *Earthquake and slow slip moment-duration scaling. From Peng & Gomberg (2010)*
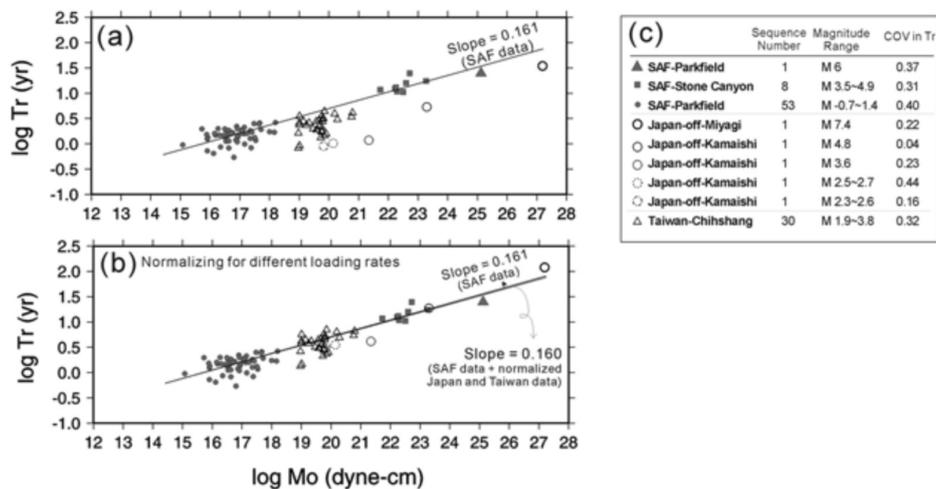
Figure 1.3: *Recurrence time vs. seismic moment for several repeating earthquake sequences in California, Japan and Taïwan. From Chen* et al. *(2007)*

The second well established statistical law of earthquakes interaction is the Omori decay of aftershock sequences (Omori, 1894; Utsu *et al.* , 1995). Following a main shock, the rate of aftershocks R_a decays as an inverse power law of time. Generally, we have:

$$R_a(t) = \frac{K_a}{(c_a + t)^{p_a}}, \tag{1.2}$$

where t is the time from the main shock, c_a is a characteristic time marking the onset of power law decay, K_a measures the productivity of events, and p_a the decay exponent. Analysis
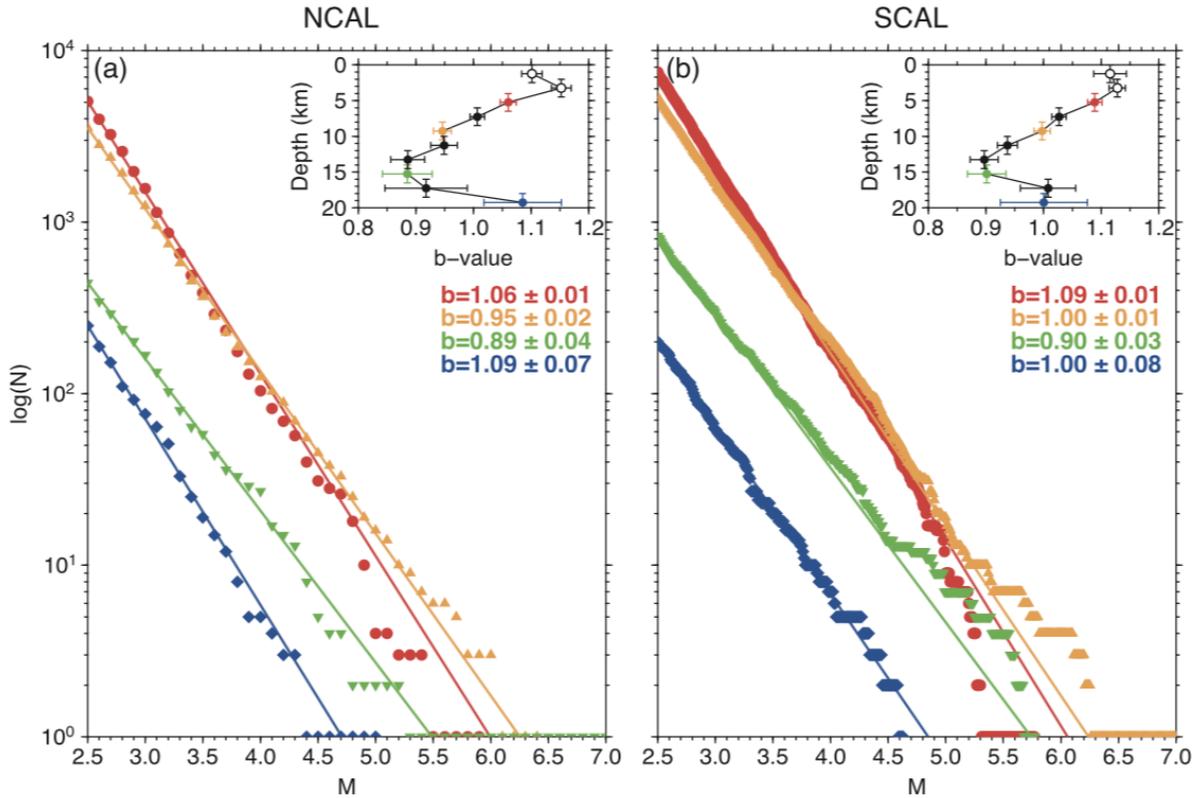
Figure 1.4: *Magnitude-frequency distributions for earthquakes in California showing the Gutenberg-Richter decay. The b-value here depends on the depth of earthquakes. From Spada et al. (2013)*

of earthquake catalogs show that p_a typically varies between 0.9 and 1.5 (Utsu *et al.* , 1995), and increases with main shock magnitude (Ouillon & Sornette, 2005; Hainzl & Marsan, 2008). The productivity K_a of aftershock sequences is also known to increase exponentially with the main shock magnitude (Console *et al.* , 2003; Helmstetter, 2003; Felzer *et al.* , 2004; Helmstetter *et al.* , 2005; Zhuang *et al.* , 2004, 2005; Hainzl & Marsan, 2008). An example of Omori decay of aftershock rate is presented in figure 1.5. The largest aftershock of the sequence is in general one point of magnitude lower than the main shock (this result is known as the Bath's law).

Foreshocks (when observed) also follow a similar Omori law, in the sense that the rate of events during foreshock sequences increases as a power law of time prior to the main shock (Jones & Molnar, 1979; Bouchon *et al.* , 2013). The acceleration of foreshock production prior to large interplate earthquakes is illustrated in figure 1.6.

More generally, the study of earthquake swarms and background activity (where no main shock aftershock sequences could be defined) has demonstrated that the time delays separating successive events follow a gamma distribution, where the power law decay at short time is an indicator of the degree of clustering in the sequence (Hainzl *et al.* , 2006). Examples of such distributions for earthquakes in California are shown in figure 1.7.

In addition to the temporal statistics and magnitude statistics, the interaction between earthquakes is characterized by influence kernels decaying as inverse power laws of the distance and time (Marsan & Lengline, 2008). An interaction kernel could be seen as the intensity of direct, or indirect seismic activity triggered by a particular event. Intensities estimated from California seismicity are illustrated in figure 1.8. The temporal component is essentially the Omori law. The spatial component could be seen as the signature of the decay of elastic stress (static and
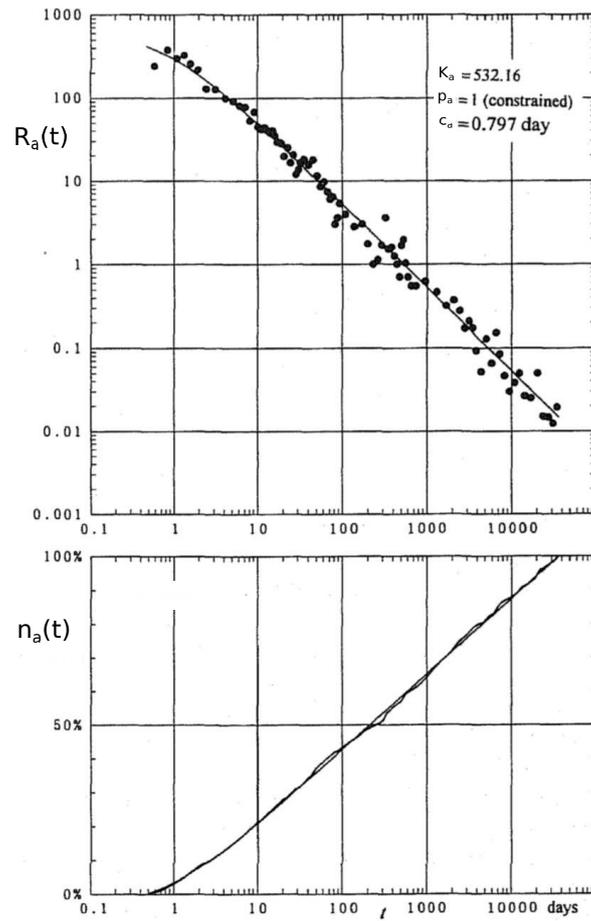
Figure 1.5: *Rate $R_a(t)$ and cumulative number $n_a(t)$ of of aftershocks felt at Gifu after the Nobi earthquake in 1891. t is time from the main shock. Dots in the top figure are observations. The smooth line is a fit of the rate of aftershocks using the Omori law (1.2) with $p_a = 1$. From Utsu et al. (1995).*
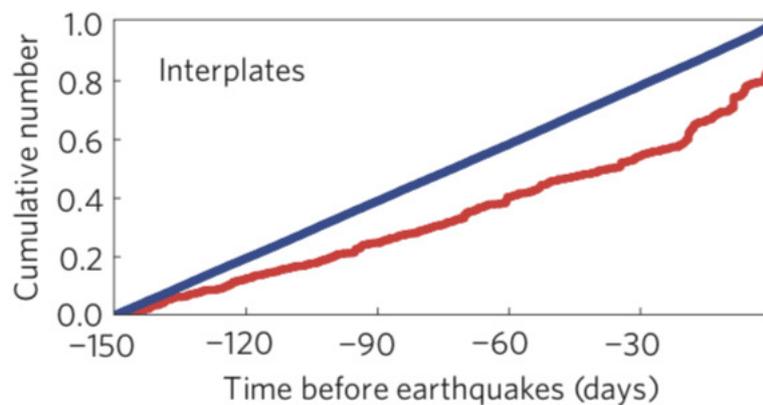
Figure 1.6: *Acceleration of foreshock production prior to large interplate earthquakes.   The red line is a stack of several sequences, the blue line is a prediction of an ETAS model. From Bouchon et al. (2013)*

14
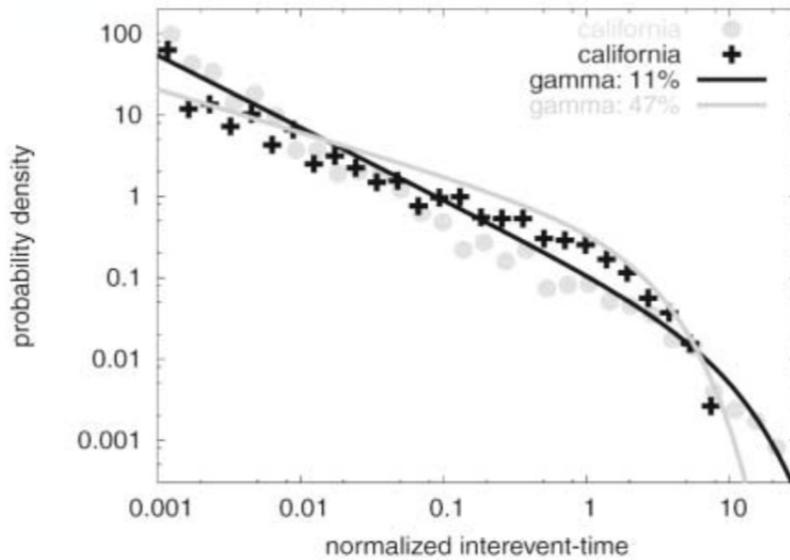
Figure 1.7: *Distributions of interevent time delays for two regions in California (black and gray symbols). The fits with a gamma distribution (corresponding to 11 % and 47 % of main shocks in the catalog) are shown by the solid lines. From Hainzl* et al. *(2006).*

dynamic) redistribution with distance associated with elastic dislocations and cracks involved in earthquake sources.

All these empirical statistical laws are well documented for regular earthquakes, and could be seen as a consequence of stress redistribution between earthquakes. However, the underlying mechanics is still poorly understood. Many mechanisms are identified as playing a role in this redistribution: static stress transfers (King *et al.* , 1994; Toda *et al.* , 1998), dynamic (wave-mediated) stress transfers (Brodsky *et al.* , 2000; Kilb *et al.* , 2000; Felzer & Brodsky, 2006), imbricated slow aseismic slip and postseismic slip (Schaff *et al.* , 1998; Perfettini & Avouac, 2004), poroelastic effects associated with fluid flow at depth (Bosl & Nur, 2002). However, the attempts to relate empirical parameters appearing in the statistical laws to mechanical parameters remain extremely limited. The b-value of Gutenberg Richter decay as been proposed to follow a linear relationship with differential stress on the basis of laboratory experiments (figure 1.9) (Amitrano, 2003; Scholz, 2015) and on the observation of b-value dependence with depth and faulting mechanism (figure 1.4) (Schorlemmer *et al.* , 2005; Spada *et al.* , 2013), but this observation is not supported by a general theory. One of the most advanced attempts to relate statistical properties to mechanical parameters is the model proposed by Dieterich (1994) leading to a relationship between Omori law parameters and frictional parameters characterizing tectonic faults.

The interaction between other types of slip events seems to lead to similar statistics. In particular, the duration of tremor bursts and the magnitude of slow slip events in Cascadia subduction zone follow a Gutenberg-Richter like distribution (Wech *et al.* , 2010; Michel *et al.* , 2019), as illustrated in figure 1.10.

Furthermore, the low frequency earthquakes (LFE) bursts observed during slow slip events seem also to follow the same spatio-temporal statistics as regular earthquakes (Lengliné *et al.* , 2017a), in the sense that interaction kernels decay as power laws of time from a main event (figure 1.11). Here again, the mechanics generating these statistics is still poorly understood.
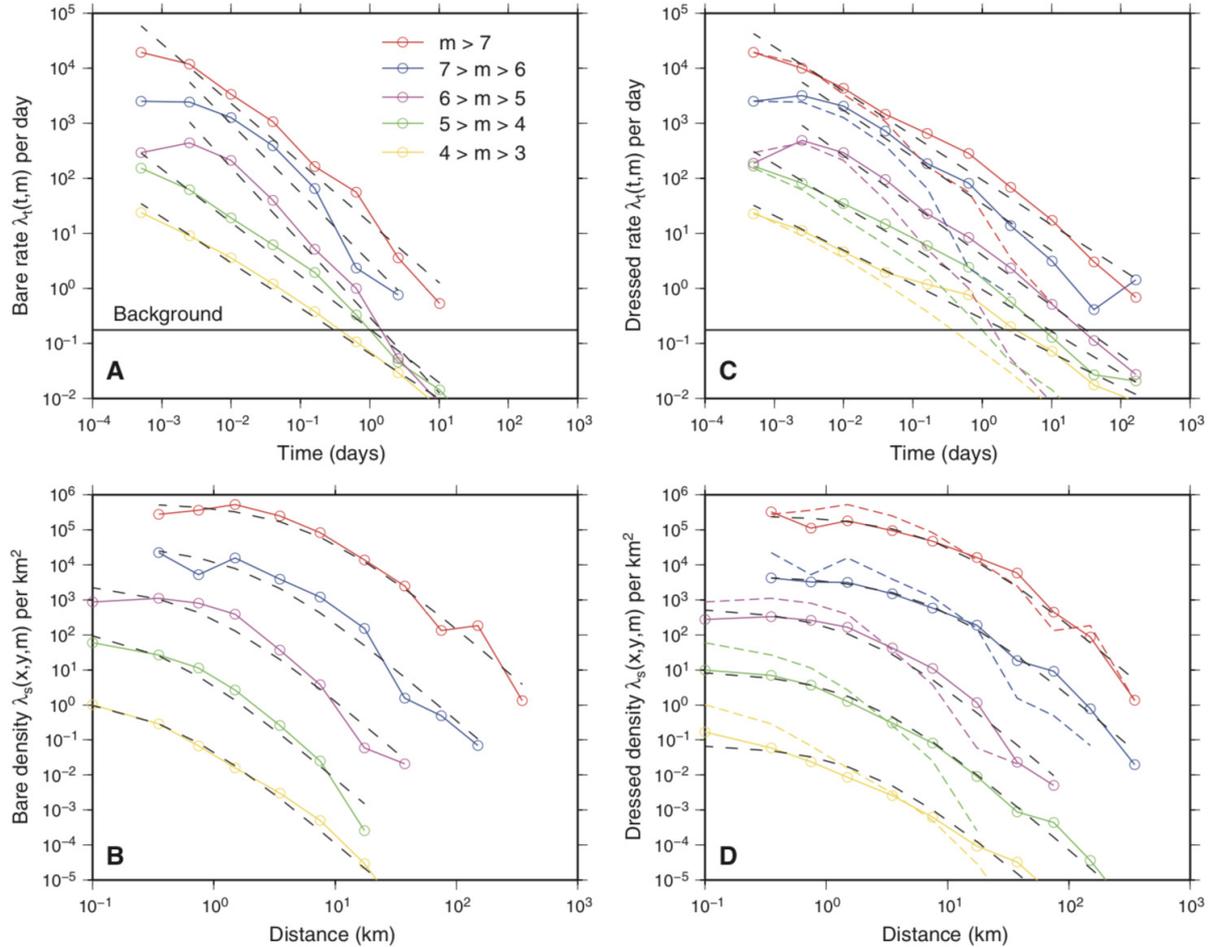
Figure 1.8: *Temporal rates and densities of aftershocks characterizing seismicity in California, for different main shock magnitudes m. A and B are bare kernels representing the direct aftershocks of a particular event. C and D represent the observed dressed kernels, accounting for all the indirectly triggered events of a particular main shock. Dashed colored lines represent the bare kernels of figure A and B. Black dashed lines are power law fits to the estimated kernels. From Marsan & Lengline (2008).*

1.1.2 Imbricated slip : seismic, aseismic and fluids

A particularly interesting observation is the common imbrication of different types of slip events on the same tectonic fault. Many earthquakes are for instance associated with aseismic slip episodes. Large earthquakes are often followed by postseismic slip that activates nearby regions of the earthquake source, several days to several years after the main event (Langbein *et al.* , 1983; Savage *et al.* , 1994; Bürgmann *et al.* , 1997; Cakir *et al.* , 2003; Ozawa *et al.* , 2011). Postseismic slip rate usually follows an Omori law. Many studies also report evidences for accelerating aseismic slip before large and moderate earthquakes. This has been shown in particular before moderate earthquakes in California (Dodge *et al.* , 1996), before the 2011 Tohoku earthquake in Japan (Kato *et al.* , 2012), before the 2014 Iquique earthquake in Chile (Ruiz *et al.* , 2014), and more generally for large interplate (subduction) earthquakes (Bouchon *et al.* , 2013).

Note also that repeating earthquakes could be interpreted as the repetitive failure of a brittle asperity loaded by slow aseismic slip. Here again, slow slip and seismic slip (earthquakes) closely interact. The seismic activity generated by a population of repeating earthquake sources is
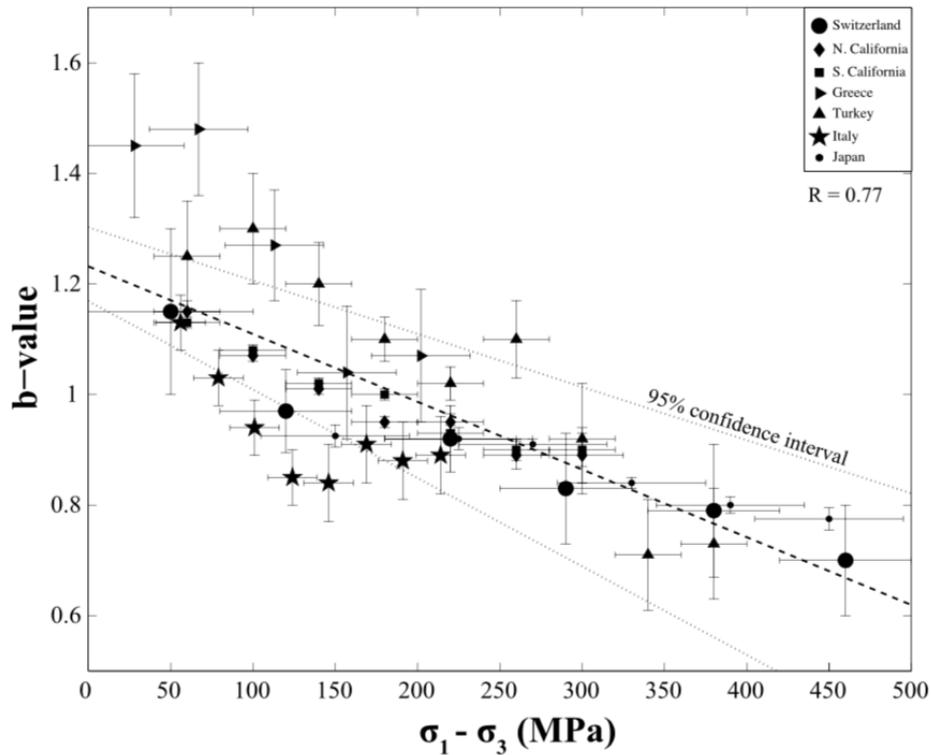
Figure 1.9: *b-value dependence with differential stress. From Scholz (2015).*
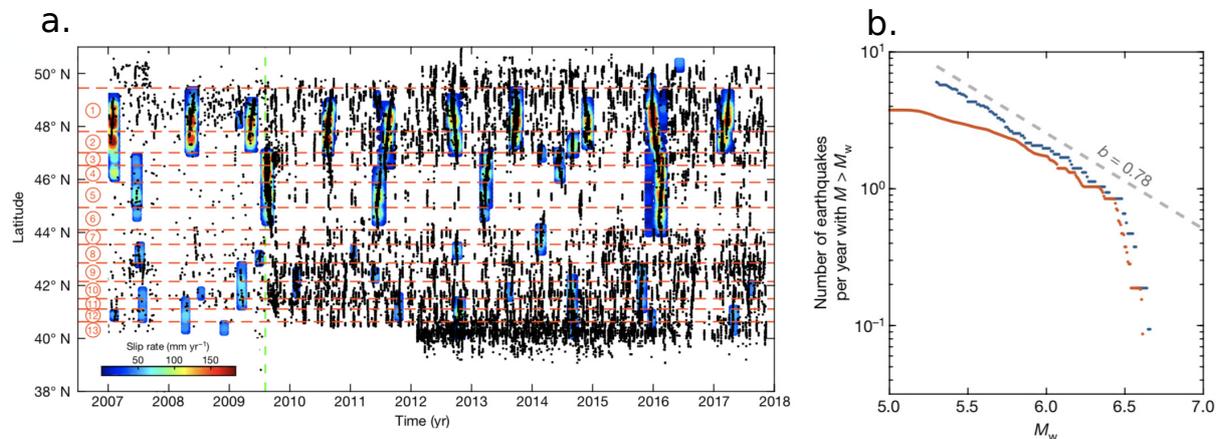
Figure 1.10: *a. Slow slip events (SSE, colored patches) and tremor bursts (black dots) in Cascadia subduction zone. b. Two estimations of the magnitude-frequency distribution of SSEs in Cascadia. From Michel et al. (2019).*

generally affected by stress transfers mediated by fault creep (Chen *et al.*, 2013).

Another interesting example of imbrication comes from the so called Episodic Tremor and Slip (ETS) that periodically activate the Cascadia and Japanese subduction zones (Rogers & Dragert, 2003; Obara *et al.*, 2004). ETS consist of the propagation of large slow slip fronts , (strong enough to be detected by geodetic methods) associated with tremor bursts. These tectonic tremor bursts are made of a superposition of smaller but faster (and thus more radiative) slip events called low frequency earthquakes. The sources of tremor are generally co-located with
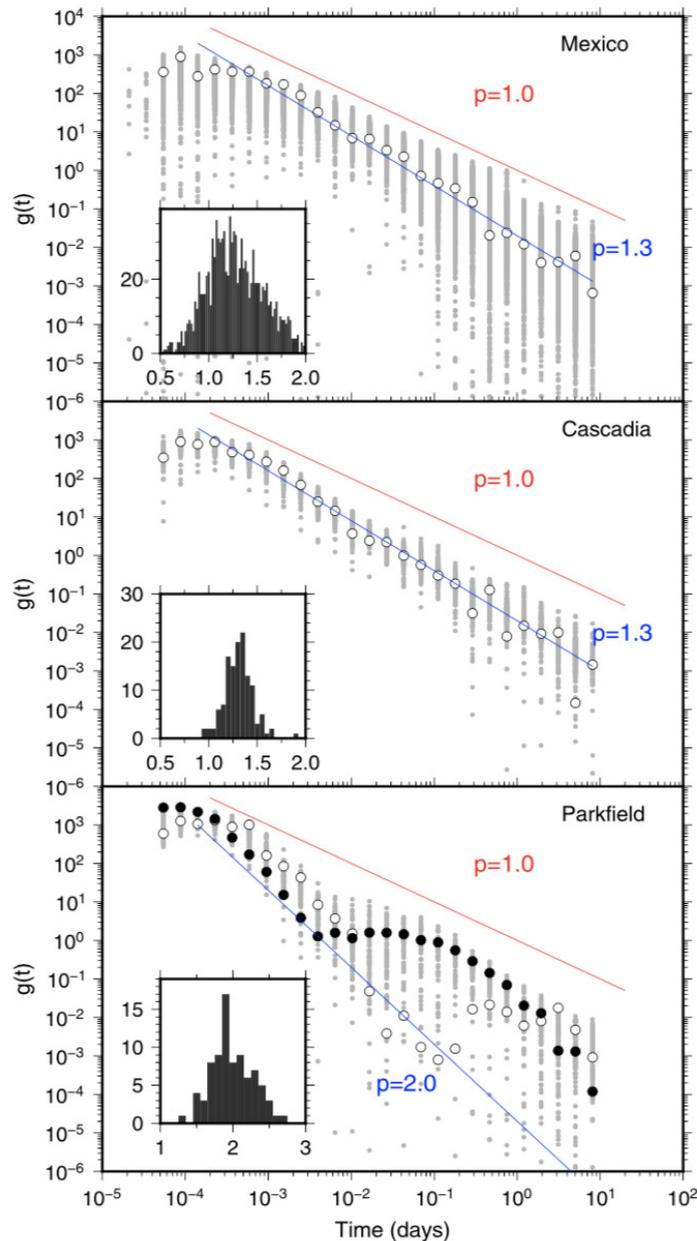
Figure 1.11: *Interaction kernel g(t) for families of low frequency earthquakes (LFE) in Cascadia, Mexico and California. t is time from the main event. From Lengliné et al. (2017a).*

slow slip fronts (Bartlow *et al.*, 2011), and the two processes are therefore strongly related.

Geophysical studies conducted over the past decades have also shown that fluids often play a significant role in the trigerring and development of fault slip. This is in particular suggested by the various seismic sequences induced by fluid operations at depth performed in the framework of georessources exploitation (hydro-fracturation, waste-water disposal, geothermal exploitation, reservoir lake impoundment etc.) (Shapiro *et al.*, 2006; Deichmann & Giardini, 2009; Shapiro & Dinske, 2009a; Dinske *et al.*, 2010; Ellsworth, 2013; Diehl *et al.*, 2017). Fluid induced seismicity could be triggered if pore pressure reduces the effective normal stress on critical faults (i.e. being critically stressed by tectonic forces) and brings them closer to the reactivation threshold (Mohr-Coulomb criterion for instance). Fluids are also strongly suspected to drive many natural micro-seismic sequences: this is for instance the case for swarms in the Corinth Rift (Bourouis

& Cornet, 2009; Duverger *et al.* , 2015; De Barros *et al.* , 2020) and in western Bohemia (Hainzl & Fischer, 2002; Hainzl *et al.* , 2012). This idea is further supported by observations of seismic swarms triggered by rainfall events (Kraft *et al.* , 2006).

In situ fluid injection experiments into tectonic faults (Guglielmi *et al.* , 2015) have furthermore demonstrated that fluids do not only trigger earthquakes but also aseismic slip on preexisting faults. Detailed analysis of induced earthquake sequences have furthermore shown that fluid injections generally result in aseismic slip and earthquakes (Bourouis & Bernard, 2007; Lengliné *et al.* , 2017b; De Barros *et al.* , 2019, 2020). The mechanism suggested by these latter observations consists of a slow (aseismic) slip front triggered by the fluid injection, with earthquakes being the byproduct of slow slip. For many fault slip phenomena, an imbrication between fluid flow, slow slip and rapid slip (earthquakes) is therefore suspected.

Although slow slip and fluid flow seem to be crucial in the processes releasing energy on tectonic faults, they tend to be more difficult to observe than regular earthquakes. This is mainly because both slow slip and fluid flow generate weaker deformation signals, and do not radiate strong elastic waves. This is particularly true when they occur at important depths. The imbrication of slow slip and fluid flow with more radiative events (regular and/or low frequency earthquakes) allows to use the dynamic radiative events to monitor the silent deformation at depth. This is what is usually done when slip on repeating earthquakes is used to estimate creep rate at depth (Uchida *et al.* , 2003), or when tectonic tremor and LFEs are used to detect slow slip events on tectonic faults (Frank, 2016; Rousset *et al.* , 2019).

1.1.3 Mechanical control

The observations summarized in the first section of this manuscript show that many unresolved questions remain concerning the quantification and the mechanical control of fault slip phenomena. Two subjects deserve particular attention:

> 1. What is the mechanical control of tectonic fault slip process and empirical scaling laws parameters?
>
> 2. What does seismic activity, and more generally radiative slip events reveal on silent slow slip process and fluid flow at depth?

These two questions have been at the core of my research activities over the past years. In order to explore them, I have developed and extensively used physics-based fault models, and performed some theoretical developments. All the numerical and theoretical results are discussed and compared to observations of fault slip. During this period, I have also been involved in different analysis of seismological data, and in one laboratory study, that are included in the following chapters.

In the next section, I will show what mechanical models could bring to our understanding of fault slip phenomena, and I will present the class of models I have been developing.

1.2 Mechanical models of faults

1.2.1 Conceptual model : creep and asperities

The observations of imbricated slow and seismic slip suggest the conceptual model of heterogeneous tectonic fault illustrated in the central diagram of figure 1.12. In this model, earthquakes, and more generally radiative (or fast) slip events result from the failure of brittle asperities embedded in a more ductile material, that creeps under tectonic loading associated with plate motion.

The heterogeneity of fault material is also suggested by outcrops of exhumed fault cores showing a mixture of brittle blocs of different sizes distributed in a ductile material (Fagereng

& Sibson, 2010). The asperity model could also explain the interseismic slip pattern shown by geodetic estimates of coupling along subduction interfaces (Yoshioka *et al.* , 1993; Vigny *et al.* , 2009; Métois *et al.* , 2012).

Geologic evidences suggest also that the fault material is permeable (Faulkner *et al.* , 2010), so that fluids can eventually flow and modify the stresses on the creeping sections and on asperities.

1.2.2   Elasticity and friction

One way to model fault slip is to consider faults as systems coupling elasticity, friction and fluids. Elasticity is what allows crustal rocks to store energy supplied by plate motion, and friction is what controls the way this energy is released through slip events.

The first attempts to model fault slip are the Burridge-Knopoff models (Burridge & Knopoff, 1967; Carlson *et al.* , 1994). They consist of arrays of sliders related by springs and pulled at a constant rate on a planar support. Many different frictional laws have been considered in the literature. The main outcome of these models is their ability to reproduce cascades of slip events following a Gutenberg-Richter statistics. However such models ignore important aspects of the physics of fault slip. In particular, the use of springs prevents the occurrence of long range stress transfers expected to occur in the brittle crust. A different approach developed at the same period is the model by Dieterich (1994) assuming a population of non-interacting spring and sliders obeying a rate-and-state friction law (Dieterich, 1979; Ruina, 1983). This model has been one of the only models providing an interpretation of the decay exponent of the Omori law in terms of frictional parameters. However, stress transfers are neglected, and no magnitude could be predicted in this model. Note also that spring and slider models reproduce the slip rate associated with postseismic slip (Marone *et al.* , 1991; Perfettini & Avouac, 2004) and more generally are able to produce the full range of slip rate observed during fault slip events (Helmstetter & Shaw, 2009).

Later models have been developed consisting in a frictional interface between continuous elastic media (Dieterich, 1992; Rice, 1993; Lapusta *et al.* , 2000). Here again, different friction laws could be used, calibrated on rock friction experiments. Such models were successful in reproducing many features of tectonic fault slip: coseismic rupture (Geubelle & Rice, 1995; Cochard & Rice, 1997; Madariaga *et al.* , 1998; Lapusta *et al.* , 2000; Ide & Aochi, 2005; Gallovič *et al.* , 2019; Ulrich *et al.* , 2019), earthquake nucleation (Dieterich, 1992; Favreau *et al.* , 1999; Rubin & Ampuero, 2005; Ampuero & Rubin, 2008), postseismic slip (Perfettini & Ampuero, 2008). At the scale of the earthquake cycle, these models are known, under rate-and-state friction (Dieterich, 1979), to generate cycles of characteristic earthquakes, and thus provide a good model for repeating earthquakes (Chen & Lapusta, 2009; Cattania & Segall, 2019). moment-duration scaling, and moment-recurrence scaling are also generally reproduced. However, earthquake complexity and the earthquake statistical laws (in particular Omori law and Gutenberg-Richter law) are difficult to obtain with such models, unless the continuum limit is exceeded and the model becomes similar to a spring and slider array (Rice, 1993), or a certain amount of frictional heterogeneity is introduced (Ide & Aochi, 2005). Recently, it has been shown that some complexity could arise if the fault length is much larger than the critical nucleation length allowing instabilities to develop (Cattania, 2019).

The collection of models coupling elasticity and friction developed over the past decades therefore reproduce most of the phenomenology about slip events. Considering the whole spectrum of models, the whole range of fault slip rate has been obtained, some scaling laws have been reproduced (constant stress drop, moment-duration scaling for earthquakes and slow slip events, some of the statistical laws). However, some observations still remain unexplained by current models. More importantly, the mechanical control on fault slip characteristics is generally not really understood. Most of the modeling studies do not propose a systematic study of what mechanical parameter is crucial in reproducing a particular observation. This is particularly the case for statistical laws reflecting interaction (Omori and Gutenberg Richter) and for scaling

laws (moment-duration and moment-recurrence), where observed tendencies are not explained in terms of mechanical parameters. Many processes are (for the same reason) not fully understood, in particular what controls the rupture speed and the stress drop during slip events on faults.

1.2.3 Using fault models to study mechanical control of fault slip

The fault models I have been developing to study fault slip belong to the category of models coupling elasticity and laboratory derived rate-and-state friction (Dieterich, 1979) at the scale of a planar fault. They are coupled, when necessary, to fluid diffusion. A summary of all the models discussed in this manuscript is presented in figure 1.12. In the following chapters, I will refer to this figure for each numerical study developed.

The rate-and-state friction law assumes that friction evolves with instantaneous slip rate v and past slip history along the fault. In this framework, the friction coefficient f could be written as (Dieterich, 1979):

$$f_f = f_0 + a \ln \frac{v}{v^*} + b \ln \frac{v^* \theta}{d_c}, \tag{1.3}$$

where f_0, a, b are dimensionless coefficients, d_c is a critical slip distance and v^* a reference slip rate. The dependence on slip history is captured by the state variable θ with dimensions of time. The evolution of θ is given by a state evolution law (Ruina, 1983) that can take different forms. The most popular state evolution laws are the aging and slip laws:

$$\begin{cases} \dot\theta = 1 - \dfrac{v\theta}{d_c}, & \text{"aging law"} \\[2mm] \dot\theta = -\dfrac{v\theta}{d_c} \ln \dfrac{v\theta}{d_c}, & \text{"slip law"} \end{cases} \tag{1.4}$$

At steady state ($\dot\theta = 0$), the friction coefficient f_{ss} only depends on slip rate v:

$$f_{ss} = f_0 + (a - b) \ln \frac{v}{v^*}. \tag{1.5}$$

It can be shown that when coupled to an elastic system, frictional instabilities (or slip acceleration) only develop when $a - b < 0$. This is called *velocity weakening* friction, since steady state friction coefficient decreases with increasing slip rate. Slip acceleration then occurs on a fault patch of characteristic length L_c (Dieterich, 1992; Rubin & Ampuero, 2005), so that such instabilities are only possible on faults larger than L_c. For that reason, L_c is called the critical nucleation length. Earthquakes could be seen as frictional instabilities bringing faults from slow to fast slip.

When $a - b > 0$ on the other hand, slip is stable. From equation (1.5), this behavior is called *velocity strengthening*, and could be used to model stable creep and slow aseismic slip.

Importantly, rate-and-state friction allows for frictional healing, that is increase of frictional strength when fault slip is negligible. As illustrated by the aging law in equations (1.4), θ increases linearly with time when the slip rate v is negligible, so that friction coefficient increases with the logarithm of time. This property allows to produce successions of frictional instabilities under slow tectonic loading, or in other words earthquake cycles.

Because it allows for rapid slip, slow asesimic slip, and earthquake cycles, rate-and-state friction is a good candidate to model fault slip processes. This is the reason why the majority of the models discussed here (figure 1.12) are based on rate-and-state friction.

As illustrated in figure 1.12, models were either 2D (i.e. 1D fault within a 2D elastic medium) or 3D (i.e. 2D fault within a 3D elastic medium). Whenever simulations are performed to study magnitudes and seismic moments, 3D models are more suitable, because they allow to compute those quantities without making any approximations. 3D simulations could however be extremely time consuming, in particular when long earthquake sequences are needed to analyze statistics.

For that reason, some of the parametric studies shown here were conducted with 2D simulations. Most of the time, the question remains whether the results could be extended to 3D, and as far as possible this issue is discussed.

The different models also consider either constant, homogeneous friction, or heterogeneous friction. In many situations, I have modeled the fault material heterogeneity as heterogeneities in the $a - b$ rate-and-state frictional parameter. This allows to generate both unstable (velocity weakening $a - b < 0$) and stable (velocity strengthening $a - b > 0$) frictional behavior on the same fault. Seismogenic asperities (brittle asperities) are typically modeled as velocity weakening patches distributed on a velocity strengthening region, subject to stable creep. The velocity strengthening regions on the fault are also called barriers hereafter. As shown later, the fault material heterogeneity has also been modeled with non uniform critical slip distance d_c.
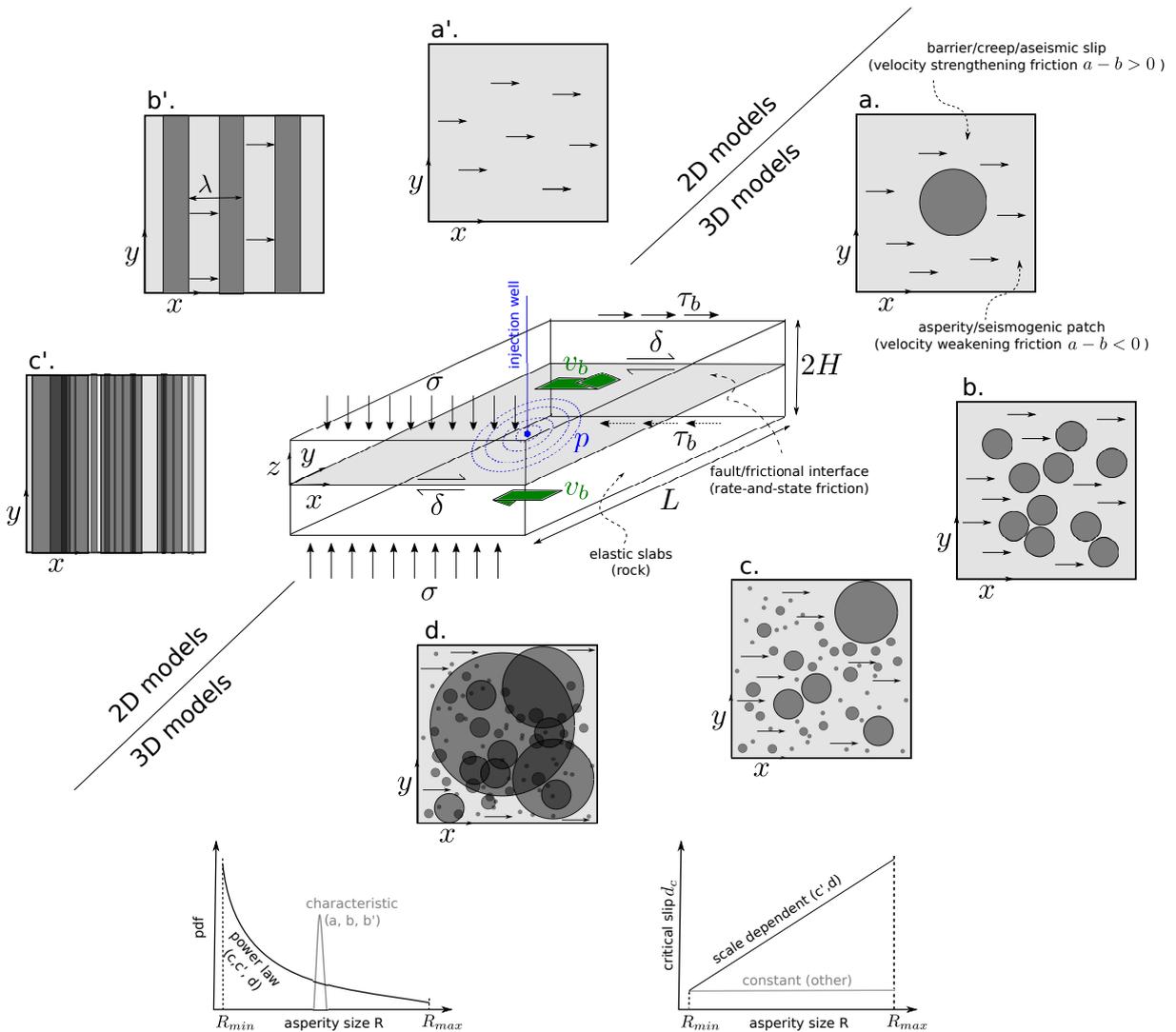
Figure 1.12: *Asperity models. In these models, a fault is a frictional planar interface embedded in an elastic medium. The fault is loaded by a normal stress σ and a remote shear stress τ_b of tectonic origin. A far field constant deformation rate v_b is sometimes assumed. The interface is also possibly permeated with a diffusing fluid at pressure P. Slip δ along the fault is resisted by rate-and-state friction (equation 1.3). Brittle asperities (dark gray patches) are distributed on the interface. Possible distributions of asperity sizes R and critical slip distances d_c are illustrated in the bottom diagrams. The different types of frictional heterogeneity discussed in this manuscript are illustrated in the diagrams a, b, c and d (3D models) and a', b' and c' (2D models).*

In computing the stress redistributions along the fault, I essentially made use of the quasi-dynamic approximation originally proposed by Rice (1993). Under this assumption, the elastic shear stress on the fault τ_e (that has to be balanced by frictional stress) could be written in the form:

$$\tau_e = \tau_b + \mathcal{K} * (\delta - v_b t) - \eta v, \tag{1.6}$$

where, τ_b incorporates the far field loading, the second term on the right hand side corresponds to the static component of stress, and the last term approximately accounts for elastic wave radiation from the fault. The static term involves a stress kernel $\mathcal{K}$ that depends on the geometry of the problem (half spaces or finite thickness slabs in contact, periodic or non periodic fault) and the reduced slip $\delta - v_b t$ (the star denotes a spatial convolution). The last term involves the slip rate v and the radiation damping η defined as:

$$\eta = \frac{\mu}{2c_s}, \tag{1.7}$$

where μ and c_s are the shear modulus and the shear wave speed of the elastic media in contact. Pore pressure is generally considered through an effective normal stress $\sigma - P$. The numerical approach consists of finding the fault slip history that satisfies the following shear stress balance:

$$\tau_e = f_f(\sigma - P). \tag{1.8}$$

In the following chapters, I will show how such models could be used to investigate the question of the mechanical control of fault slip scaling and statistical laws, and to quantify aseismic and fluid flow at depth from the analysis of seismicity. The remaining of the manuscript is organized as follows: in the second chapter, I present the progress I have made about the mechanical control on fault slip processes, scaling and statistical laws. The third chapter is dedicated to my contributions to the use of seismicity to unravel slow slip processes and fluid flow at depth. The last chapter is a description of my research projects which extend the use of physics-based model to the interpretation of deep processes and laboratory experiments.

Chapter 2

Mechanical control on earthquake statistics and fault slip scaling laws

In this chapter I present an overview of my work about the physical control of the main empirical statistical and scaling laws of seismology. The mechanisms driving the onset of swarms and damaging earthquakes, the Gutenberg-Richter magnitude-frequency distribution, the Omori decay of aftershocks, the moment-duration scaling of slow slip events, the moment-recurrence scaling of repeating earthquakes, the emergence of precursory phenomena and the self-similarity of growing earthquake ruptures are successively considered. The approach used is generally based on parametric studies making use of different frictional fault models (illustrated in figure 1.12), along with theoretical developments. Laboratory experiments and seismological data are used to some extent as well, in the study of earthquake rupture growth.

2.1 Regimes of activity : characteristic system-size ruptures vs. continuous activity

Different regimes of seismic activity are commonly observed: regular background seismicity, micro-earthquake swarms, characteristic (or repeating) earthquakes, foreshock-main shock-aftershock sequences, seismic quiescence. In many cases, the earthquakes are interpreted as the failure of brittle asperities embedded in a single creeping fault zone, loaded by a constant remote tectonic loading. In this framework, several fault models assuming a planar frictional interface embedded in an elastic rock medium have been able to reproduce these different regimes (Burridge & Knopoff, 1967; Rice, 1993; Lapusta *et al.* , 2000; Ziv, 2003; Ziv & Cochard, 2006). I have contributed to this effort by analyzing the regimes of seismic activity generated by a population of unstable rate-and-state asperities distributed on a planar creeping frictional interface (**Dublanchet, P.** *et al.* , 2013a). The model used in this study is illustrated in figure 1.12b. The main result from this study is presented in figure 2.1.

Under constant tectonic loading and quasi-dynamic stress transfers (Rice, 1993), this population of asperities releases the tectonic stresses in two different modes. The first one (regime I) consists of a continuous seismicity involving isolated ruptures of individual asperities. The magnitude content is essentially controlled by the size distribution of the asperities (in this study, all asperities had the same size, leading to one dominant magnitude). The second mode (regime II) consists of the periodic occurrence of short clusters of strong activity. These swarms involve ruptures of isolated and groups of asperities, and typically degenerate into a main shock, or system-size rupture where the whole fault (asperities and aseismic barriers) slip at radiative rates.

It could be shown that the transition between the two regimes of activity is controlled by the density of asperities ρ defined as the ratio between the fault surface occupied by seismo-
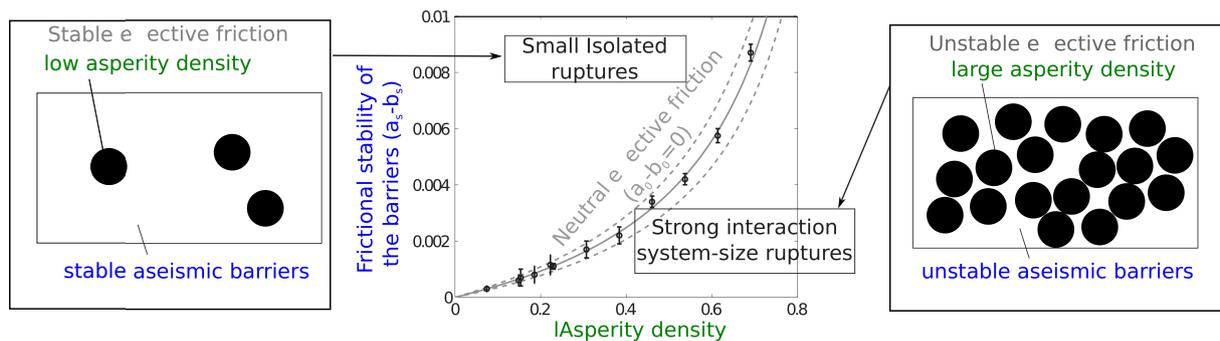
Figure 2.1: *Regimes of seismic activity generated by a population of seismogenic asperities distributed on a creeping rate-and-state fault, from **Dublanchet, P.** et al. (2013a). Barriers correspond to inter-asperity fault regions. Middle: transition from a regime of continuous activity with isolated ruptures (regime I) to clustered activity with system-size ruptures (regime II) as a function of asperity density and frictional properties of the barriers ($a_s - b_s$ rate-and-state frictional parameter). Dots indicate numerical results, gray (solid and dashed) lines to theoretical estimates assuming different values of the asperities stress drop. Theoretical estimates correspond to a vanishing average value of the $a - b$ rate-and-state parameter. Left and Right: schematic diagrams of the frictional conditions leading to the different regimes of activity.*

genic asperities and the total fault area. When ρ increases beyond a critical density ρ_c, the seismic activity switches from regime I (continuous activity) to regime II (clusters and system-size ruptures). This critical density of asperities depends on the frictional properties of the fault interface: it is precisely the asperity density leading to an effective neutral frictional behavior (the average $a - b$ rate-and-state frictional parameter vanishes).

This study has allowed to define the concept of *critical asperity density* that is used in many of the different studies I have been conducting in the following years. It is also what initiated my interest for the study of effective frictional behavior (see section 4.3 of my research perspectives for details).

2.2   Magnitude-frequency distribution : what controls b-value

Preliminary remark: in this section, b corresponds to the b-value of the Gutenberg-Richter law defined in equation (1.1), and not the rate-and-state frictional parameter b of equation (1.3).

One of the most robust observation about earthquakes is the Gutenberg-Richter magnitude-frequency distribution (Gutenberg & Richter, 1944), where magnitude distribution follows equation (1.1). If the k parameter of the Gutenberg-Richter law depends on the observation window, the b value is generally of the order of 1, with slight variations in the range $0.5 - 2$ (El-Isa & Eaton, 2014). As mentioned in the introduction section, such variations are usually attributed to differential stress acting on faults (Scholz, 1968; Amitrano, 2003; Schorlemmer *et al.*, 2005; Goebel *et al.*, 2013; Scholz, 2015). Here again, many fault models and earthquake simulators produce a power law distribution of magnitudes (or energy release) (Burridge & Knopoff, 1967; Rice, 1993; Ziv & Cochard, 2006; Ide & Aochi, 2005) characterized by a b-value of the order of one, but the physical origin of this distribution remains unclear. More importantly, the physical mechanisms underlying the stress dependence of b-value are still not well understood.

In this framework, I have analyzed the b-value in synthetic seismicity produced by different fault models in **Dublanchet, P.** *et al.* (2013a), **Dublanchet, P.** (2019a), **Dublanchet, P.** (2020) and Almakari, M.*et al.* (2019) (as co-supervisor of Michelle Almakari's PhD). Here I will focus on the last two studies which discuss in more details the mechanical origin of b-value stress

dependence. Both of them assume a planar and heterogeneous frictional interface between elastic media. The frictional heterogeneity consists here of a superposition of overlapping patches with sizes and critical slip d_c following a power law distribution as illustrated in figures 1.12c' and 1.12d. The scale dependence of d_c was initially proposed by Ide & Aochi (2005) to account for the scale dependence of fracture energy (Abercrombie & Rice, 2005). In the first case (**Dublanchet, P.**, 2020), a 2D fault was considered along with a constant remote tectonic loading (figure 1.12d). In the second case (Almakari, M.*et al.* , 2019), a 1D fault is assumed (figure 1.12c'), and slip is driven by both tectonic loading and the diffusion of pore pressure. In both cases, the simulations were performed under different levels of effective normal stress: in the first case this was achieved by changing the lithostatic stress σ, and by imposing a pore fluid pressure in the second case. Because of frictional contact, this induces changes in both normal and shear stress on the fault.
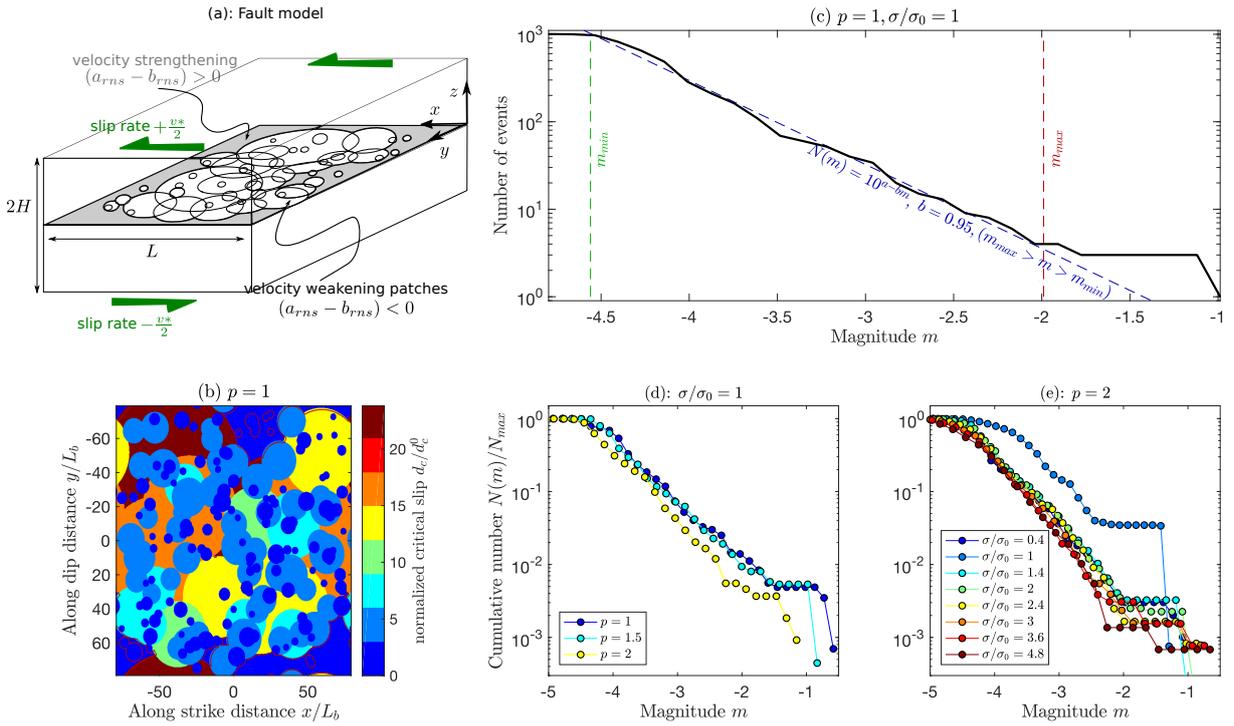
Figure 2.2: *(a) Schematic diagram of the fault model used to analyze b-value dependence on stress. a_{rns} and b_{rns} correspond to the a and b rate-and-state frictional parameters. White circles correspond to a superposition of asperities with sizes (and thus critical slip d_c) following a power law distribution of exponent p. (b) Example of critical slip distribution on the fault used in this study. (c) Example of magnitude-frequency distribution (black solid line) obtained with the fault model of figures (a) and (b). p is the exponent of the power law distribution of asperity sizes, σ and σ_0 are the normal stress and a reference normal stress used in this study. The red and green vertical lines indicate the magnitudes m_{max} and m_{min} corresponding to the rupture of the largest and smallest asperity respectively. The dashed blue lines indicate the fits of the distribution with a Gutenberg-Richter decay, considering all the events between m_{min} and m_{max}. (c) and (d): Magnitude-frequency distributions dependence on p exponent and normal stress σ. From **Dublanchet, P.** (2020).*

The results from the first study are illustrated in figures 2.2 and 2.3. If the b-value is influenced primarily by the asperity size distribution (as shown by the dependence of b-value on the exponent p of figures 2.2d. and 2.3), a slight increase of the b-value with normal stress is obtained as well. The maximum magnitude (called also main shock magnitude m_f) generated during the simulations increases also with normal stress. In **Dublanchet, P.** (2020), these

variations are interpreted in terms of normal stress dependence of the nucleation length and the stress drop. The nucleation length decreasing with increasing normal stress, the production of small events is enhanced causing an apparent increase of b-value with stress. Smaller events are indeed more frequent for two reasons. First because under smaller nucleation length smaller patches are activated (they were smaller than critical), then because the largest patches tend to produce more partial ruptures. It is shown in **Dublanchet, P.** (2020) that these two processes could be captured by an analytical formula involving a logarithmic increase of b-value with normal stress. The activation of previously stable patches leads to:

$$b = 1 + \frac{4}{9} \log \frac{\sigma}{\sigma_0}, \tag{2.1}$$

while the creation of partial ruptures is characterized by:

$$b = 1 + \frac{1}{6} \log \frac{\sigma}{\sigma_0}, \tag{2.2}$$

where σ_0 is the minimum normal stress allowing all the predefined patches to be seismic. As illustrated in figure 2.3a, the activation of new patches (equation 2.1) seems to dominate the increase of b-value for $\sigma < \sigma_0$. When $\sigma > \sigma_0$, all the predefined patches are seismogenic, so that the increase of b-value is dominated by the creation of partial ruptures (equation 2.2).

On the other hand, the stress drop of the largest events being higher under higher normal stress, the maximum magnitudes m_f increase. It is shown in **Dublanchet, P.** (2020) that this mechanism leads to a logarithmic dependence of m_f of the form:

$$m_f \sim \frac{2}{3} \log \frac{\sigma}{\sigma_0}. \tag{2.3}$$

The theoretical dependencies (2.1), (2.2) and (2.3) provide a good approximation of the numerical results (figure 2.3), and thus capture the main features of how magnitude distribution is affected by normal stress.

Neglecting the variations in friction coefficient during the seismic cycles, the normal stress could be converted into a differential stress. The increase of b-value with normal stress would then correspond to an increase with differential stress, which is in contradiction with previous observations. This is what is shown in figure 2.3a, where gray dashed lines represent the typical stress dependence of b-value derived from laboratory and seismological studies. However, the friction coefficient, and thus the shear stress varies along the fault during the seismic cycles, and this could be used to reconcile the results of figure 2.3 with previous observations. In this framework of varying friction coefficient, the decrease of b-value with stress usually reported might be a signature of varying shear stress, and not varying normal stress. It is also possible that for the simulations reported in this study (that are not exhaustive), there was no change in the ability of ruptures to propagate caused by the normal stress variations. This mechanism might however play a role in nature. Finally, the results might be different when considering a network of faults instead of the oversimplified planar fault model.

The second example of b-value variations with stress is presented in figure 2.4 from the study by Almakari, M.*et al.* (2019). Here the fault is injected at the center with a fluid that diffuses along strike (see section 3.3 of the next chapter for further details). The injection scenario consists of increasing the pore pressure at the injection point linearly in time (with rate β, Phase I) until a maximum pressure p_{max} is reached and held constant (phase II). b-values for the fluid induced seismic activity during phase I and II are reported in figure 2.4, as a function of effective normal stress and pressure rate. Phase I (pore pressure increase) is characterized by a short increase followed by a decrease of b-value with injection rate (figure 2.4c.) while no clear dependence on the effective normal stress is observed. Phase II on the other hand clearly shows a decrease of b-value with effective normal stress (figure 2.4b.). The absence of b-value dependence with injection rate during phase II arises because pressure is constant at the injection point.
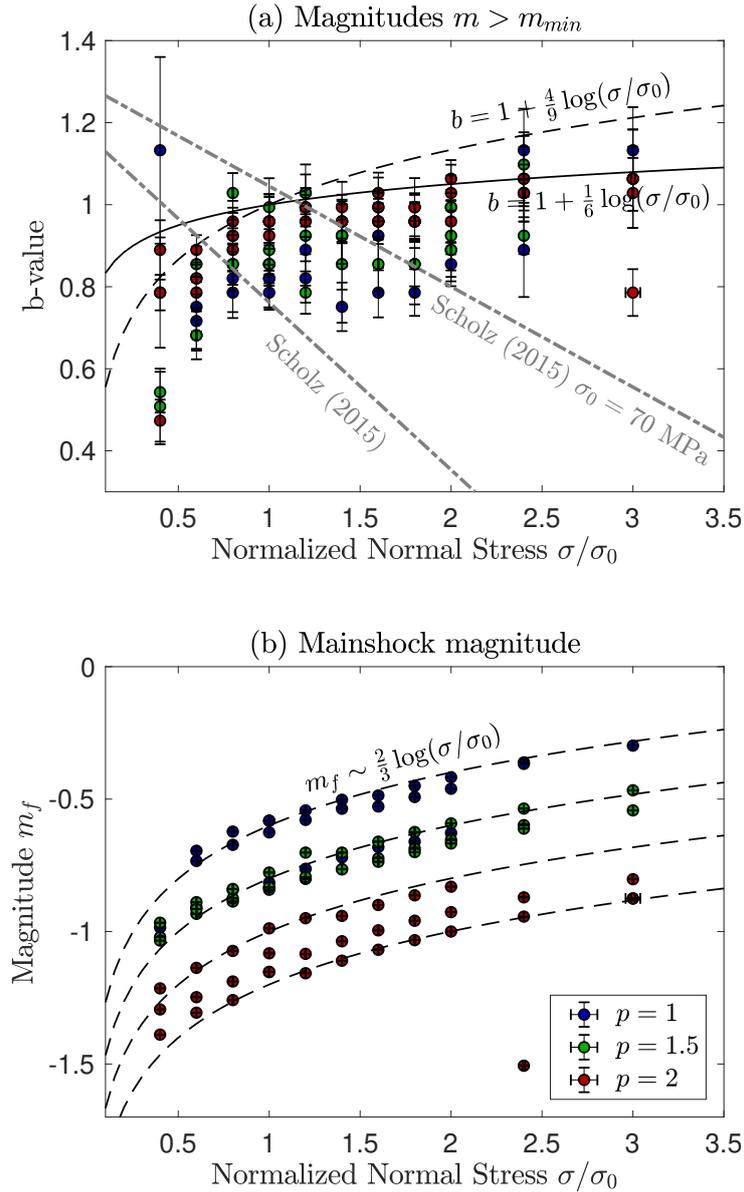
Figure 2.3: *b-value (a) and main shock magnitude m_f (b) versus normal stress σ for simulations performed with the fault model of figure 2.2. Dots are numerical estimates, color coded as a function of the p exponent of the asperity size distribution used. In (a), gray dashed lines indicate the empirical b-value stress dependence from Scholz (2015). Black dashed line is the approximation of b-value increase with stress due to changes in nucleation length at low normal stress (equation 2.1). Black solid line is the same approximation at high normal stress, due to the increase of partial ruptures (equation 2.2). In (b), the black dashed line indicates the theoretical scaling (2.3) reflecting the increase in main shock stress drop with normal stress. From* **Dublanchet, P. (2020)**.

In this case, the b-value has been computed considering all magnitudes larger than the completeness magnitude, which is slightly different from what has been done to obtain figure 2.3a. The decrease of b-value with effective normal stress here corresponds to a slower decrease than what is reported in the observations (Scholz, 2015). This could be due to multiple factors, in particular related to the quasi-dynamic interactions which may overestimate the stress redistributions associated with earthquakes (Almakari, M. *et al.*, 2019). However, the analysis of
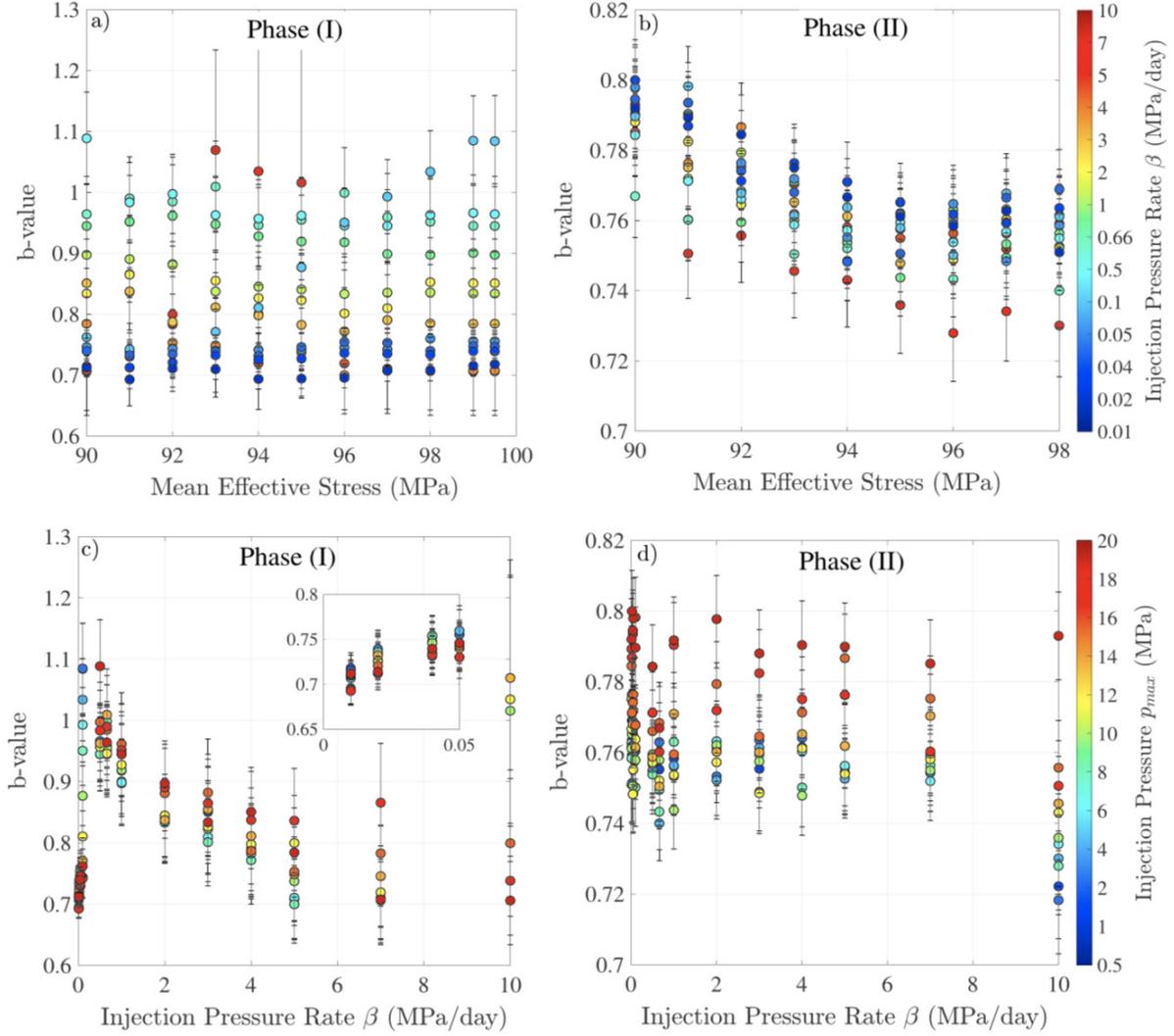
Figure 2.4: *b-value for injection induced seismicity obtained in the numerical simulations of Almakari, M.et al. (2019). Model c' of figure 1.12 is used here, which is a 1D equivalent of the fault depicted in figure 2.2a. and b. The system is permeated with a fluid injected at the fault center. The injection scenario consists of a linear increase of pore pressure at the injection point with pressure rate β (phase I) followed by a period of constant pressure p_{max} at the injection point. The b-value is here estimated from the whole magnitudes above m_{min}. (a) and (b): b-value and effective normal stress. (c) and (d) b-value and injection rate.*

b-value was not the main focus of this study (as this will be detailed in section 3.3), so that no further investigation was done concerning the origin of b-value variations with stress in the presence of fluids. This issue is nonetheless of fundamental interest since many cases of b-value variations have been reported in fluid induced seismicity sequences (Goebel *et al.* , 2016a,b; Kozłowska *et al.* , 2018). The dependence of b-values on pressure rate (figure 2.4c.) is also an interesting feature, suggesting a dependence on stressing rate, which may share some similarities with b-value variations with creep rate observed along San-Andreas Fault (Vorobieva *et al.* , 2016). This issue also requires more investigation.

2.3 Omori decay of repeating earthquakes

The other well documented empirical law of statistical seismology, the Omori decay of aftershock sequences, equation (1.2) (Omori, 1894; Utsu *et al.* , 1995), has been discussed in three of my publications (**Dublanchet, P.** *et al.* , 2013a; **Dublanchet, P.**, 2019a, 2020), and it is the main focus of one additional study (**Dublanchet, P.** *et al.* , 2013b). Here again, these studies aim at decoding the physics underlying the decay of aftershock rate as the inverse of time to the main shock. It is also assumed, as in the previous paragraphs that seismicity is caused by the failure of brittle asperities embedded in a single creeping fault. In these particular studies, asperities do not overlap, and their size is either constant (**Dublanchet, P.** *et al.* , 2013a,b), or follow a power law distribution (**Dublanchet, P.**, 2019a, 2020) (fault models a, b and c in figure 1.12).

The first result I have obtained concerning the Omori decay is discussed in **Dublanchet, P.** *et al.* (2013a): it shows that stress transfers between asperities lead to an apparent Omori decay, when stacking the aftershock sequences of all the events, in the case of sub-critical asperity density (as defined in section 2.1). It is also shown that the decay exponent is to some extent influenced by the density of asperities. Interestingly, super-critical asperity densities lead to system size ruptures unable to produce aftershocks. The main shock here does release all the stress on the fault in a somewhat artificial manner because the rupture is stopped by the fault boundaries. This feature is probably not physical as discussed in **Dublanchet, P.** *et al.* (2013a).

Obtaining aftershocks in this case would require to consider subsidiary smaller faults in the medium surrounding the main rupture. This situation is approximately achieved on a planar fault when considering a population of asperities of different sizes (models c and d in figure 1.12). In my two studies using such asperity distributions (**Dublanchet, P.**, 2019a, 2020), aftershock sequences were indeed obtained. However, the Omori decay was not the main purpose of these publications, but the synthetic catalogs produced could be reanalyzed in order to determine the temporal dynamics of these sequences.

A deeper analysis of the mechanical control on Omori decay is proposed in **Dublanchet, P.** *et al.* (2013b). This study focuses on the problem of Omori decay of repeating earthquakes during postseismic phases of large earthquakes. As in the case of global seismic activity, the rate of ruptures occurring on a repeating earthquake after the occurrence of a main shock is known to decay as the inverse time from the main event (Schaff *et al.* , 1998; Lengliné & Marsan, 2009). This feature is usually interpreted assuming a single asperity embedded in a creeping fault segment where slip rate decays as the inverse of time because of postseismic slip. In **Dublanchet, P.** *et al.* (2013b), such an asperity embedded in a creeping segment is modeled (model a. in figure 1.12), and the response to coseismic Coulomb stress changes is analyzed. The cumulative slip on the asperity and the rate of events following the stress step are shown in figures 2.5a. and b. The response is analyzed as a function of the asperity density ρ, here defined as the fraction of the fault surface occupied by the seismogenic asperity. In response to a coseismic stress step, a logarithmic increase of slip is obtained, with a characteristic time depending on the asperity density. This behavior is however observed only for sub-critical asperity densities (that is smaller than the critical asperity density defined in section 2.1), which corresponds here to a rather small asperity embedded in a much larger creeping region. In other words, the fault segment needs to obey an *effective velocity strengthening behavior* (positive spatial average of the $a - b$ rate-and-state parameter) in order to produce ruptures following an Omori decay.

It is shown in **Dublanchet, P.** *et al.* (2013b) that the characteristic time for Omori relaxation is controlled by the spatial average of the rate-and-state $a - b$ parameter. Analytical approximations are developed that fit the numerical results (solid colored lines in figures 2.5c. and d.). It results that the appropriate relaxation time t_r is a function of the spatial average noted $a_0 - b_0$ of the $a - b$ rate-and-state parameter on the fault. We have:

$$t_r = \frac{(a_0 - b_0)\sigma R}{\mu v_b},$$
(2.4)
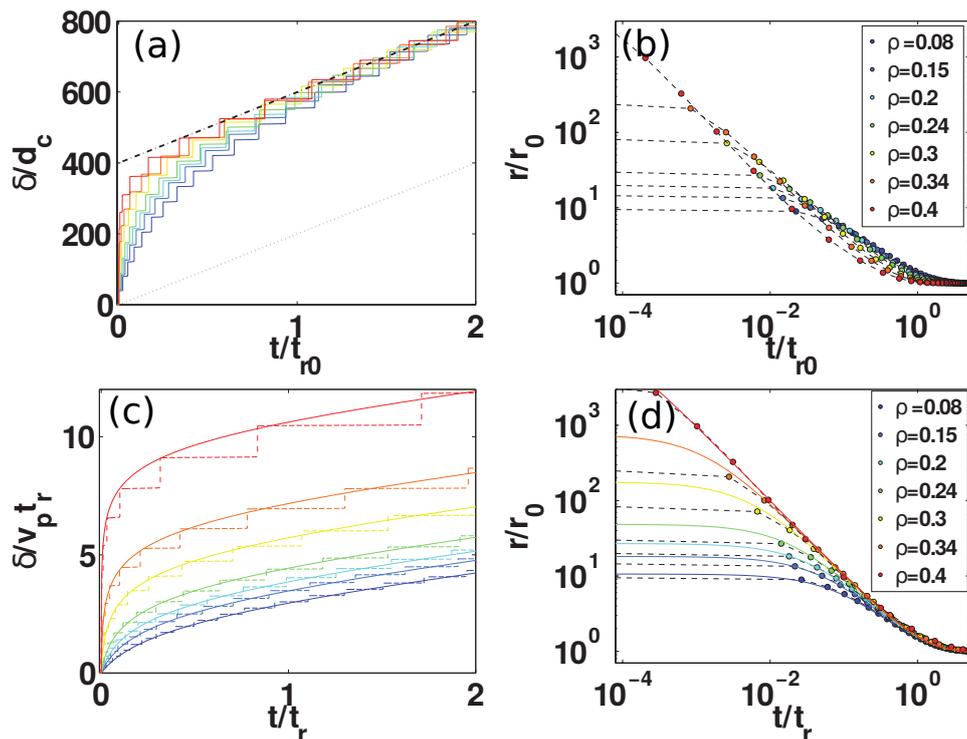
Figure 2.5: *Cumulative slip (δ, figures a. and c.) and rupture recurrence rate (r, figures b. and d.) on an asperity forced by aseismic creep (see figure 1.12a.) and loaded by a positive coseismic Coulomb stress change at $t = 0$. (a): Numerical results obtained for different asperity densities ρ (colored lines), along with the tectonic loading rate (v_p, gray dashed lines). In figures (b), (c) and (d), dots, and dashed lines indicate the numerical results, colored solid lines are analytical estimates. Time t from the coseismic stress perturbation is normalized by t_{r0} and t_r, corresponding to timescales defined from the velocity strengthening and average $a - b$ rate-and-state parameters respectively. Slip δ is normalized by either d_c (critical slip for rate-and-state friction), or $v_p t_r$. Rupture rate is normalized by the background rate r_0 (rate of ruptures before the coseismic stress perturbation). From **Dublanchet, P.** et al. (2013b).*

where σ is the normal stress, R the size of the asperity generating the repeating earthquake, μ the shear modulus, and v_b the loading slip rate (see figure 1.12). Recall that since the fault segment is characterized by effective velocity-strengthening behavior, $a_0 - b_0$ is positive.

2.4   Moment, duration, recurrence scaling : from slow slip events to earthquakes

An important observation about fault slip phenomena in general (earthquakes, slow slip events, tremors, low frequency earthquakes) is the way the moment M_0 scales with the duration T, or even with the recurrence time T_r of the events (in the case of repeating earthquakes). As mentioned in the introduction section, the scaling for the whole range of fault slip events is of the form (Ide *et al.* , 2007b; Peng & Gomberg, 2010):

$$M_0 \sim T^p, \tag{2.5}$$

where $p = 3$ for regular earthquakes, and $p = 1$ for slow slip events. Repeating earthquakes are also characterized by (Nadeau & Johnson, 1998; Chen *et al.* , 2007):

$$M_0 \sim T_r^{1/6}. \tag{2.6}$$

The mechanical interpretation of these scalings has received lots of attention since they have been established from seismological observations. The increase of seismic moment as the cube of the duration for regular earthquakes is possibly the signature of constant stress drop and rupture speed (Abercrombie, 1995; Ide & Beroza, 2001; Allmann & Shearer, 2009). In all the simulations performed on a heterogeneous rate-and-state frictional fault, the constant stress drop assumption, and the moment-duration scaling is generally reproduced, as long as the effective normal stress does not change too much (see **Dublanchet, P.** (2019a,c) for illustrations).

The mechanical origin of the moment-duration scaling for slow slip events is more debated. I have contributed to this discussion in a study in collaboration with R.C. Viesca (Tufts University, Boston) (Viesca & **Dublanchet, P.**, 2019). In this study, we consider a 1D linear viscous fault between 2D elastic half spaces (model a' in figure 1.12, but with linear viscous rheology instead of rate-and-state friction). We show (both theoretically and through numerical simulations) how a stress perturbation triggers a slip rate transient that decays as the inverse of time and expands along strike, in such a way that the seismic moment rate is constant. In this framework, a slow slip event would be triggered by an instantaneous stress perturbation (coseismic redistribution, pore pressure change), and would stop once the slip front reaches the fault boundaries. The accumulated moment is then proportional to duration. This model therefore provides a mechanical basis for the $M_0 \sim T$ observations for slow earthquakes.

Further numerical investigations with this model have shown that under rate-and-state friction, the slip transient properties are similar (constant moment rate, slip rate decay as the inverse time to stress perturbation). This work is however not yet published.

As mentioned in the introduction, the linear moment-duration scaling for slow earthquakes is still a matter of debate since recent observations report a scaling of the form $M_0 \sim T^3$ similar to regular earthquakes (Gomberg *et al.* , 2016; Michel *et al.* , 2019). Rate-and-state fault models seem also to reproduce this T^3 scaling for slow slip events (Dal Zilio *et al.* , 2020). So far, I have not analyzed what could be the moment-duration scaling in slow slip events generated with asperity models of figure 1.12, but this could be the purpose of future investigations.

Concerning the relationship between moment and recurrence time of repeating earthquakes (equation (2.6)), many mechanical models reproduce the observed scaling. As shown in section 2.3, repeating earthquakes could be interpreted as the failure of a particular seismogenic asperity forced by fault creep (model a in figure 1.12). In this framework, the moment-recurrence scaling is recovered either in the case of moment dependent stress drop (Sammis & Rice, 2001), partial creep on the asperity (Chen & Lapusta, 2009), or partial ruptures during interseismic periods (Cattania & Segall, 2019). However, all these models do not account for the slight deviation from the scaling (2.6) observed for interacting repeating earthquake sequences (Chen *et al.* , 2013). Interacting repeating earthquakes consist of a set of asperities distributed on the same fault region as depicted in figures 1.12b, c and d. Asperities are indeed usually not isolated on creeping faults, which results in stress redistributions and advances or delays in the ruptures. In **Dublanchet, P.** (2019c), I analyzed the dynamics of repeating earthquake sequences generated by a population of seismogenic asperities distributed on a creeping fault. The asperity sizes were here power-law distributed in order to generate different moments (model c in figure 1.12).

As illustrated in figure 2.6, even within a population of interacting asperities, the scaling (2.6) still arises on average, as long as the asperity density ρ is lower than critical. For higher densities (here higher than the critical density of asperity defined in section 2.1), the recurrence times T_r do not depend on the moment anymore. This is in fact a consequence of the highly clustered activity described in section 2.1, where the main shock almost synchronizes all the activity. In the low asperity density regime, a slight deviation from this scaling is nevertheless obtained, that increases with the asperity density until the critical density is reached (figure 2.7). It is shown in **Dublanchet, P.** (2019c) (and partially in figure 2.7), that the increase of variability
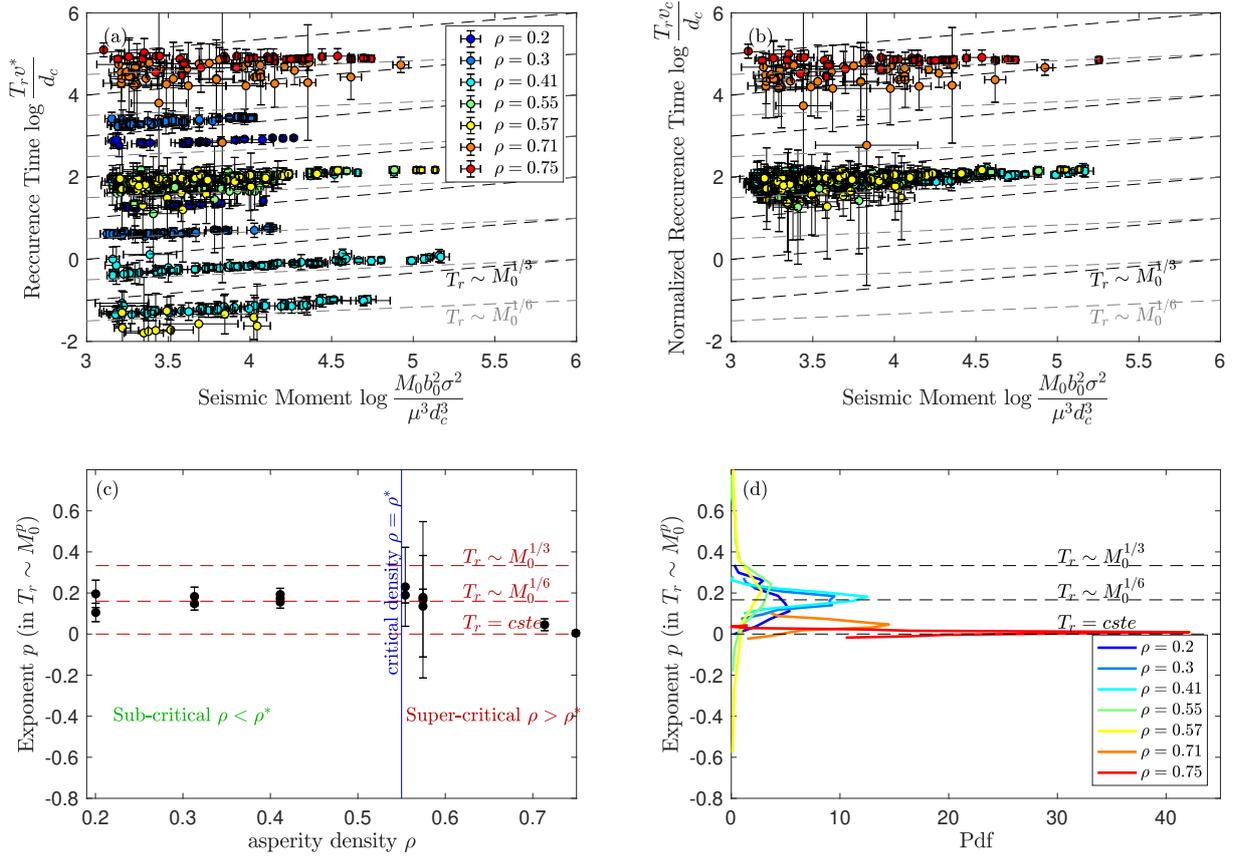
Figure 2.6: *(a) and (b): Recurrence time T_r vs. seismic moment M_0 for synthetic repeating earthquake sequences generated in a fault model consisting of a population of VW asperities distributed on a creeping fault (model c in figure 1.12). Quantities are normalized using the shear modulus μ, the rate-and-state b_0 parameter, the critical slip d_c, the remote loading rate v^* (v_b in figure 1.12), the average creep rate on the fault v_c. Colored dots are numerical estimates obtained under different asperity densities. Dashed black and gray lines indicate the characteristic scalings observed for earthquakes (equation (2.6)). When T_r is normalized by the creep rate v_c, all data for sub-critical asperity densities ($\rho < 0.55$ here) collapse on the same $M_0 \sim T_r^{1/6}$ tendency, showing the creep control on recurrence rate. (c) and (d): statistical estimates of the exponent p of the moment-recurrence scaling in numerical data. From **Dublanchet, P. (2019c)**.*

in recurrence time within individual repeating earthquake sequences is more a consequence of creep mediated stress transfers than static stress redistribution between the different asperities.

This last study provides new insights into the role of asperity density in the control of the moment-recurrence scaling, and the variability of repeating earthquakes recurrence.

2.5   Precursors to main shocks

Many evidences suggest that the initiation of large earthquakes (nucleation) is characterized by accelerating aseismic fault slip in the hypocentral region of the main shock (Dodge *et al.* , 1996; Kato *et al.* , 2012), associated from time to time with accelerating foreshock sequences (Bouchon *et al.* , 2013). Laboratory experiments and numerical models suggest that if tectonic faults are assumed to behave as frictional interfaces, slow slip precedes the onset of the largest ruptures (Ohnaka, 1992; Dieterich, 1992; Rubin & Ampuero, 2005). However, the mechanical conditions allowing both slow slip acceleration and foreshock are still unclear. I investigated this
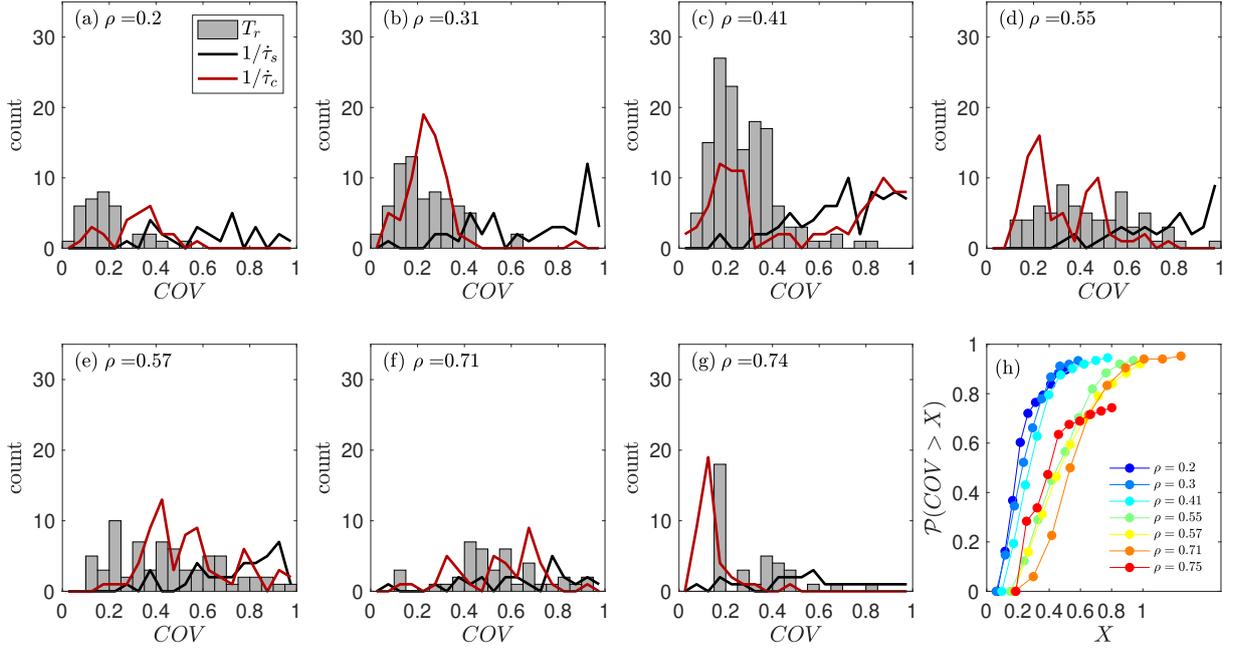
Figure 2.7: *(a. to g.) Covariance distribution for the recurrence time T_r of repeating earthquakes sequences presented in figure 2.6. The covariance COV determines the scatter of recurrence times to the mean in a particular sequence (COV = 0 corresponds to perfect periodicity). From a dimensional argument, recurrence rate is expected to scale as the inverse of stressing rate acting on the asperities. Two estimates of the covariance of inverse stressing rates are also shown for comparison: $\dot{\tau}_s$ is the stressing rate due to static stress transfers within the asperity population, $\dot{\tau}_c$ is an estimate of the creep mediated stress transfers. Covariance in T_r is closer to covariance in creep mediated inverse stressing rates than static stressing rates, indicating a creep control in the variability of recurrence times. (g) Cumulative probability distribution of the covariances in T_r for different asperity densities ρ. From* **Dublanchet, P.** *(2019c).*

question in **Dublanchet, P.** (2018) from a numerical and theoretical perspective. Following a suggestion initially proposed by Ohnaka (1992), I studied the role of frictional heterogeneity on earthquake nucleation along a 1D fault, as depicted in figure 1.12b'. Such a fault generates main shock events, corresponding to the system size ruptures described in section 2.1 for high asperity densities. In this particular study, I analyzed the nucleation process of these events under different frictional conditions. The results are shown in figures 2.8 and 2.9.

Depending on the characteristic length-scale (wavelength) of frictional heterogeneity λ (see figure 1.12b'), and on the ratio of average a and b rate-and-state frictional parameters (noted a_0 and b_0), 4 different regimes of nucleation could be defined. All of them imply a slow slip acceleration process, either localized when he ratio a_0/b_0 is small, or taking the form of an expanding crack when a_0/b_0 is close to one. Recall that main shocks occur only when $a_0/b_0 < 1$. Only one regime leads to simultaneous slow slip acceleration and an accelerating foreshock sequence (regime IV). Foreshocks occur if first the wavelength of frictional heterogeneity λ is larger than a critical value λ_c, defined by local frictional properties. λ_c is the critical nucleation length defined by Rubin & Ampuero (2005). The second condition derives from linear elastic fracture mechanics theory (LEFM (Lawn, 1993)), and could be summarized as follows: in order to get foreshocks, the first foreshock should not destabilize the whole fault (it should not degenerate into a dynamic rupture). From LEFM, this condition could be regarded as the stress intensity factor K associated with the first foreshock rupture should not exceed a critical stress intensity factor K_c characterizing the velocity strengthening barriers. This imposes that λ should be
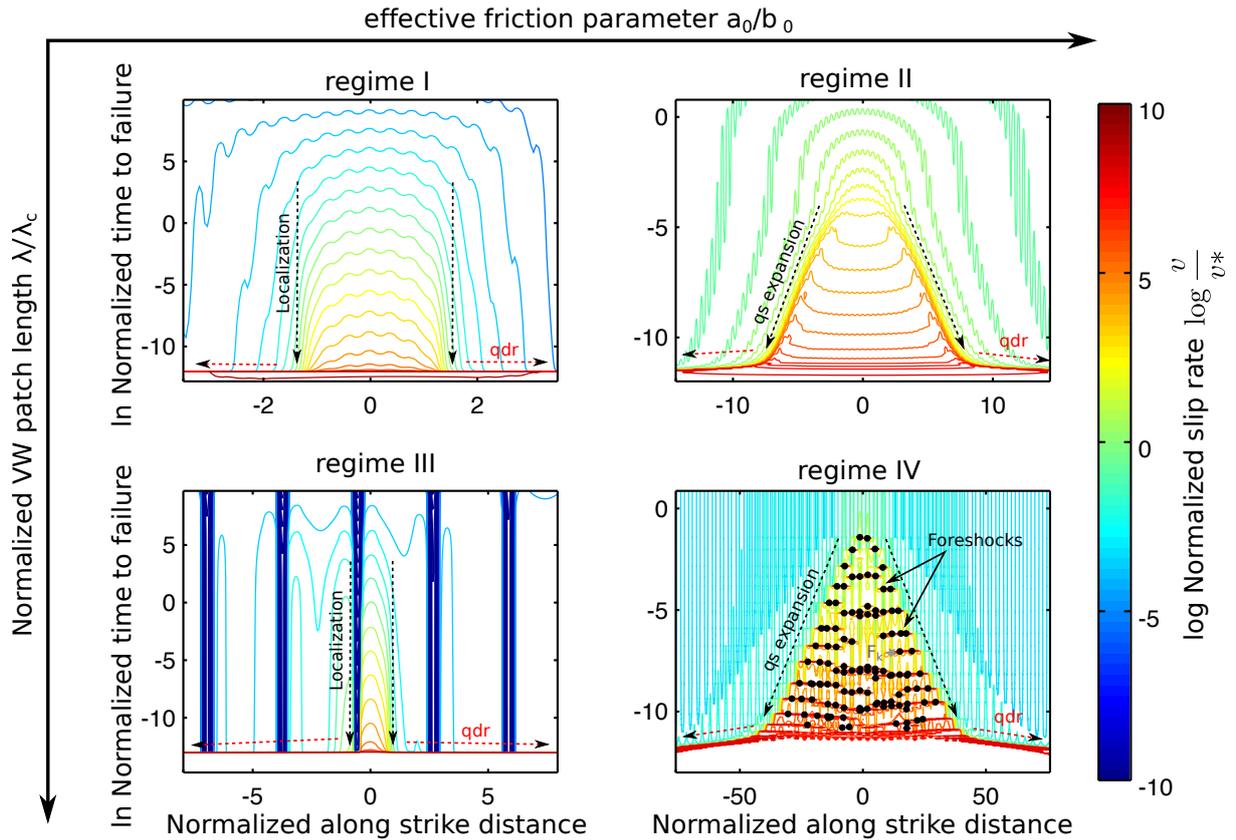
Figure 2.8: *main shock nucleation regimes observed in the fault model of figure 1.12b'. Colored contours correspond to slip rate, and time to failure indicates the time remaining from the main shock rupture onset. Slip rate is here normalized with the loading rate v^* (v_b in figure 1.12). Black dots are foreshocks location. a_0 and b_0 are the average values of a and b rate-and-state parameters (see figure 1.12b'). λ_c is the critical wavelength described in the maintext. VW denotes velocity weakening. qs and qdr correspond to quasi-static and quasi-dynamic (main shock) rupture respectively. From **Dublanchet, P.** (2018).*

smaller than another critical value. The two conditions for foreshock occurrence are schematically represented in figure 2.9 summarizing the different nucleation regimes.

Another interesting result of this study is the acceleration of foreshock activity preceding the main events under regime IV. Acceleration of foreshock activity has been evidenced in natural seismicity for a long time (Jones & Molnar, 1976; Bouchon *et al.*, 2011, 2013), in the form of an inverse Omori law.

The cumulative number of foreshocks for different fault scenarios under regime IV is reported in figure 2.10. It is shown in **Dublanchet, P.** (2018) that the total number of foreshocks is expected to grow as $\ln^2(1 - t/t_f)$, $1 - t/t_f$ being the time to failure (i.e. onset of the main shock rupture), which is in rough agreement with the numerical results shown in figure 2.10. This leads to a foreshock rate R_f blowing up as

$$R_f \sim -\frac{\ln(1 - t/t_f)}{(1 - t/t_f)}, \tag{2.7}$$

which is close to an inverse power law of time to failure (inverse Omori law), if logarithmic changes are neglected to the first order.

Note that the increase of foreshock rate as an inverse Omori law could be related to the
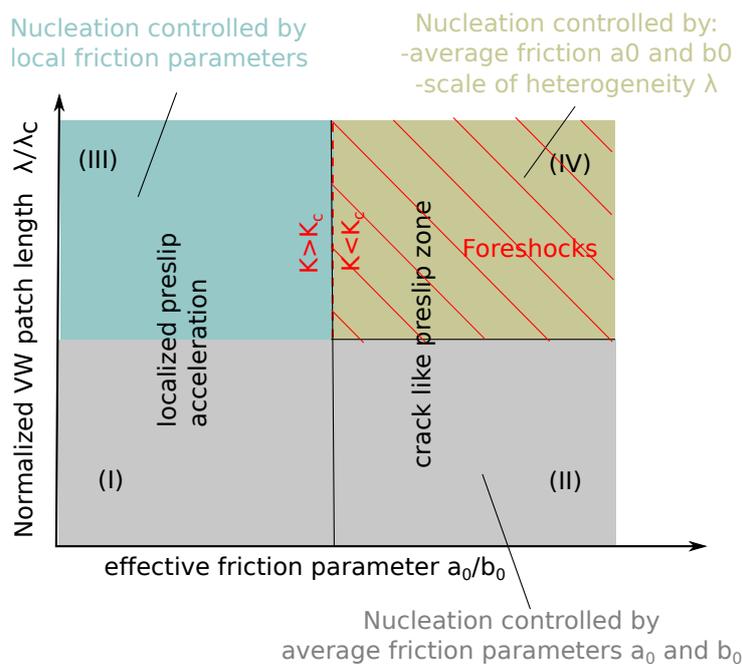
Figure 2.9: *Summary of the nucleation regimes and conditions for foreshock occurrence in the fault model of figure 1.12b'. See figure 2.8 for the definition of λ_c and a_0/b_0. The balance of stress intensity factors $K = K_c$ corresponds to a fracture mechanics condition for the existence of foreshocks. From* **Dublanchet, P.** *(2018).*

slow slip rate acceleration as inverse time to failure during these sequences, as discussed in **Dublanchet, P.** (2018). As shown before in the context of repeating earthquake sequences (section 2.4), the recurrence time of earthquake ruptures scales as the inverse slip rate in such asperity models. I suggest that this might be also the case during foreshock sequences.

This study has provided new theoretical arguments supporting the fact that major earthquakes are not necessarily preceded by foreshocks, and provides new insights on how foreshocks and pre-slip interact. Furthermore, it has shown how realistic foreshock sequences, characterized by an Omori like acceleration, could be seen as a consequence of frictional (and thus fault material) heterogeneity.

2.6 Rupture speed : the growth of seismic ruptures

The moment-duration scaling raises the question of self-similarity of slip events, and in particular the physical control on the rupture speed and the stress drop during earthquakes. The mechanical control on rupture speed is also of importance in understanding slow slip events, since they are characterized by slower rupture speeds than regular earthquakes.

I have contributed to two studies about earthquake rupture speed and rupture growth as a co-author. The first one is experimental (Passelègue *et al.* , 2020) and investigates the relationship between rupture speed and prestress conditions during laboratory earthquakes on saw-cut samples loaded by a combination of axial stress and fluid injection. The second study (Renou *et al.* , 2019) consists of a statistical analysis of source-time functions aiming at constraining the rate of moment growth during the initiation of rupture propagation for events between magnitudes 6 and 7.

The outcome of the first study is illustrated in figure 2.11. The rupture speed of the laboratory events is here controlled by the prestress conditions in agreement with linear elastic fracture mechanics predictions (Lawn, 1993): it decreases with the ratio between effective normal stress
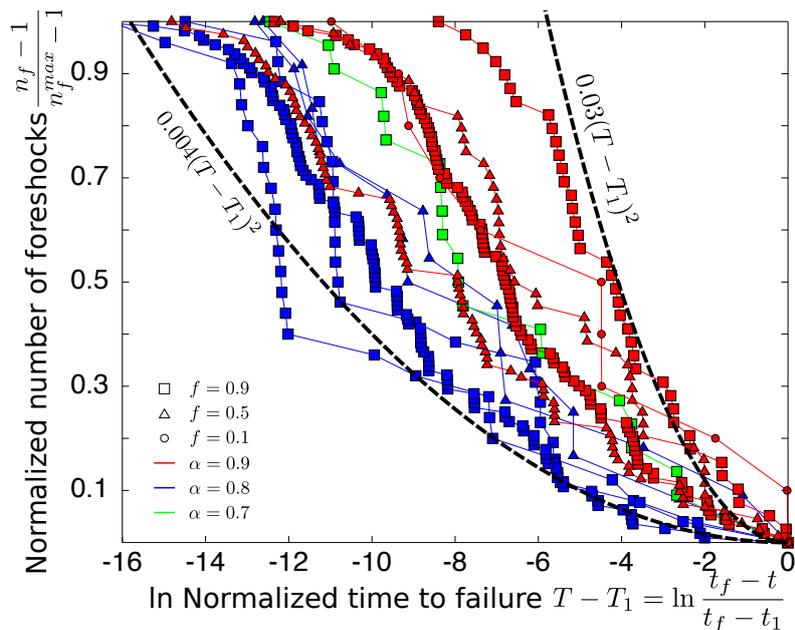
Figure 2.10: *Cumulative number of earthquakes vs. time to failure (onset of main shock rupture) in the heterogeneous rate-and-state fault model of figure 1.12b'. n_f and n_f^{max} are the number of foreshocks and the maximum number of foreshocks in the sequence. t, t_f and t_1 are time, onset time of the main shock and an arbitrary starting time respectively. Different symbols and colors refer to different scenarios of frictional heterogeneity. The parameter f controls the amplitude of the b rate-and-state parameter variation along the fault. α is the ratio of average a_0 and b_0 rate-and-state parameters. From* **Dublanchet, P.** *(2018).*

$\sigma - P$ (difference between imposed normal stress and average pore fluid pressure) and the square of the dynamic shear stress drop $\Delta\tau_d$. This result provides a first explanation about the distribution of regular earthquakes versus slow slip events in subduction zones: slow slip events indeed tend to cluster at depths where the seismic velocity ratio (S wave speed over P wave speed) is the smallest, which may indicate high fluid pressure and thus reduced effective normal stress. It also shows that depending on the stress conditions, the same fault could develop either regular earthquakes or slow events.

In the second study by Renou *et al.* (2019), it is shown that moment rate may increase faster than what is expected from a self-similar rupture growth. The mechanical interpretation of this observation could be either a slightly increasing rupture speed, and (or) a varying dynamic shear stress drop during such events. The comparison with laboratory experiments (Passelègue *et al.* , 2020) shows that both are linked to some extent.

Up to now, I have not analyzed in detail the rupture growth and the rupture speed of synthetic earthquakes generated in the frictional fault models I have developed (in particular models b, c and d in figure 1.12). One of the reason is that the quasi-dynamic approximation would certainly bias the rupture speed, and it would be more relevant to use fully dynamic models to conduct such analysis, and compare the results to both experiments and seismological observations.

However, the rupture speed of slow slip events has been analyzed in two other studies conducted on frictionally stable faults (Viesca & **Dublanchet, P.**, 2019; **Dublanchet, P.**, 2019b). The first one (discussed in section 2.4) shows that under linear viscous contact rheology, stress variations lead to slip rate perturbations Δv propagating in a self-similar manner of the form:

$$\Delta v \sim t^{-\xi} g(x/t), \tag{2.8}$$
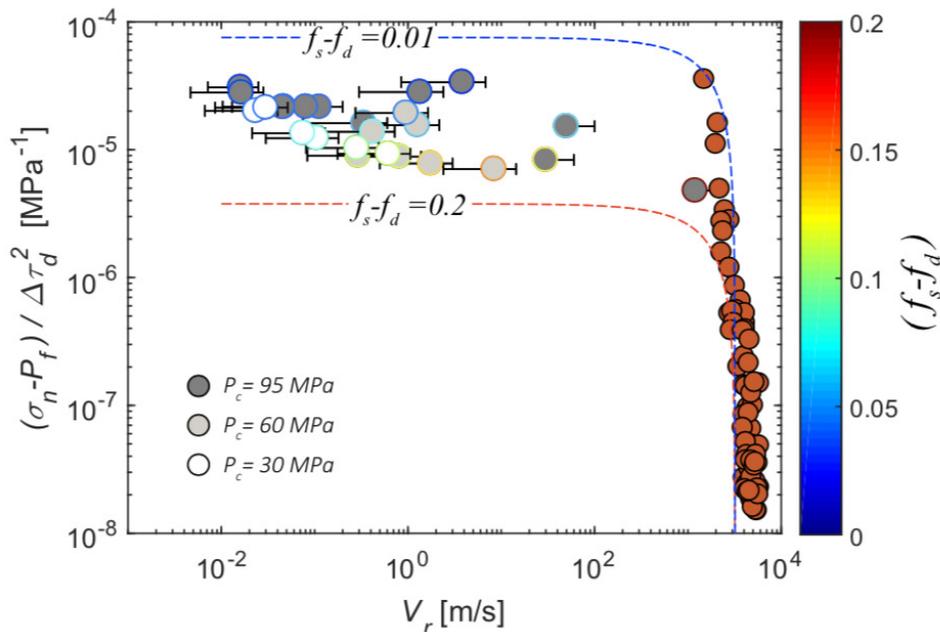
Figure 2.11: *Rupture speed V_r vs. stress ratio $(\sigma_n - P_f)/\Delta\tau_d^2$ observed during laboratory earthquakes triggered by fluid injections in an andesitic saw-cut rock sample. σ_n is the remote imposed normal stress, P_f is the mean pore fluid pressure on the fault, and $\Delta\tau_d$ the dynamic stress drop. Dots are experimental results. Dashed lines are theoretical approximations involving a static f_s and a dynamic f_d friction coefficient. From Passelègue et al. (2020).*

t being time, x the along strike distance, ξ an exponent that could be 1 or 2, and g a shape function of the similarity variable x/t. The second one (**Dublanchet, P.**, 2019b), considers a punctual injection in the same fault systems. It is shown that the fluid injection triggers an expanding slow slip event, where slip front propagates at a constant rupture speed controlled by the injection rate, the frictional properties, and the prestress conditions on the fault. This latter study will be detailed in section 3.4 of the next chapter.

2.7   Conclusion

The studies discussed in this chapter show that fault models coupling elasticity and rate-and-state friction on a planar interface reproduce many observations about fault slip phenomena, and probably more than what was shown by the first generations of models. The use of such models therefore allows to improve our understanding of what mechanical parameters control the scaling and statistical laws characterizing tectonic fault slip phenomena. As shown in this chapter, this concern has motivated nine of my publications over the past seven years, and several collaborations with R.C. Viesca (Tufts University), F.X. Passelegue (EPFL), J. Renou and M. Vallée (IPGP). The main outcome of all these results is the importance of asperity density and more generally frictional heterogenity in controlling fault slip phenomena. The question of how frictional heterogenity controls fault slip needs to be further investigated, in the framework of an effective theory for instance. This is the purpose of one of my research projects, as discussed in the last chapter (section 4.3). Recent advances have shown that the geometrical complexity is also a crucial aspect of fault slip dynamics that needs to be accounted for (Romanet *et al.* , 2018). Future developments will also have to account for this issue.

Chapter 3

Inferring slow slip and fluid flow at depth from seismicity

The main crustal processes underlying micro to moderate earthquake swarms are slow aseismic slip episodes, or transient deep fluid flow. The role of aseismic slip has been demonstrated in many places, since geodetic or in situ deformation measurements have been coupled to seismological observations. The growing interest for induced seismicity over the past years, has contributed to highlight the importance of fluid flow at depth in triggering seismicity. Recent analysis of natural sequences has also revealed the signature of fluids. However, if seismic swarms are easily detected, located and monitored, deep aseismic slip and fluid flows are more difficult to observe and to quantify. Earthquake swarm patterns provide only indirect information about these processes. In this framework, physics-based fault models and earthquake simulators (illustrated in figure 1.12) could be used to quantify aseismic slip and fluid flows. This could be achieved either through direct modeling of particular earthquake sequences, or by looking for general relationships between aseismic slip properties (extent, amount of deformation, stress changes), fluid flow properties (overpressure, volumes) and earthquake features (magnitude content, temporal clustering, migration). This is the main purpose of this chapter. The fist section presents two attempts to model specific earthquake swarms in the Corinth Rift in Greece. The second section is dedicated to the question of estimating total fault slip (i.e. seismic and aseismic) from the analysis of seismic moment released by earthquakes. The last sections present parametric and theoretical studies dedicated to the relationship between fluid flow and seismicity (third section), and between fluid flow and aseismic slip (fourth section).

3.1   Modeling seismic swarms in the Corinth rift

The Corinth rift (Greece) is a tectonically active region of intense seismic activity (more than 30,000 earthquakes of magnitude larger than 1.5 since 2001), illuminating the shallow crust by episodic swarms (Lambotte *et al.* , 2014; Duverger *et al.* , 2018). Earthquake swarms are suspected to be driven by a combination of extensional tectonics, fluid flow at depth and aseismic fault slip (Bernard *et al.* , 2006; Bourouis & Cornet, 2009; Lambotte *et al.* , 2014; Duverger *et al.* , 2018). However, the forcing mechanism of individual sequences is still in many cases unclear.

The mechanics underlying swarms development could eventually be inferred in more details, by comparing seismological data and results of mechanical modeling. In collaboration with seismologists from Géoazur (M. Godano and L. De Barros), we developed this approach for two particular swarms of the Corinth rift.

The study of the first swarm is presented in two companion papers : Godano *et al.* (2015) and **Dublanchet, P.** *et al.* (2015). The purpose of the first study (Godano *et al.* , 2015) was a Bayesian estimation of all the source parameters (moment, stress drop, source size, and fault slip) of the 52 events participating in this microseismic cluster located at 8 km depth under the

northern end of the Corinth rift, from spectral ratio analysis. This cluster was identified as a multiplet (Lambotte *et al.* , 2014), implying a common source mechanism and compact location of all the events. This multiplet activated between 2001 and 2007 a slightly north dipping interface. The estimated parameters account for the uncertainty in source location, moment and corner frequency. Earthquake locations, temporal evolution of the swarm, and estimated accumulated fault slip are presented in figure 3.1.

This irregular sequence, composed of 52 events with magnitudes between 1.1 and 2.8 produced the coseismic slip pattern shown in figure 3.1d. Up to 10 cm of slip was accumulated on this fault patch during the seven years of cluster existence. An important issue raised by this result is whether this coseismic slip was a byproduct of larger scale aseismic slip, or if on the contrary, this slip occurred in a locked fault section, increasing the stress in the vicinity of the cluster, and thus the seismic hazard.
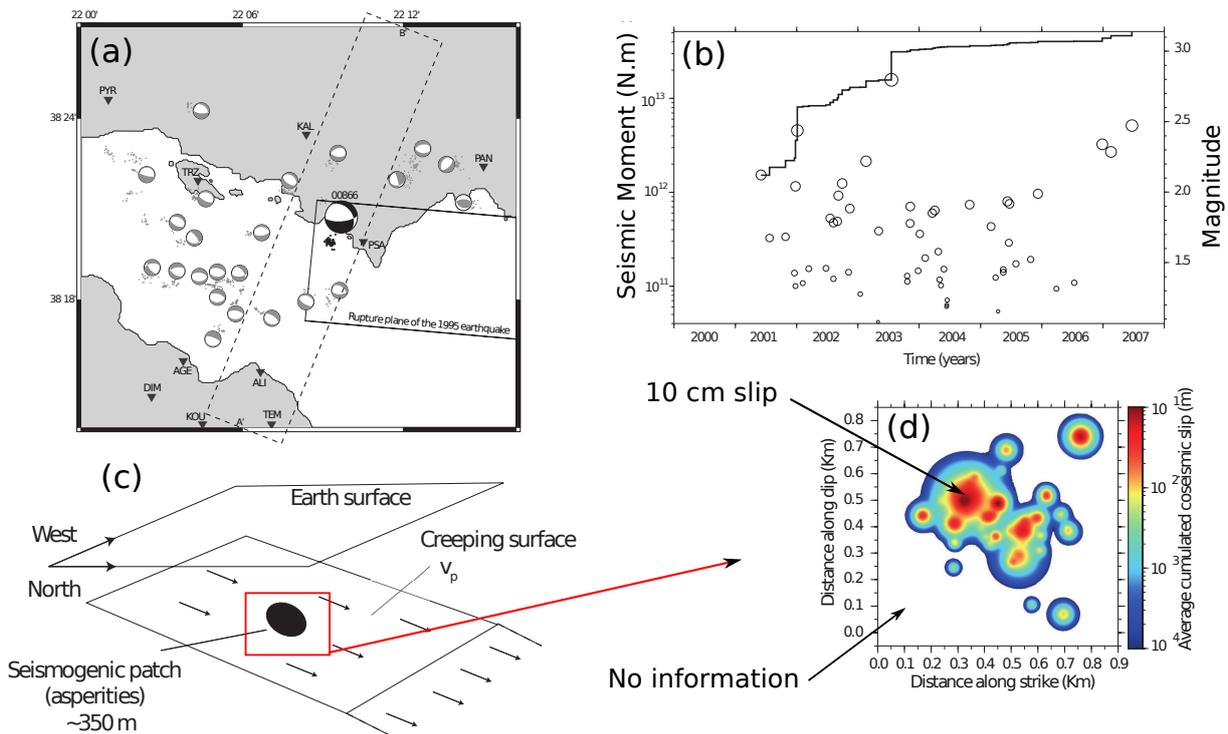
Figure 3.1: *(a) Location of the multiplet 866 (black dots) in the western Corinth rift. Other microseismic multiplets of the area are shown as gray dots. A composite focal mechanism is shown for each multiplet. The surface projection of the rupture area of the 1995 $M_w = 6.1$ earthquake is also shown. (b) Magnitudes and cumulative seismic moment released by the multiplet 866. (c) Possible conceptual model for the multiplet 866. (d) Cumulative slip pattern for multiplet 866, estimated from the Bayesian inversion of all the source parameters of the 52 events shown in (b). From Godano* et al. *(2015).*

In order to answer this question, we developed a model of the cluster's fault segment illustrated in figures 3.1c and 3.2a. Here again the fault is modeled as a rate-and-state frictional interface within an elastic medium, where a cluster of velocity weakening asperities (seismogenic patch in figure 3.2) is forced by remote loading (corresponding to the extensional loading in the rift, derived from geodetic measurements). We considered two different scenarios: in the first one, the cluster of asperities was embedded in a creeping fault zone (creep model), modeled using velocity strengthening properties, in the second one, the seismogenic patch was located at the transition between a creeping fault zone and a locked section (semi-locked model).

As shown in figure 3.2, the creep model involving 1.5 cm.yr^{-1} of aseismic slip provides a
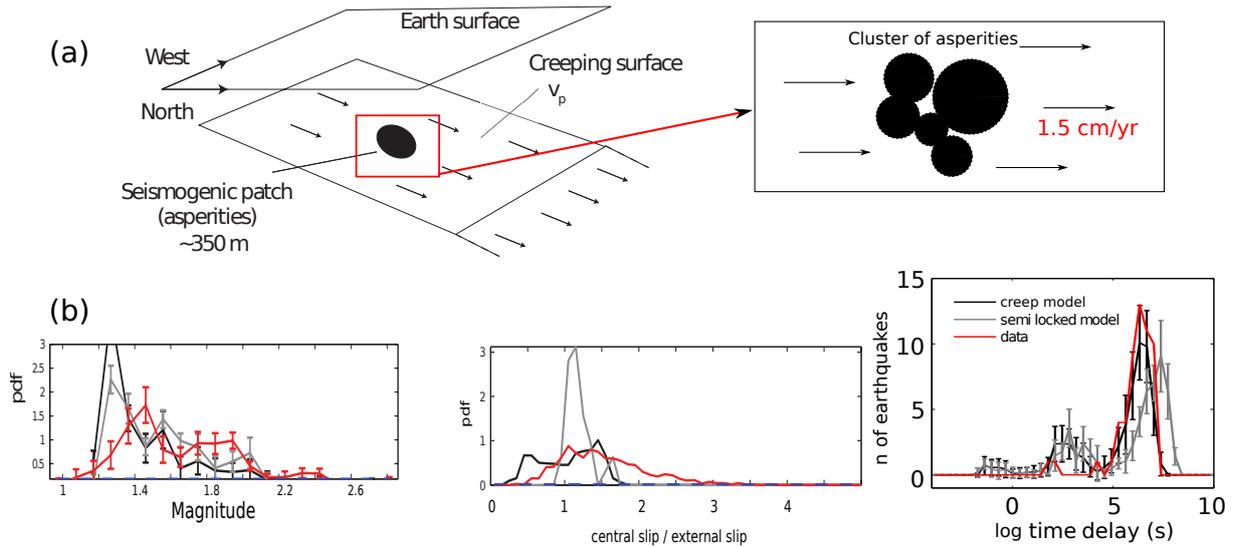
Figure 3.2: *(a) Schematic representation of the best model for the multiplet 866. (b) Magnitude content, slip pattern shape and successive time delays distribution in the observations and in two different models of the multiplet 866 (creep and semi-locked). The slip pattern shape is here characterized by the ratio between total slip at the center of the patch and slip on its periphery. See* **Dublanchet, P.** et al. *(2015) for details.*

better fit to the magnitude content and the distribution of time delays between events than the semi-locked model. The result of this modeling attempt suggests that the cluster's fault is slipping aseismically, and does not accumulate stress in the vicinity of the seismogenic cluster.

This first result is encouraging and shows how fault models could be used to infer fault conditions at depth. In the case of Corinth seismicity, this approach could be generalized to other clusters. This is one of the perspectives that will be developed in chapter 4.

Another interesting sequence of the Corinth rift has recently been analyzed by De Barros *et al.* (2020). This sequence activated for 10 days in October 2015 a 2 km long south dipping fault under the northern edge of the Corinth rift, with an interesting migration pattern illustrated in figure 3.3. As the microseismic swarm was expanding at a speed of approximately 125 m per day, at least three episodes of rapid migration (at about 10 km per day) are possibly occurring within the seismic cloud. This is interpreted by De Barros *et al.* (2020) as a reactivation process involving both aseismic slip front propagation and possible pore pressure migration, such as what is observed in induced seismicity contexts.

This swarm is the second sequence for which we proposed a mechanical model. This work has been recently accepted for publication (**Dublanchet, P.** & De Barros, 2020). The model has been designed following the interpretation of De Barros *et al.* (2020) involving the coupling between earthquakes, aseismic slip and fluid flow along a fault segment. Here again, we modeled the fault as a 1D linear interface between elastic slabs. In order to allow both aseismic slip and earthquake ruptures, we used a heterogeneous friction with velocity weakening and velocity strengthening patches (as depicted in model b' of figure 1.12). We then modeled the fluid flow along the fault assuming an injection at constant rate at the center of the fault, and a diffusion along strike. We tested different hydraulic properties leading to linear and non-linear (i.e. slip dependent) diffusivity. From simple micro-mechanical arguments, we developed a model for the diffusivity D of the form:

$$D = D_0 e^{-\theta/\tau_v}, \qquad (3.1)$$

where D_0 is a reference diffusivity, θ the state variable of the rate-and-state friction law, and τ_v
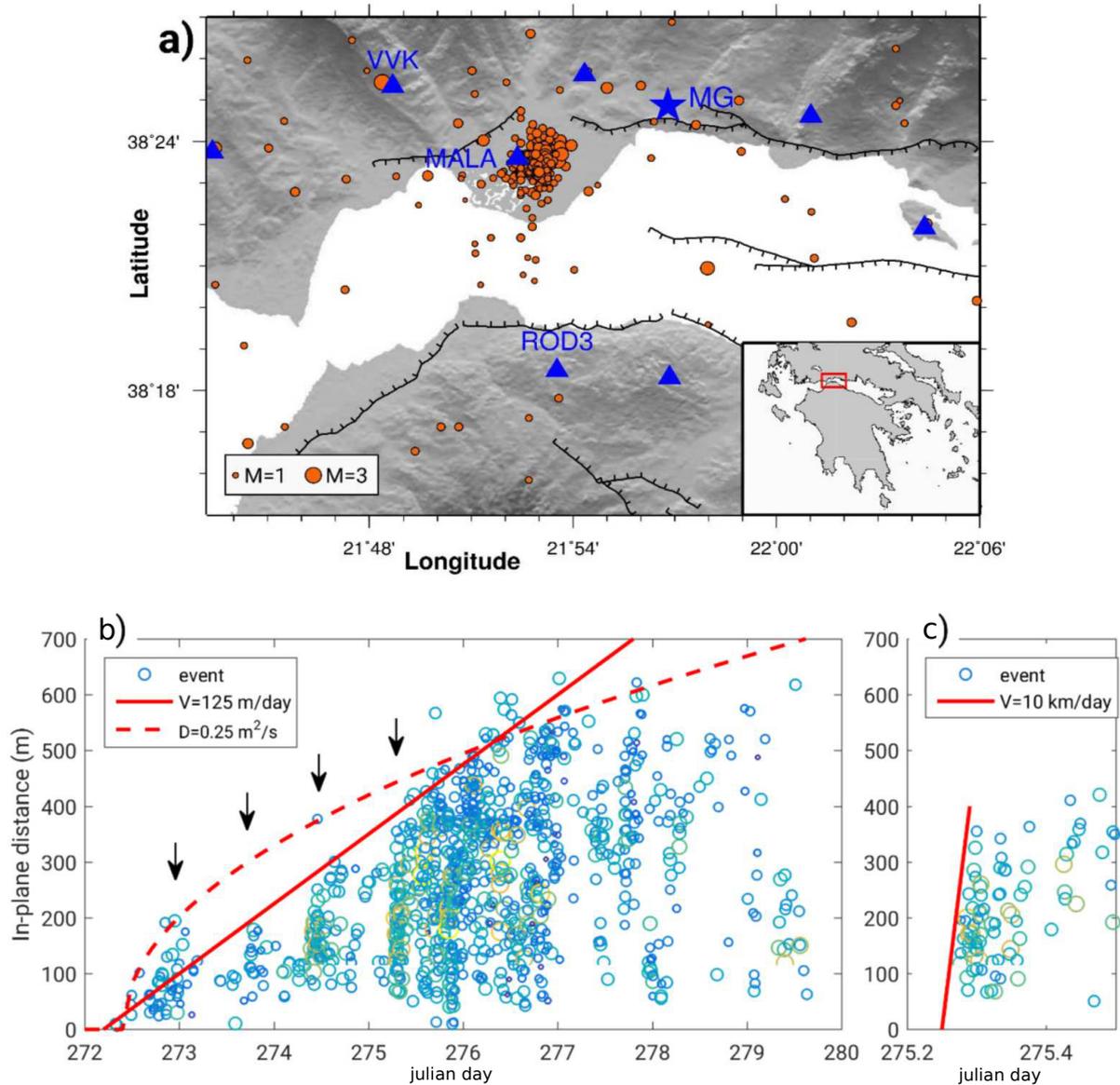
Figure 3.3: *October 2015 Corinth rift sequence. (a) Epicenter locations. (b) Migration pattern for the whole swarm. The in-plane distance is computed from the activated fault center. (c) Zoom on a particular rapid migration event. Dots are observed events, color coded with magnitude. Red solid line is a fit assuming constant expansion speed. Dotted red line is a fit assuming pore pressure diffusion from the fault center at a constant diffusivity. Black arrows indicate possible rapid migration episodes. From De Barros et al. (2020).*

a characteristic visco-elastic timescale. This diffusivity law leads to a strong slip-rate dependence of the fluid flow.

An example of fault slip response is shown in figure 3.4. In this example, the fluid injection leads to a pore pressure perturbation migrating along strike (figure 3.4a.) which triggers a slow slip front (figures 3.4b., c. and d.). The earthquakes are here triggered by the slow slip propagating from one velocity weakening patch (asperity) to another (figures 3.4b. c. and d.). The resulting seismic pattern consists of a global expansion at approximately 20 m.day^{-1}, involving several episodes of rapid (~ 300 m.day^{-1}) migrations. This pattern is very similar to the observations (figure 3.3), which confirms the role of imbricated fluid flow and aseismic slip in the reactivation of this fault.
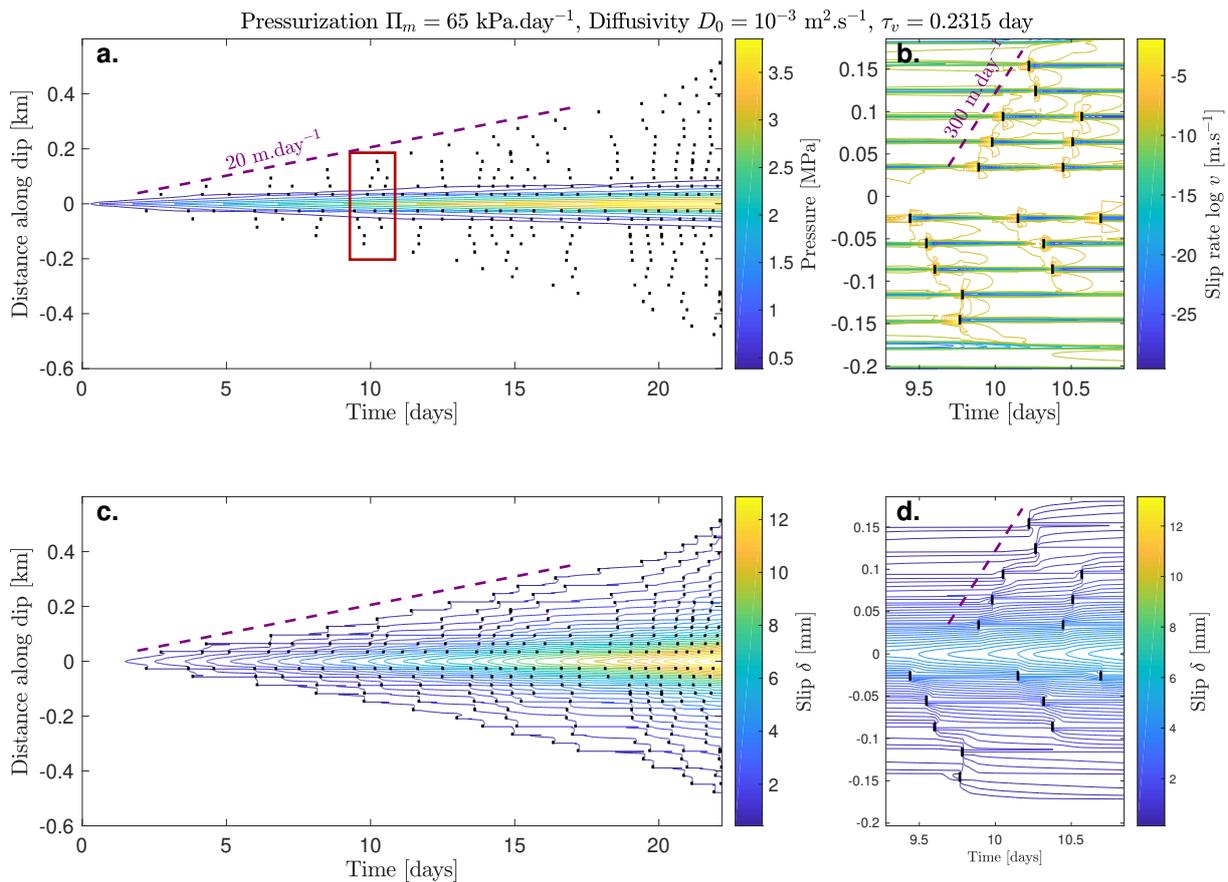
Figure 3.4: *Earthquake locations (black symbols), pore pressure, slip rate and cumulative slip evolutions following an injection in the fault model of figure 1.12b'. The hydraulic diffusivity is a non-linear function of the state variable θ of the form (3.1) involving the reference diffusivity D_0 and the characteristic visco-elastic time τ_v. The pressurization Π_m is the rate of increase of the average pore pressure in the fault. Purple dashed lines indicate earthquake migration. The red box in figure a. delineates the zoomed region in b. and d. From* **Dublanchet, P.** *& De Barros (2020).*

In this study, we also analyzed what mechanical parameters control the two different migration speeds observed in the seismic pattern (global swarm expansion and rapid migration). The dependence of the earthquake migration speeds on different mechanical parameters is illustrated in figure 3.5. The main result shown here is that the migration of earthquakes is controlled to the first order by two parameters. The first one is the *pressurization* Π_m, which is the rate of increase of the mean pore pressure within the fault. The second one is what we define as the *aseismic fracture energy density* Γ, which reflects the strength of the velocity strengthening barriers. More precisely, we show from the theoretical results of **Dublanchet, P.** (2019b) that the migration speed scales as:

$$V_m = \frac{f_0 L \Pi_m}{2\Gamma}, \tag{3.2}$$

where f_0 is the reference friction coefficient and L the fault length. The approximation (3.2) provides a first order estimate of our numerical results (figure 3.5). Interestingly, the fault diffusivity plays a minor role, since most of the earthquakes are triggered by the slow slip front, and not the pressure front itself. In this context, the difference in global expansion and rapid migration speeds correspond to differences in the Γ parameter. As discussed in **Dublanchet, P.**

& De Barros (2020) the global expansion results in an increase of Γ behind the slow slip front, which accelerates the migration of earthquakes within the swarm.
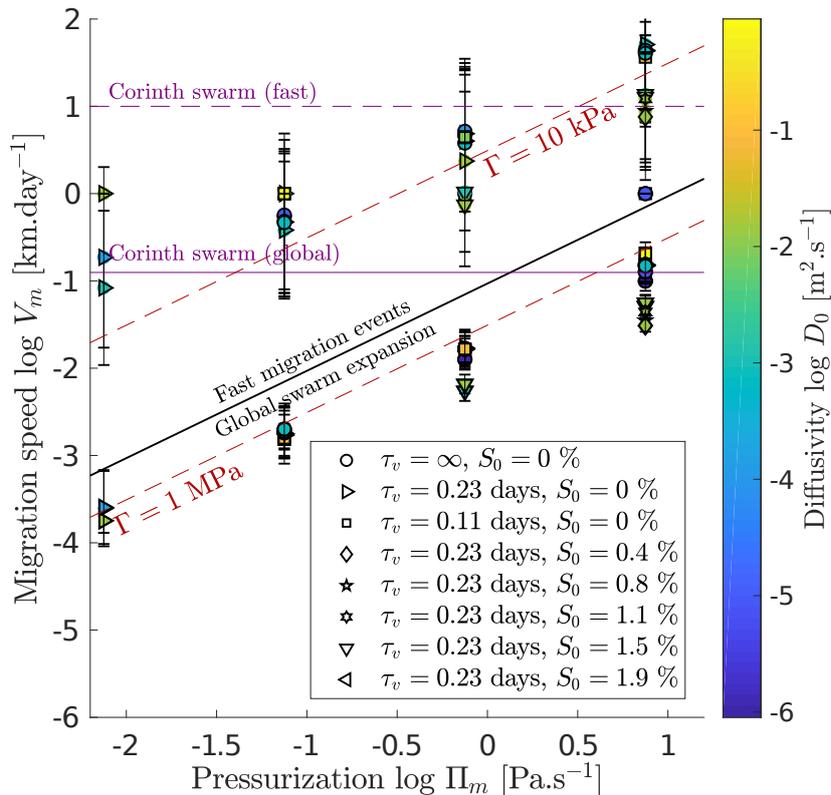
Figure 3.5: *Earthquake migration speeds in the injected fault model of figure 1.12b'. The results include the migrations observed in figure 3.4. Colored dots are numerical results. The black line separates global swarm expansion and fast migration events. Red dashed lines is the approximation (3.2) for two different values of the strengthening fracture energy density Γ. Magenta horizontal lines indicate the migration speeds observed in the Corinth swarm (figure 3.4). S_0 is the initial understress on the fault. From **Dublanchet, P.** & De Barros (2020).*

Moreover, the range of parameters considered allows to reproduce the range of migration speeds observed for the Corinth swarm. It is shown in **Dublanchet, P.** & De Barros (2020) that the range of Π_m needed to recover the observations leads approximately to a 17 MPa of overpressure in the fault at the end of the swarm.

With these two examples of microseismic swarm modeling, we have shown that it is possible to recover information about deep processes from the analysis of earthquake swarms dynamics. In the first case the model indicated a deep creep at 1.5 cm.yr^{-1}, in the second case an overpressure of the order of 17 MPa. Such information about deep creep and fluid flow could not have been obtained from direct geophysical measurements.

3.2 Fault slip from cumulative seismic moment

Beyond the modeling of a particular microseismic sequence, the question of inferring fault slip rate at depth from the analysis of microseismicity in a general case is of fundamental importance in estimating where tectonic stresses accumulate in the crust. In many situations, the slip budget on deep faults is estimated from the inversion of geodetic measurements (Nishimura *et al.* , 2004), but the analysis of repeating earthquakes generally increases the resolution of the geodetic estimates (Nadeau & McEvilly, 1999; Uchida *et al.* , 2003; Gardonio *et al.* , 2018). Using

repeating events is to some extent supported by observations and models (Chen *et al.* , 2007; **Dublanchet, P.**, 2019c) showing that the recurrence time of individual sequences scales (to the first order) as the inverse creep rate on the fault (see figure 2.6 for instance). However, the use of repeating events as creep meters on a fault relies on very strong mechanical assumptions, in particular that no interaction occurs, and that slip accumulated on earthquake sources is the same as the slip accumulated in its vicinity. Furthermore, this primarily requires to identify repeating earthquakes in the seismic data.

In **Dublanchet, P.** (2019a), I propose a different approach to estimate fault slip rate from earthquake data, that does not rely on repeating earthquake sequences. This study consists of analyzing the relationship between total fault slip and seismic slip, that is the slip derived from the cumulative seismic moment released by a population of seismogenic (velocity weakening) asperities distributed on a creeping (velocity strengthening fault) fault. Here, the fault model used is illustrated in figure 1.12c (as in section 2.4).
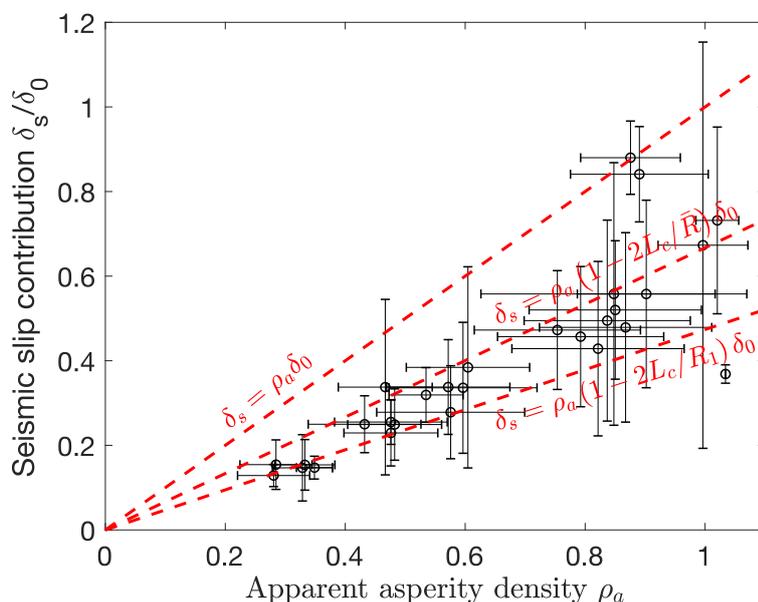
Figure 3.6: *Seismic component of total fault slip δ_s/δ_0 as a function of apparent asperity density ρ_a in the fault model illustrated in figure 1.12c. δ_s is estimated from the cumulative seismic moment released by the earthquakes, and δ_0 is the total slip accumulated on the fault during the simulation. Gray dots are numerical estimates. Red lines are the theoretical predictions of equation (3.3). R_1 and $\bar{R}$ are the minimum and mean asperity size respectively. L_c is the critical nucleation length. From* **Dublanchet, P.** *(2019a).*

This relationship is shown in figure 3.6: globally, the ratio between seismic slip (estimated from cumulative coseismic moment) and total slip linearly increases with the apparent asperity density ρ_a. ρ_a is an estimate of the true asperity density, based on the analysis of earthquake locations and source size. It is shown in **Dublanchet, P.** (2019a) that the apparent asperity density converges to the real asperity density if enough events are considered (typically, one needs to wait several cycles of the main event). In **Dublanchet, P.** (2019a), an approximate expression for the ratio δ_s/δ_0 is derived from simple mechanical arguments leading to:

$$\frac{\delta_s}{\delta_0} = \rho_a(1 - 2\frac{L_c}{R}), \qquad (3.3)$$

where L_c is the critical nucleation length of the seismogenic asperities, and R could be seen as the minimum or mean asperity size on the fault. Expression (3.3) provides a good approximation

of the numerical results 3.6.

As far as the apparent asperity density could be estimated, and a sufficient number of events are recorded, the results shown in figure 3.6 support the possibility of deriving total slip from the cumulative seismic moment released by microseismicity, without having to look for repeating earthquakes.

This result is of course only valid in the case of seismic activity restricted to a single fault. I expect therefore that it could be useful on mature fault systems, with little off fault seismicity.

3.3 Fluid induced seismicity : exploring the role of injection scenario.

The fluid operations associated with natural resources exploitation (shale gaz, geothermal energy, water resources) trigger a significant amount of seismicity (Deichmann & Giardini, 2009; Ellsworth, 2013; Stabile *et al.* , 2014). This induced activity is interpreted as the failure of preexisting critical faults following direct pore pressure variations, or indirect poro-elastic stress perturbations caused by the fluid flow at depth (Healy *et al.* , 1968; Raleigh *et al.* , 1976; Frohlich, 2012; Ellsworth, 2013).

Observations of induced seismicity sequences report a sensitivity of the seismicity rate on the injection scenario (maximum pressure in the well, rate of pressure increase, injection rate) (Healy *et al.* , 1968; Frohlich, 2012). Depending on the injection scenarios, induced sequences may be delayed, even a long time after the end of injection (post-shut in seismicity) (Healy *et al.* , 1968; Deichmann & Giardini, 2009). The magnitude content is also known to be different for induced and natural seismicity, as shown by the change of the magnitude-frequency distributions (this issue is discussed in section 2.2 of chapter 1). Here again, the injection scenario is suspected to control the magnitude content, as shown by the increase of maximum magnitude with the volume of injected fluid (McGarr, 2014; Galis *et al.* , 2017).

In this framework, earthquakes are indirect evidences of pore pressure changes at depth, that are not yet easily monitored. Induced seismicity could eventually be used to monitor fluid flow, but this requires to have a better knowledge of the physics of fluid-fault interaction. To study this issue, the fault models illustrated in figure 1.12 could be coupled to a fluid flow model (Segall & Lu, 2015; Kroll *et al.* , 2017). This was the purpose of the PhD project of Michelle Almakari. Under my co-supervision, Michelle Almakari developed a fault model coupling elasticity, rate-and-state friction, and fluid diffusion in a 2D framework. The fault configuration used in her study is depicted in figure 1.12c'. A simple linear fluid diffusion model was coupled to the mechanical part, in the form of a local injection with controlled pressure, and 1D diffusion along the fault's strike. She then conducted a parametric study, published in Almakari, M.*et al.* (2019) in order to investigate the dependence of seismicity rate and magnitude content on the injection scenario.

As illustrated in figure 3.7a., the injection scenario consists of a first phase of linear pore pressure increase at a rate β (phase I), followed by a period with constant pressure P_{max} at the injection well (phase II). Because of diffusion, the mean pore pressure in the fault follows a similar trend but delayed in time. In response to this injection, slip is activated along the fault, and seismogenic (velocity weakening patches) rupture as earthquakes.

The characteristics of the resulting seismicity are illustrated in figures 3.7a to d. Such an injection scenario leads to a transient increase followed by a decay of the seismicity rate, that tracks the pressure rate variations along the fault rather than the pressure itself (figure 3.7a.). The end of the injection is associated with a period of quiescence preceding the return to the background level (seismicity before injection). The magnitude content is also affected by the injection, in particular for the largest events of the sequence (figure 3.7b.).

The effect of the injection scenario on the increase of seismicity rate could be quantified by the maximum seismicity rate reached during the induced sequence (Almakari, M.*et al.* , 2019), as
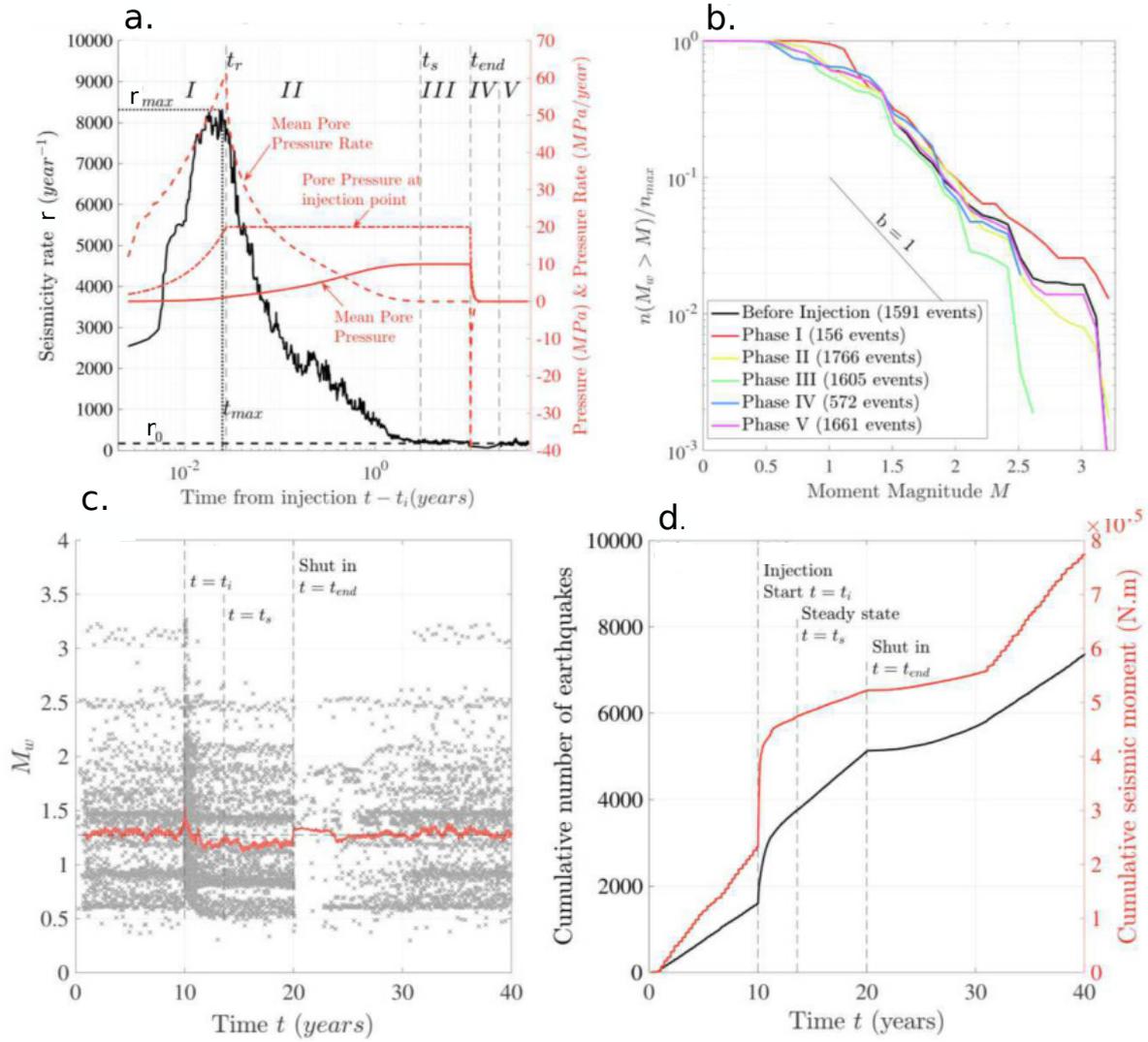
Figure 3.7: *Seismic activity and pore pressure evolution resulting from a local fluid injection into the fault model illustrated in figure 1.12c'.* **a.** *Pore pressure, pore pressure rate and seismicity rate. Numbers I to V define five different stages of the numerical experiment. r_0 is the seismicity rate before injection. r_{max} is the maximum seismicity rate achieved at time t_{max}. At time t_s, the seismicity rate returns to r_0. t_{end} marks the end of injection.* **b.** *Normalized magnitude-frequency distributions during the different stages illustrated in figure a.* **c.** *Magnitude evolution of induced earthquakes during the injection. The red line is a moving average.* **d.** *Cumulative number of earthquakes and cumulative seismic moment released during the injection. From* Almakari, M.et al. *(2019).*

illustrated in figure 3.8. Overall, the maximum seismicity rate increases with both the maximum pressure P_{max} and the injection rate β. Interestingly, the model predicts a saturation of the maximum seismicity rate increase when the pressure rate reaches a threshold. Such a saturation is not predicted by other models of induced seismicity that do not account for magnitude changes (Dieterich, 1994). As discussed in Almakari, M.et al. (2019), and in section 2.2, the saturation of the maximum seismicity rate is compensated by a change in the magnitude content where larger events become more frequent during the injection period (see figure 2.4).

This study has demonstrated the importance of both the pressure rate and the maximum pressure in the control of the seismic activity. This study would however need to be extended
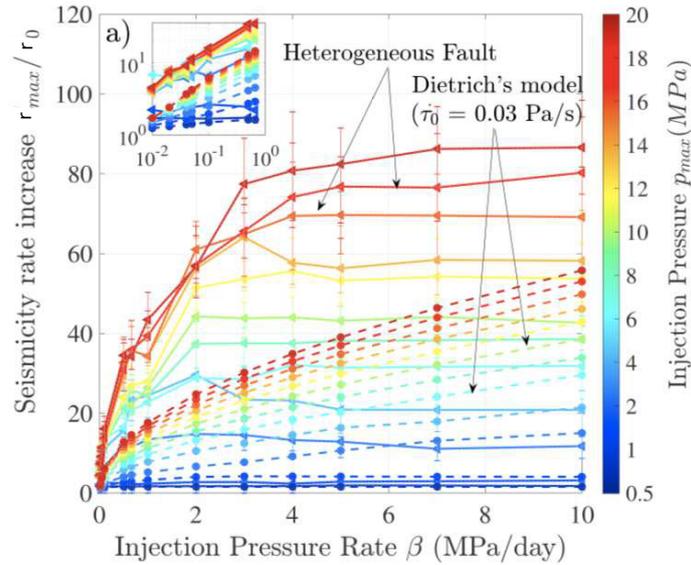
Figure 3.8: *Maximum seismicity rate increase r_{max}/r_0 for different injection scenarios in the heterogeneous fault model shown in figure 1.12c'. r_0 is the seismicity rate on the fault under constant tectonic loading alone (prior to injection). Numerical results are shown with solid lines. The dashed lines were obtained using the model by Dieterich (1994) under an effective stressing rate $\dot{\tau}_0$, that is ignoring the possibility of stress redistributions and different magnitudes. From* Almakari, M.*et al. (2019)*

to the case of a 2D fault, or to the case of a fault network, in particular to study the important question of post shut-in activity that was not present in these simulations. Note also that only one particular fault model, with a specific frictional properties distribution was used here. Frictional properties also control to some extent the characteristics of injection induced seismicity (Kroll *et al.* , 2017). This issue would require more investigation. An interesting point concerns the role of aseismic slip in such scenarios. Because of the particular frictional properties used here and the 2D geometry, a negligible amount of aseismic slip occurred, so that this issue could not be discussed in this study.

The modeling of the second earthquake swarm in Corinth by **Dublanchet, P.** & De Barros (2020) (section 3.1) also provides insights into how injection scenarios control the seismic activity. It was shown in section 3.1 that the rate of increase of the average pore pressure in the fault (the pressurization Π_m) controls the earthquake migration speeds. The other important result was that aseismic slip is an intermediate between fluid flow and earthquake triggering. Even in the presence of aseismic slip, the injection parameters are therefore crucial in the properties of induced seismicity.

Here again, a very small range of fault models have been tested against injection so far, and extensive parametric studies with different fault configurations would be necessary to assess the role of injection scenario. In this framework, the consideration of fault networks is crucial.

3.4 Fluid induced aseismic slip

Induced seismicity is not the only mode of fault slip reactivation. As suggested by the temporal dynamics of repeating earthquakes in the framework of geothermal stimulations (Bourouis & Cornet, 2009), and by in situ fault injection experiments (Guglielmi *et al.* , 2015), fluid also triggers aseismic (slow) slip events on faults. A conceptual model of hydro-mechanical fault

interactions has emerged where the fluid injection triggers an aseismic slip front propagating along the fault and causing the failure of brittle asperities, at the origin of earthquakes. This conceptual model is for instance proposed and studied by De Barros *et al.* (2020); **Dublanchet, P.** & De Barros (2020).

An alternative way of studying fault slip reactivation is to simplify the problem and consider only the interaction between fluid flow and aseismic slip. This is the purpose of a study published in **Dublanchet, P.** (2019b). It consists of a numerical and theoretical investigation of the dynamics of aseismic shear cracks trigerred by a fluid injection in a strengthening rate-and-state interface. The fault model used here is a simple 1D interface within a 2D medium, characterized by homogeneous velocity strengthening properties (i.e. the fault model a' in figure 1.12). Here again, the fault model is injected in its center, with a control on the flow rate (or according to Darcy's law, on the pressure gradient at the injection well). This numerical experiment has been conducted under different conditions of initial overstress. Under rate-and-state friction, the overstress could be defined as the difference between the initial shear stress τ_0 and the steady state frictional stress $\tau_{ss}^0 = f_{ss}\sigma$ evaluated from equation (1.5) at the loading rate v_0 (v_b in figure 1.12).

The early evolution of the slip rate along the fault is a localized slip perturbation characterized by an exponential increase in slip rate (phase I and blue symbols in figure 3.9). Assuming a constant injection rate, the maximum slip rate increases during phase I as (see figure 3.10b):

$$v_m(t) = v_0 e^{\sqrt{t/t_I}}, \qquad (3.4)$$

where t is time, v_0 the initial slip rate, and t_I a characteristic time given by:

$$t_I = \frac{\pi a^2 \sigma^2}{4 f_0^2 q^2 D}. \qquad (3.5)$$

In equation (3.5) σ the initial normal stress, D the hydraulic diffusivity along the fault, q the pressure gradient at the injection point (proportional to injection rate according to Darcy's law) and f_0 and a the reference friction coefficient, and the direct effect parameter of the rate-and-state friction law.

This localized perturbation rapidly expands (phase II and black symbols in figure 3.9). As illustrated in this figure, depending on the prestress conditions, the fluid injection triggers two different types of propagating cracks. If initial stress is lower than the steady state stress τ_{ss}^0, a so called steady crack propagates at constant speed. The maximum slip rate within the crack increases slowly, i.e. as the logarithm of time. It is shown in **Dublanchet, P.** (2019b) that the rupture speed (the crack expansion speed) v_r is given by:

$$v_r = \frac{f_0 q D}{\tau_r - \tau_0}, \qquad (3.6)$$

where τ_0 is the initial shear stress along the fault and τ_r an equivalent residual shear stress within the crack that ignores pore pressure. The stress difference $\tau_r - \tau_0$ is positive, because of velocity strengthening behavior that leads to an increase of steady state friction coefficient with slip rate. Note that equation (3.2) used in section 3.1 for the migration of fluid induced earthquakes, derives from equation (3.6). In doing so we have defined $\Gamma = \tau_r - \tau_0$ as the velocity strengthening fracture energy density, and we have rewritten qD as $\Pi_m L/2$. Γ is what slows down the slow slip front, while the injection rate qD is what forces the expansion on a frictionally stable fault. As illustrated in figure 3.10a, equation (3.6) is a good approximation for the expansion speed observed in the simulations.

Interestingly, even if the injection controls the propagation speed, the slip front expands faster (linearly in time) than the pressurized region (as $\sqrt{t}$). An approximate formula is also derived in **Dublanchet, P.** (2019b) for the maximum slip rate. It increases as :
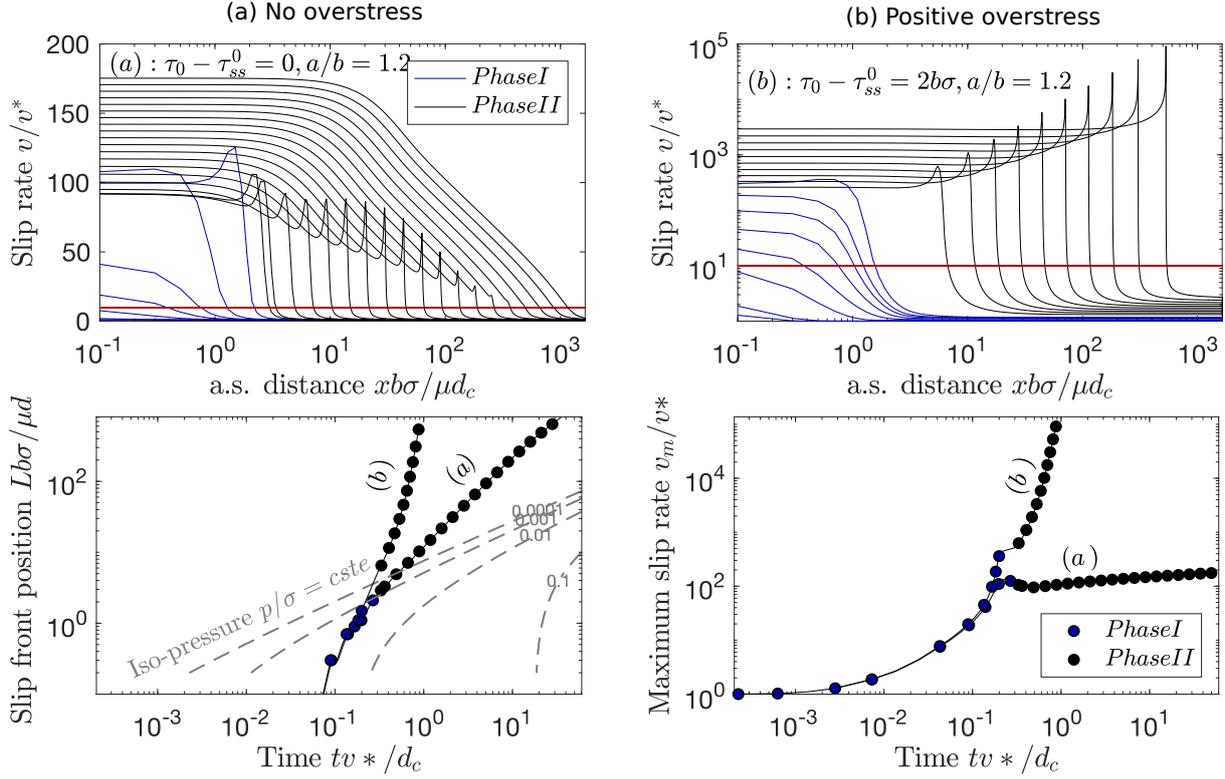
Figure 3.9: *Example of slip triggered by a local fluid injection in a velocity strengthening fault. Top figures show slip rate v profiles at different times indicated by the symbols in the bottom figures. Because of symmetry, only half profiles are shown. Bottom figures: slip front position L and maximum slip rate v_m evolution. **a.**: fault initially at steady state $\tau_0 = \tau_{ss}^0$ (no overstress). **b.**: fault initially with a slight overstress $\tau_0 > \tau_{ss}^0$. The red line in the top figures indicates the reference level for expansion speed estimation. a, b and a/b are the rate-and-state frictional parameters (and ratio of them) used here. Results are normalized using v^* (initial slip rate), μ (shear modulus), d_c (critical slip for friction evolution), σ (normal stress). From **Dublanchet, P. (2019b)**.*

$$v_m(t) = \frac{4f_0 q D}{\pi b \sigma}\left[1 + \frac{1}{2}\ln\frac{t}{t_s}\right], \tag{3.7}$$

where t_s is the characteristic timescale provided by:

$$t_s = \frac{(\tau_r - f_0\sigma)^2 - (\tau_0 - f_0\sigma)^2}{f_0^2 q^2 D}. \tag{3.8}$$

Here again, equations (3.7) and (3.8) capture the log increase of maximum slip rate during phase II (see figure 3.10b.).

If initial stress τ_0 is higher than the steady state stress τ_{ss}^0 an accelerating crack propagates, with a maximum slip rate blowing up in a finite time. As expected in such systems (Ampuero & Rubin, 2008), the rupture (propagation) speed increases proportionally to the maximum slip rate. Then, the crack expansion is not any more driven by the fluid injection, but by the initial prestress. The energy balance at the crack tip leads to self-similar profiles of slip, slip rate and stress shown in figures 3.10c, 3.10d and 3.10e.

The theoretical solutions (3.4), (3.6) and (3.7) allow to relate hydraulic and frictional properties to the expansion speed of fluid driven aseismic fronts. This result could be used to interpret

migration episodes in seismicity data, which are clearly faster than what is expected for pore pressure diffusion (Duverger *et al.*, 2015; De Barros *et al.*, 2020), as illustrated by the Corinth swarm analysis shown in section 3.1.
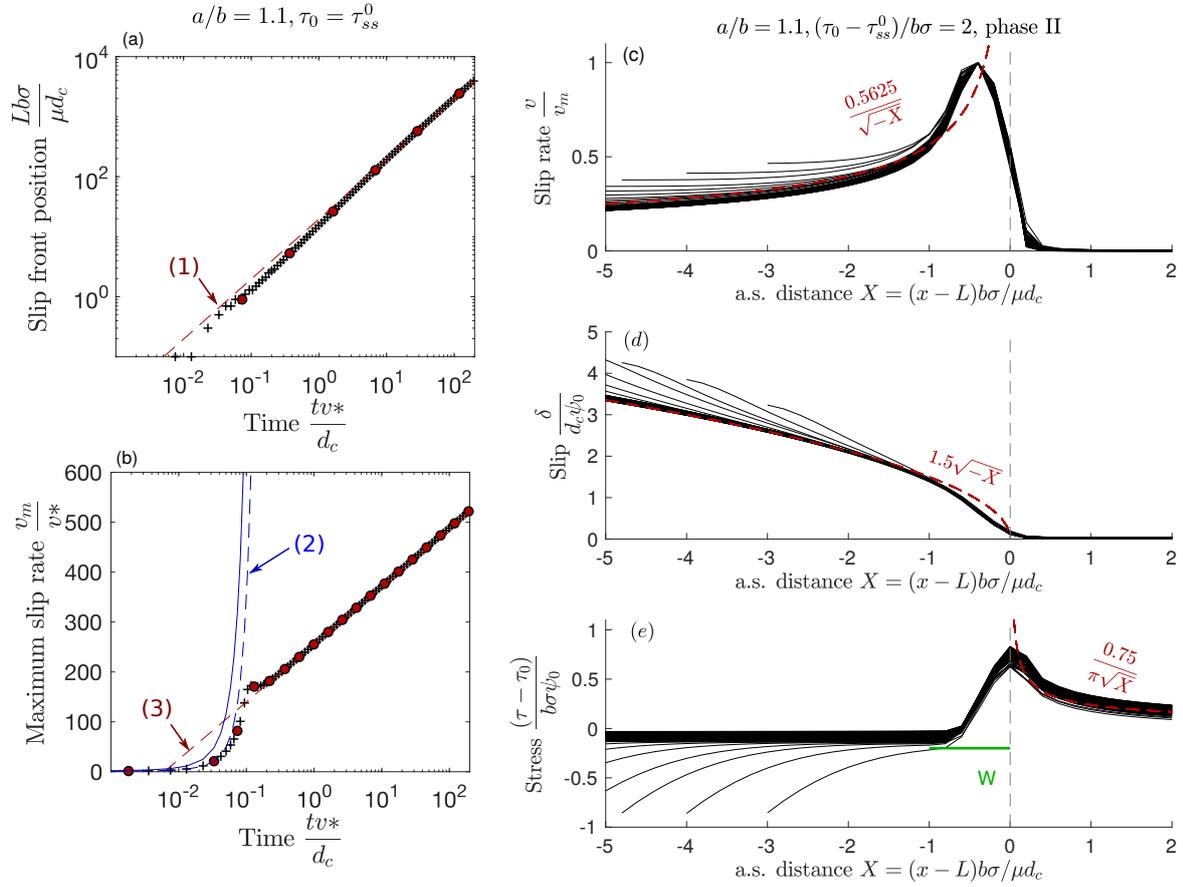
Figure 3.10: *Comparison between numerical and theoretical solutions for the slow slip front propagation illustrated in figure 3.9. Right column:* **a.** *slip front position L in the absence of initial overstress. Symbols indicate numerical solution, red dashed line labeled (1) is the solution (3.6).* **b.** *Maximum slip rate v_m evolution in the absence of initial overstress. Symbols are the numerical solution, blue dashed line labeled (2) is the solution (3.4) and the red dashed line labeled (3), the solution (3.7). Left column: Normalized slip rate v (**c.**), normalized slip δ (**d.**) and normalized stress τ (**e.**) profiles for an injection on a fault with a slight overstress. Black lines are numerical solutions. The profiles are centered at the slipping patch tip (L is the length of the slipping patch). Red dashed lines indicate theoretical solutions from fracture mechanics theory (Lawn, 1993). ψ_0 is a normalizing factor. a, b and d_c are rate-and-state parameters. μ is the shear modulus, σ the initial normal stress, and v^* the initial slip rate before injection. From* **Dublanchet, P. (2019b).**

3.5 Conclusion

As illustrated in this chapter, different approaches could be developed to improve our ability to quantify slow slip and fluid flow from earthquake swarms, with the use of mechanical models. One approach consists of developing mechanical models for particular, well analyzed swarms, such as in the case of the Corinth rift. A second approach is to perform parametric studies with models, in order to extract general relationships between seismic activity, aseismic slip and

fluid flow. My contribution to these efforts lead to six publications over the past seven year. One of them is the outcome of Michelle Almakari's PhD project, co-advised by myself. Four of these studies were made in collaboration with seismologists from Géoazur (University of Nice Sophia Antipolis), in particular with M. Godano and L. De Barros. Because of the amount of unknown parameters, parametric studies are often laborious, and it is still difficult to generalize their conclusions to particular swarms, unless theoretical relationships are extracted. On the other hand, the growing amount of seismological data about earthquake swarms is an interesting opportunity to develop the first approach. This is one of my research projects, as detailed in the last chapter (see section 4.1).

Chapter 4

Research perspectives

In this last chapter I present how I intend to pursue my research projects in the future. The studies summarized in the last two chapters have shown the importance of coupling seismological observations and physics-based models to unravel fault processes. Another interesting and complementary approach is to study fault slip in the laboratory. Fault reactivation experiments present the advantage of being controlled, and allow a detailed monitoring of slip, stresses and fluid flow. Therefore, I plan to extend the study of fault slip phenomena by confronting model predictions to both seismological and laboratory experiments. For that, I suggest first to pursue the modeling of specific earthquake swarms, making use of the near fault observatories data delivered in the framework of the EPOS program (first section of the chapter). In a second step, I propose to develop the modeling of rock mechanics experiments: this is the purpose of the second section, where a preliminary study about shear induced permeability enhancement is presented. Permeability enhancement during fault slip reactivation is indeed suspected to play an important role in the hydro-mechanical processes of fault zones. My final project is to extend the theoretical and numerical investigations of fault models coupling elasticity and friction by the study of effective frictional properties. This latter issue is crucial in the perspective of connecting seismological and laboratory experiments.

4.1   Quantifying slow slip and fluid flow underlying seismic swarms

In Europe, seven geophysical observatories maintained through the EPOS project record thousands of earthquakes yearly between magnitude 0-1 and 4. Such microearthquakes are able to provide unprecedented in situ information about the stress accumulation associated with fundamental geological processes (volcanic eruption, reactive fluid flow, nucleation of damaging earthquakes), at a daily and meter scale resolution. However, this intense activity remains largely under exploited in the analysis of deep processes. In the coming years, I propose to tackle this problem by the use of physics-based fault models discussed in the previous sections.

   Microseismic analyses usually provide earthquake catalogs, listing the location in space and time, the magnitude, and from time to time the source parameters (fault orientation, amount of slip and stress drop) of each earthquake recorded in a given area. This information is traditionally used to image fault structures at depth (Chiaraluce *et al.* , 2011), or interpreted in terms of tectonic stress conditions (Hardebeck & Michael, 2006; Narteau *et al.* , 2009). This latter approach has allowed to identify many processes triggering earthquakes: slow aseismic slip on major tectonic faults (Uchida *et al.* , 2003), fluid migration and operations at depth (Shapiro & Dinske, 2009b), rainfall events (Hainzl *et al.* , 2006), stress redistribution after large earthquakes (King *et al.* , 1994), volcanic intrusions (Ágústsdóttir *et al.* , 2016), the flow of ice in glaciers (Faillettaz *et al.* , 2011), landslides (Helmstetter & Garambois, 2010) tidal stresses (Cochran *et al.* , 2004), mining operations (Gibowicz, 2009), impoundment of reservoirs behind dams (Gupta *et al.* , 1969). Among all these processes, aseismic slip and fluid flow seem to play

an important role in triggering seismicity.

A large majority of these studies rely on the Coulomb failure model (Brace & Byerlee, 1966), which leads to instantaneous triggering if a stress perturbation exceeds a frictional resistance on a specific fault. Although this model indicates how stresses and seismicity rates could be correlated, it ignores many important aspects of the earthquake physics (stress redistribution, time and slip dependent friction (Dieterich, 1979)). It is furthermore unable to make any magnitude predictions. Alternatively, seismicity could be interpreted in light of experimental results obtained at the laboratory scale (Amitrano, 2003). However, the physical models supporting the experimental results are usually not fully understood.

At the same time, advanced mechanical models of fault generating earthquakes have been developed (see introduction section for a brief description). As shown in the previous chapters, I have contributed to this modeling effort. Unfortunately, this class of models is rarely used to interpret specific microseismic sequences. One of the reasons is that too few of them are really adapted to study the problems of microearthquake sequence dynamics: current earthquake models do not account at the same time for a 3D geometry, full elasto-dynamic stress interactions, slip dependent frictional behavior, and earthquake related permeability enhancements. Nevertheless, in very specific situations involving for instance the reactivation of a particular fault, existing models could be used to improve traditional interpretation. The work on the Corinth swarms (section 3.1) is an example of what could currently be done to quantify aseismic slip and fluid flow from seismicity observations.

Near Fault Observatories (NFOs) monitoring seismicity in the most active regions of Europe in the framework of the EPOS project (Festa *et al.* , 2018) is an unprecedented opportunity to fill the existing gap between earthquake models and microseismic observations. The seven geophysical observatories will continuously monitor and distribute in open access geophysical data, in particular earthquake catalogs. The seismicity occurring in these areas is in many cases suspected to be driven by fluid (eventually magmatic) flow or deep aseismic slip on tectonic faults. The EPOS dataset is the ideal candidate to probe our ability to quantify these processes with seismicity.

In this framework, I propose to pursue the quantification of aseismic slip and hydraulic properties underlying seismic sequences with physics-based fault models initiated with the modeling of Corinth swarms. This will eventually require to develop new fault models that are adapted to microseismic sequences, and to perform an important amount of data analysis, in order to extract as much information as possible about the events of a particular sequence (location, source parameters).

New fault models for microseismic sequences will have to incorporate fundamental aspects of earthquake physics: a distributed fault population in a 3D geometry, the presence of fluids, rate-and-state friction (Dieterich, 1979), elastodynamic stress redistributions, permeability enhancement. The objective is that thousands of earthquakes could be computed within hours or days. For that, both a physical and a numerical optimization will have to be conducted. The physical optimization could rely on a simplification of the elastodynamic interaction computation. The numerical optimization will essentially consist of a parallelization of the simulators, mixing shared memory (open MP) and distributed memory (MPI) approaches. Such earthquake simulator dedicated to microseismicity has never been developed. The main challenge consists of achieving a satisfactory balance between computational efficiency and physical accuracy. This could be achieved through successive benchmarking steps, after each simplification of the elastic interactions.

Importantly, the fault model conception will have to be guided by the seismic sequence itself. Preliminary location will allow to discriminate between the reactivation of a single fault or a network of faults for instance. Magnitudes provide an idea of the typical fault sizes to consider. For that purpose, the development of the models should be accompanied by an analysis of the seismological data. Depending on the specific sequence considered, earthquake relocation, focal

mechanism and source parameter estimations will be of great support. For that reason, I would like to develop further the collaborations with seismologists, possibly in the framework of an ANR or ERC project.

As shown in section 3.1, the quantification of deep aseismic slip and fluid flow will rely on the comparison between synthetic (coming from fault models) and real earthquake sequences. This could be done from first order statistical features of the sequences such as the distribution of magnitudes and time delays between earthquakes, or eventually from the migration speeds (if migration occurs). In other words, the aim is to find the amplitude of forcing necessary to explain these characteristics.

4.2 Modeling laboratory fault slip

My second research perspective is to make use of mechanical fault models in the framework of rock mechanics experiments. As shown in section 2.6, fault slip phenomena could be studied in the laboratory, using saw-cut rock samples loaded in a press. Such experimental devices have been known to generate stick slip behavior for a long time (Brace & Byerlee, 1966), an analog to natural earthquakes. In the laboratory, loading mechanisms are controlled and fault slip could be monitored in great details, which is not always possible for natural faults. However, experimental results on fault slip processes are rarely confronted to mechanical model predictions. This however could bring a new light on our understanding of fault processes, as illustrated by the preliminary study about shear induced permeability enhancement detailed in the following.

Many evidences report that permeability is not constant during fluid induced fault slip, first because it depends on effective stress which is reduced by pore pressure (Zoback & Byerlee, 1975; Rutter & Mecklenburgh, 2018), then because of shear induced dilatancy that promotes permeability enhancement (Wu *et al.*, 2017; Im *et al.*, 2018; Guglielmi *et al.*, 2015).

Estimating permeability enhancement during fault slip reactivation was the purpose of an experimental study conducted in the framework of Michelle Almakari's PhD project, and in collaboration with F.X. Passelegue (EPFL). It was recently been published in Almakari, M.*et al.* (2020). A schematic view of the sample is shown in figure 4.1. The experiment consisted of: first loading the sample in a tri-axial press up to 90 percent of the peak strength of the fault, then injecting a fluid (pump A) while measuring average fault slip, local strain, average shear stress and pore pressure. These measurements were performed with a displacement sensor, a set of strain gauges, and through pumps A and B. This protocol was applied under three different levels of confining stress (30, 60 and 95 MPa). Typical results are shown in figures 4.2a., 4.2b. and 4.2c. Before starting the injection, the sample was saturated with a fluid so that the pore pressure within the fault is initially at 10 MPa. After the loading phase, pore pressure increases in boreholes A and B, with a time delay corresponding to the fluid diffusion along the fault (bulk permeability being in these samples much smaller than along fault permeability). In all cases, the injection triggers fault slip releasing shear stress. Fault slip is here a combination of aseismic slip and rapid slip events (shown as black dots in figures 4.2a., 4.2b. and 4.2c.).

In a second step, we used the pressure measurements (pumps A and B) to invert for an effective time-dependent diffusivity along the fault. For that, we used both a deterministic inversion approach and a Bayesian method in order to properly estimate the uncertainty on the inverted diffusivity. The deterministic approach makes use of the adjoint state method (Plessix, 2006), the Bayesian inversion is built on a Monte Carlo Markov Chain algorithm (MCMC) (Metropolis *et al.*, 1953; Hastings, 1970). The inversion was conducted in collaboration with H. Chauris and A. Gesret (MINES ParisTech). In all cases, the forward problem was a 2D diffusion equation with a time dependent effective diffusivity $D(t)$ and a source term located at borehole A. The source term consists of a controlled injection pressure taken from the measurements of pump A. The diffusion equation was solved numerically with a finite difference scheme on the elliptical fault depicted in figure 4.1 (i.e. the saw cut fault geometry), assuming homogeneous
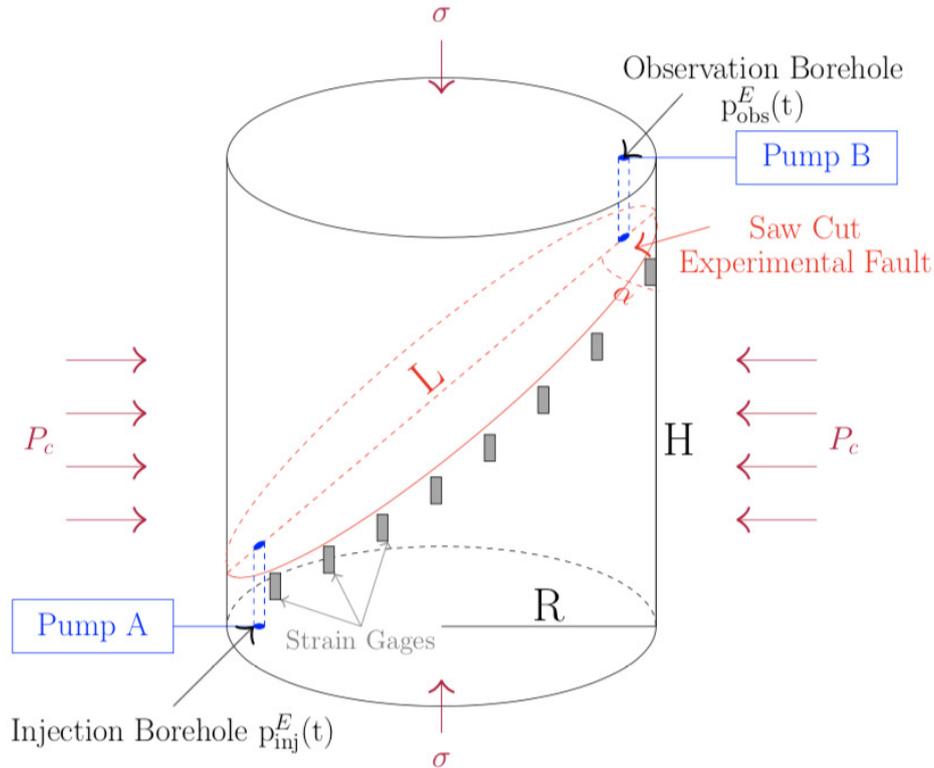
Figure 4.1: *Schematic diagram of the andesite saw cut sample used to perform fluid injection experiments. The fluid is injected in pump A. P_c is the confining pressure, and σ the axial load. From* Almakari, M.*et al. (2020).*

Neumann boundary conditions (no fluid flux on the boundaries of the fault, as expected in the experiment).

The inverted diffusivity history is shown in figures 4.2d., 4.2e. and 4.2f. In each case, the effective diffusivity increases by one order of magnitude during fault slip reactivation. The mechanical origin of the diffusivity enhancement observed in this study in however still unclear. The most robust feature outlined in Almakari, M.*et al.* (2020) is that effective diffusivity increases with decreasing effective normal stress acting on the fault (difference between applied load projected on the normal to the fault surface and average pore pressure derived from the numerical solution of pore pressure diffusion equation). Normal stress dependence of permeability has already been reported in many experiments (Zoback & Byerlee, 1975; Rutter & Mecklenburgh, 2018), and could easily be interpreted as the (possibly non-linear) closure of joints and cracks. If one considers the fault as one of such cracks, this could explain the increasing diffusivity. As fluid is injected and diffuses along the fault, normal stress is reduced and permeability enhancement leads to an effective diffusivity increase. An effect of fault slip is however not excluded here, but we were not able to provide a robust evidence for permeability changes related to shear slip. If slip induced permeability enhancement occurred in these experiments, this study shows that it was likely a second-order effect compared to the effective stress reduction.

Note that the slip events recorded during these experiments were used to evaluate the effect of prestress on the rupture speed discussed in section 2.6.

This preliminary study of fault diffusivity enhancement during slip activation has demonstrated the important potential of analyzing laboratory experiments in light of hydro-mechanical models and advanced inversion techniques. A short term research perspective is to develop further such approaches in order to get a better understanding of slip related fault permeability
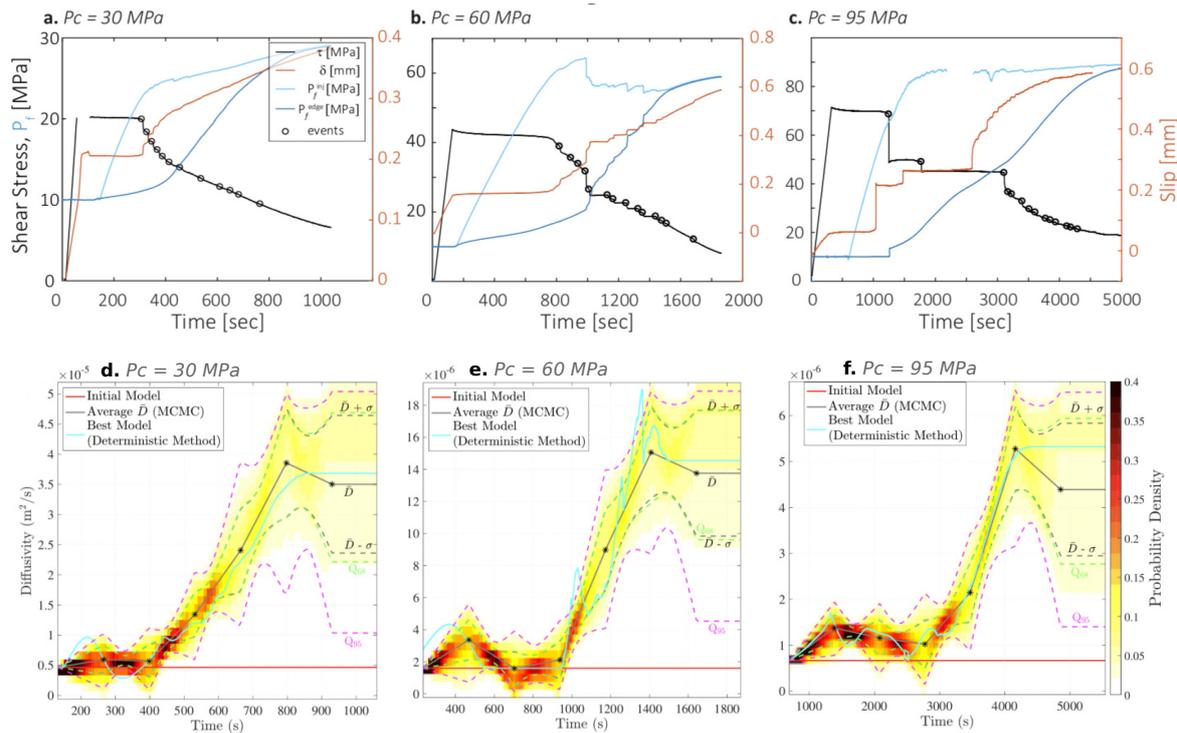
Figure 4.2: *Top line: pore pressure recorded in pumps A and B (blue), fault slip (red), and fault shear stress (black) during experiments at 30 MPa (**a.**), 60 MPa (**b.**) and 95 MPa (**c.**) of confining pressure. Black dots indicate rapid slip (stick slip events). Bottom line: effective time-dependent diffusivity inverted from the pressure measurements shown in the top figures for confining pressures 30 MPa (**d.**), 60 MPa (**e.**) and 95 MPa (**f.**). The effective diffusivity is considered uniform on the fault, and time-dependent. The red and blue solid lines correspond to the initial and final diffusivity models obtained from deterministic inversion. The colors show the probability density function resulting from the Bayesian inversion (MCMC). The mean model obtained by MCMC is shown in black, and the quantiles are represented with the dashed colored lines. From Almakari, M.et al.   (2020).*

enhancement. It could be possible for instance to include the fault slip data in the inversion procedure. This requires to use a coupled hydro-mechanical model to solve the direct problem, such as the ones developed in Almakari, M.*et al.*   (2019) and **Dublanchet, P.** (2019b). The inversion procedure should also be modified to account for these new data. Similarly, new experiments using a network of pressure sensors are planned (in collaboration with F.X. Passelegue and collaborators in EPFL) and will allow to solve for the complete space and time diffusivity pattern. The increase of pressure and slip observations will therefore lead to a finer understanding of diffusivity changes. Another improvement will be to consider the full geometry of the rock sample in the hydro-mechanical model, and not the simple interface geometry of the models illustrated in figure 1.12. This latter issue is one of the motivations for Jinlin Jiang, who started his PhD one year ago in the geophysical group of MINES ParisTech.

4.3   Effective friction

In the perspective of connecting experimental and natural fault behavior, the question of upscaling mechanical properties arises. It is particularly true for frictional properties. The rate-and-state friction law, used to explain many observations of fault slip at the kilometer scale, has been

derived from laboratory experiments, on centimeter to meter scale rock samples. Many studies suggest that rate-and-state friction could govern fault slip at large scales, but what is the link between frictional properties estimated in the laboratory and frictional properties of kilometric scale faults? Is it possible to define effective frictional properties?

The numerical studies presented in the last chapters have revealed that many processes are controlled by an effective rate-and-state parameter defined as the difference between the spatial average a_0 of the rate-and-state parameter a and the spatial average b_0 of the rate-and-state parameter b. The transition between isolated ruptures and system-size ruptures occurs when $a_0 - b_0 = 0$, for a set of asperities distributed on a creeping fault (**Dublanchet, P.** *et al.* , 2013a). Isolated ruptures and system size ruptures would then correspond to an effective velocity strengthening and effective velocity weakening behavior respectively. In this particular model involving seismogenic asperities and fault creep, $a_0 - b_0$ could be regarded as the distance between the actual and a critical asperity density (see section 2.1). In this sense, $a_0 - b_0$ controls also the regularity of interacting repeating earthquakes (see section 2.4). The difference $a_0 - b_0$ is also the main parameter controlling the characteristic timescale for the Omori decay of repeating earthquake activation following a coseismic stress perturbation (**Dublanchet, P.** *et al.* , 2013b). This is presented in details in section 2.3.

The ratio a_0/b_0 is also one of the parameters controlling the nucleation regimes on a heterogeneous rate-and-state fault, as discussed in section 2.5 and in **Dublanchet, P.** (2018). Importantly, nucleation regimes observed under heterogeneous friction are similar to what is obtained under homogeneous friction (Rubin & Ampuero, 2005), and it is possible to define a critical nucleation length for each of these regimes, as illustrated in figure 4.3. The expressions derived in **Dublanchet, P.** (2018) for the critical nucleation length not only involve the spatial averages a_0 and b_0, but also different characteristics of the frictional heterogeneity, in particular the characteristic wavelength λ of friction variations along the fault. On one hand, these results show that at a larger scale, earthquake nucleation is similar to what happens at small scale, so that we can define effective properties. On the other hand, it is not sufficient to consider the spatial average of frictional parameters to upscale the friction law, other properties need to be taken into account.

This latter example is the main motivation to extend the investigation towards the definition of an effective frictional theory. The second motivation is that so far, I have not analyzed the effect of spatial heterogeneities in d_c, which is a possible property characterizing natural faults, as suggested by the scale dependence of fracture energy (Ide & Aochi, 2005; Abercrombie & Rice, 2005). Furthermore, previous work about effective friction only focused on slip-weakening law (Campillo *et al.* , 2001; Voisin *et al.* , 2002; Latour *et al.* , 2011). To further investigate this issue, I propose two approaches.

First I will reanalyze the whole synthetic database developed over the last years from models with heterogeneous friction. This database is made of all the synthetic earthquake catalogs produced for the studies presented in the last chapters. Synthetic catalogs include source location, time, extent, the source time function. In addition, I have also conserved the mean slip, mean shear stress and mean slip rate history of the fault. The purpose would be to compute all the statistical properties of earthquakes and slow slip events that were not yet considered in previous studies, and to determine whether the mechanical control involves effective frictional parameters.

In a second step, I will perform new numerical simulations inspired from the original laboratory experiments that led to rate-and-state friction theory. These experiments consist of velocity stepping tests (Dieterich, 1979), where the slip rate on the fault is controlled, while friction is measured. The idea here is to perform numerical velocity stepping tests on a wide range of faults, characterized by different kinds of frictional heterogeneity (involving variable a, b or d_c). The synthetic averaged frictional response would allow to define effective a, b and d_c parameters.

Finally, this research project about effective friction could benefit from an experimental approach, such as the one detailed in the previous section. Fault slip experiments with heteroge-

neous rock samples are currently developed by collaborators in EPFL rock mechanics laboratory.
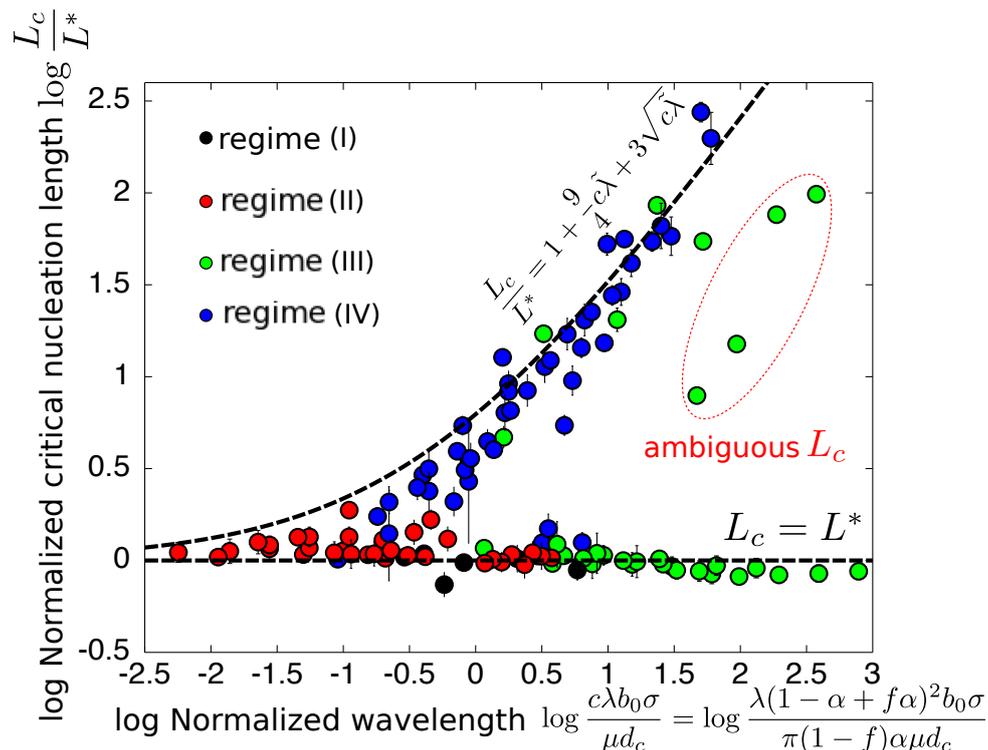
Figure 4.3: *Critical length for the main shock nucleation regimes illustrated in figure 2.8. L_c is the critical nucleation length, L^* is a characteristic length scale of the problem. b_0 is the average rate-and-state parameter b, d_c is the critical slip of rate-and-state friction, σ is the normal stress, μ the shear modulus. f and α are the parameters characterizing the frictional heterogeneity. c is a constant involving the frictional parameters. λ is the wavelength of $a - b$ variations along the fault, and $\tilde{\lambda}$ the normalized wavelength λ/L_b. See **Dublanchet, P.** (2018) for details.*

4.4 Conclusion

The three research perspectives discussed in this chapter aim at extending the use of mechanical fault models in three different directions. First to provide a new interpretation of natural and induced seismic swarms. Then, to analyze new laboratory fault slip experiments. Finally to bridge the gap between the scale of laboratory faults and the scale of natural faults. For all these projects, preliminary studies have been conducted and show promising results. Two seismic swarms of the Corinth area have been used to quantify aseismic slip and overpressure in the Corinth rift area, some progress has been made on shear induced diffusivity enhancement, and effective rate-and-state frictional parameters have been identified has controlling fault slip process on heterogeneous faults. These preliminary studies are summarized in 3 publications. The study of permeability enhancement from modeling of laboratory data is one of the results of Michelle Almakari's PhD, and the first publication obtained in the framework of our collaboration with the rock-mechanics laboratory in EPFL.

These different projects will require new developments, in particular new fault models more adapted to seismic swarms and laboratory samples. A new approach to model experimental faults is currently developed by J. Jiang, a PhD student co-advised by F. Pellet (INSA Lyon), D. Bruel (MINES ParisTech) and myself. Inversion techniques will need to be developed for specific problems of fault slip, as initiated in the study of diffusivity enhancement. For that,

the expertise of the Geophysical research group of MINES ParisTech in the field of inverse problem will be of great help. Finally, seismological analysis of earthquake swarms will need to be conducted in parallel with model developments. This latter part will rely on my collaborations with seismologists of Géoazur.

Bibliography

Abercrombie, R.E. 1995. Earthquake source scaling relationships from- 1 to 5 ML using seismograms recorded at 2.5-km depth. *Journal of Geophysical Research: Solid Earth*, **100**(B12), 24015–24036.

Abercrombie, R.E., & Rice, J.R. 2005. Can observations of earthquake scaling constrain slip weakening? *Geophysical Journal International*, **162**(2), 406–424.

Ágústsdóttir, T., Woods, J., Greenfield, T., Green, R.G., White, R.S., Winder, T., Brandsdóttir, B., Steinthórsson, S., & Soosalu, H. 2016. Strike-slip faulting during the 2014 Bárðarbunga-Holuhraun dike intrusion, central Iceland. *Geophysical Research Letters*, **43**(4), 1495–1503.

Allmann, B. P., & Shearer, P. M. 2009. Global variations of stress drop for moderate to large earthquakes. *Journal of Geophysical Research: Solid Earth*, **114**(B1).

Almakari, M., **Dublanchet, P.**, Chauris, H., & Pellet, F. 2019. Effect of the Injection Scenario on the Rate and Magnitude Content of Injection-Induced Seismicity : case of a Heterogeneous Fault. *Journal of Geophysical Research: Solid Earth*, **124**(8), 8426–8448.

Almakari, M., Chauris, H., Passelègue, F.X., Dublanchet, P., & Gesret, A. 2020. Fault's hydraulic diffusivity enhancement during injection induced fault reactivation : application of pore pressure diffusion inversions to laboratory injection experiments. *Geophysical Journal International*, **223**(3), 2117–2132.

Amitrano, D. 2003. Brittle-ductile transition and associated seismicity: Experimental and numerical studies and relationship with the b value. *Journal of Geophysical Research: Solid Earth*, **108**(B1).

Ampuero, J.P., & Rubin, A.M. 2008. Earthquake nucleation on rate and state faults–Aging and slip laws. *Journal of Geophysical Research: Solid Earth*, **113**(B1).

Baltay, A., Prieto, G., & Beroza, G. C. 2010. Radiated seismic energy from coda measurements and no scaling in apparent stress with seismic moment. *Journal of Geophysical Research: Solid Earth*, **115**(B8).

Bartlow, N.M., Miyazaki, S., Bradley, A.M., & Segall, P. 2011. Space-time correlation of slip and tremor during the 2009 Cascadia slow slip event. *Geophysical Research Letters*, **38**(18).

Bernard, P., Lyon-Caen, H., Briole, P., Deschamps, A., Boudin, F., Makropoulos, K., Papadimitriou, P., Lemeille, F., Patau, G., Billiris, H., *et al.* . 2006. Seismicity, deformation and seismic hazard in the western rift of Corinth: New insights from the Corinth Rift Laboratory (CRL). *Tectonophysics*, **426**(1-2), 7–30.

Bosl, W.J., & Nur, A. 2002. Aftershocks and pore fluid diffusion following the 1992 Landers earthquake. *Journal of Geophysical Research: Solid Earth*, **107**(B12), ESE–17.

Bouchon, M., Karabulut, H., Aktar, M., Özalaybey, S., Schmittbuhl, J., & Bouin, M.P. 2011. Extended nucleation of the 1999 Mw 7.6 Izmit earthquake. *Science*, **331**(6019), 877–880.

Bouchon, M., Durand, V., Marsan, D., Karabulut, H., & Schmittbuhl, J. 2013. The long precursory phase of most large interplate earthquakes. *Nature Geoscience*, **6**(4), 299–302.

Bourouis, S., & Bernard, P. 2007. Evidence for coupled seismic and aseismic fault slip during water injection in the geothermal site of Soultz (France), and implications for seismogenic transients. *Geophysical Journal International*, **169**(2), 723–732.

Bourouis, S., & Cornet, F.H. 2009. Microseismic activity and fluid fault interactions: some results from the Corinth Rift Laboratory (CRL), Greece. *Geophysical Journal International*, **178**(1), 561–580.

Brace, W.F., & Byerlee, J.D. 1966. Stick-slip as a mechanism for earthquakes. *Science*, **153**(3739), 990–992.

Brodsky, E.E., Karakostas, V., & Kanamori, H. 2000. A new observation of dynamically triggered regional seismicity: Earthquakes in Greece following the August 1999 Izmit, Turkey earthquake. *Geophysical Research Letters*, **27**(17), 2741–2744.

Bürgmann, R., Segall, P., Lisowski, M., & Svarc, J. 1997. Postseismic strain following the 1989 Loma Prieta earthquake from GPS and leveling measurements. *Journal of Geophysical Research: Solid Earth*, **102**(B3), 4933–4955.

Bürgmann, R., Schmidt, D., Nadeau, R.M., d'Alessio, M., Fielding, E., Manaker, D., McEvilly, T.V., & Murray, M.H. 2000. Earthquake potential along the northern Hayward fault, California. *Science*, **289**(5482), 1178–1182.

Burridge, R., & Knopoff, L. 1967. Model and Theoretical Seismicity. *Bulletin of the Seismological Society of America*, **57**, 341–371.

Cakir, Z., De Chabalier, J.B., Armijo, R., Meyer, B., Barka, A., & Peltzer, G. 2003. Coseismic and early post-seismic slip associated with the 1999 Izmit earthquake (Turkey), from SAR interferometry and tectonic field observations. *Geophysical Journal International*, **155**(1), 93–110.

Campillo, M., Favreau, P., Ionescu, I.R., & Voisin, C. 2001. On the effective friction law of a heterogeneous fault. *Journal of Geophysical Research: Solid Earth*, **106**(B8), 16307–16322.

Carlson, J.M., Langer, J.S., & Shaw, B.E. 1994. Dynamics of earthquake faults. *Reviews of Modern Physics*, **66**(2), 657.

Cattania, C. 2019. Complex earthquake sequences on simple faults. *Geophysical Research Letters*, **46**(17-18), 10384–10393.

Cattania, C., & Segall, P. 2019. Crack models of repeating earthquakes predict observed moment-recurrence scaling. *Journal of Geophysical Research: Solid Earth*, **124**(1), 476–503.

Chen, K.H., Nadeau, R.M., & Rau, R.J. 2007. Towards a universal rule on the recurrence interval scaling of repeating earthquakes? *Geophysical Research Letters*, **34**(16).

Chen, K.H., Bürgmann, R., & Nadeau, R.M. 2013. Do earthquakes talk to each other? Triggering and interaction of repeating sequences at Parkfield. *Journal of Geophysical Research: Solid Earth*, **118**(1), 165–182.

Chen, T., & Lapusta, N. 2009. Scaling of small repeating earthquakes explained by interaction of seismic and aseismic slip in a rate and state fault model. *Journal of Geophysical Research: Solid Earth*, **114**(B1).

Chiaraluce, L., Valoroso, L., Piccinini, D., Di Stefano, R., & De Gori, P. 2011. The anatomy of the 2009 L'Aquila normal fault system (central Italy) imaged by high resolution foreshock and aftershock locations. *Journal of Geophysical Research: Solid Earth*, **116**(B12).

Cochard, A., & Rice, J.R. 1997. A spectral method for numerical elastodynamic fracture analysis without spatial replication of the rupture event. *Journal of the Mechanics and Physics of Solids*, **45**(8), 1393–1418.

Cochran, E.S., Vidale, J.E., & Tanaka, S. 2004. Earth tides can trigger shallow thrust fault earthquakes. *Science*, **306**(5699), 1164–1166.

Console, R., Murru, M., & Lombardi, A.M. 2003. Refining earthquake clustering models. *Journal of Geophysical Research: Solid Earth*, **108**(B10).

Dal Zilio, Luca, Lapusta, Nadia, & Avouac, Jean-Philippe. 2020. Unraveling Scaling Properties of Slow-Slip Events. *Geophysical Research Letters*, **47**(10), e2020GL087477.

De Barros, L., Baques, M., Godano, M., Helmstetter, A., Deschamps, A., Larroque, C., & Courboulex, F. 2019. Fluid-induced swarms and coseismic stress transfer: A dual process highlighted in the aftershock sequence of the 7 April 2014 earthquake (Ml 4.8, Ubaye, France). *Journal of Geophysical Research: Solid Earth*, **124**(4), 3918–3932.

De Barros, L., Cappa, F., Deschamps, A., & **Dublanchet, P.** 2020. Imbricated Aseismic Slip and Fluid Diffusion Drive a Seismic Swarm in the Corinth Gulf, Greece. *Geophysical Research Letters*, **47**(9), e2020GL087142.

Deichmann, N., & Giardini, D. 2009. Earthquakes induced by the stimulation of an enhanced geothermal system below Basel (Switzerland). *Seismological Research Letters*, **80**(5), 784–798.

Diehl, T., Kraft, T., Kissling, E., & Wiemer, S. 2017. The induced earthquake sequence related to the St. Gallen deep geothermal project (Switzerland): Fault reactivation and fluid interactions imaged by microseismicity. *Journal of Geophysical Research: Solid Earth*, **122**(9), 7272–7290.

Dieterich, J.H. 1979. Modeling of rock friction: 1. Experimental results and constitutive equations. *Journal of Geophysical Research: Solid Earth*, **84**(B5), 2161–2168.

Dieterich, J.H. 1992. Earthquake nucleation on faults with rate-and state-dependent strength. *Tectonophysics*, **211**(1-4), 115–134.

Dieterich, J.H. 1994. A constitutive law for rate of earthquake production and its application to earthquake clustering. *Journal of Geophysical Research: Solid Earth*, **99**(B2), 2601–2618.

Dinske, C., Shapiro, S.A., & Rutledge, J.T. 2010. Interpretation of microseismicity resulting from gel and water fracturing of tight gas reservoirs. *Pure and Applied Geophysics*, **167**(1-2), 169–182.

Dodge, D.A., Beroza, G.C., & Ellsworth, W.L. 1996. Detailed observations of California foreshock sequences: Implications for the earthquake initiation process. *Journal of Geophysical Research: Solid Earth*, **101**(B10), 22371–22392.

Dragert, H., Wang, K., & James, T.S. 2001. A silent slip event on the deeper Cascadia subduction interface. *Science*, **292**(5521), 1525–1528.

Dublanchet, P., Bernard, P., & Favreau, P. 2013a. Interactions and triggering in a 3-D rate-and-state asperity model. *Journal of Geophysical Research: Solid Earth*, **118**(5), 2225–2245.

Dublanchet, P., Bernard, P., & Favreau, P. 2013b. Creep modulation of Omori law generated by a Coulomb stress perturbation in a 3-D rate-and-state asperity model. *Journal of Geophysical Research: Solid Earth*, **118**(9), 4774–4793.

Dublanchet, P., Godano, M., & Bernard, P. 2015. Inferring fault mechanical conditions from the source parameters of a complex microseismic multiplet in the Corinth rift, Greece. *Journal of Geophysical Research: Solid Earth*, **120**(11), 7655–7682.

Dublanchet, P. 2018. The dynamics of earthquake precursors controlled by effective friction. *Geophysical Journal International*, **212**(2), 853–871.

Dublanchet, P. 2019b. Fluid driven shear cracks on a strengthening rate-and-state frictional fault. *Journal of the Mechanics and Physics of Solids*, **132**, 103672.

Dublanchet, P. 2019a. Inferring fault slip rates from cumulative seismic moment in a multiple asperity context. *Geophysical Journal International*, **216**(1), 395–413.

Dublanchet, P. 2019c. Scaling and Variability of Interacting Repeating Earthquake Sequences Controlled by Asperity Density. *Geophysical Research Letters*, **46**(21), 11950–11958.

Dublanchet, P. 2020. Stress-Dependent b Value Variations in a Heterogeneous Rate-and-State Fault Model. *Geophysical Research Letters*, **47**(13), e2020GL087434.

Dublanchet, P., & De Barros, L. 2020. Dual seismic migration velocities in seismic swarms. *In press, Geophysical Research Letters*.

Duverger, C., Godano, M., Bernard, P., Lyon-Caen, H., & Lambotte, S. 2015. The 2003–2004 seismic swarm in the western Corinth rift: Evidence for a multiscale pore pressure diffusion process along a permeable fault system. *Geophysical Research Letters*, **42**(18), 7374–7382.

Duverger, C., Lambotte, S., Bernard, P., Lyon-Caen, H., Deschamps, A., & Nercessian, A. 2018. Dynamics of microseismicity and its relationship with the active structures in the western Corinth Rift (Greece). *Geophysical Journal International*, **215**(1), 196–221.

El-Isa, Z.H., & Eaton, D.W. 2014. Spatiotemporal variations in the b-value of earthquake magnitude–frequency distributions: Classification and causes. *Tectonophysics*, **615**, 1–11.

Ellsworth, W.L. 2013. Injection-induced earthquakes. *Science*, **341**(6142), 1225942.

Fagereng, Å., & Sibson, R.H. 2010. Melange rheology and seismic style. *Geology*, **38**(8), 751–754.

Faillettaz, J., Funk, M., & Sornette, D. 2011. Icequakes coupled with surface displacements for predicting glacier break-off. *Journal of Glaciology*, **57**(203), 453–460.

Faulkner, D.R., Jackson, C.A.L., Lunn, R.J., Schlische, R.W., Shipton, Z.K., Wibberley, C.A.J., & Withjack, M.O. 2010. A review of recent developments concerning the structure, mechanics and fluid flow properties of fault zones. *Journal of Structural Geology*, **32**(11), 1557–1575.

Favreau, P., Campillo, M., & Ionescu, I.R. 1999. Initiation of in-plane shear instability under slip-dependent friction. *Bulletin of the Seismological Society of America*, **89**(5), 1280–1295.

Felzer, K.R., & Brodsky, E.E. 2006. Decay of aftershock density with distance indicates triggering by dynamic stress. *Nature*, **441**(7094), 735–738.

Felzer, K.R., Abercrombie, R.E., & Ekstroİĺm, G. 2004. A common origin for aftershocks, foreshocks, and multiplets. *Bulletin of the Seismological Society of America*, **94**(1), 88–98.

Festa, G., Chiaraluce, L., Valdimarsdóttir, H., & Ergintav, S. 2018. Near Fault Observatories within EPOS-IP: multidisciplinary data, high-level data products and community web services. *Page 17081 of: EGU General Assembly Conference Abstracts*, vol. 20.

Frank, W.B. 2016. Slow slip hidden in the noise: The intermittence of tectonic release. *Geophysical Research Letters*, **43**(19), 10–125.

Frohlich, C. 2012. Two-year survey comparing earthquake activity and injection-well locations in the Barnett Shale, Texas. *Proceedings of the National Academy of Sciences*, **109**(35), 13934–13938.

Galis, Martin, Ampuero, Jean Paul, Mai, P Martin, & Cappa, Frédéric. 2017. Induced seismicity provides insight into why earthquake ruptures stop. *Science Advances*, **3**(12), eaap7528.

Gallovič, F., Valentová, L., Ampuero, J.P., & Gabriel, A.A. 2019. Bayesian dynamic finite-fault inversion: 1. Method and synthetic test. *Journal of Geophysical Research: Solid Earth*, **124**(7), 6949–6969.

Gardonio, B., Marsan, D., Socquet, A., Bouchon, M., Jara, J., Sun, Q., Cotte, N., & Campillo, M. 2018. Revisiting slow slip events occurrence in Boso Peninsula, Japan, combining GPS data and repeating earthquakes analysis. *Journal of Geophysical Research: Solid Earth*, **123**(2), 1502–1515.

Geubelle, P.H., & Rice, J.R. 1995. A spectral method for three-dimensional elastodynamic fracture problems. *Journal of the Mechanics and Physics of Solids*, **43**(11), 1791–1824.

Gibowicz, S.J. 2009. Seismicity induced by mining: Recent research. *Pages 1–53 of: Advances in Geophysics*, vol. 51. Elsevier.

Godano, M., Bernard, P., & **Dublanchet, P.** 2015. Bayesian inversion of seismic spectral ratio for source scaling: Application to a persistent multiplet in the western Corinth rift. *Journal of Geophysical Research: Solid Earth*, **120**(11), 7683–7712.

Goebel, T., Aminzadeh, F., Haffener, J., & Chen, X. 2016a. Statistical seismicity analysis methods for the detection of fault activation during fluid injection. *Pages 2087–2092 of: SEG Technical Program Expanded Abstracts 2016*. Society of Exploration Geophysicists.

Goebel, T.H., Schorlemmer, D., Becker, T.W., Dresen, G., & Sammis, C.G. 2013. Acoustic emissions document stress changes over many seismic cycles in stick-slip experiments. *Geophysical Research Letters*, **40**(10), 2049–2054.

Goebel, T.H.W., Hosseini, S.M., Cappa, F., Hauksson, E., Ampuero, J.P., Aminzadeh, F., & Saleeby, J.B. 2016b. Wastewater disposal and earthquake swarm activity at the southern end of the Central Valley, California. *Geophysical Research Letters*, **43**(3), 1092–1099.

Gomberg, J.and Wech, A., Creager, K., Obara, K., & Agnew, D. 2016. Reconsidering earthquake scaling. *Geophysical Research Letters*, **43**(12), 6243–6251.

Guglielmi, Y., Cappa, F., Avouac, J.P., Henry, P., & Elsworth, D. 2015. Seismicity triggered by fluid injection–induced aseismic slip. *Science*, **348**(6240), 1224–1226.

Gupta, H., Narain, H., Rastogi, B.K., & Mohan, I. 1969. A study of the Koyna earthquake of December 10, 1967. *Bulletin of the Seismological Society of America*, **59**(3), 1149–1162.

Gutenberg, B., & Richter, C.F. 1944. Frequency of earthquakes in California. *Bulletin of the Seismological Society of America*, **34**(4), 185–188.

Hainzl, S., & Fischer, T. 2002. Indications for a successively triggered rupture growth underlying the 2000 earthquake swarm in Vogtland/NW Bohemia. *Journal of Geophysical Research: Solid Earth*, **107**(B12), ESE–5.

Hainzl, S., & Marsan, D. 2008. Dependence of the Omori-Utsu law parameters on main shock magnitude: Observations and modeling. *Journal of Geophysical Research: Solid Earth*, **113**(B10).

Hainzl, S., Scherbaum, F., & Beauval, C. 2006. Estimating background activity based on interevent-time distribution. *Bulletin of the Seismological Society of America*, **96**(1), 313–320.

Hainzl, S., Fischer, T., & Dahm, T. 2012. Seismicity-based estimation of the driving fluid pressure in the case of swarm activity in Western Bohemia. *Geophysical Journal International*, **191**(1), 271–281.

Hardebeck, J.L., & Michael, A.J. 2006. Damped regional-scale stress inversions: Methodology and examples for southern California and the Coalinga aftershock sequence. *Journal of Geophysical Research: Solid Earth*, **111**(B11).

Hastings, W.K. 1970. Monte Carlo sampling methods using Markov chains and their applications.

Healy, J.H., Rubey, W.W., Griggs, D.T., & Raleigh, C.B. 1968. The denver earthquakes. *Science*, **161**(3848), 1301–1310.

Helmstetter, A. 2003. Is earthquake triggering driven by small earthquakes? *Physical Review Letters*, **91**(5), 058501.

Helmstetter, A., & Garambois, S. 2010. Seismic monitoring of Séchilienne rockslide (French Alps): Analysis of seismic signals and their correlation with rainfalls. *Journal of Geophysical Research: Earth Surface*, **115**(F3).

Helmstetter, A., & Shaw, B.E. 2009. Afterslip and aftershocks in the rate-and-state friction law. *Journal of Geophysical Research: Solid Earth*, **114**(B1).

Helmstetter, A., Kagan, Y.Y., & Jackson, D.D. 2005. Importance of small earthquakes for stress transfers and earthquake triggering. *Journal of Geophysical Research: Solid Earth*, **110**(B5).

Ide, S., & Aochi, H. 2005. Earthquakes as multiscale dynamic ruptures with heterogeneous fracture surface energy. *Journal of Geophysical Research: Solid Earth*, **110**(B11).

Ide, S., & Beroza, G. C. 2001. Does apparent stress vary with earthquake size? *Geophysical Research Letters*, **28**(17), 3349–3352.

Ide, S., Shelly, D.R., & Beroza, G.C. 2007a. Mechanism of deep low frequency earthquakes: Further evidence that deep non-volcanic tremor is generated by shear slip on the plate interface. *Geophysical Research Letters*, **34**(3).

Ide, S., Beroza, G.C., Shelly, D.R., & Uchide, T. 2007b. A scaling law for slow earthquakes. *Nature*, **447**(7140), 76–79.

Im, K., Elsworth, D., & Fang, Y. 2018. The influence of preslip sealing on the permeability evolution of fractures and faults. *Geophysical Research Letters*, **45**(1), 166–175.

Jones, L., & Molnar, P. 1976. Frequency of foreshocks. *Nature*, **262**(5570), 677–679.

Jones, L.M., & Molnar, P. 1979. Some characteristics of foreshocks and their possible relationship to earthquake prediction and premonitory slip on faults. *Journal of Geophysical Research: Solid Earth*, **84**(B7), 3596–3608.

Kato, A., Obara, K., Igarashi, T., Tsuruoka, H., Nakagawa, S., & Hirata, N. 2012. Propagation of slow slip leading up to the 2011 Mw 9.0 Tohoku-Oki earthquake. *Science*, **335**(6069), 705–708.

Kazantsev, A., Chauris, H., **Dublanchet, P.**, & Huguet, F. 2019. Rayleigh wave amplitude distortions above a reservoir: new insights from elastic modelling. *Geophysical Journal International*, **217**(2), 1267–1289.

Kilb, D., Gomberg, J., & Bodin, P. 2000. Triggering of earthquake aftershocks by dynamic stresses. *Nature*, **408**(6812), 570–574.

King, G.C.P., Stein, R.S., & Lin, J. 1994. Static stress changes and the triggering of earthquakes. *Bulletin of the Seismological Society of America*, **84**(3), 935–953.

Kozłowska, M., Brudzinski, M.R., Friberg, P., Skoumal, R.J., Baxter, N.D., & Currie, Brian S. 2018. Maturity of nearby faults influences seismic hazard from hydraulic fracturing. *Proceedings of the National Academy of Sciences*, **115**(8), E1720–E1729.

Kraft, T., Wassermann, J., Schmedes, E., & Igel, H. 2006. Meteorological triggering of earthquake swarms at Mt. Hochstaufen, SE-Germany. *Tectonophysics*, **424**(3-4), 245–258.

Kroll, K.A., Richards-Dinger, K.B., & Dieterich, J.H. 2017. Sensitivity of induced seismic sequences to rate-and-state frictional processes. *Journal of Geophysical Research: Solid Earth*, **122**(12), 10–207.

Lambotte, S., Lyon-Caen, H., Bernard, P., Deschamps, A., Patau, G., Nercessian, A., Pacchiani, F., Bourouis, S., Drilleau, M., & Adamova, P. 2014. Reassessment of the rifting process in the Western Corinth Rift from relocated seismicity. *Geophysical Journal International*, **197**(3), 1822–1844.

Langbein, J., McGarr, A., Johnston, M.J.S., & Harsh, P.W. 1983. Geodetic measurements of postseismic crustal deformation following the 1979 Imperial Valley earthquake, California. *Bulletin of the Seismological Society of America*, **73**(4), 1203–1224.

Langbein, J.O. 1990. Post-seismic slip on the San Andreas Fault at the northwestern end of the 1989 Loma Prieta Earthquake rupture zone. *Geophysical Research Letters*, **17**(8), 1223–1226.

Lapusta, N., Rice, J.R., Ben-Zion, Y., & Zheng, G. 2000. Elastodynamic analysis for slow tectonic loading with spontaneous rupture episodes on faults with rate-and state-dependent friction. *Journal of Geophysical Research: Solid Earth*, **105**(B10), 23765–23789.

Latour, S., Campillo, M., Voisin, C., Ionescu, I.R., Schmedes, J., & Lavallée, D. 2011. Effective friction law for small-scale fault heterogeneity in 3D dynamic rupture. *Journal of Geophysical Research: Solid Earth*, **116**(B10).

Lawn, B. 1993. *Fracture of brittle solids*. Cambridge university press.

Lengliné, O., & Marsan, D. 2009. Inferring the coseismic and postseismic stress changes caused by the 2004 Mw= 6 Parkfield earthquake from variations of recurrence times of microearthquakes. *Journal of Geophysical Research: Solid Earth*, **114**(B10).

Lengliné, O., Frank, W.B., Marsan, D., & Ampuero, J.P. 2017a. Imbricated slip rate processes during slow slip transients imaged by low-frequency earthquakes. *Earth and Planetary Science Letters*, **476**, 122–131.

Lengliné, O., Boubacar, M., & Schmittbuhl, J. 2017b. Seismicity related to the hydraulic stimulation of GRT1, Rittershoffen, France. *Geophysical Journal International*, **208**(3), 1704–1715.

Madariaga, R., Olsen, K., & Archuleta, R. 1998. Modeling dynamic rupture in a 3D earthquake fault model. *Bulletin of the Seismological Society of America*, **88**(5), 1182–1197.

Marone, C.J., Scholtz, C.H., & Bilham, R. 1991. On the mechanics of earthquake afterslip. *Journal of Geophysical Research: Solid Earth*, **96**(B5), 8441–8452.

Marsan, D., & Lengline, O. 2008. Extending earthquakes' reach through cascading. *Science*, **319**(5866), 1076–1079.

Marsan, D., Helmstetter, A., Bouchon, M., & **Dublanchet, P.** 2014. Foreshock activity related to enhanced aftershock production. *Geophysical Research Letters*, **41**(19), 6652–6658.

McGarr, A. 2014. Maximum magnitude earthquakes induced by fluid injection. *Journal of Geophysical Research: Solid Earth*, **119**(2), 1008–1019.

Métois, M., Socquet, A., & Vigny, C. 2012. Interseismic coupling, segmentation and mechanical behavior of the central Chile subduction zone. *Journal of Geophysical Research: Solid Earth*, **117**(B3).

Metropolis, N., Rosenbluth, A.W., Rosenbluth, M.N., Teller, A.H., & Teller, E. 1953. Equation of state calculations by fast computing machines. *The Journal of Chemical Physics*, **21**(6), 1087–1092.

Michel, S., Gualandi, A., & Avouac, J.P. 2019. Similar scaling laws for earthquakes and Cascadia slow-slip events. *Nature*, **574**(7779), 522–526.

Nadeau, R. M, & Dolenc, D. 2005. Nonvolcanic tremors deep beneath the San Andreas Fault. *Science*, **307**(5708), 389–389.

Nadeau, R.M., & Johnson, L.R. 1998. Seismological studies at Parkfield VI: Moment release rates and estimates of source parameters for small repeating earthquakes. *Bulletin of the Seismological Society of America*, **88**(3), 790–814.

Nadeau, R.M., & McEvilly, T.V. 1997. Seimological studies at Parkfield V: Characteristic microearthquake sequences as fault-zone drilling targets. *Bulletin of the Seismological Society of America*, **87**(6), 1463–1472.

Nadeau, R.M., & McEvilly, T.V. 1999. Fault slip rates at depth from recurrence intervals of repeating microearthquakes. *Science*, **285**(5428), 718–721.

Nadeau, R.M., Foxall, W., & McEvilly, T.V. 1995. Clustering and periodic recurrence of microearthquakes on the San Andreas fault at Parkfield, California. *Science*, **267**(5197), 503–507.

Narteau, C., Byrdina, S., Shebalin, P., & Schorlemmer, D. 2009. Common dependence on stress for the two fundamental laws of statistical seismology. *Nature*, **462**(7273), 642–645.

Nishimura, T., Hirasawa, T., Miyazaki, S., Sagiya, T., Tada, T., Miura, S., & Tanaka, K. 2004. Temporal change of interplate coupling in northeastern Japan during 1995–2002 estimated from continuous GPS observations. *Geophysical Journal International*, **157**(2), 901–916.

Obara, K. 2002. Non-volcanic deep tremor associated with subduction in southwest Japan. *Science*, **296**, 1679–1681.

Obara, K., & Ito, Y. 2005. Very low frequency earthquakes excited by the 2004 off the Kii peninsula earthquakes: A dynamic deformation process in the large accretionary prism. *Earth, Planets and Space*, **57**(4), 321–326.

Obara, K., Hirose, H., Yamamizu, F., & Kasahara, K. 2004. Episodic slow slip events accompanied by non-volcanic tremors in southwest Japan subduction zone. *Geophysical Research Letters*, **31**(23).

Ohnaka, M. 1992. Earthquake source nucleation: a physical model for short-term precursors. *Tectonophysics*, **211**(1-4), 149–178.

Olive, J.A., & **Dublanchet, P.** 2020. Controls on the magmatic fraction of extension at mid-ocean ridges. *Earth and Planetary Science Letters*, **549**, 116541.

Omori, F. 1894. *On the after-shocks of earthquakes*. Vol. 7. The University.

Ouillon, G., & Sornette, D. 2005. Magnitude-dependent Omori law: Theory and empirical study. *Journal of Geophysical Research: Solid Earth*, **110**(B4).

Ozawa, S., Nishimura, T., Suito, H., Kobayashi, T., Tobita, M., & Imakiire, T. 2011. Coseismic and postseismic slip of the 2011 magnitude-9 Tohoku-Oki earthquake. *Nature*, **475**(7356), 373–376.

Passelègue, F. X., Almakari, M., Dublanchet, P., Barras, F., Fortin, J., & Violay, M. 2020. Initial effective stress controls the nature of earthquakes. *Nature Communications*, **11**(1), 1–8.

Peng, Z., & Gomberg, J. 2010. An integrated perspective of the continuum between earthquakes and slow-slip phenomena. *Nature GeoScience*, **3**(9), 599–607.

Perfettini, H., & Ampuero, J.P. 2008. Dynamics of a velocity strengthening fault region: Implications for slow earthquakes and postseismic slip. *Journal of Geophysical Research: Solid Earth*, **113**(B9).

Perfettini, H., & Avouac, J.P. 2004. Postseismic relaxation driven by brittle creep: A possible mechanism to reconcile geodetic measurements and the decay rate of aftershocks, application to the Chi-Chi earthquake, Taiwan. *Journal of Geophysical Research: Solid Earth*, **109**(B2).

Plessix, R.E. 2006. A review of the adjoint-state method for computing the gradient of a functional with geophysical applications. *Geophysical Journal International*, **167**(2), 495–503.

Poupinet, G., Ellsworth, W.L., & Frechet, J. 1984. Monitoring velocity variations in the crust using earthquake doublets: An application to the Calaveras Fault, California. *Journal of Geophysical Research: Solid Earth*, **89**(B7), 5719–5731.

Raleigh, C.B., Healy, J.H., & Bredehoeft, J.D. 1976. An experiment in earthquake control at Rangely, Colorado. *Science*, **191**(4233), 1230–1237.

Renou, J., Vallée, M., & **Dublanchet, P.** 2019. How does seismic rupture accelerate? Observational insights from earthquake source time functions. *Journal of Geophysical Research: Solid Earth*, **124**(8), 8942–8952.

Rice, J.R. 1993. Spatio-temporal complexity of slip on a fault. *Journal of Geophysical Research: Solid Earth*, **98**(B6), 9885–9907.

Rogers, G., & Dragert, H. 2003. Episodic tremor and slip on the Cascadia subduction zone: The chatter of silent slip. *Science*, **300**(5627), 1942–1943.

Romanet, P., Bhat, H.S., Jolivet, R., & Madariaga, R. 2018. Fast and slow slip events emerge due to fault geometrical complexity. *Geophysical Research Letters*, **45**(10), 4809–4819.

Rousset, B., Bürgmann, R., & Campillo, M. 2019. Slow slip events in the roots of the San Andreas fault. *Science Advances*, **5**(2), eaav3274.

Rubin, A.M., & Ampuero, J.P. 2005. Earthquake nucleation on (aging) rate and state faults. *Journal of Geophysical Research: Solid Earth*, **110**(B11).

Ruina, A. 1983. Slip instability and state variable friction laws. *Journal of Geophysical Research: Solid Earth*, **88**(B12), 10359–10370.

Ruiz, S., Metois, M., Fuenzalida, A., Ruiz, J., Leyton, F., Grandin, R., Vigny, C., Madariaga, R., & Campos, J. 2014. Intense foreshocks and a slow slip event preceded the 2014 Iquique Mw 8.1 earthquake. *Science*, **345**(6201), 1165–1169.

Rutter, E.H., & Mecklenburgh, J. 2018. Influence of normal and shear stress on the hydraulic transmissivity of thin cracks in a tight quartz sandstone, a granite, and a shale. *Journal of Geophysical Research: Solid Earth*, **123**(2), 1262–1285.

Sammis, C.G., & Rice, J.R. 2001. Repeating earthquakes as low-stress-drop events at a border between locked and creeping fault patches. *Bulletin of the Seismological Society of America*, **91**(3), 532–537.

Savage, J.C., Lisowski, M., & Svarc, J.L. 1994. Postseismic deformation following the 1989 (M= 7.1) Loma Prieta, California, earthquake. *Journal of Geophysical Research: Solid Earth*, **99**(B7), 13757–13765.

Schaff, D.P., Beroza, G.C., & Shaw, B.E. 1998. Postseismic response of repeating aftershocks. *Geophysical Research Letters*, **25**(24), 4549–4552.

Schmidt, DA, & Gao, H. 2010. Source parameters and time-dependent slip distributions of slow slip events on the Cascadia subduction zone from 1998 to 2008. *Journal of Geophysical Research: Solid Earth*, **115**(B4).

Scholz, C.H. 1968. The frequency-magnitude relation of microfracturing in rock and its relation to earthquakes. *Bulletin of the Seismological Society of America*, **58**(1), 399–415.

Scholz, C.H. 2015. On the stress dependence of the earthquake b value. *Geophysical Research Letters*, **42**(5), 1399–1402.

Schorlemmer, D., Wiemer, S., & Wyss, M. 2005. Variations in earthquake-size distribution across different stress regimes. *Nature*, **437**(7058), 539.

Segall, P., & Lu, S. 2015. Injection-induced seismicity: Poroelastic and earthquake nucleation effects. *Journal of Geophysical Research: Solid Earth*, **120**(7), 5082–5103.

Shapiro, S.A., & Dinske, C. 2009a. Fluid-induced seismicity: Pressure diffusion and hydraulic fracturing. *Geophysical Prospecting*, **57**(2), 301–310.

Shapiro, S.A., & Dinske, C. 2009b. Scaling of seismicity induced by nonlinear fluid-rock interaction. *Journal of Geophysical Research: Solid Earth*, **114**(B9).

Shapiro, S.A., Kummerow, J., Dinske, C., Asch, G., Rothert, E., Erzinger, J., Kümpel, H.J., & Kind, R. 2006. Fluid induced seismicity guided by a continental fault: Injection experiment of 2004/2005 at the German Deep Drilling Site (KTB). *Geophysical Research Letters*, **33**(1).

Shelly, D.R., Beroza, G.C., Ide, S., & Nakamula, S. 2006. Low-frequency earthquakes in Shikoku, Japan, and their relationship to episodic tremor and slip. *Nature*, **442**(7099), 188–191.

Spada, M., Tormann, T., Wiemer, S., & Enescu, B. 2013. Generic dependence of the frequency-size distribution of earthquakes on depth and its relation to the strength profile of the crust. *Geophysical Research Letters*, **40**(4), 709–714.

Stabile, T.A., Giocoli, A., Lapenna, V., Perrone, A., Piscitelli, S., & Telesca, L. 2014. Evidence of low-magnitude continued reservoir-induced seismicity associated with the Pertusillo Artificial Lake (southern Italy). *Bulletin of the Seismological Society of America*, **104**(4), 1820–1828.

Toda, S., Stein, R.S., Reasenberg, P.A., Dieterich, J.H., & Yoshida, A. 1998. Stress transferred by the 1995 Mw= 6.9 Kobe, Japan, shock: Effect on aftershocks and future earthquake probabilities. *Journal of Geophysical Research: Solid Earth*, **103**(B10), 24543–24565.

Uchida, N., Matsuzawa, T., Hasegawa, A., & Igarashi, T. 2003. Interplate quasi-static slip off Sanriku, NE Japan, estimated from repeating earthquakes. *Geophysical Research Letters*, **30**(15).

Ulrich, T., Gabriel, A.A., Ampuero, J.P., & Xu, W. 2019. Dynamic viability of the 2016 Mw 7.8 Kaikōura earthquake cascade on weak crustal faults. *Nature Communications*, **10**(1), 1–16.

Utsu, T., Ogata, Y., *et al.* . 1995. The centenary of the Omori formula for a decay law of aftershock activity. *Journal of Physics of the Earth*, **43**(1), 1–33.

Viesca, R. C., & **Dublanchet, P.** 2019. The slow slip of viscous faults. *Journal of Geophysical Research: Solid Earth*, **124**(5), 4959–4983.

Vigny, C., Rudloff, A., Ruegg, J.C., Madariaga, R., Campos, J., & Alvarez, M. 2009. Upper plate deformation measured by GPS in the Coquimbo Gap, Chile. *Physics of the Earth and Planetary Interiors*, **175**(1-2), 86–95.

Voisin, C., Campillo, M., Ionescu, I., Hassani, R., & Nguyen, Q.L. 2002. Process and signature of initiation on a finite fault system: a spectral approach. *Geophysical Journal International*, **148**(1), 120–131.

Vorobieva, I., Shebalin, P., & Narteau, C. 2016. Break of slope in earthquake size distribution and creep rate along the San Andreas Fault system. *Geophysical Research Letters*, **43**(13), 6869–6875.

Wech, A.G., Creager, K.C., Houston, H., & Vidale, J.E. 2010. An earthquake-like magnitude-frequency distribution of slow slip in northern Cascadia. *Geophysical Research Letters*, **37**(22).

Wesson, R.L. 1988. Dynamics of fault creep. *Journal of Geophysical Research: Solid Earth*, **93**(B8), 8929–8951.

Wu, W., Reece, J.S., Gensterblum, Y., & Zoback, M.D. 2017. Permeability evolution of slowly slipping faults in shale reservoirs. *Geophysical Research Letters*, **44**(22), 11–368.

Yoshioka, S., Yabuki, T., Sagiya, T., Tada, T., & Matsu'Ura, M. 1993. Interplate coupling and relative plate motion in the Tokai district, central Japan, deduced from geodetic data inversion using ABIC. *Geophysical Journal International*, **113**(3), 607–621.

Zhuang, J., Ogata, Y., & Vere-Jones, D. 2004. Analyzing earthquake clustering features by using stochastic reconstruction. *Journal of Geophysical Research: Solid Earth*, **109**(B5).

Zhuang, J., Chang, C.P., & Ogata, Y.and Chen, Y.I. 2005. A study on the background and clustering seismicity in the Taiwan region by using point process models. *Journal of Geophysical Research: Solid Earth*, **110**(B5).

Ziv, A. 2003. Foreshocks, aftershocks, and remote triggering in quasi-static fault models. *Journal of Geophysical Research: Solid Earth*, **108**(B10).

Ziv, A., & Cochard, A. 2006. Quasi-dynamic modeling of seismicity on a fault with depth-variable rate-and state-dependent friction. *Journal of Geophysical Research: Solid Earth*, **111**(B8).

Zoback, M.D., & Byerlee, J.D. 1975. Permeability and effective stress. *AAPG Bulletin*, **59**(1), 154–158.

Chapter 5

Appendices

5.1 Curriculum Vitae

Pierre Dublanchet
Date of Birth: 10th June 1985

Researcher, MINES ParisTech
Centre de Géosciences - Geophysical research group
35 rue saint-Honoré
77305 Fontainebleau, France
tel:+33(0)1 64 69 49 38
e-mail: pierre.dublanchet@mines-paristech.fr

5.1.1 Academic positions

Sept 2018- : Assistant Professor in Geophysics, MINES ParisTech
Sept 2015 - Sept 2018: Assistant Professor Tenure Track in Geophysics, MINES ParisTech
Jan 2014 - Aug 2015 : Post-Doctoral Scholar, Swiss Seismological Service , ETH Zürich
Sept 2013 - Dec 2013 : Post-Doctoral Scholar, IPGP, Seismological Laboratory

5.1.2 Education

2013: PhD in Geophysics, Institut de Physique du Globe de Paris (IPGP), Seismological Laboratory. Title: *"Étude des régimes de sismicité dans un modèle quasi-dynamique d'aspérités rate-and-state"*. Supervision: P. Bernard.
2009: M.S. in Geophysics, IPGP and École Normale Supérieure (ENS Ulm), Paris
2007: B.S. in Earth and Planetary Science, ENS Ulm, Paris (France)
2006: Entered ENS Ulm, Paris (France) after competitive examination

5.1.3 Teaching

Since 2015, my teaching charge is about 90 hours per year. Here is a list of my teaching activities:

- Since 2020- Co-organizor of the research semester DENATURA (Dynamique DEs milieux NATURels Anthropisés, MINES ParisTech)

- Since 2019- Co-organizor of the master 2 Science de la Terre, des Planètes, Environnement, PSL Research University

- Since 2019- Fracture and seismic rupture mechanics, master 1 (Science de la Terre, des Planètes, Environnement, PSL Research University)

- Since 2019- Training on induced seismicity, Geoscience option (MINES ParisTech)

- Since 2019- Rock mechanics, master 1 (Geophysics and Natural Hazards, Institut de Physique du Globe de Paris)

- Since 2019- Jury member (Geosciences), École Normale Supérieure competitive exam.

- 2017- Oral exams in geology, BS degree (Lycée François premier, Fontainebleau)

- Since 2016- Advanced Rock Mechanics, master 2 (Geophysics and Natural Hazards, Institut de Physique du Globe)

- Since 2016- Subsurface Geophysics and Introduction to Geology, field courses MINES Paris-Tech

- 2016-2018 Rock Physics, master 2 GPX (Geophysical Paris Exploration Group, Institut de Physique du Globe de Paris)

- 2014 Co-organizor of the master course "Seismotectonics" (Earth Science Department, ETH Zürich)

- 2013 Teaching Assistant in Geophysics and Geochemistry (Smith College,Paris)

- 2010-2013 Teaching Assistant (Moniteur) in Physics and Geophysics (Institut de Physique du Globe de Paris)

5.1.4   Supervision

Graduate students

2019- Jinlin Jiang (co-supervision 50 %). Civil engineering degree, Wuhan University; M.S. Rock Mechanics, Chinese Academy of Science. Numerical modeling of fluid induced fault slip reactivation, application to Geo-Energy systems.
2016-2019 Michelle Almakari (co-supervision 80 %). Civil engineering degree, Lebanese University; M.S., Geophysics, Université Joseph Fourier, Grenoble. Réactivation Hydro-Mécanique d'une Faille Rate-and-State : Glissement, Sismicité et Évolution de Perméabilité. Now post-doctoral scholar at École Normale Supérieure.
2015-2018 Alexandre Kazantsev (co-supervision 30 %). Civil engineering degree, MINES Paris-Tech, Paris. Extraction and interpretation of a low frequency seismic noise anomaly related to a gaz storage field. Now researcher at Storengy.

Master projects

Andrea M. Valerius (M1, 2020 & M2, 2021), Inès Ben-Khaled (M1, 2020), Hugo Lestrelin (M2, 2021), Thomas Dubard (MINES ParisTech, 2020), Aymeric Plessier (MINES ParisTech, 2020)

5.1.5   Editorial activities

2020- Reviewer for Nature Communications, Journal of Geodynamics, Geology
2017- Reviewer for the Journal of Mechanics and Physics of Solids
2015- Reviewer for Geophysical Journal International
2014- Reviewer for Journal of Geophysical Research

5.1.6 Workshop organization

2019-2020 Earthquakes: from slow to fast, from the field to the laboratory and models (EGU general assembly, Vienna)
2018 Understanding fluid driven ruptures, from natural earthquakes to reservoirs induced seismicity (EGU general assembly, Vienna)

5.1.7 Projects

2019 Contributor on INSU TelluS project INSIDE (INduced Seismicity in southern Italy associateD with Energy technology).
2020 Collaborator on the INSU TelluS project ESCOR (Earthquake Swarms in the Corinth Rift), P.I. : M. Godano (Géoazur).
2015-2020 Contributor on the GEODENERGY project TEMPERER (Seismicity of geothermal reservoirs).

5.1.8 Publications (peer reviewed)

NB: underlined authors refer to supervised PhD candidates

1. **Dublanchet, P.**, Bernard, P., & Favreau, P. 2013a. Interactions and triggering in a 3-D rate-and-state asperity model. *Journal of Geophysical Research: Solid Earth*, **118**(5), 2225–2245

2. **Dublanchet, P.**, Bernard, P., & Favreau, P. 2013b. Creep modulation of Omori law generated by a Coulomb stress perturbation in a 3-D rate-and-state asperity model. *Journal of Geophysical Research: Solid Earth*, **118**(9), 4774–4793

3. Marsan, D., Helmstetter, A., Bouchon, M., & **Dublanchet, P.** 2014. Foreshock activity related to enhanced aftershock production. *Geophysical Research Letters*, **41**(19), 6652–6658

4. Godano, M., Bernard, P., & **Dublanchet, P.** 2015. Bayesian inversion of seismic spectral ratio for source scaling: Application to a persistent multiplet in the western Corinth rift. *Journal of Geophysical Research: Solid Earth*, **120**(11), 7683–7712

5. **Dublanchet, P.**, Godano, M., & Bernard, P. 2015. Inferring fault mechanical conditions from the source parameters of a complex microseismic multiplet in the Corinth rift, Greece. *Journal of Geophysical Research: Solid Earth*, **120**(11), 7655–7682

6. **Dublanchet, P.** 2018. The dynamics of earthquake precursors controlled by effective friction. *Geophysical Journal International*, **212**(2), 853–871

7. **Dublanchet, P.** 2019a. Inferring fault slip rates from cumulative seismic moment in a multiple asperity context. *Geophysical Journal International*, **216**(1), 395–413

8. **Dublanchet, P.** 2019b. Fluid driven shear cracks on a strengthening rate-and-state frictional fault. *Journal of the Mechanics and Physics of Solids*, **132**, 103672

9. **Dublanchet, P.** 2019c. Scaling and Variability of Interacting Repeating Earthquake Sequences Controlled by Asperity Density. *Geophysical Research Letters*, **46**(21), 11950–11958

10. Kazantsev, A., Chauris, H., **Dublanchet, P.**, & Huguet, F. 2019. Rayleigh wave amplitude distortions above a reservoir: new insights from elastic modelling. *Geophysical Journal International*, **217**(2), 1267–1289

11. Viesca, R. C., & **Dublanchet, P.** 2019. The slow slip of viscous faults. *Journal of Geophysical Research: Solid Earth*, **124**(5), 4959–4983

12. Renou, J., Vallée, M., & **Dublanchet, P.** 2019. How does seismic rupture accelerate? Observational insights from earthquake source time functions. *Journal of Geophysical Research: Solid Earth*, **124**(8), 8942–8952

13. Almakari, M., **Dublanchet, P.**, Chauris, H., & Pellet, F. 2019. Effect of the Injection Scenario on the Rate and Magnitude Content of Injection-Induced Seismicity : case of a Heterogeneous Fault. *Journal of Geophysical Research: Solid Earth*, **124**(8), 8426–8448

14. De Barros, L., Cappa, F., Deschamps, A., & **Dublanchet, P.** 2020. Imbricated Aseismic Slip and Fluid Diffusion Drive a Seismic Swarm in the Corinth Gulf, Greece. *Geophysical Research Letters*, **47**(9), e2020GL087142

15. **Dublanchet, P.** 2020. Stress-Dependent b Value Variations in a Heterogeneous Rate-and-State Fault Model. *Geophysical Research Letters*, **47**(13), e2020GL087434

16. Passelègue, F. X., Almakari, M., Dublanchet, P., Barras, F., Fortin, J., & Violay, M. 2020. Initial effective stress controls the nature of earthquakes. *Nature Communications*, **11**(1), 1–8

17. Almakari, M., Chauris, H., Passelègue, F.X., Dublanchet, P., & Gesret, A. 2020. Fault's hydraulic diffusivity enhancement during injection induced fault reactivation : application of pore pressure diffusion inversions to laboratory injection experiments. *Geophysical Journal International*, **223**(3), 2117–2132

18. Olive, J.A., & **Dublanchet, P.** 2020. Controls on the magmatic fraction of extension at mid-ocean ridges. *Earth and Planetary Science Letters*, **549**, 116541

19. **Dublanchet, P.**, & De Barros, L. 2020. Dual seismic migration velocities in seismic swarms. *In press, Geophysical Research Letters*

5.1.9 Invited communications

1. The long-term dynamics of fluid induced fault slip reactivation *Seminar EPFL, January 2019*

2. Fault slip reactivation by fluid injections : aseismic slip and induced seismicity in rate-and-state fault models *Computational Methods in Water Resources XXII, Saint-Malo, June 2018*

3. Dynamics of fluid induced aseismic slip *7th EAGE Workshop on Passice Seismic, Krakow, March 2018*

4. Fault creep and earthquake interaction *CECAM Workshop, The Flow of Amorphous Solids, ENS Lyon, June 2016*

5. Mechanical modeling of microseismicity *Seminar ETHZ, October 2015*

6. Mechanical behavior of microseismic multiplet *Seminar Mécanique des failles ISTerre Université Grenoble, March 2015*

7. Destabilization of a heterogeneous rate-and-state interface *AGU Fall meeting, San Francisco, December 2014*

8. Seismic and aseismic activity of a heterogeneous frictional interface *Seminar Géoazur Nice, September 2014*

9. Seismicity regimes produced by a rate-and-state asperity model *Seminar Université Montpellier, April 2014*

10. Effective behavior of a heterogeneous rate-and-state interface *Caltech Seismological Laboratory, December 2013*

11. Effective behavior of a heterogeneous rate-and-state interface *SED Seminar ETHZ,September 2013*

12. Seismic cycle and triggering in a rate-and-state asperity model *Seminar Mécanique des failles ISTerre Grenoble, November 2011*

5.1.10 Conferences

1. Passelegue, F.X., Almakari, M., **Dublanchet, P.**, Violay, M., Barras, F. On the Nature of Fault Slip: From the Field to the Lab. *EGU General Assembly, 2020*

2. **Dublanchet, P.** What controls b-value variations: insights from a physics based numerical model. *EGU General Assembly, 2020*

3. Almakari, M., Chauris, H., Passelegue, F.X., **Dublanchet, P.**, Gesret, A. Induced Fault Reactivation and Hydraulic Diffusivity Enhancement : Insights from Pressure Diffusion Inversion in Laboratory Injection Tests. *EGU General Assembly, 2020*

4. **Dublanchet, P.**, Almakari, M., 2019. Stability of fault slip: effects of fluids and frictional heterogeneity. *Forecasting unstable frictional slip and the failure of geomaterials workshop, Ecole polytechnique, Palaiseau, France.*

5. **Dublanchet, P.**, 2019. The dynamics of interacting repeating earthquake sequences in an asperity model. *Reapeating Earthquakes Workshop, Paris, France.*

6. Almakari, M., Passelegue, F., **Dublanchet, P.**, 2019. Shear induced fluid flow and permeability enhancement during fluid injection lab experiment. *Schatzalp 3rd Induced Seismicity Workshop, Davos, Switzerland.*

7. Passelegue, F.X., Almakari, M., **Dublanchet, P.**, Barras, F., 2019. On the nature of induced seismicity: Control from initial state of stress. *Schatzalp 3rd Induced Seismicity Workshop, Davos, Switzerland.*

8. Almakari, M., **Dublanchet, P.**, Chauris, H., 2018. Dependence of Injection-Induced Seismicity on the Injection Scenario. *AGU Fall meeting, abstract S33C-0593, Washington, USA.*

9. Wang, L., Ray, S., **Dublanchet, P.**, Viesca, R.C., 2018. Accelerated creep of a landslide with slip rate-and-state dependent basal friction, *EGU General Assembly, Vienna, Austria.*

10. Almakari, M., **Dublanchet, P.**, Chauris, H., Injection-induced seismicity controlled by the pore-pressure rate, *EGU General Assembly, 2018*

11. **Dublanchet, P.**, 2018. Earthquake nucleation under heterogeneous friction : aseismic slip and foreshocks interaction. *EGU General Assembly, Vienna, Austria.*

12. Kazantsev, A., Peruzzetto, M., Chauris, H., **Dublanchet, P.**, Huguet, F. 2018. Origins of Lg phase and Rayleigh overtones in ambient noise. *7th EAGE Workshop on Passive Seismic, Krakow, Poland.*

13. Almakari, M., **Dublanchet, P.**, Chauris, H., 2017. Induced seismicity in a rate-and-state asperity model. *Cargèse school on Earthquakes : nucleation, triggering rupture and relationship with aseismic processes, Corsica, France.*

14. **Dublanchet, P.**, 2017. Earthquake nucleation on a heterogeneous rate-and-state fault : aseismic slip acceleration and foreshock sequences. *Cargèse school on Earthquakes : nucleation, triggering rupture and relationship with aseismic processes, Corsica, France.*

15. **Dublanchet, P.**, Viesca, R.C., 2017. Dynamics of Fluid Induced Aseismic Slip. *79th EAGE Conference and Exhibition, Paris, France.*

16. Kazantsev, A., Chauris., H., **Dublanchet, P.** and Huguet, F. 2017. Near-field Elastic Scattering of Rayleigh Waves A Model for Interpreting Hydrocarbon Micro-tremors. *79th EAGE Conference and Exhibition, Paris, France.*

17. Viesca, R.C., **Dublanchet, P.**, 2016. Slow slip and self-similar asymptotics of rate-strengthening faults. *AGU Fall Meeting, San Francisco, USA.*

18. Viesca, R.C., **Dublanchet, P.**, 2016. Self-similar asymptotics of rate-strengthening faults. *SCEC annual meeting, Palm Springs, USA.*

19. **Dublanchet, P.**, 2016. Earthquake Nucleation on a Heterogeneous rate-and-state interface. *Conference on Mathematical Geophysics, Paris, France.*

20. Rinaldi, A.P., Urpi, L., Karvounis, D., **Dublanchet, P.**, 2016. Effects of asperities distribution on induced seismicity and permeability during deep underground exploitation. *EGU General Assembly, Vienna, Austria.*

21. **Dublanchet, P.**, Rinaldi, A.P., Karvounis, D., Wiemer, S. 2015. Pressure front interacting with a rate-and-state fault of heterogeneous permeability. *Scahtzalp 1st Induced Seismicity Workshop, Davos, Switzerland.*

22. **Dublanchet, P.**, 2015. Mechanical environment of a complex multiplet. *Caltech Seismological Laboratory, USA.*

23. **Dublanchet, P.**, 2014. Seismic and aseismic behavior of a heterogeneous rate-and-state interface. *Cargèse school on Earthquakes : nucleation, triggering and interaction with aseismic processes, Corsica, France.*

24. **Dublanchet, P.**, Bernard, P., Godano, M., 2013. Effective frictional behavior of a heterogeneous rate-and-state fault. *AGU Fall meeting, Abstract S41B-2453, San Francisco, USA.*

25. **Dublanchet, P.**, Bernard, P., 2013. How density of asperity controls statistical properties of seismicity: insights from a 3D rate-and-state asperity model.*40th Workshop of the International School of Geophysics on Properties and Processes of Crustal Fault Zones, Erice (TP), Sicily, Italy.*

26. Godano, M., Bernard, P., **Dublanchet, P.**, Canitano, A., Marsan, M., 2013. Analysis of the 2003-2004 microseismic sequence in the western part of the Corinth Rift. *In Proceedings of the EGU General Assembly, Vol. 15 : EGU2013-5325, EGU General Assembly, Vienna, Austria.*

27. **Dublanchet, P.**, Bernard, P., Favreau, P., 2012. Interactions and triggering in a 3D rate-and-state asperity model. *In AGU Fall meeting abstracts, Abstract S53A-2469, San Francisco, USA.*

28. **Dublanchet, P.**, Bernard, P., Favreau, P., 2011. Cycle and triggering in a rate-and-state asperity model. *In AGU Fall meeting abstracts, Vol. 1, p.2265.*

29. **Dublanchet, P.**, Bernard, P., Favreau, P., 2011. Cycle and triggering in a rate-and-state asperity model. *In Geophysical Research Abstracts, Vol. 13 : EGU2011-3765, EGU General Assembly, Vienna, Austria.*

5.2 Selected publications

In this section, I provide the full text of three of my main publications :

- **Dublanchet, P.** 2018. The dynamics of earthquake precursors controlled by effective friction. *Geophysical Journal International*, **212**(2), 853–871

- **Dublanchet, P.** 2019b. Fluid driven shear cracks on a strengthening rate-and-state frictional fault. *Journal of the Mechanics and Physics of Solids*, **132**, 103672

- **Dublanchet, P.** 2019c. Scaling and Variability of Interacting Repeating Earthquake Sequences Controlled by Asperity Density. *Geophysical Research Letters*, **46**(21), 11950–11958

The dynamics of earthquake precursors controlled by effective friction

P. Dublanchet

MINES ParisTech, PSL Research University, Centre de Géosciences, 35 *rue saint-honoré,* 77305 *Fontainebleau, France.*
E-mail: pierre.dublanchet@mines-paristech.fr

SUMMARY

Many large earthquakes are preceded by slow slip and foreshock sequences. These precursory phenomena activate the hypocentral region of the main-shock fault. However, slow slip events and earthquake swarms do not systematically lead to large earthquakes and cannot be considered for short-term prediction. Understanding what controls the occurrence and the dynamics of precursors on tectonic faults is of critical importance to improve seismic hazard assessment. This study shows how frictional heterogeneity on a finite planar fault can explain the different fault behaviours preceding a large earthquake in a unified manner. It is demonstrated that under heterogeneous conditions, four different regimes of earthquake nucleation occur. All of them are characterized by slow slip acceleration, but only one involves a growing foreshock activity. The transitions between the different regimes, and the fault slip history preceding the main-shock are in the four regimes controlled by effective friction parameters, and by a fracture mechanics criterion involving the characteristic wavelength of heterogeneity. The effective friction theory developed here for earthquake nucleation may have major implications in the understanding of other fault processes under heterogeneous conditions, such as dynamic rupture or episodic slow slip events.

Key words: Friction; Seismic cycle; Rheology and friction of fault zones; Earthquake hazards; Mechanics, theory, and modelling.

1 INTRODUCTION

Understanding the initiation of large earthquakes (nucleation) is critical to improve short-term prediction. Large earthquakes are often preceded by foreshock sequences lasting from less than one hour to several months (Jones & Molnar 1976, 1979; Bouchon *et al.* 2013), located in the vicinity of the main-shock hypocentre, and characterized by an increasing seismicity rate. Many evidences suggest that these foreshock sequences are driven by the progressive acceleration of slow slip in the hypocentre region of the main-shock (Dodge *et al.* 1996; Bouchon *et al.* 2011; Kato *et al.* 2012; Bouchon *et al.* 2013; Chen *et al.* 2013). Precursory slow slip is also frequently observed in the laboratory before stick-slip events on pre-existing faults (Dieterich 1978; Okubo & Dieterich 1984; Ohnaka & Shen 1999; Nielsen *et al.* 2010; Latour *et al.* 2013). Foreshock sequences associated with precursory aseismic slip are also reported on laboratory faults (McLaskey & Kilgore 2013). The mechanics of these earthquake nucleation phenomena is still poorly understood: it is for instance not clear why foreshock sequences are not systematically observed before natural large earthquakes. Furthermore, the dynamics of slow slip acceleration is still debated. Many fault models considering earthquakes as slip instabilities developing along a frictional fault have been proposed to explain precursory slip

(Dieterich 1992; Ohnaka 1992; Campillo & Ionescu 1997; Uenishi & Rice 2003; Rubin & Ampuero 2005; Ampuero & Rubin 2008; Viesca 2016a). In these models, the dynamic rupture (main-shock) is preceded by slow slip acceleration on a fault segment either of constant width or enlarging as slip rate blows up. Dynamic rupture starts when this small patch expands at a rate of the order of elastic wave speeds. This usually occurs when the fault patch has reached a critical size called the critical nucleation length, and the slip rate is high enough. Very few models provide a general framework to account for simultaneous foreshock occurrence and aseismic slip acceleration. It therefore remains unclear whether foreshocks are mainly driven by aseismic slip, or triggered through an independent cascading effect. As suggested by Ohnaka (1992) and Abercrombie & Mori (1996), the heterogeneity of fault frictional resistance might play a role in foreshock triggering. In this model, foreshocks are triggered as the nucleation slow slip front reaches a lower resistance asperity so that slow slip dominates the whole process. However, foreshocks may also perturb the slow slip, and this effect is usually not considered.

Here a new fault model for earthquake nucleation is proposed, allowing to investigate in more details the role of fault heterogeneity. The model consists in a finite planar fault sheared between two elastic media, where slip is resisted by a heterogeneous Dieterich–Ruina

853

rate-and-state friction (Dieterich 1979; Ruina 1983). This formulation allows aseismic slip and small earthquakes to spontaneously emerge and interact along the fault. In the following, fault slip evolution on the heterogeneous fault will be computed numerically in order to identify how frictional parameters control the main features of the nucleation process. The results will be confronted to theoretical developments based on linear fracture mechanics (Lawn 1993) and on a new frictional homogenization theory extending the studies by Campillo *et al.* (2001), Voisin *et al.* (2002) and Latour *et al.* (2011) on the slip weakening friction law. This will allow to characterize the dynamics of slip acceleration, the conditions for foreshock occurrence and the critical nucleation length under heterogeneous frictional conditions.

2 METHOD

Let assume the fault model depicted in Fig. 1, consisting in a linear infinite interface between 2-D elastic half-spaces. Let consider a constant stressing rate $\dot{\tau}_b$ in the far field so that the medium undergoes antiplane (mode III) deformation. Let assume mixed boundary conditions on the fault: Dieterich–Ruina type rate-and-state friction (Dieterich 1979; Ruina 1983) on a finite fault segment of length $2L$, and vanishing slip outside. Normal stress σ is constant along the fault. Fault heterogeneity is modelled by a constant $a = a_0$ rate-and-state parameter along the fault, and a λ periodic b parameter (Fig. 1b), so that velocity weakening (VW) and velocity strengthening (VS) patches alternate. $b(x)$ is parametrized as

$$b(x) = b_0 + \Delta b \phi(x), \qquad (1)$$

where b_0 and Δb are constants, and the functional ϕ is defined by

$$\phi(x) = \begin{cases} -1 & \text{if } 1/4 < E[x/\lambda] < 3/4 \\ +1 & \text{otherwise,} \end{cases} \qquad (2)$$

E being the fractional part. Δb has been chosen so that b is always positive, and $a - b$ alternates in sign. This constrains $\Delta b/b_0$ to remain between $1 - \alpha$ and 1, $\alpha = a_0/b_0$. The parameter $0 < f < 1$ is therefore introduced so that

$$\frac{\Delta b}{b_0} = 1 - \alpha + f\alpha. \qquad (3)$$

As mentioned in Appendix C, small earthquakes may nucleate on the VW patches if they are larger than the local nucleation length $2L_w$. The ratio $\rho_w = \lambda/4L_w$ between the VW patch length and $2L_w$ (eq. C1) is therefore introduced.

This study focuses on the effect of frictional heterogeneity (parametrized by α, f and ρ_w) on the nucleation of large earthquakes on the fault. Boundary conditions (no slip for $|x| > L$), remote loading (normalized stressing rate $\dot{\tau}_b = 10^{-5}$) and normalized damping parameter ($\beta = 10^{-8}$) will remain unchanged in this study. Initial conditions are defined as follows: normalized slip rate $v(x, 0) = 1$ and normalized state variable $\theta(x, 0)$ randomly distributed between 10^{-5} and 10. The initial conditions do not influence the results reported here. The governing equations for the fault evolution are provided in Appendix B, along with the main non-dimensional parameters. For a set of α, f and ρ_w, governing eq. (B9) are solved numerically to get the slip rate evolution $v(x, t) = \dot{\delta}(x, t)$ along the fault. Details about the numerical method are provided in Appendix B.
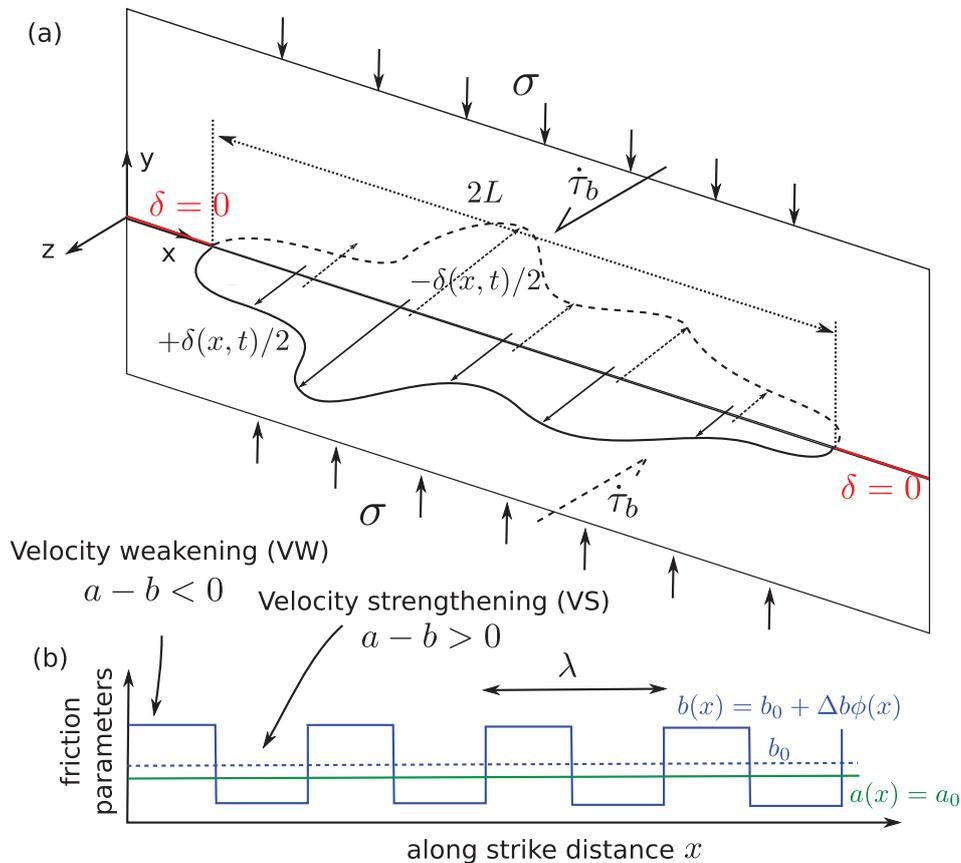
**Figure 1.** 2-D heterogeneous finite fault model. (a) Geometry and boundary conditions. σ is the normal stress, $\dot{\tau}_b$ is the remote stressing rate, δ is antiplane slip on the fault, L is the half fault length. (b) Distribution of a and b rate-and-state frictional parameters along the fault.
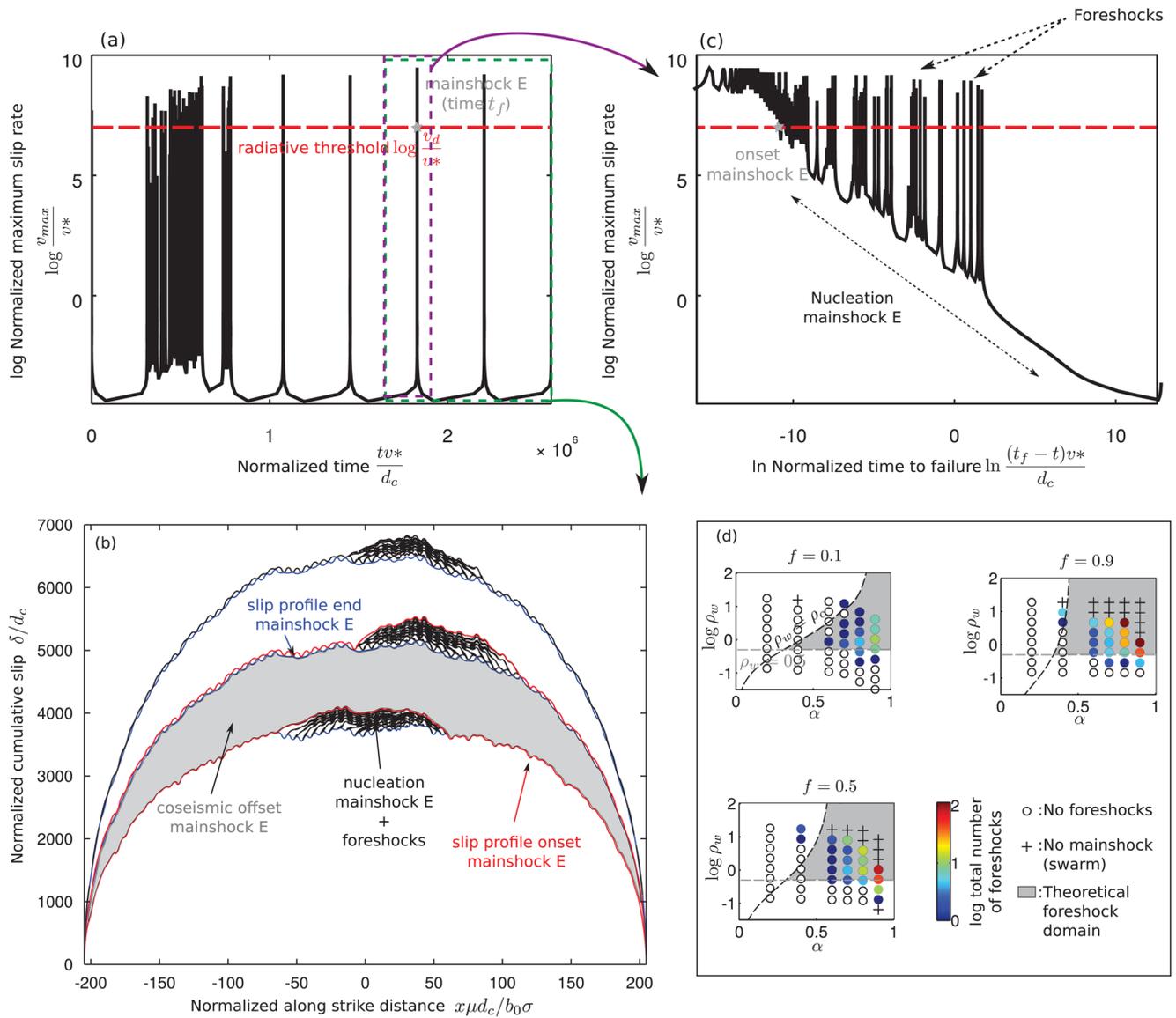
Figure 2. General slip behaviour for $\alpha < 1$. (a) Maximum slip rate history. (b) Cumulative slip profiles for the period highlighted in green in panel (a). One profile is represented at the onset and at the end of each earthquake occurring on the fault. (c) Slip rate evolution during the nucleation of the main-shock E. Horizontal axis indicates time remaining to main-shock E. Results were obtained with $\alpha = 0.9$, $f = 0.5$ and $\lambda = 6.4$ ($\rho_w = 1.04$). (d) Total number of foreshocks observed during the nucleation process of a main-shock. $\alpha = a_0/b_0$ is the ratio between averaged rate-and-state friction parameters. $\rho_w = \lambda/4L_w$ is the normalized wavelength of heterogeneity. f measures the amplitude of b parameter heterogeneity. ρ_c is the theoretical critical normalized wavelength of eq. (4) allowing foreshocks sequences to occur when $\rho_w > 0.5$.

3 RESULTS

As shown by Dublanchet *et al.* (2013), large earthquakes under heterogeneous frictional conditions may rupture the entire fault segment only when $\alpha < 1$. The parametric study will therefore be restricted to this domain. For $\alpha < 1$, the fault undergoes a global stick-slip cycle, as depicted in Figs 2(a) and (b). Locked phases (negligible slip rate, no accumulation of slip) alternate with rapid slip events affecting the whole fault segment (main-shocks). After several cycles, the fault looses the memory of the initial conditions which do not influence the nucleation process of the main-shock.

As illustrated in Figs 2(b) and (c), the main-shock nucleation involves a progressive acceleration of the background slip rate towards the radiative threshold v_d defined in Appendix B. Simultaneously, some slip is accumulated on a small segment of the fault, which

will be called nucleation patch in the remaining text. These general features are observed for the entire parameter range investigated here. In the example of Fig. 2, the slip rate increase is accompanied by rapid excursions of maximum slip rate above v_d associated with the emplacement of a small offsets on the fault. These events could be considered as foreshocks. They are not systematically observed during nucleation. As shown in Fig. 2(d), foreshock occurrence is mainly controlled by α and ρ_w who need to be high enough. Moreover, foreshock productivity increases as the averaged frictional properties get closer to the critical value $\alpha = 1$. Note that the amplitude of the b perturbation (parametrized by f) does not modify significantly these features.

These results suggest that two conditions are needed to get foreshocks on the fault. First VW patches need to be larger than critical to rupture as an earthquake. In other words, ρ_w has to be larger

than some value of order 1, such as $\rho_w > 0.5$ (Fig. 2d). The second condition is satisfied if the rupture of a single VW patch is not able to degenerate into a large rupture. From the results shown in Fig. 2(b), the rupture of a single patch could be modelled as a small crack. The accumulation of such small ruptures forms a larger crack (the nucleation patch itself). In this framework, one could use linear fracture mechanics theory and assume that dynamic rupture (main earthquake) occurs when the stress concentration ahead of the nucleation crack (quantified by the stress intensity factor) is large enough. The second condition could therefore be formulated in terms of Irwin's criterion (Lawn 1993): foreshock sequence occurs if the stress intensity factor for the rupture of a single patch is too small to allow rupture propagation through a VS patch. This idea is developed in Appendices D1 and D2 and leads to the following foreshock condition:

$$\alpha < \alpha_c = \left[1 + \left(\frac{3\pi}{4} - 1\right)f\right]^{-1}, \text{ or,}$$

$$\rho_w < \rho_c = \frac{3\pi}{16\tilde{L}_w(\alpha)}\frac{(1-f)\alpha}{(1-\alpha/\alpha_c)^2}, \tag{4}$$

where $\tilde{L}_w(\alpha) = L_w(\alpha)b_0\sigma/\mu d_c$. As shown in Fig. 2(d), condition $\rho_w > 0.5$ along with (4) delimit to the first order the foreshock domain in the parameter space. Note that for the set of parameters

considered in this study, the second condition (4) could approximately be replaced by $\alpha > 0.5$.

Interestingly, some simulations did not produce any main-shocks, especially for large α and large ρ_w (Fig. 2d). For this parameter range, seismic activity consists in a swarm of small events interpreted as a frustrated foreshock sequence. This point will be discussed later.

More generally, one could identify four domains in the phase diagrams of Fig. 2(d): (I), $\alpha < 0.5$ and $\rho_w < 0.5$, (II) $\alpha > 0.5$ and $\rho_w < 0.5$, (III) $\alpha < 0.5$ and $\rho_w > 0.5$ and (IV) $\alpha > 0.5$ and $\rho_w > 0.5$. Domain (IV) is the foreshocks domain. Each of these domains is associated with a specific nucleation regime, as depicted in Fig. 3. In addition to the presence (or absence) of foreshocks, they are characterized by a different evolution of background aseismic slip rate along the fault. In regime (I), slip rate increases progressively towards failure on a fault patch of constant length. This constant length is much larger than the typical wavelength λ of heterogeneity. Slip rate evolution in regime (II) is similar, but the fault patch characterized by accelerated slip becomes larger as the slip rate increases. The slip rate distribution is typical of a quasi-static crack expanding as a linear function of log time to main-shock. The third regime (III) is characterized by a localized acceleration of slip on a single VW patch. Finally, in regime (IV), foreshocks are coupled with a background slip rate increase. This background slip
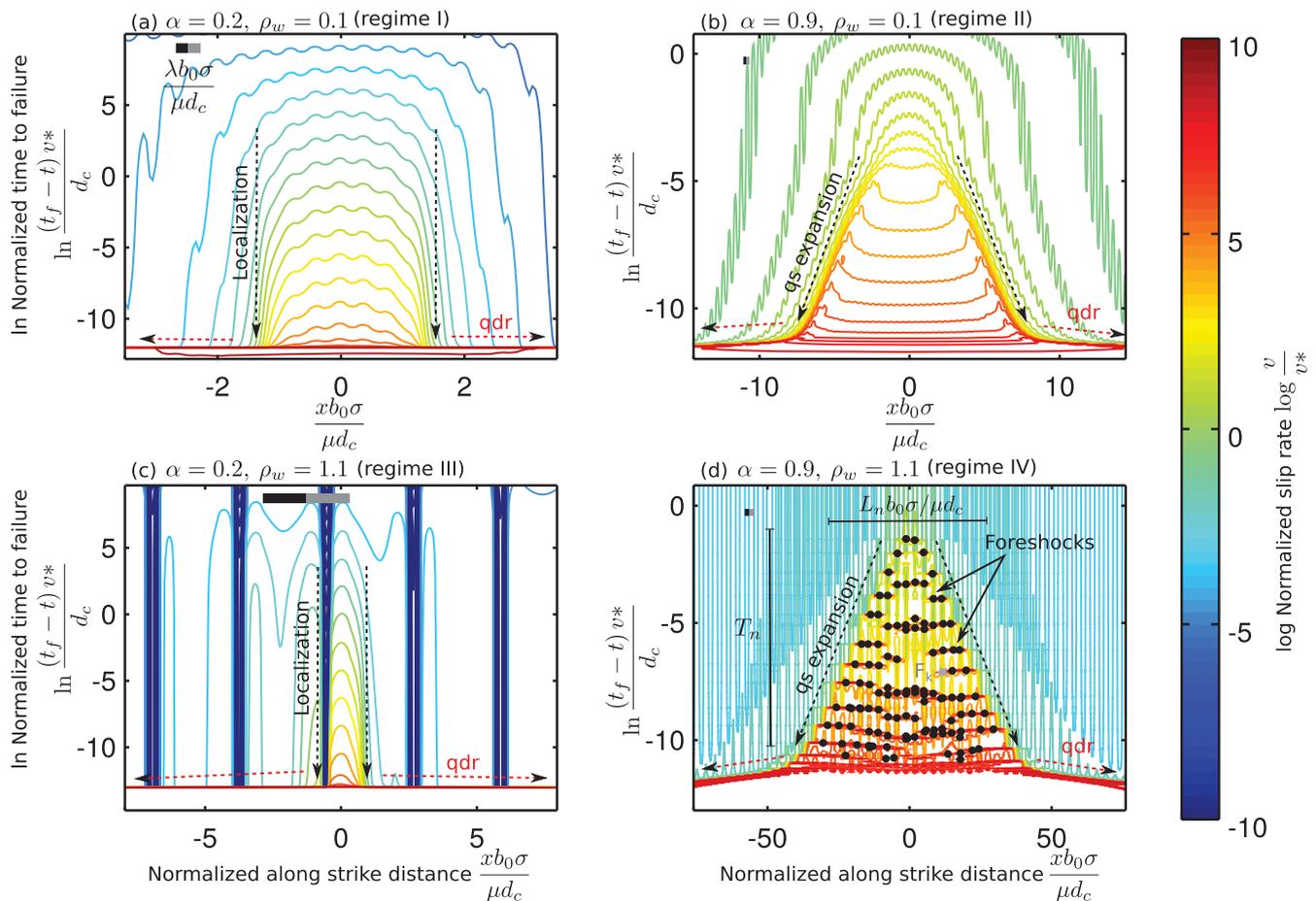
Figure 3. Slip rate evolution during the four possible regimes of main-shock nucleation. Coloured solid lines correspond to contours of equal slip rate in the distance along strike–ln time to failure space. The slip rate corresponding to one colour is indicated by the colour bar. Horizontal thick lines indicate the position of a velocity weakening (in grey) and velocity strengthening (in black) patch motif of size λ. qs indicates quasi-static, qdr corresponds to quasi-dynamic rupture (main-shock). Black dots in panel (d) correspond to foreshocks. The grey star indicates foreshock F_k detailed in Fig. D4. T_n and L_n denote the typical log duration of the nucleation process and nucleation patch size respectively.
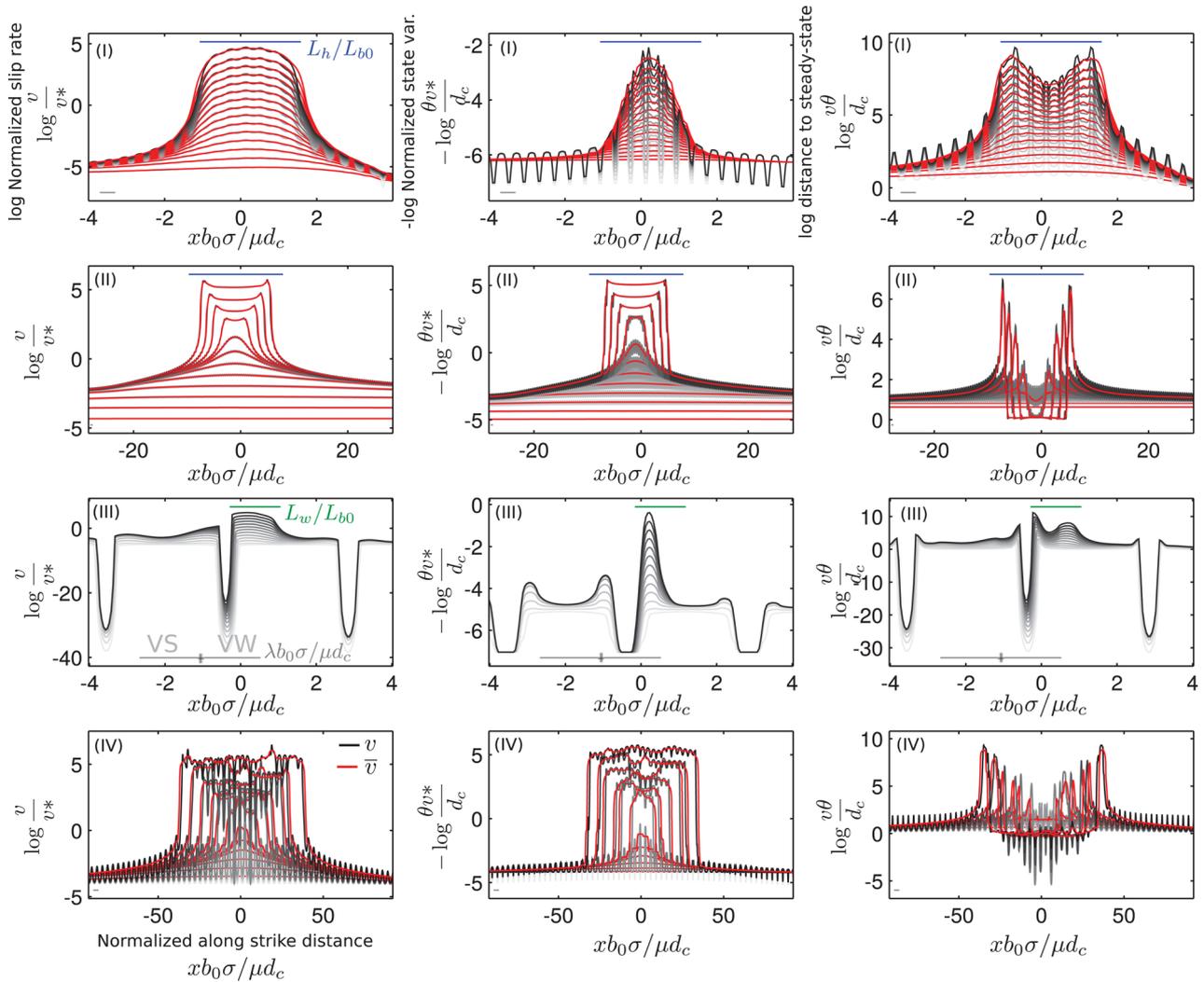
Figure 4. Background slip rate v, state variable θ and distance to steady state $\Omega = v\theta/d_c$ evolution during nucleation of a main-shock. One profile is represented each 10 time increase in maximum slip rate. Numerical solution is represented with the grey scale: darker colours corresponding to later times. Red profiles correspond to λ averaged variables. For regime (IV), grey profiles correspond to low passed filtered version of the raw numerical solution, in order to remove the foreshocks effect. Red profiles indicate averaged versions of the low passed filtered profiles. Blue lines indicate the homogenized length L_h defined in eq. (C2). Green lines correspond to the local length L_w defined in eq. (C1). $L_{b0} = \mu d_c/b_0\sigma$. The grey horizontal lines labelled $\lambda b_0\sigma/\mu d_c$ indicate the position of a velocity strengthening (VS) and velocity weakening (VW) patch.

acceleration here again occurs as the expanding quasi-static crack of regime (II). The nucleation crack expansion controls the spatial distribution of foreshocks. Note that according to Appendices D1 and D2, regimes (III) and (IV) could both be regarded as coupling aseismic slip acceleration and foreshocks. In this framework, regime (III) is a special case of regime (IV) where the first foreshock immediately degenerates into the main rupture.

The most important feature is the difference between localized acceleration process for low α values [regimes (I) and (III)], and the expanding acceleration process for α values close to unity [regimes (II) and (IV)]. More details about the evolution of background slip rate v and state variable θ during nucleation are provided in Fig. 4, along with the evolution of the variable $\Omega = v\theta/d_c$ quantifying the distance to steady state (Rubin & Ampuero 2005). Note that in Fig. 4(IV), the contribution of foreshocks has been removed to highlight the evolution of background slip. To do that, numerical solutions have been low passed filtered in $T = \ln(t_f - t)$ so that signals of the order of a foreshock duration have been removed. The difference between localized and expanding acceleration is

also clear in the evolution of state variable θ and Ω. Localized acceleration is indeed systematically associated with Ω values much larger than unity within the nucleation patch, whereas for expanding nucleation regimes, Ω is close to unity within the nucleation patch.

The slip rate evolution obtained in regime (III) corresponds to the solution of Rubin & Ampuero (2005), for small a/b ratio. Here nucleation consists in the acceleration of slip on a single VW patch, which immediately leads to the rupture of the entire fault, the evolution of slip rate is to the first order only controlled by the local friction parameters a_0 and b_w. Since by definition $a_0/b_w < \alpha < 0.5$, the fixed length solution of Rubin & Ampuero (2005) for slip acceleration is obtained. The evolution of slip rate in the three remaining regimes could also be interpreted in the framework developed by Rubin & Ampuero (2005) and Ampuero & Rubin (2008) for VW faults under constant frictional conditions. In Appendix D3, it is shown that slip rate and state variable evolution could be decomposed into a large scale background contribution of typical wavelength L_n plus a fluctuation of typical length scale $\lambda \ll L_n$. To the first order, the background large scale evolution is obtained by applying
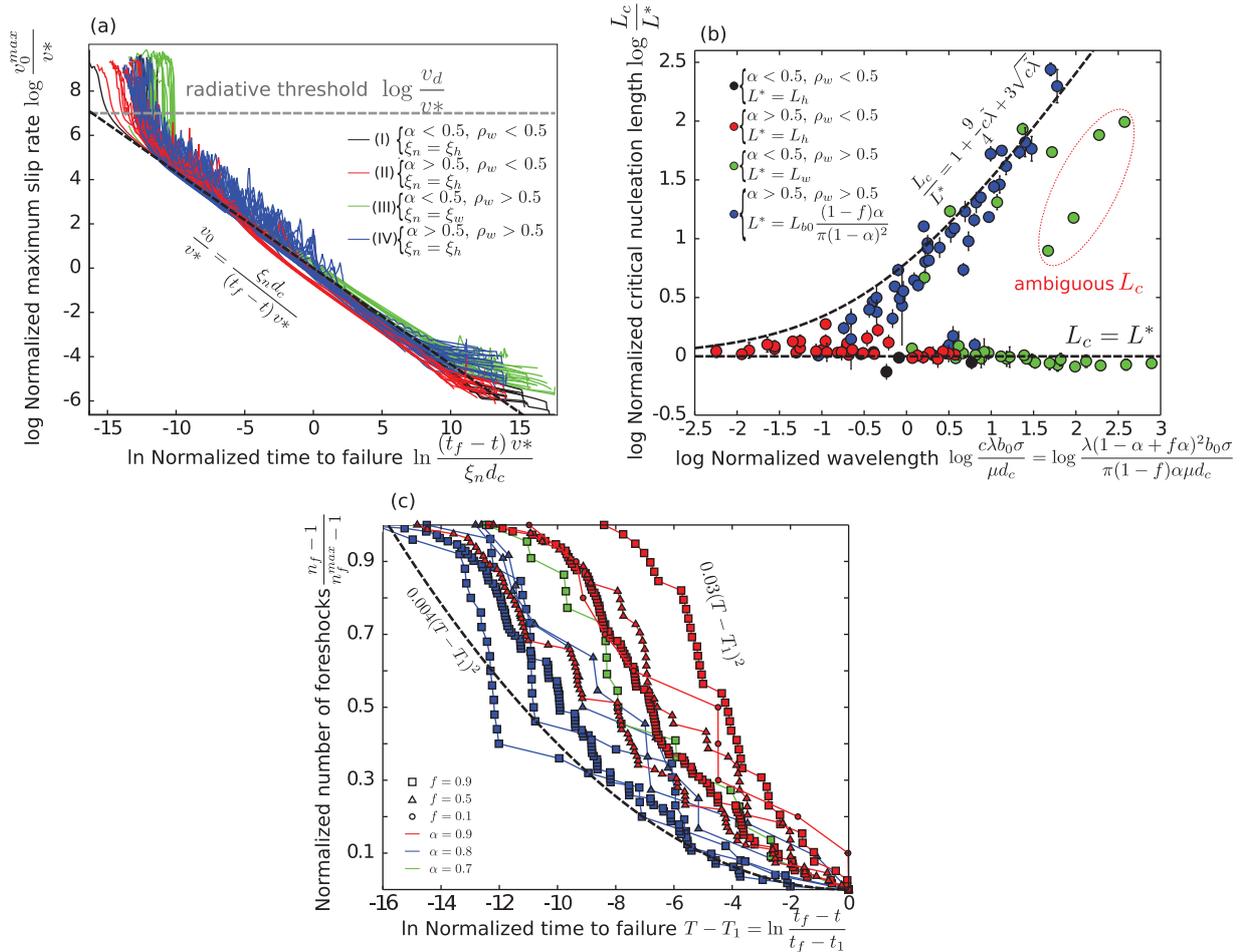
Figure 5. General nucleation characteristics in the four possible regimes. (a) Maximum background slip rate evolution. The normalization factor ξ_n for the horizontal axis is defined in the legend for each regime. ξ_h and ξ_w correspond to the homogenized and local normalization factors for nucleation duration defined in eqs (C5) and (C4). Black dashed line indicates the inverse time to failure asymptote. (b) Critical nucleation length. Coloured circles are the numerical estimates. Error bars indicate the variability of L_c for one simulation. Black dashed lines correspond to theoretical approximations. L^* is defined in the legend for each nucleation regime, from the homogenized or local length scales L_h and L_w defined in eqs (C2) and (C1). The four points outlined by the red dashed ellipse correspond to failure of the algorithm to detect L_c from the numerical solutions. (c) Seismicity increase before the main-shock occurrence in regime (IV). n_f is the cumulative number of foreshocks, $n_f^{\max}$ the total number of foreshocks in the sequence. t_f is the onset time of the main-shock. T_1 and t_1 refer to the first foreshock of the sequence. Coloured lines are the numerical results. Each symbol corresponds to a single foreshock. Only sequences with more than 10 foreshocks are represented. Heavy black dashed lines indicate two different approximations of the increase of seismic activity.

a λ moving average to the solution. After separating the two spatial scales, the different contributions could be isolated. It is then shown that the large scale background evolution obeys homogenized equations involving only the ratio of averaged parameters α (eq. D41). Neglecting the fluctuations of v and θ, the fault is therefore equivalent to an effective fault characterized by constant frictional properties.

These theoretical results are supported by numerical simulations. In particular by the shape of the averaged v, θ and Ω profiles shown in Fig. 4, which are qualitatively similar to what is expected for constant friction faults (Rubin & Ampuero 2005). It is further supported by the rescaled evolution of maximum slip rate represented in Fig. 5(a): as expected for nucleation under constant frictional conditions, maximum background slip rate blows up as the inverse time to failure. Furthermore, the timescale for this evolution during regimes (I), (II) and (IV) is to the first order well explained by the homogenized nucleation duration, that is, by the asymptotic values proposed by Rubin & Ampuero (2005) assuming a_0 and b_0 as the relevant parameters. Similarly, the nucleation duration under

regime (III) is reasonably approximated by the asymptotic values of Rubin & Ampuero (2005) assuming a_0 and b_w as the relevant parameters. The last evidence that nucleation under heterogeneous frictional conditions could be derived (at least to some extent) from the work by Rubin & Ampuero (2005) is provided by the nucleation length, as shown below.

One important feature is that the evolution of background slip rate under regime (IV) seems to be unaffected by foreshock occurrence, at least to the first order in $\varepsilon = \lambda/L_n$. Foreshocks are therefore byproducts of the acceleration of background slip rate that could be regarded as an aseismic slip acceleration. However, foreshocks have important consequences concerning the transition to quasi-dynamic rupture.

The end of the nucleation process could be characterized by the critical nucleation length L_c marking the transition to quasi-dynamic rupture. For all the simulations reported here, the nucleation length has been estimated as half the distance between peaks of shear stresses delimiting the nucleation patch at the onset of quasi-dynamic rupture (Fig. D1b). For a given set of parameters, L_c

has been estimated for at least three different main-shocks. Results are presented in Fig. 5(b). As shown in Appendix D4, the nucleation length for regimes (I), (II) and (III) could be derived from the nucleation length under homogeneous frictional conditions. For regime (III) the half nucleation length is controlled by the local VW friction parameters, and it is well approximated by the local nucleation length L_w (eq. C1, Fig. 5b). Since no foreshocks occur in regimes (I) and (II), the whole nucleation process is governed by the averaged parameters, and the homogenized nucleation length L_h defined in eq. (C2) provides a good approximation of the nucleation half-length. As shown in Fig. 5(b), this latter approach fails to explain nucleation lengths obtained in regime (IV), and this comes from the significant contribution of foreshocks that cannot be neglected. To account for the foreshock effect, it is here again useful to refer to linear fracture mechanics. In this framework, the nucleation length L_c is the nucleation crack half-length leading to a high enough stress intensity factor ahead of the crack. It is shown in Appendix D4 that the critical stress intensity factor is reached for L_c given by eq. (D59) as

$$L_c = L^* \left(1 + 3\sqrt{c\tilde{\lambda}} + \frac{9}{4}c\tilde{\lambda} \right), \tag{5}$$

where $L^* = \mu d_c (1 - f)\alpha/\pi b_0 \sigma (1 - \alpha)^2$, $c = (1 - \alpha + f\alpha)^2/\pi(1 - f)\alpha$ and $\tilde{\lambda} = \lambda b_0 \sigma/\mu d_c$. Note that the critical nucleation length increases with λ. Eq. (D59) provides a good approximation for the nucleation length obtained in regime (IV) (Fig. 5b). As λ goes to zero, the estimate of eq. (5) gets closer to L_h, and provides an upper bound for the critical nucleation length under regime (II). This is because in both regimes (II) and (IV), the nucleation occurs as an expanding crack characterized by steady state frictional conditions within the crack (Fig. 4). Stress intensity factors expressions (D16) and (D20) therefore hold for regime (II). Note that the nucleation length given by eq. (5) converges to L^* as λ vanishes. From eq. (3), L^* could be expressed as

$$L^* = \frac{L_{b0}}{\pi} \frac{1 - \Delta b/b_0}{(1 - \alpha)^2}, \tag{6}$$

which converges to the L_∞ proposed by Rubin & Ampuero (2005) for the constant a and b fault as the b perturbation $\Delta b/b_0$ vanishes.

The space-time pattern of foreshocks in regime (IV) (Fig. 3d) is characterized by two important features. First, several VW patches repeatedly rupture before the main-shock. They could be considered as repeating events occurring fairly regularly in log time to failure. The cumulative number of ruptures on a particular VW patch increases as $-\ln(t_f - t)$. More generally, the foreshock rate accelerates before the main-shock, as the nucleation patch expands. From Fig. 3(d), let assume that each time the nucleation patch size increases by 2λ, the number of additional foreshocks is proportional to $l/\lambda + 1$. The cumulative number of foreshocks n_f on the fault therefore grows as $n_f \sim (l/\lambda)^2$. Since l increases approximately linearly with log time to failure, n_f increases as $\ln^2(t_f - t)$. The increase of seismicity before the main-shock is represented in Fig. 5(c) for the largest foreshock sequences in regime (IV). The numerical results suggest that n_f/n_f^{max} grows approximately as $A\ln^2(t_f - t)$, A being a constant between 0.004 and 0.03. However, this simple analysis does not allow to capture the f, α and possibly λ dependence of A. This requires to provide a closed form expression for l since $n_f/n_f^{max} \simeq (l/l_{max})^2$, l_{max} being the maximum half-length of the nucleation patch. The closed form expression of l in turn depends on the stress distribution ahead of the nucleation patch. This problem is beyond the scope of this study. Note the $\ln^2(t_f - t)$ dependence of the cumulative number of foreshocks implies a seismicity rate increasing as $-\ln(t_f - t)/(t_f - t)$, which is approximately similar to a $1/(t_f - t)$ growth long enough before the main-shock.

4 DISCUSSION

The nucleation of large earthquakes on a heterogeneous fault reproduces many features observed for natural and laboratory earthquakes: aseismic slip acceleration in the hypocentre region, possible but not systematic occurrence of foreshocks in the same area. As illustrated in Fig. 3(d), the foreshock sequences produced in regime (IV) are characterized by a progressive along strike expansion that is often observed before natural earthquakes (Kato *et al.* 2012; Kato & Nakagawa 2014). The acceleration of repeating events has furthermore already been reported prior to Izmit earthquake (Bouchon *et al.* 2011), and the $1/(t_f - t)$ acceleration of seismicity rate is a common features of many foreshock sequences (Papazachos 1973; Kagan & Knopoff 1978; Jones & Molnar 1979; Bouchon *et al.* 2013).

As noted in Fig. 2(d), some foreshock sequences in regime (IV) do not lead to a main-shock, in particular when α is close to one and ρ_w (or λ) is large enough. Since the nucleation length increases with λ in regime (IV), this could be interpreted as situations where the critical nucleation length is larger than the whole fault segment considered here. Such sequences could be regarded as seismic swarms dying when the tectonic stress is released on the fault, or continuous background seismic activity. Frictional heterogeneity on a finite fault therefore allows to explain either seismic swarms or large earthquakes with or without precursory foreshock activity.

From the simulations presented here, foreshock sequences are strongly coupled to the aseismic slip, and it was not possible to generate foreshock cascades with negligible aseismic deformation leading to a main-shock, as suggested by other studies (Jones & Molnar 1979; Helmstetter & Sornette 2003). However the possibility of such processes is not precluded, as other types of friction laws, boundary conditions, and heterogeneity have not been considered. More than that, the foreshock sequences seem to be driven by the increase of background aseismic slip rate. In the developments presented in Appendix D, it is shown that foreshocks generate very localized perturbations of the slip rate, of the state, and of the stress, which are negligible compared to the perturbations generated by the large scale increase in background slip rate. On the other hand, the dynamics of one particular event is not only controlled by local friction parameters, but more importantly by local values of the background slip rate (eq. D53). Foreshocks could therefore be considered as by-products of a large scale nucleation process, as suggested by Ohnaka (1992); Dodge *et al.* (1996); Bouchon *et al.* (2011) and Bouchon *et al.* (2013).

The developments presented so far show that many features of nucleation could be understood with an effective friction law defined from the spatial average of the local friction parameters. This conclusion holds in the case of a small-scale heterogeneity, at least smaller than the minimum local nucleation length. The theoretical framework developed for constant rate-and-state friction faults (Dieterich 1992; Rubin & Ampuero 2005; Ampuero & Rubin 2008) could be used for heterogeneous faults, in particular to define effective critical nucleation lengths and effective nucleation durations. The existence of effective rate and state parameters extends the concept of effective slip-weakening friction defined by Campillo *et al.* (2001) and Voisin *et al.* (2002). In particular when the rate-and-state fault is far above steady state, rate-and-state friction almost reduces to a slip-weakening friction law in which the weakening rate $\partial f/\partial \delta$

is given by $-b/d_c$, f being the friction coefficient, δ the fault slip, and b, d_c rate and-state parameters. The effective b defined here as the spatial average of b leads to a single effective weakening rate, which is different from the two successive effective weakening rates proposed by Campillo *et al.* (2001). More investigation is needed to determine whether the effective weakening of rate-and-state and slip-weakening merge at some point.

When frictional properties vary over a scale λ larger than the minimum nucleation length, nucleation is not only controlled by an effective friction law, but also by an Irwin's criterion involving λ. More generally, such a fracture mechanics criterion controls the transition to quasi-dynamic rupture at least in regimes (II), (III) and (IV). Accordingly, the nucleation crack expansion in regime (IV) occurs with $K < K_c$, that is with an energy release rate smaller than critical, and could be seen as a subcritical crack growth (Rice 1978). The expansion of the crack is here driven by localized destabilization of self-accelerating VW patches at the edges of the crack. On average, the expansion is controlled by effective friction. This could be compared to the subcritical mode I crack growth on a heterogeneous interface analysed by Lengliné *et al.* (2011) and Lengliné *et al.* (2012). The expansion of the crack was in their experiment controlled by effective fracture energy. This is an indication that effective fracture energy could be defined from effective friction, as primarily suggested by Campillo *et al.* (2001). This point will be further discussed later.

Although only periodic frictional heterogeneities have been considered, the conclusion could be extended to non-periodic heterogeneities. Heterogeneity is indeed suspected to exist at all scales on natural faults (Power *et al.* 1987; Renard *et al.* 2006). Furthermore, foreshock sequences are usually characterized by a Gutenberg-Richter distribution, which suggests a fractal distribution of heterogeneity. However, the developments leading to an effective law for the background slip rate do not use at any time the periodicity assumption. Let consider a fault made of a succession of small segments, the ith subfault having a length λ_i and a critical nucleation length L_{wi}. If the maximum value of $\rho_w = \lambda_i/4L_{wi}$ is smaller than critical, the fault will not produce any foreshocks, and the slip rate increase will be controlled by the effective friction law, as in regimes (I) and (II). If one of the subpatches is larger than critical, foreshocks may occur during nucleation, but as long as the typical length scale over which the background nucleation proceeds is larger than the maximum subpatch length, foreshocks have a negligible influence. As in regimes (I) and (II), the effective friction law here controls the nucleation. This conclusion supports the idea that homogenization may explain (at least to the first order) the behaviour of faults characterized by a complex non-periodic heterogeneity (Latour *et al.* 2011). However, as mentioned by Latour *et al.* (2011), the homogenization procedure could become a difficult task in such situations. In the rate-and-state framework studied here, difficulties could arise in defining the critical nucleation length for regime (IV), and the transition from regime (III) to regime (IV). This is because the expression for the stress intensity factor K and the critical stress intensity factor K_c developed here depend on the stress change distribution within the nucleation crack, which will no longer be periodic. This analysis requires more attention.

This study has focused on the ageing version of the rate-and-state friction, and the slip version has not been considered so far. This could considerably change the conclusions, precisely because nucleation under slip law is characterized by extreme localization (Ampuero & Rubin 2008). In some cases, nucleation consists in very narrow slip pulses travelling through the fault plane. In other words, the typical nucleation patch size L_n will be very small. Ho-

mogenization would be theoretically possible for very small scale heterogeneity $\lambda \ll L_n$. If homogenization is not possible, nucleation would proceed as sequences of foreshocks which would have a dominant effect in the process. Depending on the way foreshocks and accelerated slow slip interact, the foreshock production rate may differ from the acceleration expected with the ageing law. If the slip law generates localization instead of crack expansion, a smaller foreshock productivity is expected.

Similarly, more investigations are needed to understand nucleation under heterogeneities in the a parameter and more importantly in the critical slip d_c, which influences greatly the characteristic length scales. Rate-and-state faults characterized by heterogeneous d_c may generate large ruptures preceded by a sequence of accelerated foreshock activity (Hillers *et al.* 2006). Hillers *et al.* (2006) also noted that some characteristics of the foreshock activity (magnitude–frequency distribution, total number of foreshocks) are controlled by the typical wavelength of the d_c heterogeneity. These features are similar to what is obtained here under regime (IV). It would be worth extending Hillers *et al.* (2006) study to investigate whether the nucleation of large events are controlled by an effective d_c parameter. Defining an effective d_c is of critical importance for a more general effective friction theory, because it is a common parameter of different friction laws (rate-and-state, slip weakening) invoked in earthquake mechanics theories. It plays an important role in nucleation under these different formulations (Rubin & Ampuero 2005; Ampuero & Rubin 2008; Campillo & Ionescu 1997; Uenishi & Rice 2003). More generally, d_c is proportional to the fracture energy G_c that controls many earthquake processes from nucleation to dynamic rupture propagation. Up-scaling friction parameters such as d_c would be a first step in up-scaling fracture energy.

In the framework of heterogeneous slip-weakening friction law, an effective d_c could be derived (Campillo *et al.* 2001; Voisin *et al.* 2002). An important result of Campillo *et al.* (2001) is that even if d_c is constant along the fault, for strong heterogeneities in static friction coefficient, the effective d_c is larger than the local (constant) d_c. The effective d_c is therefore not always a simple functional of the local d_c distribution, but involves the distribution of the other frictional parameters along the fault. A similar situation arises in the rate-and-state framework as this is suggested by the critical nucleation length in the presence of b heterogeneities (Fig. 5b). For homogeneous rate-and-state faults, the critical nucleation length is proportional to d_c (Dieterich 1992; Rubin & Ampuero 2005; Ampuero & Rubin 2008). Although an effective d_c has not been derived in this study, an effective nucleation length L_c^{het} has been obtained for the different nucleation regimes in Appendix D4. Let L_c^{hom} be the critical nucleation half-length under constant friction conditions a_0, b_0 and d_c. From Appendix C, $L_c^{\text{hom}}(d_c) = \mu d_c \phi(\alpha)/b_0\sigma$, where ϕ is a function of the ratio $\alpha = a_0/b_0$. An effective parameter d_c^{eff} for the heterogeneous fault could then be defined as $L_c^{\text{hom}}(d_c^{\text{eff}}) = L_c^{\text{het}}$. From the results of Appendix D4 for L_c^{het}, one gets:

$$d_c^{\text{eff}} = \begin{cases} d_c & \text{for regimes (I), (II)} \\ & \text{and (III)} \\ \dfrac{(1-f)\alpha}{\pi(1-\alpha)^2}\left[1 + 3\sqrt{c\tilde{\lambda}} + \dfrac{9}{4}c\tilde{\lambda}\right]d_c & \text{for regime (IV).} \end{cases}$$

(7)

Note that under regime (III) there is no proper homogenized nucleation length since nucleation is entirely governed by local VW parameters. d_c is therefore the relevant large scale critical slip. If d_c^{eff} is equal to the local d_c under regimes (I), (II) and (III), it may

be drastically larger than d_c under regime (IV). This reflects that multiple foreshocks are needed to break all the strengthening barriers along the fault and promote large scale slip. The weakening of the entire fault thus occurs when the VW patches have slept much more than the local d_c (at least the number of successive foreshocks on the patch times d_c), just as in the strong heterogeneous case of Campillo *et al.* (2001). Eq. (7) could further be used to define an effective fracture energy density G_c^{eff} from the definition (D18) one gets G_c^{eff} proportional to $b_0 \sigma d_c^{\text{eff}}$. As in the strong heterogeneity case discussed by Campillo *et al.* (2001), the fracture energy under regime (IV) may be much larger on a large scale heterogeneous fault than on a small-scale homogeneous fault. This may explain the discrepancy between d_c (and G_c) estimates for natural earthquakes and for laboratory samples (Ohnaka & Shen 1999; Peyrat *et al.* 2001).

In order to make comparison with nucleation of natural earthquakes, the results presented here need to be extended to a 2-D heterogeneous fault embedded in a 3-D medium. In particular, this would allow to derive more realistic foreshock production rates. The difficulty of extending to 3-D essentially comes from the elastic interactions that become more complex, mixing in-plane and antiplane modes (Latour *et al.* 2011). However, under the quasi-dynamic assumption, this complexity will be limited, and would only appear in the static interaction term, which would still be a convolution product of the slip gradients (Andrews 1974). The derivations of Appendix D may therefore be generalized to the 2-D fault.

5 CONCLUSION

This study has demonstrated how frictional heterogeneity could explain in a simple framework the principal features of large earthquakes nucleation process. In particular, it suggests a physical interpretation of why foreshock sequences are not systematically observed, and why microseismic swarm sometimes do not develop to a large event. Under heterogeneous conditions, the aseismic slip rate increase, the growth of foreshock activity and the critical nucleation length are controlled by an effective rate-and-state friction law and a simple fracture criterion. One of the most important implications is that rate-and-state friction could be up scaled, so that frictional heterogeneity could be studied through effective media approaches. This has been demonstrated for nucleation only, but may have great implications in the understanding of other processes such as dynamic rupture or aseismic transients when heterogeneous friction conditions prevail on faults.

REFERENCES

Abercrombie, R.E. & Mori, J., 1996. Occurrence patterns of foreshocks to large earthquakes in the western United States, *Nature,* **381**(6580), 303–307.

Ampuero, J. & Rubin, A., 2008. Earthquake nucleation on rate and state faults: aging and slip laws, *J. geophys. Res.,* **113,** B01302, doi:10.1029/2007JB005082.

Andrews, D., 1974. Evaluation of static stress on a fault plane from a Green's function, *Bull. seism. Soc. Am.,* **64**(6), 1629–1633.

Bouchon, M., Karabulut, H., Aktar, M., Özalaybey, S., Schmittbuhl, J. & Bouin, M., 2011. Extended nucleation of the 1999 M_w 7.6 Izmit earthquake, *Science,* **331**(6019), 877–880.

Bouchon, M., Durand, V., Marsan, D., Karabulut, H. & Schmittbuhl, J., 2013. The long precursory phase of most large interplate earthquakes, *Nat. Geosci.,* **6**(4), 299–302.

Campillo, M. & Ionescu, I.R., 1997. Initiation of antiplane shear instability under slip dependent friction, *J. geophys. Res.,* **102**(B9), 20 363–20 371.

Campillo, M., Favreau, P., Ionescu, I.R. & Voisin, C., 2001. On the effective friction law of a heterogeneous fault, *J. geophys. Res.,* **106**(B8), 16 307–16 322.

Chen, K.H., Bürgmann, R. & Nadeau, R.M., 2013. Do earthquakes talk to each other? Triggering and interaction of repeating sequences at Parkfield, *J. geophys. Res.,* **118**(1), 165–182.

Cochard, A. & Rice, J.R., 1997. A spectral method for numerical elastodynamic fracture analysis without spatial replication of the rupture event, *J. Mech. Phys. Solids,* **45**(8), 1393–1418.

Dieterich, J.H., 1978. Time-dependent friction and the mechanics of stick-slip, *Pure appl. Geophys.,* **116**(4-5), 790–806.

Dieterich, J.H., 1979. Modeling of rock friction-1. Experimental results and constitutive equations, *J. geophys. Res.,* **84,** 2161–2168.

Dieterich, J.H., 1992. Earthquake nucleation on faults with rate and state-dependent strength, *Tectonophysics,* **211,** 115–134.

Dodge, D.A., Beroza, G.C. & Ellsworth, W., 1996. Detailed observations of california foreshock sequences: implications for the earthquake initiation process, *J. geophys. Res.,* **101**(B10), 22 371–22 392.

Dublanchet, P., Bernard, P. & Favreau, P., 2013. Interactions and triggering in a 3-D rate-and-state asperity model, *J. geophys. Res.,* **118**(5), 2225–2245.

Helmstetter, A. & Sornette, D., 2003. Foreshocks explained by cascades of triggered seismicity, *J. geophys. Res.,* **108**(B10), 2457, doi:10.1029/2003JB002409.

Hillers, G., Ben-Zion, Y. & Mai, P., 2006. Seismicity on a fault controlled by rate-and-state-dependent friction with spatial variations of the critical slip distance, *J. geophys. Res.,* **111**(B1), B01403, doi:10.1029/2005JB003859.

Jones, L. & Molnar, P., 1976. Frequency of foreshocks, *Nature,* **262**(5570), 677–679.

Jones, L.M. & Molnar, P., 1979. Some characteristics of foreshocks and their possible relationship to earthquake prediction and premonitory slip on faults, *J. geophys. Res.,* **84**(B7), 3596–3608.

Kagan, Y. & Knopoff, L., 1978. Statistical study of the occurrence of shallow earthquakes, *Geophys. J. Int.,* **55**(1), 67–86.

Kato, A. & Nakagawa, S., 2014. Multiple slow-slip events during a foreshock sequence of the 2014 Iquique, Chile M_w 8.1 earthquake, *Geophys. Res. Lett.,* **41**(15), 5420–5427.

Kato, A., Obara, K., Igarashi, T., Tsuruoka, H., Nakagawa, S. & Hirata, N., 2012. Propagation of slow slip leading up to the 2011 M_w 9.0 Tohoku-oki earthquake, *Science,* **335**(6069), 705–708.

Latour, S., Campillo, M., Voisin, C., Ionescu, I., Schmedes, J. & Lavallée, D., 2011. Effective friction law for small-scale fault heterogeneity in 3D dynamic rupture, *J. geophys. Res.,* **116,** B10306, doi:10.1029/2010JB008118.

Latour, S., Schubnel, A., Nielsen, S., Madariaga, R. & Vinciguerra, S., 2013. Characterization of nucleation during laboratory earthquakes, *Geophys. Res. Lett.,* **40**(19), 5064–5069.

Lawn, B., 1993. *Fracture of Brittle Solids,* Cambridge Univ. Press.

Lengliné, O., Toussaint, R., Schmittbuhl, J., Elkhoury, J.E., Ampuero, J., Tallakstad, K.T., Santucci, S. & Måløy, K.J., 2011. Average crack-front velocity during subcritical fracture propagation in a heterogeneous medium, *Phys. Rev. E,* **84**(3), 036104, doi:10.1103/PhysRevE.84.036104.

Lengliné, O., Elkhoury, J., Daniel, G., Schmittbuhl, J., Toussaint, R., Ampuero, J.-P. & Bouchon, M., 2012. Interplay of seismic and aseismic deformations during earthquake swarms: an experimental approach, *Earth planet. Sci. Lett.,* **331,** 215–223.

Marone, C., 1998. Laboratory-derived friction laws and their application to seismic faulting, *Annu. Rev. Earth Planet. Sci.,* **26**(1), 643–696.

McLaskey, G.C. & Kilgore, B.D., 2013. Foreshocks during the nucleation of stick-slip instability, *J. geophys. Res.,* **118**(6), 2982–2997.

Nielsen, S., Taddeucci, J. & Vinciguerra, S., 2010. Experimental observation of stick-slip instability fronts, *Geophys. J. Int.,* **180**(2), 697–702.

Ohnaka, M., 1992. Earthquake source nucleation: a physical model for short-term precursors, *Tectonophysics*, **211**(1-4), 149–178.

Ohnaka, M. & Shen, L.-f., 1999. Scaling of the shear rupture process from nucleation to dynamic propagation: implications of geometric irregularity of the rupturing surfaces, *J. geophys. Res.,* **104**(B1), 817–844.

Okubo, P.G. & Dieterich, J.H., 1984. Effects of physical fault properties on frictional instabilities produced on simulated faults, *J. geophys. Res.,* **89**(B7), 5817–5827.

Papazachos, B., 1973. The time distribution of the reservoir-associated foreshocks and its importance to the prediction of the principal shock, *Bull. seism. Soc. Am.,* **63**(6-1), 1973–1978.

Peyrat, S., Olsen, K. & Madariaga, R., 2001. Dynamic modeling of the 1992 Landers earthquake, *J. geophys. Res.,* **106**(B11), 26 467–26 482.

Power, W., Tullis, T., Brown, S., Boitnott, G. & Scholz, C., 1987. Roughness of natural fault surfaces, *Geophys. Res. Lett.,* **14**(1), 29–32.

Renard, F., Voisin, C., Marsan, D. & Schmittbuhl, J., 2006. High resolution 3D laser scanner measurements of a strike-slip fault quantify its morphological anisotropy at all scales, *Geophys. Res. Lett.,* **33**(4), L04305, doi:10.1029/2005GL025038.

Rice, J., 1978. Thermodynamics of the quasi-static growth of griffith cracks, *J. Mech. Phys. Solids,* **26**(2), 61–78.

Rice, J., 1979. *The Mechanics of Earthquake Rupture,* Division of Engineering, Brown University.

Rice, J.R., 1993. Spatio-temporal complexity of slip on a fault, *J. geophys. Res., 98,* 9885–9907.

Rubin, A. & Ampuero, J., 2005. Earthquake nucleation on (aging) rate and state faults, *J. geophys. Res,* **110,** B11312, doi:10.1029/2005JB003686.

Ruina, A.L., 1983. Slip instability and state variable friction laws, *J. geophys. Res., 88,* 10 359–10 370.

Uenishi, K. & Rice, J.R., 2003. Universal nucleation length for slip-weakening rupture instability under nonuniform fault loading, *J. geophys. Res.,* **108**(B1), 2042, doi:10.1029/2001JB001681.

Viesca, R.C., 2016a. Stable and unstable development of an interfacial sliding instability, *Phys. Rev. E,* **93,** 060202, doi:10.1103/PhysRevE.93.060202.

Viesca, R.C., 2016b. Self-similar slip instability on interfaces with rate- and state-dependent friction, *Proc. R. Soc. A,* **472**(2192), doi:10.1098/rspa.2016.0254.

Voisin, C., Campillo, M., Ionescu, I., Hassani, R. & Nguyen, Q.-L., 2002. Process and signature of initiation on a finite fault system: a spectral approach, *Geophys. J. Int.,* **148**(1), 120–131.

APPENDIX A: NOTATIONS

Consider a scalar function $f(x, t)$. In the following, $\mathcal{H}[f]$ is the Hilbert transform of the function f, that is,

$$\mathcal{H}[f](x, t) = \frac{1}{\pi} \int_{-\infty}^{+\infty} \frac{f(s, t)}{x - s} ds. \tag{A1}$$

In the following, f' and $\dot{f}$ indicate partial derivatives with respect to the first and the second variables of f, that is here $\partial/\partial x$ and $\partial/\partial t$. In case of a variable change, for a scalar function $f(y(x), s(t))$, I will note $f' = \partial f/\partial y$ and $\dot{f} = \partial f/\partial s$. The moving λ-average with respect to the first variable $\overline{f}^\lambda(x, t)$ is defined by

$$\overline{f}^\lambda(x, t) = \frac{1}{\lambda} \int_{x-\lambda/2}^{x+\lambda/2} f(x', t) dx'. \tag{A2}$$

Let f be a scalar function of the variable x and ε a very small positive number compared to the typical wavelength of f variations. Let g be a scalar function of the variable $y = x/\varepsilon$, then,

$$\overline{fg}^\varepsilon(x, y) = \frac{1}{\varepsilon} \int_{x-\varepsilon/2}^{x+\varepsilon/2} f(x') g\left(\frac{x'}{\varepsilon}\right) dx'$$
$$\simeq f(x) \int_{y-1/2}^{y+1/2} g(y') dy' = f(x) \overline{g}(y), \tag{A3}$$

where for simplicity $\overline{g}$ corresponds to $\overline{g}^1$.

APPENDIX B: GOVERNING EQUATIONS

Consider the planar 1-D fault depicted in Fig. 1(a) under antiplane deformation. The slip discontinuity $\delta(x, t) = u(x, 0^+, t) - u(x, 0^-, t)$ (u being the displacement in the z direction) vanishes for $|x| > L$ at all times. The evolution of δ is governed by the quasi-static stress balance:

$$\tau_f(x, t) = \tau_b(x, t) + \tau_{el}(x, t) + \tau_{rad}(x, t), \tag{B1}$$

where τ_f is the frictional stress, τ_b the remote loading, that is, the stress that would act on the fault if $\delta = 0$, τ_{el} the static stress interaction, and τ_{rad} the local dynamic stress change associated with shear wave radiation. The elastic stress $\tau_{el}(x, t)$ is given by

$$\tau_{el}(x, t) = -\frac{\mu}{2} \mathcal{H}[\delta'](x, t), \tag{B2}$$

where μ is the shear modulus. With $v(x, t) = \dot{\delta}(x, t)$, the rate-and-state frictional stress $\tau_f(x, t)$ in $|x| < L$ is given by

$$\tau_f(x, t) = f_0\sigma + a(x)\sigma \ln \frac{v(x, t)}{v^*} + b(x)\sigma \ln \frac{\theta(x, t)v^*}{d_c}, \tag{B3}$$

where v is the slip rate and θ the state variable. f_0, σ, v^* and d_c are constant friction coefficient, normal stress, typical slip rate and critical slip for state evolution respectively. $a(x)$ and $b(x)$ are the rate-and-state friction parameters that might vary along the fault. The evolution of the state variable is given by the ageing law:

$$\dot{\theta}(x, t) = 1 - \frac{v\theta}{d_c}(x, t). \tag{B4}$$

At steady state ($\dot{\theta} = 0$), the frictional stress τ_{ss} is given by

$$\tau_{ss}(x, t) = f_0\sigma + [a(x) - b(x)]\sigma \ln \frac{v(x, t)}{v^*}. \tag{B5}$$

τ_{ss} is either a decreasing (if $a - b < 0$) or increasing (if $a - b > 0$) function of slip rate v, which correspond to VW and VS behaviours, respectively. The stress change associated with wave radiation is approximately given by

$$\tau_{rad}(x, t) = -\eta v(x, t), \tag{B6}$$

where $\eta = \mu/2c_s$ is the radiation damping introduced by Rice (1993), c_s being the shear wave speed of the elastic medium. Taking the time derivative of the stress balance (B1), and making use of (B2), (B3), (B4) and (B6), I get

$$\begin{cases} a\sigma \dfrac{\dot{v}}{v} + b\sigma \dfrac{\dot{\theta}}{\theta} = \dot{\tau}_b - \dfrac{\mu}{2}\mathcal{H}[v'] - \eta\dot{v} \\ \dot{\theta} = 1 - \dfrac{v\theta}{d_c}. \end{cases} \tag{B7}$$

Assuming a_0 and b_0 are the spatial averages of $a(x)$ and $b(x)$, I next define the following non-dimensional quantities:

$$\begin{cases} \tilde{t} = \dfrac{tv^*}{d_c}, \ (\tilde{x}, \tilde{L}) = \dfrac{(x, L)b_0\sigma}{\mu d_c} \\ \tilde{a}(\tilde{x}) = \dfrac{a(x)}{a_0}, \ \tilde{b}(\tilde{x}) = \dfrac{b(x)}{b_0} \\ \tilde{v}(\tilde{x}, \tilde{t}) = \dfrac{v(x, t)}{v^*}, \ \tilde{\theta}(\tilde{x}, \tilde{t}) = \dfrac{\theta(x, t)v^*}{d_c}, \ \tilde{\tau}_b(\tilde{x}, \tilde{t}) = \dfrac{\tau_b(x, t)}{b_0\sigma}, \end{cases} \tag{B8}$$

where the tildes indicate non-dimensional variables. Typical values of the different parameters are reported and commented in Table B1.

Table B1. List of typical mechanical parameters, and computational parameters.

Physical Parameter	Value	Comment
f_0	0.6	Typical friction coefficient (Marone 1998)
v^*	10^{-9} m s^{-1}	Typical relative plate motion or creep rate on tectonic faults
d_c	10^{-2} mm	In the laboratory (Marone 1998)
b_0	5×10^{-3}	In the laboratory (Marone 1998)
μ	30 GPa	Typical for rocks
σ	100 MPa	Approximate lithostatic stress at 3 km depth
c_s	3 km s^{-1}	Typical shear wave speed for rocks
$\dot{\tau}_b$	5.10^{-4} Pa s^{-1}	Typical tectonic stressing rate on faults
Computational parameters	**Value**	**Comment**
n	2^{13}	Number of computational points
h	0.03 m	Computational cell size
L	245.73 m	Fault length (Magnitude $\sim$3 event)

Table B2. List of characteristic scales and non-dimensional parameters.

Characteristic Scales	Value	Comment
$L_{b0} = \mu d_c / b_0 \sigma$	0.6 m	Typical length used for distance normalization
L_n	see Figs 3(d) and D3(a)	Typical nucleation patch size
T_n	see Fig. 3(d)	Typical log duration of the nucleation process
L_w / L_{b0}	eq. (C1)	Local critical nucleation length
L_h / L_{b0}	eq. (C2)	homogenized critical nucleation length
$t_w v^* / d_c$	eq. (C1)	Local nucleation duration
$t_h v^* / d_c$	eq. (C2)	homogenized nucleation duration
Non-dimensional parameters	**value**	**comment**
$\dot{\tilde{\tau}}_b = \dot{\tau}_b d_c / b_0 \sigma v^*$	10^{-5}	Normalized far-field stressing rate
$\beta = \mu v^* / 2 c_s b_0 \sigma$	10^{-8}	Normalized damping parameter
$\tilde{v}_d = v_d / v^*$	10^7	Normalized radiative slip rate
λ / L_{b0}	from 0.4 to 51.2	Normalized wavelength of heterogeneity
$\alpha = a_0 / b_0$	from 0.2 to 0.9	Ratio of averaged frictional parameters
f	from 0.1 to 0.9	Amplitude factor for the b parameter heterogeneity

The dynamical system (B7) becomes (after removing the tildes for simplicity):

$$\begin{cases} \alpha a \dfrac{\dot{v}}{v} + b \dfrac{\dot{\theta}}{\theta} = \dot{\tau}_b - \dfrac{1}{2}\mathcal{H}\left[v'\right] - \beta \dot{v} \\ \dfrac{\dot{\theta}}{\theta} = \dfrac{1}{\theta} - v, \end{cases} \qquad (B9)$$

where $\alpha = a_0/b_0$, $\beta = \eta v^*/b_0\sigma$. Considering the typical values of Table B1, I will assume in the whole study $\beta = 10^{-8}$ and $\dot{\tau}_b = 10^{-5}$. Note that ageing law (B4) has been divided by θ in order to simplify further developments.

From a set of parameters α, $a(x)$, $b(x)$, and the definition of initial conditions $v(x, 0)$ and $\theta(x, 0)$, the system (B9) is solved numerically using a standard finite difference approach (fourth-order Runge–Kutta algorithm with adaptive time stepping). This requires the evaluation of the Hilbert transform of the slip rate gradient at each time step, which is performed with the method proposed by Cochard & Rice (1997) for finite faults. This also requires the discretization of the fault segment in a set of n equal computational cells of size h. In order to ensure continuity, I choose h to be much smaller than the minimum size of a process zone on the fault segment. From Rubin & Ampuero (2005) and Ampuero & Rubin (2008), this condition is respected if $h < 0.1 \min(L_b)$, $L_b = \mu d_c / b\sigma$. All the results presented here were obtained with $h b_0 \sigma / \mu d_c = 0.05$, which is sufficient to ensure continuity. The computational parameters, and the range of non-dimensional parameters studied here are summarized in Tables B1 and B2.

In this study an earthquake is defined as a slip event on the fault occurring with a high enough slip rate, that is, larger than the dynamical slip rate v_d. Following Rubin & Ampuero (2005), v_d could be interpreted as the minimum slip rate where wave radiation dominates over the direct effect of the friction law, that is when $\dot{\tau}_{rad}$ dominates over the $a\sigma\dot{v}/v$ term of $\dot{\tau}_f$. From eqs (B3) and (B6), $v_d/v^* \simeq \alpha/\beta$. With the present choice of parameters, this value lies between 10^7 and 10^8. I will assume in my applications $v_d/v^* = 10^7$, which corresponds to $v_d \simeq 0.01$ m s^{-1} considering the value of v^* provided in Table B1.

APPENDIX C: NUCLEATION ON A HOMOGENEOUS FAULT, MAIN FEATURES

In this section, all the variables are non-dimensional variables defined from the rules (B8). Earlier work by Dieterich (1992), Rubin & Ampuero (2005), Ampuero & Rubin (2008) Viesca (2016a) and Viesca (2016b) has considered nucleation of slip instabilities under constant frictional properties (i.e. with constants $a(x) = 1$, $b(x) = 1$). In general, the nucleation of a slip instability consists in a progressive acceleration of slip rate as inverse time to failure, either on a fault patch of fixed length (for small $\alpha = a_0/b_0$), or as an expanding crack (for α close to 1). When a radiative slip rate (v_d) is reached at some point of the fault, the typical size of the accelerating patch (i.e. nucleation length) could be expressed as a simple function of the parameters a_0 and b_0. Similarly, Rubin & Ampuero (2005), Ampuero & Rubin (2008) showed how nucleation duration could scale with a_0 and b_0.
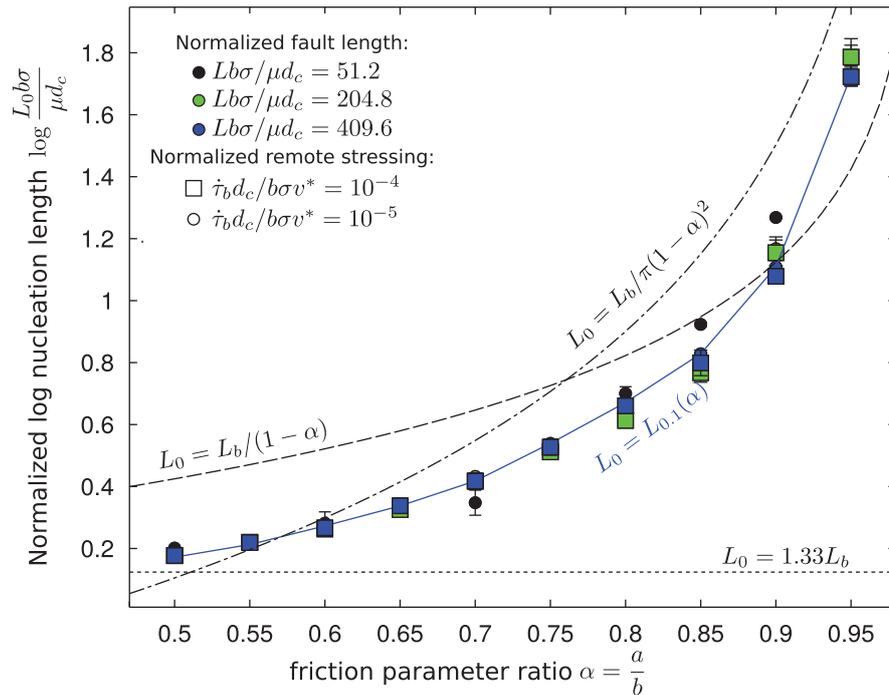
Figure C1. Critical nucleation length for a constant *a* and *b* fault, assuming different fault lengths and different remote stressing rates. Numerical estimates are represented with coloured symbols. The dotted black line corresponds to the fixed length solution of Rubin & Ampuero (2005). The dashed-dotted line corresponds to the approximation proposed by Rubin & Ampuero (2005) for α close to 1. The dashed line is the Ruina (1983) critical length estimate. The solid blue line labelled $L_{0.1}(\alpha)$ is the linear interpolation of the numerical estimates obtained with $Lb\sigma/\mu d_c = 409.6$ and $\dot{\tau}_b d_c / b\sigma v^* = 10^{-5}$ (blue dots).

The fault geometry considered here (Fig. 1a) is different from the infinite periodic fault assumed by Dieterich (1992), Rubin & Ampuero (2005) and Ampuero & Rubin (2008), and from the infinite fault of Viesca (2016a) and Viesca (2016b). Nucleation on a finite fault therefore starts with different initial conditions than what was assumed in these previous studies. Since nucleation is sensitive to initial conditions (at least for *a/b* close to one) (Rubin & Ampuero 2005), nucleation characteristics (duration, critical length) may be different in the fault model considered here. I conducted a few tests with the fault model depicted in Fig. 1(a), assuming $a(x) = 1$ and $b(x) = 1$. For different values of α, different fault sizes *L* and different remote stressing rates $\dot{\tau}_b$, I estimated first the nucleation duration, then the critical nucleation half-length L_0 as half the distance between peak shear stresses when slip rate reaches the dynamical threshold v_d. In all cases, the nucleation duration was consistent with Rubin & Ampuero (2005) approximation. Furthermore, for $\alpha < 0.5$, the constant length of Rubin & Ampuero (2005) is a good approximation to L_0. For larger α, L_0 values reported in Fig. C1 neither follow the $(1-\alpha)^{-2}$ asymptote proposed by Rubin & Ampuero (2005), nor the $(1-\alpha)^{-1}$ one expected from Ruina (1983). In the following, I will therefore consider the numerical estimate $L_{0.1}(\alpha)$ as the relevant reference critical nucleation half-length under homogeneous frictional conditions. The functional $L_{0.1}(\alpha)$ is a linear interpolation (the blue solid line in Fig. C1) of the L_0 values obtained with $Lb\sigma/\mu d_c = 409.6$ and $\dot{\tau}_b d_c / b\sigma v^* = 10^{-5}$. $L_{0.1}$ could be regarded as the critical nucleation half-length expected for the homogeneous equivalent of the heterogeneous fault studied here, when $\alpha > 0.5$.

These results about nucleation length under constant *a* and *b* are used here to characterize the behaviour of a single VW patch. Let L_w be the typical nucleation length of a VW patch. In the following I will use the Rubin & Ampuero (2005) approximation for L_w when $\alpha < 0.5$, and for α close to one L_w will be evaluated

numerically by $L_{0.1}$. Based on this rule, the nucleation length L_w for velocity weakening patches defined by $b_w = b_0 + \Delta b$ depends on $a_0/b_w = \alpha/(2 - \alpha + f\alpha)$ as

$$L_w = \begin{cases} \dfrac{1.33}{2 - \alpha + f\alpha} & \text{if } \dfrac{\alpha}{2 - \alpha + f\alpha} < 0.5, \\[2mm] & \text{that is, } \alpha < \dfrac{2}{3 - f} \\[3mm] L_{0.1}\left(\dfrac{\alpha}{2 - \alpha + f\alpha}\right) & \text{if } \alpha > \dfrac{2}{3 - f}. \end{cases} \quad \text{(C1)}$$

Recall that L_w and $L_{0.1}$ are normalized lengths as defined in (B8). As shown later, I will also consider the so called homogenized nucleation length L_h, which is simply L_w defined with a_0 and b_0. L_h can be obtained from (C1) substituting $b_w = b_0(2 - \alpha + f\alpha)$ by b_0. I have

$$L_h = \begin{cases} 1.33 & \text{if } \alpha < 0.5 \\ L_{0.1}(\alpha) & \text{if } \alpha > 0.5. \end{cases} \quad \text{(C2)}$$

Here again L_h is normalized according to (B8). The second important feature of nucleation when *a* and *b* are constant is the slip rate acceleration as the inverse time to failure. Rubin & Ampuero (2005) and Ampuero & Rubin (2008) show that maximum slip rate v_{max} during nucleation has the form:

$$v_{max} = v_0 \left(1 - \frac{t}{t_n}\right)^{-1}, \quad \text{(C3)}$$

where v_0 is the initial normalized slip rate on the fault, *t* is the normalized time, and t_n the duration of slip rate acceleration. A t_n can be defined locally for a velocity weakening patch. I call it t_w. From Rubin & Ampuero (2005) and Ampuero & Rubin (2008) t_w

depends on α, in a similar manner than L_w does. I have

$$t_w = \frac{1}{v_0}\xi_w, \quad \xi_w = \begin{cases} \dfrac{\alpha}{0.3781(2 - \alpha + f\alpha)} & \text{if} \quad \alpha < \dfrac{2}{3 - f} \\ \dfrac{2}{\pi}\left(1 - \dfrac{\alpha}{2 - \alpha + f\alpha}\right)^{-1} & \text{if} \quad \alpha > \dfrac{2}{3 - f}, \end{cases} \tag{C4}$$

where the condition on α indicates whether a_0/b_w is larger or smaller than 0.5. In the following, I will consider the so called homogenized duration t_h as the value of t_w defined with a_0 and b_0. As for L_h, I make use of eq. (C4) to get

$$t_h = \frac{1}{v_0}\xi_h, \quad \xi_h = \begin{cases} \dfrac{\alpha}{0.3781} & \text{if} \quad \alpha < 0.5 \\ \dfrac{2}{\pi}\dfrac{1}{(1 - \alpha)} & \text{if} \quad \alpha > 0.5. \end{cases} \tag{C5}$$

APPENDIX D: NUCLEATION ON A HETEROGENEOUS FAULT, MAIN FEATURES

D1 Stability of the nucleation crack, transition to dynamic rupture

As shown in Figs 2(b) and D1(a), the nucleation phase consists in the growing of a crack, with slip profiles vanishing outside a fault segment of half-length l. The stress distribution inside the crack is at steady state: it is λ periodic and oscillates between velocity strengthening and velocity weakening steady-state values. The transition to quasi-dynamic rupture could be interpreted as the crossing of a fracture criterion leading to rapid expansion of the nucleation crack. Let assume that the fracture criterion is reached when the stress intensity factor K of the crack exceeds a critical value K_c [Irwin's criterion (Lawn 1993)].

In the following, I assume that the nucleation consists in the approximate finite crack Γ depicted in Fig. D1(c). Γ has a half-length l. Since I am interested in the crack behaviour at the transition to quasi-dynamic rupture, I will assume that slip rate inside the crack is approximately given by v_d. However, this choice is not of primarily importance as shown below. From the stress profile in Fig. D1(b), I assume a shear stress drop $\Delta\tau$ within Γ of the form:

$$\Delta\tau(x) = [b(x) - a_0]\sigma \ln v_d/v^*, \text{ for } |x| < l. \tag{D1}$$

The distribution $b(x)$ is given by eqs (1) and (2). From Rice (1979), the corresponding stress intensity factor K at the right tip of the crack ($x = l$) is

$$K = \frac{1}{\sqrt{\pi l}}\int_{-l}^{+l}\sqrt{\frac{l + x}{l - x}}\Delta\tau(x)\mathrm{d}x. \tag{D2}$$

Making use of eqs (D1), (1) and (D2), the stress intensity factor K could be expressed as

$$K(z) = K^*\sqrt{\frac{\tilde{\lambda}}{\pi}}\left[(1 - \alpha)\pi\sqrt{z} + \frac{\Delta b}{b_0}\frac{F(z)}{\sqrt{z}}\right], \tag{D3}$$

where $K^* = \sqrt{\mu b_0\sigma d_c}\ln v_d/v^*$, $z = l/\lambda > 0$, $\tilde{\lambda} = \lambda b_0\sigma/\mu d_c$. The functional F is given by

$$F(z) = \int_{-z}^{+z}\tilde{\phi}(u)g(z, u)\mathrm{d}u, \tag{D4}$$

where $u = x/\lambda$, $\tilde{\phi}(u) = \phi(x)$ and the weight function $g(z, u) = \sqrt{z + u}/\sqrt{z - u}$. The functional F could be evaluated numerically.

However, I will use two different approximations of this integral: first when the crack involves only one velocity weakening patch and its two immediate velocity strengthening neighbours (i.e. at $z = z_0 = 3/4$), then when the crack is large enough (i.e. $z > > 1$), and its tip is situated at the end of a velocity strengthening patch (i.e. if $z = z_{sw} = 3/4 + m$, m being an integer).

At $z = z_0$, F could be rewritten as:

$$F(z_0) = -\int_{-z_0}^{-1/4}g(z_0, u)\mathrm{d}u + \int_{-1/4}^{+1/4}g(z_0, u)\mathrm{d}u \\ - \int_{1/4}^{z_0}g(z_0, u)\mathrm{d}u. \tag{D5}$$

These two integrals could be written explicitly so that

$$F(z_0) = 3\arctan\frac{1}{2\sqrt{2}} - \frac{3}{4}\pi \simeq 1 - \frac{3\pi}{4}, \tag{D6}$$

which is negative. The stress intensity factor K_0 at z_0 is therefore given by

$$K_0 = K^*\sqrt{\frac{\tilde{\lambda}}{\pi}}\left[(1 - \alpha)\pi\sqrt{\frac{3}{4}} - \frac{\Delta b}{b_0}c_0\right], \tag{D7}$$

where $c_0 = -2F(z_0)/\sqrt{3} \simeq \sqrt{3}\pi/2 - 2/\sqrt{3}$.

At $z = z_{sw}$, F could be rewritten as:

$$F(z_{sw}) = \sum_{i=1}^{n}\left(\int_{u_i-1/2}^{u_i+1/2}\tilde{\phi}(u)g(z_{sw}, u)\mathrm{d}u\right) - \int_{z_{sw}-1/2}^{z_{sw}}g(z_{sw}, u)\mathrm{d}u \tag{D8}$$

$$= \sum_{i=1}^{n}\left(\int_{u_i}^{u_i+1/2}g(z_{sw}, u)\mathrm{d}u - \int_{u_i-1/2}^{u_i}g(z_{sw}, u)\mathrm{d}u\right) \\ - \int_{z_{sw}-1/2}^{z_{sw}}g(z_{sw}, u)\mathrm{d}u, \tag{D9}$$

where $u_i = i - 1/2 - z_{sw}$ and $n = 2m + 1$. For $z_{sw} > > 1$, $g(z_{sw}, u)$ could be approximated by its Taylor expansion around u_i. Noting $s = u - u_i$, this leads to

$$g(z_{sw}, u) = g(z_{sw}, u_i) + sg'(z_{sw}, u_i) + \frac{s^2}{2}g''(z_{sw}, u_i) + \mathcal{O}(s^3). \tag{D10}$$

Eliminating terms of order $\mathcal{O}(s^3)$, I get

$$F(z_{sw}) = \sum_{i=1}^{n}2g'(z_{sw}, u_i)\left(\int_0^{1/2}s\mathrm{d}s\right) - \int_{z_{sw}-1/2}^{z_{sw}}g(z_{sw}, u)\mathrm{d}u \tag{D11}$$

$$= \frac{1}{4}\sum_{i=1}^{n}g'(z_{sw}, u_i) - \int_{z_{sw}-1/2}^{z_{sw}}g(z_{sw}, u)\mathrm{d}u. \tag{D12}$$

The sum could be approximated by the integral of g' from $-z_{sw}$ to $z_{sw} - 1/2$, which is equal to $g(z_{sw}, z_{sw} - 1/2) - g(z_{sw}, -z_{sw})$. Since $g(z_{sw}, -z_{sw}) = 0$, I get

$$F(z_{sw}) = \frac{1}{4}\sqrt{4z_{sw} - 1} - \int_{z_{sw}-1/2}^{z_{sw}}g(z_{sw}, u)\mathrm{d}u. \tag{D13}$$

The last integral term could be approximated for $z_{sw} \gg 1$ as follows:

$$\int_{z_{sw}-1/2}^{z_{sw}}g(z_{sw}, u)\mathrm{d}u \simeq \sqrt{2z_{sw}}\int_{z_{sw}-1/2}^{z_{sw}}\frac{\mathrm{d}u}{\sqrt{z_{sw} - u}} \simeq 2\sqrt{z_{sw}}. \tag{D14}$$
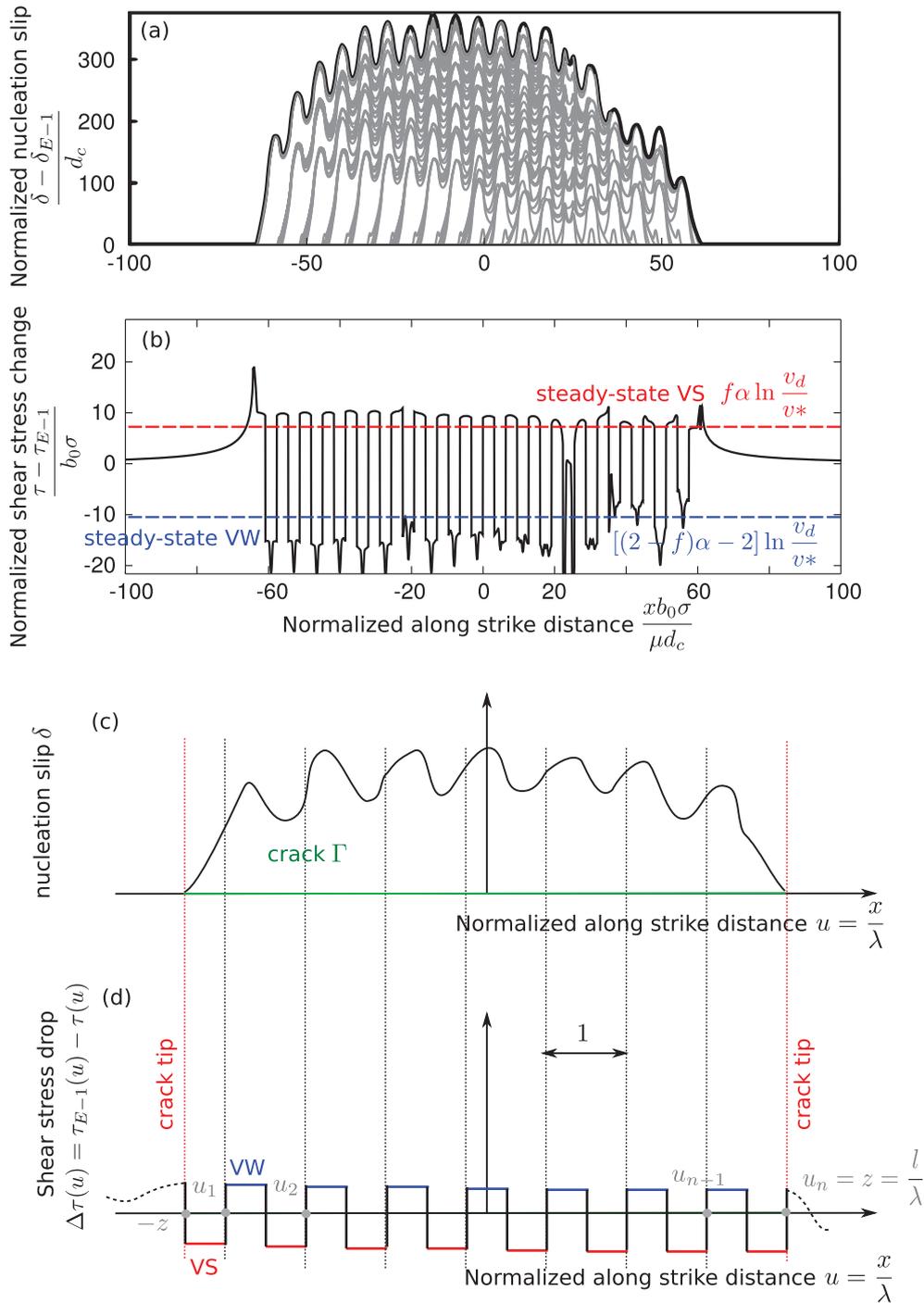
Figure D1. Typical slip and shear stress during nucleation in regime (IV). (a) Nucleation slip profiles (δ_{E-1} is the cumulative slip at the end of main-shock $E-1$). One grey profile is represented at the onset and at the end of each foreshock. The black profile corresponds to the onset of main-shock E. (b) Shear stress profile at the onset of main-shock E (corresponds to the black profile in panel a). (c) Approximate crack-like slip profile Γ at the onset of main-shock E (approximation of the black profile in panel a). (d) Approximate shear stress change within the crack Γ (approximation of shear stress in panel b). In (c) and (d), u is the along strike distance normalized by the wavelength of heterogeneity. $u_1, u_2,..., u_{n-1}$ and u_n are coordinates used in the developments of Appendix D1. VW and VS segments indicate velocity weakening and velocity strengthening segments respectively. l is the half-length of the approximate crack Γ. Results in (a) and (b) were obtained with $\alpha = 0.9, f = 0.5$ and $\lambda = 6.4$ ($\rho_w = 1.04$).

We end up with

$$F(z_{\text{sw}}) \simeq \frac{1}{4}\sqrt{4z_{\text{sw}} - 1} - 2\sqrt{z_{\text{sw}}} \simeq -\frac{3}{2}\sqrt{z_{\text{sw}}}. \tag{D15}$$

The stress intensity factor K_m at these strengthening to weakening transitions is therefore approximated by

$$K_m(z_{\text{sw}}) = K^* \sqrt{\frac{\tilde{\lambda}}{\pi}} \left[(1-\alpha)\pi\sqrt{z_{\text{sw}}} - \frac{3}{2}\frac{\Delta b}{b_0} \right]. \tag{D16}$$

The critical stress intensity factor K_c could be defined from the fracture energy $G_c(l)$ at the crack tip:

$$K_c = \sqrt{2\mu G_c(l)}, \tag{D17}$$

μ being the shear modulus of the elastic medium. As proposed by Rubin & Ampuero (2005), the fracture energy could be approximated by

$$G_c(l) = \frac{b(l)\sigma d_c}{2}\left(\ln v_d/v^*\right)^2, \tag{D18}$$

where $b(l)$ is given by (1) at $x = l$. Using the same normalization as for K, I end up with:

$$K_c(z) = K^*\sqrt{1 + \frac{\Delta b}{b_0}\tilde{\phi}(z)}. \tag{D19}$$

At $z = z_{sw}$, I have

$$K_c(z_{sw}) = K^*\sqrt{1 - \frac{\Delta b}{b_0}}. \tag{D20}$$

The numerical evaluation of the stress intensity factor K (eq. D3) is represented in Fig. D2 along with its approximation K_m (eq. D16), and the critical stress intensity factor K_c (eq. D19). The global increase in K with the crack length is modulated by a variation at the typical length-scale λ: K is successively increasing then decreasing as the crack tip goes through a velocity weakening and a velocity strengthening region. In this framework, unstable crack growth (i.e. quasi-dynamic rupture) occurs when z is large enough so that K remains larger than K_c at the end of a velocity strengthening patch. However, when $K < K_c$ crack expansion may occur but at a slower rate, because of local self-driven destabilizations on VW patches at the edges of the crack. The inset of Fig. D2 illustrates the transition from quasi-static crack growth to quasi-dynamic rupture.

D2 Condition for foreshock sequence

In this framework, a foreshock sequence occurs if K_0 is smaller than $K_c(z_0)$. From eqs (D7) and (D20), this condition becomes

$$\sqrt{\frac{\tilde{\lambda}}{\pi}}\left[(1-\alpha)\pi\frac{\sqrt{3}}{2} - c_0\frac{\Delta b}{b_0}\right] < \sqrt{1 - \frac{\Delta b}{b_0}}. \tag{D21}$$

(D21) is always satisfied as long as the bracket term on the left-hand side is negative, which occurs when $\alpha > \alpha_c$ given by

$$\alpha_c = \left[1 + f\left(\frac{3\pi}{4} - 1\right)\right]^{-1}, \tag{D22}$$

where I have used the definition of $\Delta b/b_0$. α_c is approximately 0.88, 0.6 and 0.45 for $f = 0.1$, $f = 0.5$ and $f = 0.9$. If $\alpha < \alpha_c$, foreshock sequence occur if $\tilde{\lambda}$ is smaller than the critical value $\tilde{\lambda}_c$ defined by

$$\tilde{\lambda}_c = \frac{3\pi}{4}\frac{(1-f)\alpha}{(1 - \alpha/\alpha_c)^2}. \tag{D23}$$

From eqs (D23) and (C1), one can define the critical ρ_w parameter $\rho_c = \tilde{\lambda}_c/4\tilde{L}_w$. This leads to

$$\rho_c = \frac{3\pi}{16}\frac{(1-f)\alpha}{\tilde{L}_w(\alpha)(1 - \alpha/\alpha_c)^2}, \tag{D24}$$

where $\tilde{L}_w(\alpha) = L_w(\alpha)b_0\sigma/\mu d_c$.

D3 Background slip-rate evolution

This section is dedicated to the equations controlling the background slip acceleration during nucleation under regimes (I), (II) and (IV),

that is when more than a single VW patch is involved. All the quantities used in the remaining text are non-dimensional as defined by eq. (B8). Let L_n be the typical nucleation patch size under such conditions. By definition, $L_n > \lambda$. Let t_n be an order of magnitude of the nucleation duration. For $t < t_f$, it is convenient to use the substitution:

$$\begin{cases} T = \ln\left(t_f - t\right)/T_n \\ X = \dfrac{x}{L_n} \\ \tilde{v}(X, T) = v(x, t),\ \tilde{\theta}(X, T) = \theta(x, t) \\ \tilde{a}(X) = a(x),\ \tilde{b}(X) = b(x), \end{cases} \tag{D25}$$

where $T_n = \ln(t_f - t_n)$ is the logarithmic duration of the nucleation. The system (B9) becomes (after removing the tildes for simplicity):

$$\begin{cases} \alpha a\dfrac{\dot{v}}{v} + b\dfrac{\dot{\theta}}{\theta} = \dot{\tau}_b + \dfrac{T_n e^{T_n T}}{2L_n}\mathcal{H}\left[v'\right] - \beta\dot{v} \\ \dfrac{\dot{\theta}}{\theta}\dfrac{e^{-T_n T}}{T_n} = v - \dfrac{1}{\theta}. \end{cases} \tag{D26}$$

D3.1 Regimes (I) and (II) ($\rho_w < 0.5$)

When $\rho_w < 0.5$, each VW patch is too small to rupture individually. The nucleation of the main-shock therefore occurs without foreshocks. Since $\lambda < < L_n$ I will consider λ as a small positive number compared to the typical wavelength I am interested in, and I note $\varepsilon = \lambda/L_n$. a and b are ε periodic, with $\overline{a}^\varepsilon(X) = \overline{b}^\varepsilon(X) = 1$. In the numerical solution (Figs 4 and D3a) v and $1/\theta$ consist in a background evolution localized around the typical wavelength L_n and a small amplitude fluctuation of typical wavelength λ. This suggest the following decomposition:

$$\begin{cases} v(X, T) = v_0(X, T)\left[1 + \varphi(Y, T)\right] \\ \theta(X, T) = \theta_0(X, T)\left[1 + \vartheta(Y, T)\right]^{-1}, \end{cases} \tag{D27}$$

where $Y = X/\varepsilon$, v_0 and θ_0 describe the background large scale evolution, and φ and ϑ are the fluctuations of v and $1/\theta$. The frictional parameters could be written as $a(Y)$ and $b(Y)$. The functional $a(Y)$ and $b(Y)$ are periodic in Y, and verify:

$$\overline{a}(Y) = \overline{b}(Y) = 1. \tag{D28}$$

As shown in Figs 4 and D3(a), when a moving average is applied to v and $1/\theta$, the fluctuation of $\overline{v}^\varepsilon$ and $\overline{1/\theta}^\varepsilon$ are reduced in amplitude. From expressions (A3) and (D27), I have

$$\begin{cases} \overline{v}^\varepsilon(X, T) = v_0(X, T)\left[1 + \overline{\varphi}(Y, T)\right] \\ \overline{\dfrac{1}{\theta}}^\varepsilon(X, T) = \dfrac{1}{\theta_0}(X, T)\left[1 + \overline{\vartheta}(Y, T)\right]. \end{cases} \tag{D29}$$

Applying a second moving average leads to the same equations, where the over-bar is replaced by a double overbar. However, the amplitude of the fluctuation is not further reduced by this second operation (Fig. D3a). To quantify this, I plot in Fig. D3(b) the amplitudes A of the variable fluctuations as a function of ε. As illustrated in Fig. D3(a), for a given fault segment of length ε centred on X_0, I define the local amplitude $a_\varphi(X_0, T)$ of the variable φ from the extreme values v^+ and v^- of v on this segment, so that

$$\begin{cases} v^+ = v_0(X_0, T)\left[1 + a_\varphi(X_0, T)\right] \\ v^- = v_0(X_0, T)\left[1 - a_\varphi(X_0, T)\right], \end{cases} \tag{D30}$$
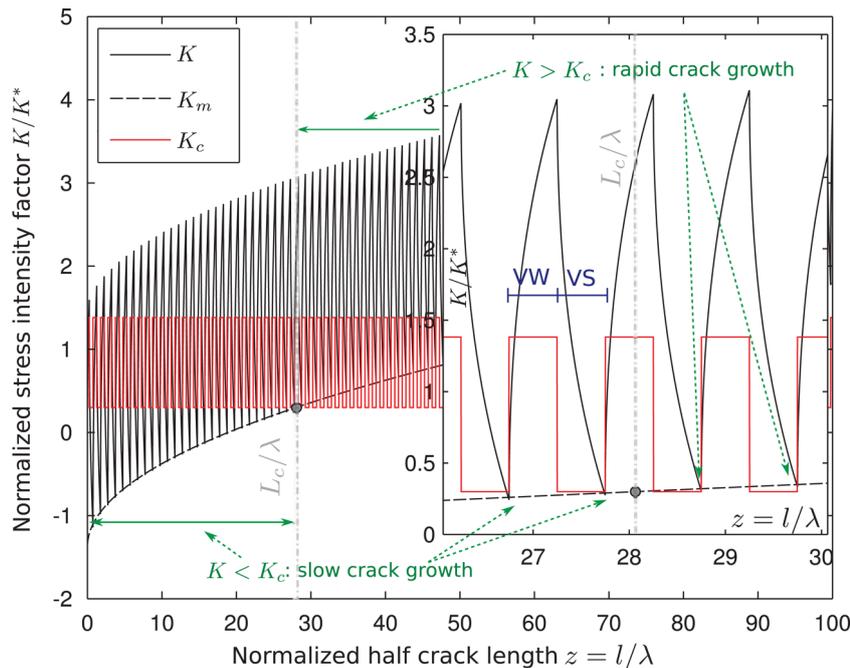
Figure D2. Nucleation crack energy balance. Numerically computed stress intensity factor K (eq. D3) at the right tip of the approximate crack Γ depicted in Fig. D1(c) (black solid line), critical stress intensity factor K_c (red solid line, eq. D19), and stress intensity factor approximation K_m (black dashed line, eq. D16). The inset shows the crack behaviour around the critical value L_c/λ, L_c being the critical half-length of Γ. K^* is defined in Appendix D1. Blue line indicates the position of a velocity weakening (VW) and velocity strengthening (VS) patch. Results were obtained for $\alpha = 0.9, f = 0.9, \lambda b_0 \sigma / \mu d_c = 3.2$.

where I assume that v_0 is approximately constant between $X_0 - \varepsilon/2$ and $X_0 + \varepsilon/2$. I therefore have

$$a_\varphi(X_0, T) = \frac{v^+ - v^-}{v^+ + v^-}(X_0, T). \tag{D31}$$

A_φ is then the average value of a_φ taken over the fault length and the whole nucleation process. Similarly, I define A_ϑ from the extremal values of $1/\theta$ taken on a collection of segments of length ε. $A_{\overline{\varphi}}$, $A_{\overline{\vartheta}}$, $A_{\overline{\overline{\varphi}}}$ and $A_{\overline{\overline{\vartheta}}}$ are defined in the same way from $\overline{v}$, $\overline{\overline{v}}$, $\overline{1/\theta}$ and $\overline{\overline{1/\theta}}$. From Figs D3(b) and (c), while $A_\varphi \sim A_\vartheta \sim 1$, I generally have $A_{\overline{\varphi}}, A_{\overline{\vartheta}}, A_{\overline{\overline{\varphi}}}, A_{\overline{\overline{\vartheta}}} < \varepsilon$. I will therefore assume the following property:

$$\begin{cases} \varphi, \vartheta = \mathcal{O}(1) \\ \overline{\varphi}, \overline{\vartheta}, \overline{\overline{\varphi}}, \overline{\overline{\vartheta}} = \mathcal{O}(\varepsilon). \end{cases} \tag{D32}$$

The second important property of φ and ϑ concerns their growth rate. From expansion (D27), I have

$$\begin{cases} \dfrac{\dot{v}}{v} = \dfrac{\dot{v}_0}{v_0} + \dfrac{\dot{\varphi}}{1+\varphi} \\ \dfrac{\dot{\theta}}{\theta} = \dfrac{\dot{\theta}_0}{\theta_0} + \dfrac{\dot{\vartheta}}{1+\vartheta}. \end{cases} \tag{D33}$$

Between instants T_1 and T_2, the ratio between the two right hand terms of the first equation can be approximated by

$$\frac{|\dot{\varphi}/(1+\varphi)|}{|\dot{v}_0/v_0|}(X, T_1) \sim r_\varphi(X, T_1)$$

$$= \frac{\ln\{[1 + \varphi(X, T_2)] / [1 + \varphi(X, T_1)]\}}{\ln [v_0(X, T_2)/v_0(X, T_1)]}. \tag{D34}$$

To the order ε^0, I have from property (D32) $\overline{v}^\varepsilon \simeq v_0$, so that $1 + \varphi = v/\overline{v}^\varepsilon$. The local growth rate ratio r_φ is therefore given by

$$r_\varphi(X, T_1) = \frac{\ln v(X, T_2)\overline{v}^\varepsilon(X, T_1)/v(X, T_1)\overline{v}^\varepsilon(X, T_2)}{\ln \overline{v}^\varepsilon(X, T_2)/\overline{v}^\varepsilon(X, T_1)}. \tag{D35}$$

I then define R_φ as the average value of r_φ over the fault length and over T. R_ϑ is defined similarly from $1/\theta$ and $\overline{1/\theta}^\varepsilon$. R_φ and R_ϑ, when plotted against ε in Figs D3(d) and (e), align approximately along the $R = \varepsilon$ line, so that I will assume in the following that:

$$\begin{cases} \dfrac{\dot{v}_0}{v_0}, \dfrac{\dot{\theta}_0}{\theta_0} = \mathcal{O}(1) \\ \dfrac{\dot{\varphi}}{1+\varphi}, \dfrac{\dot{\vartheta}}{1+\vartheta} = \mathcal{O}(\varepsilon). \end{cases} \tag{D36}$$

Assuming (D27), the system (D26) becomes

$$\begin{cases} \alpha a \left[\dfrac{\dot{v}_0}{v_0} + \dfrac{\dot{\varphi}}{1+\varphi}\right] + b\left[\dfrac{\dot{\theta}_0}{\theta_0} + \dfrac{\dot{\vartheta}}{1+\vartheta}\right] = \dot{\tau}_b + \dfrac{T_n e^{T_n T}}{2L_n}\left\{\mathcal{H}\left[v'_0\right] \right. \\ \left. + \mathcal{H}\left[v'_0\varphi\right] + \dfrac{1}{\varepsilon}\mathcal{H}\left[v_0\varphi'\right]\right\} - \beta\dot{v}_0 - \beta(\dot{v}_0\varphi + v_0\dot{\varphi}) \\ \dfrac{\dot{\theta}_0}{\theta_0} + \dfrac{\dot{\vartheta}}{1+\vartheta} = T_n e^{T_n T}\left[v_0(1+\varphi) - \dfrac{(1+\vartheta)}{\theta_0}\right]. \end{cases} \tag{D37}$$

The use of property (D36) allows to remove $\mathcal{O}(\varepsilon)$ terms, and I end up with

$$\begin{cases} \alpha a \dfrac{\dot{v}_0}{v_0} + b\dfrac{\dot{\theta}_0}{\theta_0} = \dot{\tau}_b + \dfrac{T_n e^{T_n T}}{2L_n}\left\{\mathcal{H}\left[v'_0\right] + \mathcal{H}\left[v'_0\varphi\right] + \dfrac{1}{\varepsilon}\mathcal{H}\left[v_0\varphi'\right]\right\} \\ \quad - \beta\dot{v}_0 - \beta(\dot{v}_0\varphi + v_0\dot{\varphi}) \\ \dfrac{\dot{\theta}_0}{\theta_0} = T_n e^{T_n T}\left[v_0(1+\varphi) - \dfrac{(1+\vartheta)}{\theta_0}\right]. \end{cases} \tag{D38}$$
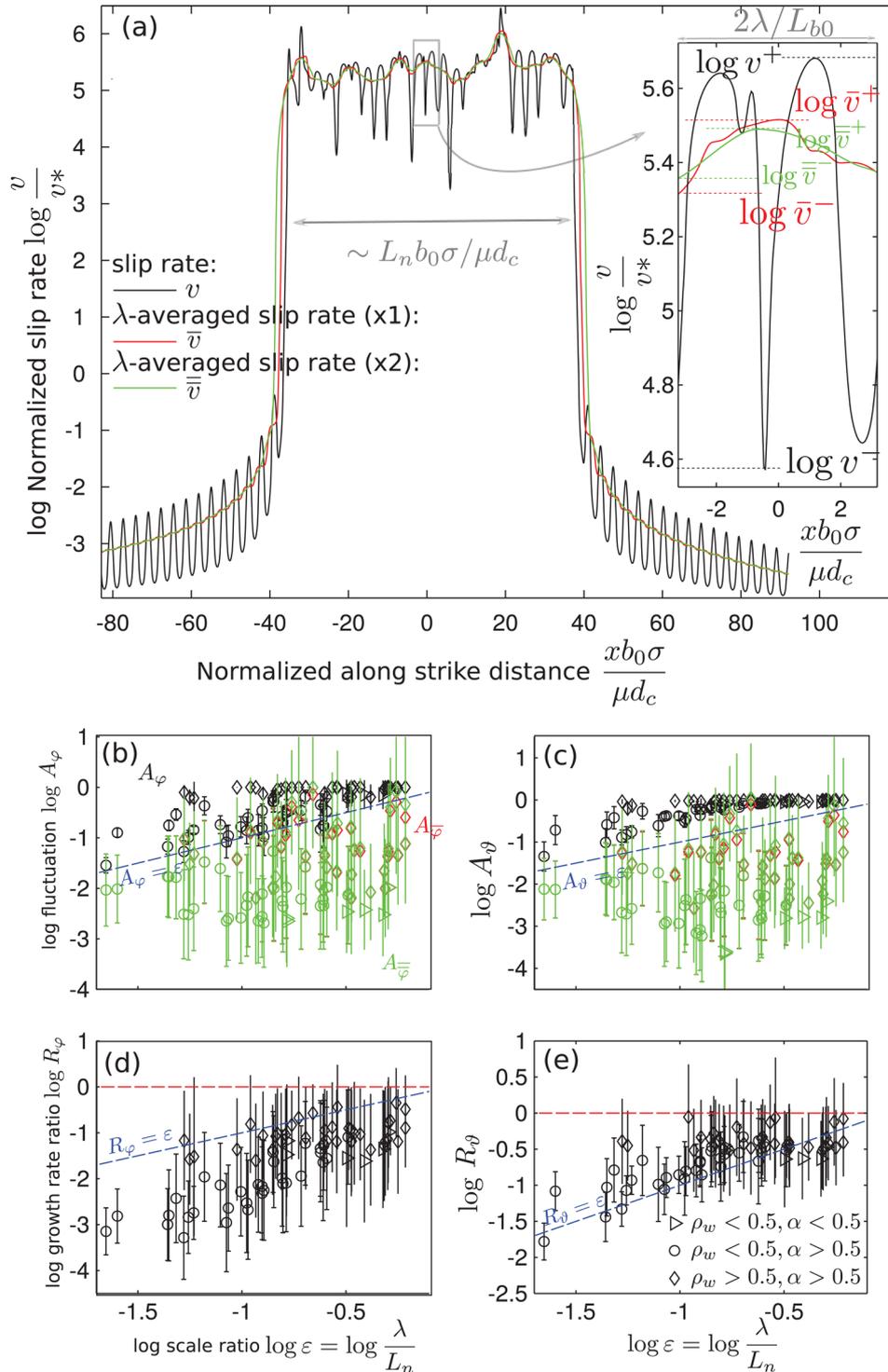
Figure D3. Short wavelength fluctuation of slip rate and state variable during nucleation under regimes (I), (II) and (IV). (a) Typical slip rate and λ averaged slip rate profiles. Results correspond to $\alpha = 0.9$, $f = 0.5$ and $\rho_w = 1.04$. The inset indicates the behaviour over a period λ. (b,c) Statistics of fluctuation amplitude for slip rate (b) and state variable (c). Symbols are colour-coded in the same manner as in panel (a). (d,e) Ratio between fluctuation growth rate and background growth rate. Symbol type in panels (b)–(e) indicates the nucleation regime, blue dashed lines correspond to order ε quantities and horizontal red lines to order 1 quantities. The precise definition of A_φ, A_ϑ, R_φ and R_ϑ are given in Appendix D3.

Taking two successive moving averages of the first equation, the second Hilbert transform term gives

$$\overline{\overline{\mathcal{H}\left[v_0'\varphi\right]}}^{\varepsilon} = \mathcal{H}\left[\overline{\overline{v_0'\varphi}}^{\varepsilon}\right] = \mathcal{H}\left[v_0'\overline{\overline{\varphi}}\right], \tag{D39}$$

and the third Hilbert transform term becomes

$$\overline{\overline{\mathcal{H}\left[v_0\varphi'\right]}}^{\varepsilon} = \mathcal{H}\left[\overline{\overline{v_0\varphi'}}^{\varepsilon}\right] = \mathcal{H}\left[v_0\overline{\overline{\varphi}}'\right], \tag{D40}$$

where I have used successively the commutativity and associativity of the convolution product along with property (A3). After making

use of (D28), (D32) and keeping the $\mathcal{O}(\varepsilon^0)$ terms, I end up with the following dynamical system:

$$\begin{cases} \alpha \dfrac{\dot{v}_0}{v_0} + \dfrac{\dot{\theta}_0}{\theta_0} = \dot{\tau}_b + \dfrac{T_n e^{T_n T}}{2L_n} \mathcal{H}\left[v_0'\right] - \beta \dot{v}_0 \\[2ex] \dfrac{\dot{\theta}_0}{\theta_0} = T_n e^{T_n T}\left[v_0 - \dfrac{1}{\theta_0}\right]. \end{cases} \tag{D41}$$

v_0 and θ_0 obey a dynamical system where the main parameters are α, β and $\dot{\tau}_b$. The evolution of the background slip rate v_0 and the background state variable θ_0 are therefore similar to what is expected for a fault with homogeneous frictional properties a_0 and b_0.

D3.2   Regime (IV) ($\rho_c > \rho_w > 0.5$)

The nucleation consists in a background acceleration of slip over the log duration T_n, associated with foreshocks (rupture of single patches). I am interested in the global large scale background acceleration that represents the envelop of the slip rate evolution. For that, I will first estimate and separate the contribution of the foreshocks in the evolution equation.

During foreshocks, v and θ vary over a typical normalized log timescale $T_f \ll T_n$ and over a typical length scale $\lambda \ll L_n$ (Fig. D4). Here I denote $\varepsilon_f = T_f / T_n$, and $\varepsilon_x = \lambda / L_n$ and look for solutions of (D26) in the form:

$$\begin{cases} v(X, T) = V(X, T)\left[1 + \dfrac{1}{\varepsilon_f}\sum_k v_k(Y_k, \mathcal{T}_k)\right] \\[2ex] \theta(X, T) = \Theta(X, T)\left[1 + \dfrac{1}{\varepsilon_f}\sum_k \omega_k(Y_k, \mathcal{T}_k)\right]^{-1}, \end{cases} \tag{D42}$$

where:

$$\begin{cases} Y_k = \dfrac{X - X_k}{\varepsilon_x} \\[2ex] \mathcal{T}_k = \dfrac{T - T_k}{\varepsilon_f}, \end{cases} \tag{D43}$$

(X_k, T_k) being the coordinates of the kth foreshock. In (D. 42), the sum is taken over all the foreshocks. V and Θ are the envelops of v and θ, and v_k and ω_k are positive functions describing the change in v and θ during the kth foreshock. The $1/\varepsilon_f$ factor indicates that v and $1/\theta$ perturbations created by foreshocks have a higher amplitude than V and $1/\Theta$, as shown in Fig. D4. As expected from Fig. D4, v_k and ω_k and their derivatives are non-zero only in the vicinity of (X_k, T_k). From (D. 42), I get:

$$\dfrac{\dot{v}}{v} = \dfrac{\dot{V}}{V} + \dfrac{1}{\varepsilon_f}\left\{\dfrac{\sum_k \dot{v}_k}{\varepsilon_f + \sum_k v_k}\right\}. \tag{D44}$$

v_k, $\dot{v}_k$ and $\dot{v}_k/(\varepsilon_f + v_k)$ are only non-zero in a domain of size $(\varepsilon_x, \varepsilon_f)$ around (X_k, T_k). Because the different foreshocks do not overlap, I have, in the vicinity of (X_j, T_j):

$$\dfrac{\sum_k \dot{v}_k}{\varepsilon_f + \sum_k v_k} = \dfrac{\dot{v}_j(Y_j, \mathcal{T}_j)}{\varepsilon_f + v_j(Y_j, \mathcal{T}_j)} = \sum_k \dfrac{\dot{v}_k}{\varepsilon_f + v_k}. \tag{D45}$$

Since the last equation is valid for any j, I end up with

$$\dfrac{\dot{v}}{v} = \dfrac{\dot{V}}{V} + \dfrac{1}{\varepsilon_f}\sum_k \dfrac{\dot{v}_k}{\varepsilon_f + v_k} \simeq \dfrac{\dot{V}}{V} + \dfrac{1}{\varepsilon_f}\sum_k \dfrac{\dot{v}_k}{v_k}. \tag{D46}$$

Similarly, it is straightforward to show that

$$\dfrac{\dot{\theta}}{\theta} = \dfrac{\dot{\Theta}}{\Theta} + \dfrac{1}{\varepsilon_f}\sum_k \dfrac{\dot{\omega}_k}{\varepsilon_f + \omega_k} \simeq \dfrac{\dot{\Theta}}{\Theta} + \dfrac{1}{\varepsilon_f}\sum_k \dfrac{\dot{\omega}_k}{\omega_k}. \tag{D47}$$

The spatial derivative of v becomes

$$v' = V'\left[1 + \dfrac{1}{\varepsilon_f}\sum_k v_k\right] + \dfrac{1}{\varepsilon_f \varepsilon_x} V \sum_k v_k' \tag{D48}$$

$$\simeq V' + \dfrac{1}{\varepsilon_f}\sum_k V_k' v_k + \dfrac{1}{\varepsilon_f \varepsilon_x}\sum_k V_k v_k', \tag{D49}$$

where $V_k = V(X_k, T_k)$, and $V_k' = V'(X_k, T_k)$. Therefore I can rewrite the elastic interactions as

$$\mathcal{H}\left[v'\right](X, T) \simeq \mathcal{H}\left[V'\right](X, T) + \dfrac{1}{\varepsilon_f}\sum_k V_k' \mathcal{H}\left[v_k\right](Y_k, \mathcal{T}_k)$$
$$+ \dfrac{1}{\varepsilon_f \varepsilon_x}\sum_k V_k \mathcal{H}\left[v_k'\right](Y_k, \mathcal{T}_k), \tag{D50}$$

Similarly, the time derivative of v is given by

$$\dot{v} \simeq \dot{V} + \dfrac{1}{\varepsilon_f}\sum_k \dot{V}_k v_k + \dfrac{1}{\varepsilon_f^2}\sum_k V_k \dot{v}_k, \tag{D51}$$

where $\dot{V}_k = \dot{V}(X_k, T_k)$. When re-injected into (D26), the expansion (D42) therefore leads to the following balance between $\mathcal{O}(\varepsilon_f^0 \varepsilon_x^0)$ terms:

$$\begin{cases} \alpha a \dfrac{\dot{V}}{V} + b \dfrac{\dot{\Theta}}{\Theta} = \dot{\tau}_b + \dfrac{T_n e^{T_n T}}{2L_n} \mathcal{H}\left[V'\right] - \beta \dot{V} \\[2ex] \dfrac{\dot{\Theta}}{\Theta} = T_n e^{T_n T}\left[V - \dfrac{1}{\Theta}\right], \end{cases} \tag{D52}$$

which indicates that V and Θ obey to the first order the dynamical system (D26).

Note that balancing terms of order $\varepsilon_f^{-1}\varepsilon_x^0$ leads to a second system governing the evolution of each v_k and ω_k:

$$\begin{cases} \alpha a_k \dfrac{\dot{v}_k}{v_k} + b_k \dfrac{\dot{\omega}_k}{\omega_k} = \dfrac{T_n e^{T_n T_k}}{2L_n}\sum_k V_k' \mathcal{H}\left[v_k\right] - \beta \dot{V}_k v_k \\[2ex] \dfrac{\dot{\omega}_k}{\omega_k} = T_n e^{T_n T_k}\left[V_k v_k - \dfrac{\omega_k}{\Theta_k}\right], \end{cases} \tag{D53}$$

where $\Theta_k = \Theta(X_k, T_k)$, $a_k = a(X_k)$ and $b_k = b(X_k)$.

In the following, I focus on V and Θ as represented in Fig. 4 (IV), that is the envelops of v and θ which remain after removing the foreshock contribution. From Fig. 4, V and Θ consist in a large scale variation (typical wavelength L_n) plus a short wavelength contribution (typical wavelength λ). Here again, let $\varepsilon = \lambda / L_n$, and let assume the following expansion for V and Θ:

$$\begin{cases} V(X, T) = v_0(X, T)\left[1 + \varphi(Y, T)\right] \\[2ex] \Theta(X, T) = \theta_0(X, T)\left[1 + \vartheta(Y, T)\right]^{-1}, \end{cases} \tag{D54}$$

where $Y = X/\varepsilon$, v_0 and θ_0 represent the large scale evolution of V and Θ, and φ and ϑ the short wavelength fluctuation of V and Θ. As shown in Fig. D3, φ and ϑ also verify properties (D32) and (D36). Therefore, I can follow the derivation developed for regimes (I) and (II) and retrieve the same governing eq. (D41).

Here again, the background evolution is controlled by the parameters α, β and τ_b. The evolution of the background slip rate v_0 and the background state variable θ_0 is once again similar to what is expected for a fault with homogeneous frictional properties a_0 and b_0.
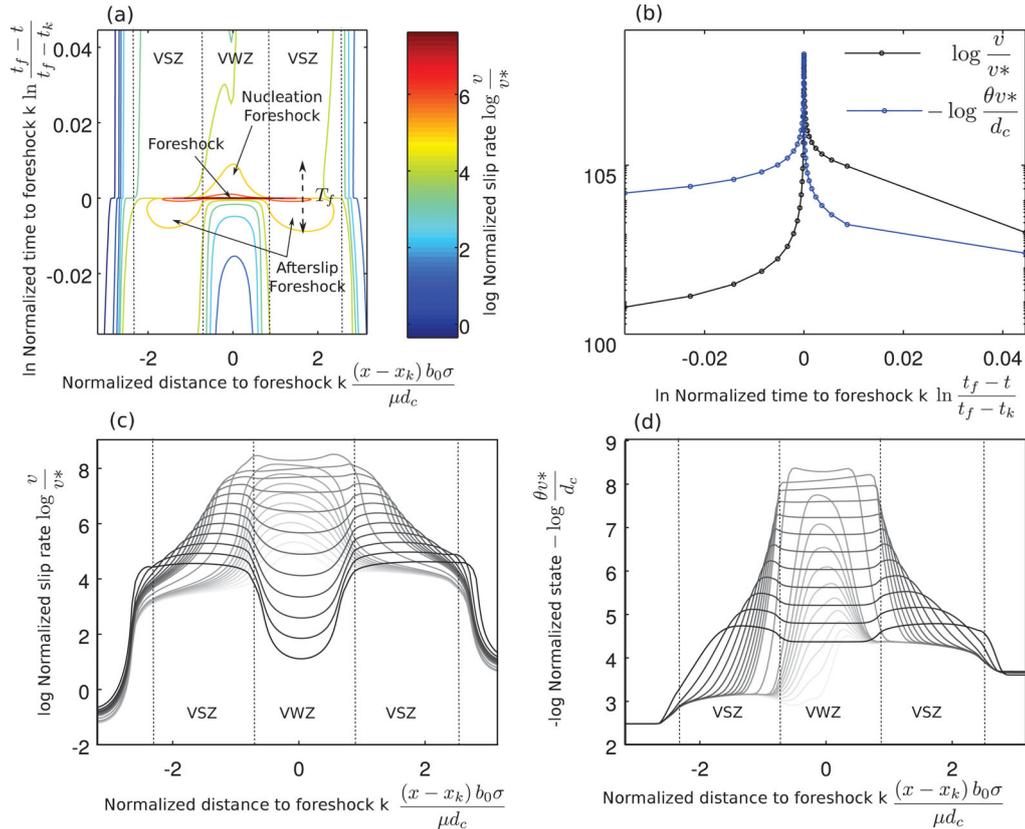
Figure D4. Typical foreshock detail (foreshock F_k in Fig. 3d). (a) Slip rate evolution. The representation is the same as in Fig. 3. (b) Slip rate v and inverse state variable $1/\theta$ at $x = x_k$. (c,d) Slip rate and state variable profiles during foreshock k. One profile is represented per black (blue) dot in panel (b). Darker colours correspond to later times. T_f is the typical foreshock log duration. VSZ and VWZ stand for velocity strengthening zone and velocity weakening zone, respectively.

D4 Critical length and nucleation duration

D4.1 Regimes (I) and (II) ($\rho_w < 0.5$)

As shown in the previous section, the heterogeneous fault is equivalent to a homogeneous velocity weakening fault characterized by a_0 and b_0 when $\rho_w < 0.5$. The nucleation of the main-shock is governed by eq. (D41), so that I expect to retrieve the nucleation lengths of Appendix C defined with a_0 and b_0. The critical half-length L_c is therefore given by eq. (C2). I have:

$$L_c = L_h. \tag{D55}$$

For similar reasons, the nucleation duration t_n is given by the homogenized duration t_h (eq. C5). I have

$$t_n = t_h. \tag{D56}$$

D4.2 Regime (III) ($\rho_w > 0.5$ and $\rho_w > \rho_c$)

If $\rho_w > \rho_c$, the first event on the fault degenerates. The critical length and the nucleation duration are in this case controlled by the local velocity weakening parameters a_0 and $b_0 + \Delta b$. L_c is therefore given by eq. (C1) as

$$L_c = L_w, \tag{D57}$$

and t_n by eq. (C4) as

$$t_n = t_w. \tag{D58}$$

D4.3 Regime (IV) ($\rho_c > \rho_w > 0.5$)

In this case, a foreshock sequence is expected, so that it becomes impossible to use the homogenized nucleation quantities L_h and t_h of Appendix C. In order to account for the effect of foreshocks, I use the critical nucleation crack approach presented in Appendix D1. This time, the critical value z_c of z could be approximated (with a precision of $\pm 1/2$) by the solution of $K_m(z) = K_{cs}(z)$. The critical crack length is then obtained by $L_c = z_c \lambda$. From eqs (D16) and (D20), I get the critical length L_c as

$$L_c = \frac{(1-f)\alpha}{\pi(1-\alpha)^2}\left(1 + 3\sqrt{c\tilde{\lambda}} + \frac{9}{4}c\tilde{\lambda}\right), \tag{D59}$$

where the constant c is given by

$$c = \frac{(1 - \alpha + f\alpha)^2}{\pi(1-f)\alpha}. \tag{D60}$$

As shown in the previous section, the evolution of the background slip rate is governed by eq. (D41), which solution is controlled by the average parameters a_0 and b_0 through the factor α. Foreshocks do not participate to this overall acceleration (they only contribute to the nucleation length). The nucleation duration t_n is therefore the homogenized one t_h. In this case I have

$$t_n = t_h. \tag{D61}$$

Fluid driven shear cracks on a rate-and-state frictional fault

P. Dublanchet[a]

[a] MINES ParisTech, PSL Research University, Centre de Géosciences, 35 rue saint-honoré 77305 Fontainebleau, France

Abstract

This study is dedicated to the dynamics of slow slip reactivation on faults stimulated by a fluid injection. Such fluid driven slow aseismic slip events are commonly observed on natural faults either in tectonic active areas or in the framework of deep energy exploitation. We model the fault as a planar 2D velocity strengthening rate-and-state frictional interface embedded in an elastic medium. The fluid is injected at a constant rate and spreads diffusively along the fault reducing the effective normal stress. We show that the fluid injection initiates a shear crack on the fault. In a first phase, the shear crack remains confined to the pressurized zone, and slip-rate increases exponentially with time. A second phase starts at the onset of a rapid crack expansion. The shear crack during phase two propagates faster than the pressurized zone. Depending on the pre-stress conditions, the shear crack evolves towards two different regimes. If the initial shear stress τ_0 is larger than the steady-state frictional stress τ_r at the seismic slip rate v_{sis}, the slip rate and the crack expansion rate keep increasing. This accelerating crack regime is similar to the nucleation of a dynamic rupture on the fault. On the other hand, if $\tau_0 < \tau_r$, the accelerated expansion progressively slows down so that the crack enters a steady regime, characterized by a constant expansion speed and a logarithmic increase of slip-rate. However, a large majority of fault scenarios ultimately lead to this steady expansion regime. In addition to the numerical results, we develop asymptotic expressions for the the maximum slip rate history on the fault and the crack length history, showing how initial prestress τ_0, frictional conditions (ratio a/b), hydraulic properties

and injection history control the dynamics of fluid induced aseismic slip events.

1. Introduction

Many observations suggest that fluid flow at depth can reactivate slip on preexisting crustal faults. Fluids may have a natural origin (rainfall events, deep source), or can be related to geo-resource exploitation (geothermal oper-

5   ations, waste water injection, reservoir lake impoundment). If rapid enough slip is reactivated (typically at slip rates greater than 1 cm.s^{-1}), the fault ruptures in an earthquake, such as the commonly oberved induced earthquakes (Deichmann and Giardini, 2009; Ellsworth, 2013). However, the fluid-induced reactivation of faults can lead to much slower slip speeds, leading to the occur-

10   rence of a slow or aseismic event (Cornet et al., 1997; Cornet, 2016; Guglielmi et al., 2015). Aseismic slip in turn may trigger earthquake sequences (Schaff et al., 1998; Bourouis and Bernard, 2007; Wei et al., 2015; Lengliné et al., 2017). Aseismic slip is even suspected to be one of the dominant mechanisms releasing injected energy at depth (Goodfellow et al., 2015; Duboeuf et al., 2017). Under-

15   standing the physics controlling the dynamics of aseismic slip events triggered by fluid injections is therefore crucial to better constrain the energy partitioning in the subsurface or in a geological reservoir, and to better assess the associated seismogenic hazard.

Recent advances in the study of the mechanics of fluid-fault interaction

20   have essentially focused on the stability of frictional slip when a fluid is locally injected and diffuses within a fault (Garagash and Germanovich, 2012; Cappa et al., 2018; Bhattacharya and Viesca, 2019), or when a hydraulic fracture propagates along a frictional fault (Azad et al., 2017). All these studies have shown how the pore pressure related reduction in effective normal stress

25   triggers the reactivation of a slow aseismic slip, that eventually degenerates into

a dynamic rupture. In most of the fault scenarios investigated, the aseismic slip (and the dynamic slip if initiated) is excited well beyond the pressurized region of the fault. This strong aseismic response (stronger that the pore pressure perturbation) is even more pronounced when the fault experiences significant frictional weakening (Garagash and Germanovich, 2012; Azad et al., 2017; Cappa et al., 2018), or if slip-induced permeability enhancement takes place (Cappa et al., 2018; Bhattacharya and Viesca, 2019). The transition to dynamic rupture is furthermore facilitated by initial stress conditions closer to failure, and by an injection scenario leading to an abrupt increase of over-pressure within the fault zone (Garagash and Germanovich, 2012; Azad et al., 2017).

All these studies rely on a frictional description involving either a constant friction coefficient or a slip weakening friction coefficient. Such descriptions impose a minimum over-pressure to trigger aseismic slip. Below this reactivation threshold, no slip occurs. Furthermore, the slip-rate dependence of friction needed to explain the dynamics of aseismic slip on tectonic faults (Marone et al., 1991; Perfettini and Avouac, 2004; Helmstetter and Shaw, 2009; Jolivet et al., 2013) is not accounted for by such frictional models. A long history of rock friction experiments has demonstrated that the rate-and-state friction (Dieterich, 1979; Ruina, 1983) captures both the slip-rate and slip history dependance of friction. Contrary to the slip weakening description, the rate-and-state law does not imposes a stress threshold to activate slip, which may lead to a fairly different behavior than what has been obtained under slip weakening or constant friction. This point still needs to be investigated. A rate-and-state friction coefficient has however been tested by Cappa et al. (2018) to model the in-situ fault reactivation experiment by Guglielmi et al. (2015), leading to a somewhat larger aseismic response than the classical constant friction coefficient. However, more efforts still need to be done to understand the effects of the rate-and-state frictional rheology on fluid induced aseismic slip.

Here we propose to study the fluid induced reactivation of aseismic slip on a Dieterich-Ruina rate-and-state frictional fault. We will extend the previous studies on fluid fault interaction by studying the effect of the rate-and-state

parameters and the initial stress conditions on the induced aseismic slip. In particular, we will focus on the evolution of maximum slip rate and the size of the perturbed slip zone as the pore pressure perturbation proceeds. As far as possible we will derive closed form approximate solutions for the maximum slip rate history and for the size evolution of the aseismic slow slip events.

2. Fault model

We consider the anti-plane fault model depicted in figure 1, consisting in a linear 1D interface separating two 2D semi-infinite elastic media. The fault is loaded by a constant normal stress σ, and a remote shear stress τ_0. Anti-plane slip - $\delta(x, y, t) = w(x, 0^+, t) - w(x, 0^-, t)$, w being the z component of the displacement, and t the elapsed time - is resisted by friction within a finite length crack of size $2L_0$. Outside the crack, the slip-rate is imposed at a constant rate $v*$. Here we consider rate-and-state friction within the crack, which accounts for the slip rate and slip history dependence of friction usually observed in laboratory experiments (Dieterich, 1979; Marone, 1998). The fault is furthermore permeated by a fluid injected at $x = 0$, and diffusing in the $\pm x$ directions with pore pressure p. In this framework, the frictional stress along the x direction τ_f is given by :

$$\tau_f(x, t) = f(x, t) \left[\sigma - p(x, t) \right],$$ (1)

f being the rate-and-state friction coefficient defined as :

$$f(x, t) = f_0 + a \ln \frac{v(x, t)}{v*} + b \ln \frac{\theta(x, t) v*}{d_c},$$ (2)

where f_0 is a constant friction coefficient, a and b are rate-and-state parameters, d_c the critical slip of rate-and-state friction needed to renew a population of microscopic contacts. Since we are interested in the dynamics of slow aseismic slip, rate strengthening properties are considered so that $a > b$. v is the slip rate defined as $v = \dot{\delta}$. The state variable θ incorporates the slip history dependence

4
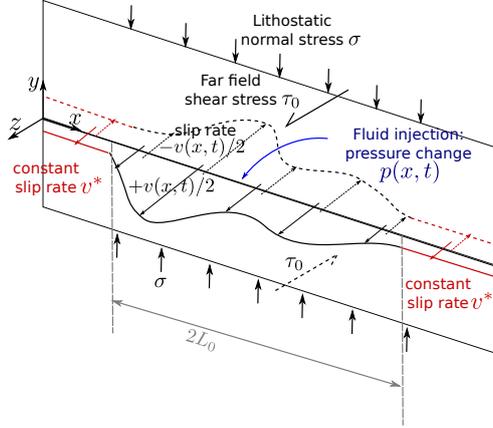
Figure 1: 2D mode III fault model considered in this study.

of the friction coefficient. Here it is assumed to evolve with time and slip rate on the fault according to the ageing law (Ruina, 1983; Marone, 1998) :

$$\dot{\theta}(x,t) = 1 - \frac{v(x,t)\theta(x,t)}{d_c}. \tag{3}$$

The steady-state friction coefficient f_{ss} at the slip rate v is obtained when $\dot{\theta} = 0$, so that $\theta = d_c/v$ from equation (3). We get:

$$f_{ss} = f_0 + (a - b)\ln\frac{v}{v*}. \tag{4}$$

85 The steady-state frictional stress τ_{ss} is then defined as $\tau_{ss} = f_{ss}(\sigma - p)$. Following Rubin and Ampuero (2005), we note $\Omega = v\theta/d_c$ the distance to steady state, since $f - f_{ss} = \ln\Omega$.

We further assume that the slip distribution on the fault results from a balance between the frictional stress τ_f (equation 1) and the z component of

90 the elastostatic stress $\tau_{el} = \tau_{yz}(x,0,t) = \mu\partial w/\partial y(x,0,t)$. τ_{el} could be written as :

$$\tau_{el}(x,t) = \tau_0(x) - \frac{\mu}{2}\mathcal{H}\left[\delta'\right](x,t), \tag{5}$$

5

where τ_0 corresponds to the prestress, that is the stress prevailing on the fault before the onset of slip. The second term on the right-hand side is the static shear stress generated by the slip distribution δ. The operator $\mathcal{H}$ is the Hilbert transform, and the prime denotes a derivative with respect to the spatial coordinate x.

The fluid injection is modeled as a prescribed pore pressure history resulting from a constant injection rate imposed at $x = 0$, and a diffusion along the infinite x axis with a constant diffusivity D. Under such conditions, the pore pressure history p is given by (see Turcotte and Schubert (2014) for details of the derivation):

$$p(x, t) = 2q\sqrt{Dt} \left[|\eta|(erf(|\eta|) - 1) + \frac{e^{-\eta^2}}{\sqrt{\pi}} \right], \tag{6}$$

where the similarity variable η is defined as $\eta = x/2\sqrt{Dt}$ and q is the change in pressure gradient (directly related to the fluid flux according to the Darcy's law) at the origin.

The time derivative of the quasi-static stress balance $\tau_f = \tau_{el}$, along with the state evolution law (3) leads to the following differential equations for the evolution of slip rate v and state variable θ under prescribed pore pressure history p:

$$\begin{cases} (\sigma - p) \left[a\frac{\dot{v}}{v} + b\frac{\dot{\theta}}{\theta} \right] = \dot{\tau}_b + f(v, \theta)\dot{p} - \frac{\mu}{2}\mathcal{H}\left[v'\right] \\ \dot{\theta} = 1 - \frac{v\theta}{d_c}. \end{cases} \tag{7}$$

Considering a characteristic slip rate $v_c = v*$, a characteristic time $t_c = d_c/v*$, a characteristic length $x_c = \mu d_c/b\sigma$, and a characteristic pore pressure $p_c = \sigma$, we can make the substitution:

$$v \Rightarrow v/v_c, \qquad t \Rightarrow t/t_c, \qquad x \Rightarrow x/x_c, \qquad p \Rightarrow p/p_c, \tag{8}$$

6

so that the system (7) becomes in non-dimensional form:

$$
\begin{cases}
(1-p)\left[\alpha\dfrac{\dot{v}}{v}+\dfrac{\dot{\theta}}{\theta}\right]=\bar{f}(v,\theta)\dot{p}-\dfrac{1}{2}\mathcal{H}\left[v'\right] \\[2mm]
\dot{\theta}=1-v\theta,
\end{cases}
\tag{9}
$$

where $\alpha=a/b$ and $\bar{f}=\bar{f}_0+\alpha\ln v+\ln\theta$, $\bar{f}_0$ corresponding to f_0/b. Similarly, the pore pressure history (6) could be made non-dimensional. From the characteristic lenth x_c the characteristic time t_c, and the characteristic pore pressure p_c, we construct the characteristic diffusivity $D_c=x_c^2/t_c=\mu^2 d_c v*/b^2\sigma^2$, and the characteristic pore pressure gradient $q_c=p_c/x_c=b\sigma^2/\mu d_c$. Assuming the substitution

$$
D\Rightarrow D/D_c,\qquad q\Rightarrow q/q_c,
\tag{10}
$$

along with (8), the non-dimensional pore pressure history keeps the form (6).

In order to simplify the developments in the main text, we will in the following make only use of non-dimensional quantities removing the over-bar on f and f_0. However, the figures will be labeled with dimensional quantities, so that the relevant physical parameters appear more explicitly. A length L in the main text will therefore correspond to the non-dimensional $\bar{L}=Lb\sigma/\mu d_c$, but not in the figure label.

For a specific choice of the parameters α, q, D, and initial conditions $v(x,0)$, $\theta(x,0)$ the system (9) is solved numerically using a standard Runge-Kutta Fehlberg scheme (Fehlberg, 1969) with adaptative time stepping. This requires to evaluate the Hilbert transform of the slip rate gradient at each time step. For that we follow the method proposed by Cochard and Rice (1997), on a grid of $n=8192$ identical computational cells of normalized size $h=0.03$ much smaller than the typical normalized process zone size $L_b=1$ (Perfettini and Ampuero, 2008; Rubin and Ampuero, 2005) in order to ensure continuity. This algorithm results in the slip rate and state variable history $v(x,t)$ and $\theta(x,t)$, in response to a fluid injection.

7

3. Results

We performed several fluid injection tests at constant rate in our fault model. In each scenario, we considered a normalized diffusivity $D = 4.369$, which corresponds to hydraulic diffusivities ranging between 10^{-6} m^2.s^{-1} and 0.1 m^2.s^{-1} assuming standard values for the shear modulus $\mu \sim 3.10^{10}$ Pa, for the rate-and-state parameter $b \sim 10^{-3} - 10^{-2}$, for the reference creep rate $v* = 10^{-9} - 10^{-10}$ m.s^{-1} (representative of creeping faults), for the lithostatic stress $\sigma \sim 100$ MPa (representative of approximately 3 km depth) and the critical slip distance d_c between 1 mm and 1 μm (Marone, 1998). Typical diffusivities within fault gouge are expected to vary within this range (Rice, 2006; Jaeger et al., 2009). We considered a constant normalized pore pressure gradient at the origin $q = 0.01$, which corresponds to a pressure gradient of the order of 300 Pa.m^{-1} to 100 MPa.m^{-1} with the same reference parameters. We tested 8 values of the velocity strengthening frictional parameter α between 1.1 (weakly strengthening behavior) to 2.5 (strongly strengthening behavior). All the injection scenarios were performed on a fault initially slipping at the background slip rate $v = 1$. For all the frictional parameters, we considered three different uniform initial state variable $\theta_0 = 1, e^2$ and e^{-2}, so that the initial stress on the fault is respectively equal to, slightly above or slightly below steady state at $v = 1$ from equations (2) and (4). The three initial stress conditions indeed correspond to $\tau_0 - \tau_{ss}^0 = 0, 2$ or -2, τ_{ss}^0 being the steady state frictional stress at the reference slip rate $v = 1$, and with $p = 0$. All the simulations were stopped before the maximum pore pressure exceeds the lithostatic normal stress σ, so that no mode I hydraulic fracture is created (which implies a loss of frictional contact, so that the model used here is no longer valid).

Two characteristic slip responses to a fluid injection are illustrated in figure 2: as the pore pressure perturbation develops, slip accelerates on a patch centered on the injection point (figures 2(a) and (b)). Within the slipping patch, the initial stress is reduced, and redistributed on the non perturbed remote portions of the fault (figures 2(c) and (d)). The fluid injection therefore initiates the
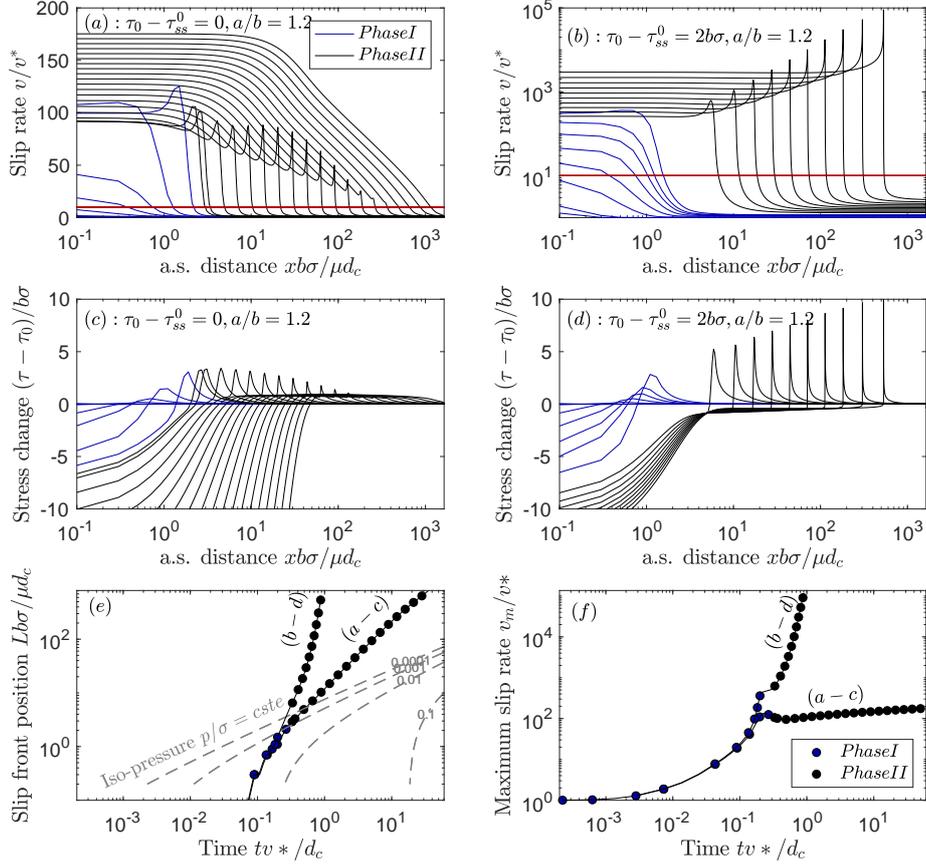
Figure 2: Two examples of fluid driven fault slip reactivation: fault initially at steady state (a,c), and initially above steady state (b,d).(a,b): Normalized slip rate. (c,d): Normalized shear stress change. τ_0 is the initial stress on the fault before the injection, and τ_{ss}^0 the steady-state frictional stress at the reference slip rate v^* and pore pressure $p = 0$. The profiles being symmetric around $x = 0$, only the right half profiles are represented. a.s. corresponds to along strike. (e): Slipping patch normalized half-length (or slip front position), defined as the size of the patch where slip rate exceeds the red line in figures (a,b). Gray dotted lines indicate iso-pressure levels. The grey numbers are levels of normalized pore pressure. (f): Maximum normalized slip rate. Each dot in (e,f) corresponds to a profile in figures (a,b,c,d). Blue lines and symbols correspond to phase I of slip reactivation, black lines and symbols correspond to the second phase of slip reactivation (see main text for details).

9

development of a shear crack on the fault. As this will be discussed later, two mechanisms drive the development of this crack: the reduction of effective normal stress due to the presence of fluid, or the initial prestress.

We observe two successive phases in the evolution of such a pressurized crack: at the very beginning of the injection (phase I), the accelerated patch approximately conserves a constant length, but rapidly, it starts to expand along strike (phase II). During phase I, the maximum slip rate on the crack increases exponentially with time from injection start. As illustrated in figure 2, we get a different behavior during phase II for different initial stress conditions: for a fault initially at steady state, the crack expansion occurs approximately at a constant rupture speed (figure 2(a,c,e)), and the maximum slip rate increases logarithmically in time (figure 2(f)). For a fault initially above steady state, both the crack length and the maximum slip rate diverge in a finite time (figure 2(b,d,e,f)). In the following we will refer to these two modes as the steady crack (constant rupture speed), or the accelerating crack (diverging slip rate).

The half crack length $L(t)$ and the maximum slip rate $v_m(t)$ histories for all the fault scenarios investigated are shown in figure 3. As illustrated in figure 2, $L(t)$ is defined as the half length of the patch experiencing more than a 10 times increase in slip rate. From figure 3, $L(t)$ and $v_m(t)$ are both influenced by the frictional conditions α and by the initial state of stress. Interestingly, neither the steady nor the accelerating crack follows an iso-pressure path: the crack dynamics is not directly controlled by the pore pressure diffusion. In all the scenarios the crack propagates faster than the pressurized zone does. However, all the results lead either to the steady crack, or to the accelerating crack. The latter fault response is typically obtained for a α parameter close to the weakening transition (i.e. for α close to 1), and for a fault initially stressed above steady state.

In the following, we will study the details of slip rate acceleration during phase I, the transition to phase II, and the crack expansion during phase II.

10
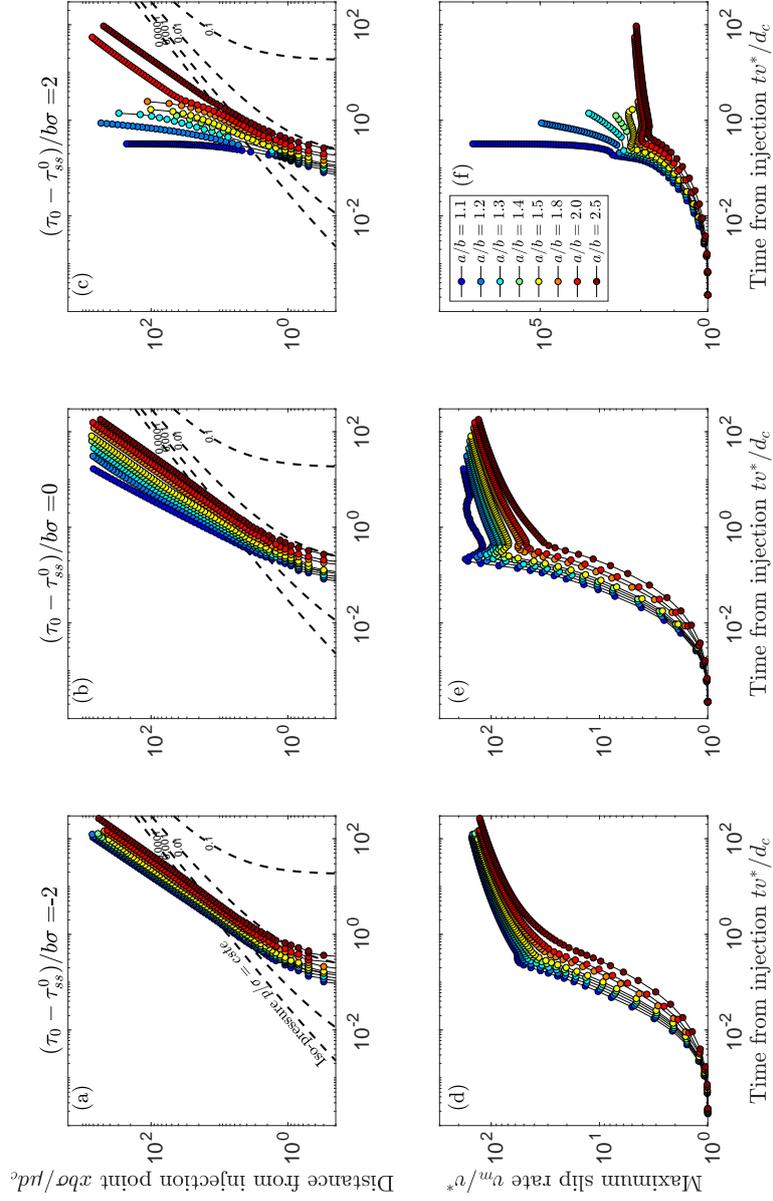
Figure 3: Shear crack half length (a,b,c) and maximum slip rate (d,e,f) as a function of time from the start of injection for all the fault scenarios investigated here. (a,d): Fault initially slightly below steady state $(\tau_0 - \tau_{ss}^0 = -2b\sigma)$. (b,e): Fault initially at steady state $(\tau_0 - \tau_{ss}^0 = 0)$. (c,f): Fault initially slightly above steady state $(\tau_0 - \tau_{ss}^0 = 2b\sigma)$. The color scale refers to the rate-and-state frictional parameter $\alpha = a/b$. Black dashed lines in figures (a,b,c) indicate iso-pressure levels. See figure 2 for details.

11

3.1. Phase I: initial slip rate acceleration

As shown in appendix A, the initial localized slip rate acceleration could be understood to the first order as a balance between the direct effect term $\alpha \dot{v}/v$ and the approximate rate of change of effective normal stress $f_0 \dot{p}$. The other terms appearing in the first equation of (9) being negligible. In this framework, the maximum slip rate v_m is reached where the pore pressure is maximum, that is at the injection point. It is shown in appendix A that v_m evolves approximately as:

$$v_m(t) = exp(\sqrt{t/t_a}),\tag{11}$$

where t_a is a characteristic time scale given by:

$$t_a = \frac{\pi}{4}\frac{\alpha^2}{Df_0^2q^2}.\tag{12}$$

This first phase ends when steady state is reached at the fault center (see figure A.8), marking the onset of crack expansion. It is shown in appendix A, that the onset of phase II occurs at time t_I given by:

$$t_I \simeq t_a(\ln 2t_a)^2.\tag{13}$$

As illustrated in figure 4, equation (11) provides a good estimates of the exponential increase of the maximum slip rate along the fault. Furthermore, the expression (13) for t_I provides the correct order of magnitude for the transition time to phase II, in particular for small values of α. For larger values, it anticipates the transition by a factor of 2. This is certainly due to all the approximations leading to equation (13).

During phase I, we do not detect any significant increase of the length of the crack (no points for phase I in figures 3(a), (b) and (c)). This does not mean that the accelerating patch does not slightly expands: initially the slip rate is below the threshold used to track the crack size ($v = 10$). Because of the balance between the direct effect and the pore pressure rate, the size of the
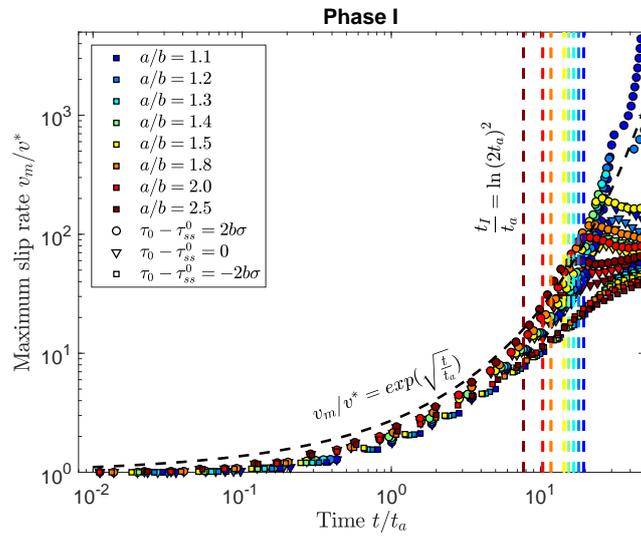
Figure 4: Normalized maximum slip rate increase during phase I. Colored symbols correspond to the different fault scenarios (different rate-and-state frictional parameter $\alpha = a/b$ and different initial stress). The black dashed line is the theoretical prediction of equation (11). The colored dashed lines are the theoretical estimates for the end of phase I (t_I) provided by equation (13). Characteristic times t_a and t_I are defined in the main text.

13

accelerating patch is directly controlled by the diffusion length $\sqrt{Dt}$, as shown in figures A.9(a) and A.10(a).

3.2. Phase II: slip rate increase and expansion

The onset of phase II is characterized by a steepening of the slip rate profile at the crack tip (last blue profiles in figure 2(a) and (b)). Simultaneously, the slip rate maximum v_m moves from the fault center to the crack front. The initiation of such a sharp slip front was observed for all the fault scenarios considered here. As noted earlier, the slip front then evolves in two different ways: either the peak slip rate increases, and the front accelerates in the case of an accelerating crack (figure 2(b-d)), or the peak slip rate decreases so that the sharp front dies away (figure 2(a-c), leading to a smoother front propagating at a constant speed (steady crack). In this latter case, the slip rate is maximum at the crack center. In the following, we will make the distinction between the maximum slip rate v_m and the peak slip rate v_p, that is the slip rate at the tip of sharp propagating fronts. In the case of an accelerating crack (figure 2(b)), $v_m = v_p$.

3.2.1. Accelerating crack

In order to study in detail the dynamics of the accelerating crack, we concentrate on the fault scenarios characterized by $\alpha = 1.1$ or 1.2 and an initial state of stress above steady state $(\tau_0 - \tau_{ss}^0 > 0)$, which provide the most characteristic examples of such a dynamics (figure 3). In appendix A, it is shown that the accelerating crack is characterized by a square-root shaped displacement profile at the crack tip, and a positive stress drop $\Delta\tau_{tip}$ near the tip of the crack (i.e. the difference between the initial stress and the residual stress left by the process zone). A quasi-static energy balance at the tip indicates that the crack half-length is approximately given by the characteristic length L_c defined by Rubin and Ampuero (2005):

$$L \sim L_c = \frac{1}{\pi} \left[\frac{\ln v_m \theta_0}{\ln \theta_0 - (\alpha - 1) \ln v_m} \right]^2 . \tag{14}$$

14

Furthermore, the rupture speed (crack expansion rate) $\dot{L}$ depends on the maximum (peak) slip rate v_m (Ampuero and Rubin, 2008), so that we have:

$$\dot{L} = 0.75 \frac{v_m}{\ln v_m \theta_0}. \tag{15}$$

As shown in figure 5(a) and (b), the results of the numerical simulations converge to the predictions of equations (14) and (15), for the two examples of accelerating cracks detailed here.

The simple quasi-static crack model defined by equations (14) and (15) provides an explanation to the observed diverging crack length and maximum (or peak) slip rate. Under velocity strengthening rheology ($\alpha > 1$) and an initial prestress above steady state ($\ln \theta_0 > 0$), the two equations constrain L, $\dot{L}$, v_m (or v_p) and $\dot{v}_m$ to be increasing functions of time. In particular, according to (14), as v_m increases, L blows up and diverges at a finite slip rate v_l, approximately given by:

$$v_l = \theta_0^{1/(\alpha-1)}. \tag{16}$$

However, we did not try to find a closed form solution to equations (14) and (15) and we did not solve this system numerically. The solutions $L(t)$ and $v_m(t)$ would indeed be strongly influenced by our choice of initial conditions (poorly defined at the end of phase I), and by the fact that equation (14) is approached relatively slowly (see figure 5(a)). Note that in this case, since the pore pressure term does not enter into equation (14), the propagation is exclusively driven by the release of initial prestress. Beyond the limit speed v_l, the quasi-static crack model fails, since the stress drop at the crack tip (denominator in equation (14), see appendix A for details) becomes negative.

More generally, such a mode of propagation is only possible if the stress drop at the crack tip is positive. In all the simulations this kind of crack front was observed, we computed the stress drop evolution $\Delta\tau_{tip}$. The results are reported in figure 6 as a function of the (increasing) crack length. $\Delta\tau_{tip}$ is always positive at the onset of the propagation, then it strongly decreases as crack propagation

15
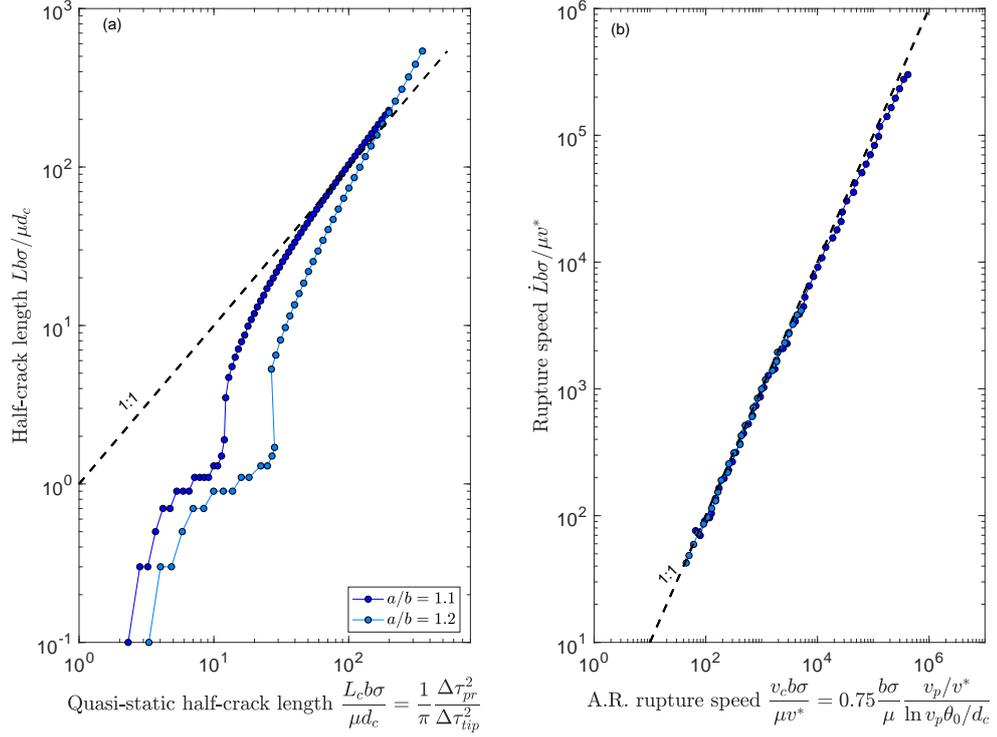
Figure 5: Numerical vs. theoretical dynamics of accelerating cracks, obtained with initial stress above steady state $(\tau_0 - \tau_{ss}0 = 2b\sigma)$. (a): crack half-length as a function of the theoretical length L_c (expected from a quasi-static energy balance at the crack tip). $\Delta\tau_{pr}$ is the peak to residual stress drop, $\Delta\tau_{tip}$ is the stress drop at the crack tip (see main text for details). (b): rupture speed (crack expansion speed), as a function of the theoretical prediction by (Ampuero and Rubin, 2008) (A.R. rupture speed v_c). v_m is the maximum slip rate. Colored dots indicate the numerical solution. Black dashed lines indicate the perfect match between numerical solution and theoretical estimates L_c and v_c.

16
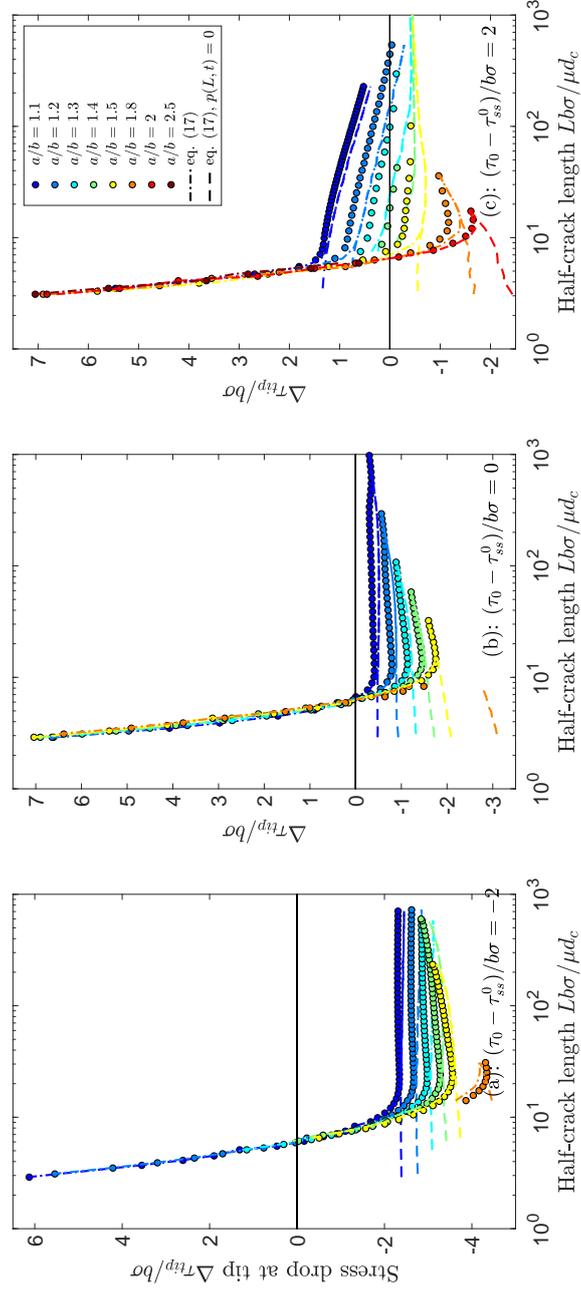
Figure 6: Stress drop at the crack tip $\Delta\tau_{tip}$ during crack expansion (phase II) for all the scenarios an accelerating crack was enough developped to be observed. (a): Fault initially slightly below steady state $(\tau_0 - \tau_{ss}^0 = -2b\sigma)$. (b): Fault initially at steady state $(\tau_0 - \tau_{ss}^0 = 0)$. (c): Fault initially slightly above steady state $(\tau_0 - \tau_{ss}^0 = 2b\sigma)$. Color scale corresponds to the rate-and-state friction parameter $\alpha = a/b$. Dots are the numerical results. Dashed and dashed dotted lines are the approximations of equation (17). The balck horizontal line indicates $\Delta\tau_{tip} = 0$. The fault scenarios not represented (or partially represented) correspond to situations where the accelerating crack was too short lived.

proceeds and eventually becomes negative. At larger crack length, $\Delta\tau_{tip}$ either increases smoothly if negative, or decreases smoothly if positive. As shown in figure 6, the evolution of $\Delta\tau_{tip}$ is well captured by the approximate expression of $\Delta\tau_{tip}$ provided in appendix A:

$$\Delta\tau_{tip}(t) = \ln\theta_0 - (\alpha - 1)\ln v_p(t) + f_0 p(L, t), \tag{17}$$

275 where $p(L, t)$ is the pressure at the crack front $x = L$ and time t. Initially, when the crack process zone is within the pressurized region, the third term dominates, so that $\Delta\tau_{tip}$ is positive. The initiation of an accelerating crack could therefore be attributed to the decrease of effective normal stress within the pressurized region. As the crack expands faster than the pressurized region, this

280 term decreases, and the first two term become important, until they dominate (figure 6). When the pore pressure term becomes negligible, the evolution of $\Delta\tau_{tip}$ becomes smoother.

The evolution of $\Delta\tau_{tip}$ shows that if in many cases, an accelerating crack could be initiated at early times, this kind of solution can not be sustained

285 during the whole simulation, because $\Delta\tau_{tip}$ quickly becomes negative. This is typically what happens in figure 2(a,c). The only way of maintaining this accelerating crack beyond the pressurized zone is to keep the first two terms of equation (17) positive, that is if $v_p < v_l$. From equation (16), we see that if the initial stress is below steady state ($\theta_0 \leq 0$), then v_l is smaller than the initial slip

290 rate $v = 1$, and the accelerating crack can not develop towards instability. For faults initially above steady state ($\theta_0 > 0$), we obtain $v_l = 4.85 \times 10^8$ for $\alpha = 1.1$, $v_l = 2.2 \times 10^4$ for $\alpha = 1.2$, which is well above the observed maximum slip rates (figure 3(f)). Under stronger velocity strengthening properties ($\alpha > 1.2$), we get v_l between 3 and 800, which is of the order of (or below) the observed maximum

295 slip rates. Equation (16) therefore provides a first order estimate of the range of slip rates that could be obtained on a prestressed velocity strengthening fault.

As the accelerating crack dies away, the simulations evolve towards a steady propagation, that is detailed in the next section.

18

3.2.2. Steady crack

It is shown in appendix A that this second mode of crack propagation is to the first order controlled by a balance between the elasticity (i.e. the elastic stress transfers) and the approximate rate of effective normal stress change $f_0\dot{p}$. In other words, the crack evolves as if it were governed by a constant friction coefficient within the slipping zone. Here the pore pressure increase drives the crack expansion (and not the initial prestress). When assuming this simplified stress balance within the crack along with the conservation of total stress along the fault, it could be shown (appendix A) that the crack half size grows linearly in time as:

$$L(t) = v_r t = \frac{f_0 q D}{\lambda(\alpha - 1) - \ln\theta_0} t, .$$

(18)

where v_r is a constant rupture speed. As during phase I, the maximum slip rate v_m is reached at the injection point, and approximately increases as the logarithm of time:

$$v_m(t) = c\left(1 + \ln\sqrt{\frac{t}{t_s}}\right), \qquad c = \frac{4 f_0 q D}{\pi}, \qquad t_s = 4\frac{\lambda^2(\alpha-1)^2 - \ln{\theta_0}^2}{f_0^2 q^2 D}.$$

(19)

c and t_s are a typical slip rate and a characteristic time scale respectively. In both equations (18) and (19), λ corresponds to the logarithm of maximum slip rate on the fault, which has been assumed constant in the derivations of appendix A. Since the maximum slip rate approximately increases logarithmically in time for the steady crack, the changes in $\lambda = \ln v_m$ are negligible compared to the linear increase of crack length L, and the variations of v_m. If we consider λ as the average value of $\ln v_m$ during phase II for the steady crack, we get $4.6 < \lambda < 5.2$. In the following we therefore assume $\lambda = 5$.

Numerical simulations leading to a steady crack approximately converge to the predictions of equations (18) and (19), as illustrated in figure 7. For $t > 10t_s$, the maximum slip rate and the crack half size follow a logarithmic and linear increase respectively. The approach to the asymptotic solution for v_m is in some

19
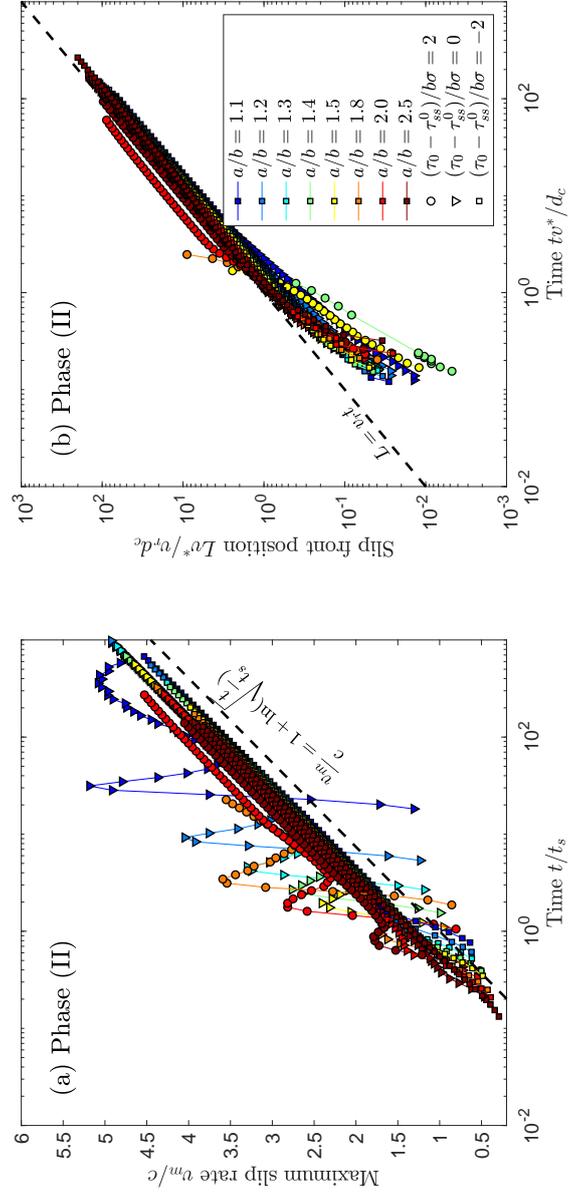
Figure 7: Normalized maximum slip rate (a) and normalized slip front position (b) for the simulations leading to a steady crack expansion during phase II. Only times $t > t_I$ are represented (phase II). Colored dots are the numerical results. The black dashed lines are the approximations of equations (18) and (19) the characteristic slip rate c, rupture speed v_r and time t_s are defined in the main text: equations (18) and (19).

Geophysical Research Letters

Scaling and Variability of Interacting Repeating Earthquake Sequences Controlled by Asperity Density

P. Dublanchet[1] iD

[1]Centre de Géosciences, MINES ParisTech, PSL Research University, Fontainebleau, France

Abstract The period T_r of repeating earthquakes scales as $V_c^{-1}M_0^{1/6}$, V_c being the creep rate of the fault and M_0 the seismic moment of the events. Models consisting of a single asperity embedded in a creeping fault capture this scaling but fail to explain the variability in recurrence time observed during natural sequences. Here I show by a statistical analysis of repeating earthquakes generated in a rate-and-state fault model, that the observed scaling and variability in T_r are reproduced if a population of asperities is considered. For that, the density of asperities needs to be smaller than a critical threshold allowing system-size ruptures. Creep mediated stress transfers control the variability in T_r in this regime, which increases with asperity density. Beyond that density, the seismicity is highly clustered leading to moment-independent recurrence. The dynamics of repeating earthquakes could therefore be an indicator of the amount of seismogenic asperities on creeping faults.

Plain Language Summary Repeating earthquakes are particular events rupturing periodically the same patch of a fault. The time delay separating two successive events increases as the energy liberated during one event to the power 1/6 and decreases as the inverse long-term slip rate on the fault. Models considering an isolated source reproduce this scaling but fail to explain the slight deviations in periodicity reported for many repeating earthquake sequences. Here I present a statistical analysis of repeating earthquake sequences generated in a model of interacting sources distributed on a planar slowly slipping fault (at typical slip rates of cm yr^{-1}). If the density of sources is small enough, the relationship between periodicity and liberated energy is reproduced. At higher densities seismicity is clustered leading to and energy-independent recurrence. I also show that variability in recurrence increases with the source density. This is mainly related to variations in fault slip rate between the sources.

1. Introduction

Repeating earthquakes are particular events consisting of a quasiperiodic release of the same amount of seismic moment on a specific fault patch (asperity). Such events are commonly observed on major creeping faults (Bürgmann et al., 2000; Nadeau & McEvilly, 1997; Nadeau et al., 1995; Nadeau & Johnson, 1998; Poupinet et al., 1984). An important observation about repeating earthquakes is that their recurrence time (period T_r) scales as $V_c^{-1}M_0^{1/6}$, V_c being the long-term slip rate of the fault and M_0 the seismic moment of individual events (Chen et al., 2007; Nadeau & Johnson, 1998).

Several mechanical models have been proposed to explain the periodicity and the recurrence-moment scaling. They all consist of an isolated asperity embedded in a fault creeping at a constant rate because of tectonic loading (Beeler et al., 2001; T. Chen & Lapusta, 2009; Sammis & Rice, 2001). The asperity is characterized by periodic stick-slip oscillations supporting the observed regularity (the slip phase corresponds to an earthquake). If the stress drop is constant and if no slip is accumulated on the asperity during interseismic periods, T_r increases as $M_0^{1/3}$. However, considering a moment dependent stress drop, or a small amount of aseismic creep, or partial ruptures during interseismic periods of the asperity, the $T_r \sim V_c^{-1}M_0^{1/6}$ scaling is usually recovered (Cattania & Segall, 2019; Beeler et al., 2001; T. Chen & Lapusta, 2009, 2019; Sammis & Rice, 2001). This success has motivated the use of repeating earthquake sequences to monitor aseismic creep on deep faults (Bürgmann et al., 2000; Chen et al., 2008; Gardonio et al., 2015, 2018; Igarashi et al., 2003; Nadeau & McEvilly, 1999; Schmidt et al., 2005; Templeton et al., 2008; Uchida & Matsuzawa, 2011; Uchida et al., 2003, 2006, 2009).

Such ideal models however do not fully reproduce other observations such as the deviations from perfect periodicity and constant moment reported for many repeating earthquake sequences. This is in particular the case of the transient variations in T_r associated with accelerated creep following the Loma-Prieta earthquake (Schaff et al., 1998), or the changes in T_r and M_0 observed for repeating earthquake sequences on the San Andreas fault following moderate size earthquakes (K. H. Chen et al., 2009, 2013; Lengliné & Marsan, 2009). Even though some of the variability could be attributed to partial ruptures of the main asperity (Cattania & Segall, 2019; T. Chen & Lapusta, 2019), seismological observations suggest more complex models. Asperities are in particular far from being isolated on faults, and a precise analysis of source parameters often suggest a set of overlapping sources of slightly different sizes rather than a single asperity (Dublanchet et al., 2015; Ellsworth & Bulut, 2018; Godano et al., 2015). Perturbations from the perfect repeating earthquake model are therefore also attributed to the (static and dynamic) stress redistributions occurring within a population of repeating asperities and between the asperities and the creeping fault (K. H. Chen et al., 2009, 2013; Lui & Lapusta, 2016, 2018).

A better understanding of the dynamics of repeating earthquake sequences therefore requires to consider the mechanical interaction between different sources. Under which mechanical conditions a population of interacting asperities generates quasiperiodic earthquakes, what kind of asperity distribution is required to get the observed $T_r \sim V_c^{-1} M_0^{1/6}$ scaling, and what mechanical parameter controls the variability in recurrence time are the main unanswered questions raised by seismological observations. In order to study these issues, I analyze here the synthetic repeating earthquake sequences generated by a rate-and-state fault model. After a brief description of the model and the synthetic dataset, I will present the statistical analysis of the recurrence times and seismic moments. Finally I will relate the statistical properties of the repeating earthquake sequences to the mechanical properties prevailing on the fault.

2. Model and Data

In this study, I use the fault model and the synthetic earthquake catalogs produced by Dublanchet (2018). The fault model consists of a planar 2D interface separating two 3D elastic slabs of thickness H. Constant slip rate is imposed at the boundaries ($z = \pm H$) so that relative slip is forced in the x direction on the fault (see supporting information, Figure S1 for the fault geometry). Slip on the fault results from a balance between (aging) rate-and-state friction (J. H. Dieterich, 1979; Ruina, 1983) and elastic stresses. Elastic stresses incorporate the loading due to moving boundaries, and the quasi-dynamic stress transfers between the different fault patches (Rice, 1993).

Seismogenic asperities (sources of repeating earthquakes) are modeled as unstable circular velocity weakening patches ($a - b < 0$, a and b being the rate-and-state friction parameters) distributed on a stable velocity strengthening fault ($a - b > 0$). Asperities are large enough to allow for the nucleation of earthquakes. Velocity strengthening regions favor stable creep. The asperity distribution is characterized by the asperity density ρ defined as the ratio between velocity weakening area and total fault area.

From a given loading rate v^*, slab thickness H, asperity distribution and initial conditions (slip rate and stress), the model allows to compute the slip rate and stress history on each point of the fault. A synthetic earthquake catalog is then extracted from the slip rate history assuming an earthquake occurs each time the slip rate exceeds a threshold of the order of 1 cm s^{-1} (Rubin & Ampuero, 2005). The catalog lists the location in space and time, the source size, and the seismic moment of each event.

Here I use the synthetic catalogs of Dublanchet (2018), obtained under 29 different fault scenarios considering different values of H and different asperity densities ρ. In all the scenarios, asperity sizes R are distributed between two values R_1 and $R_2 = 10R_1$ according to a power law of exponent $p = -3/2$, and the asperities do not overlap. H is in any case much larger than R_2 so that it does not influence significantly my results. In order to simplify the analysis detailed in the next section, I selected the catalogs corresponding to periods of quasi constant average slip rate V_c on the fault. I end up with a total of 12,204 events out of 14 different fault scenarios (details about the selected simulations are provided in S1 Introduction, Figure S1, and Table S1).

In each selected catalog, I then extract repeating earthquake sequences assuming that two events belong to the same sequence if their hypocenter is separated by less than the minimum asperity size R_1. For the following analysis, I only considered the 456 sequences consisting of at least five events, with normalized magnitude larger than -4 (see Data Set S1 and Figure S2 for the definition of the normalized magnitude).
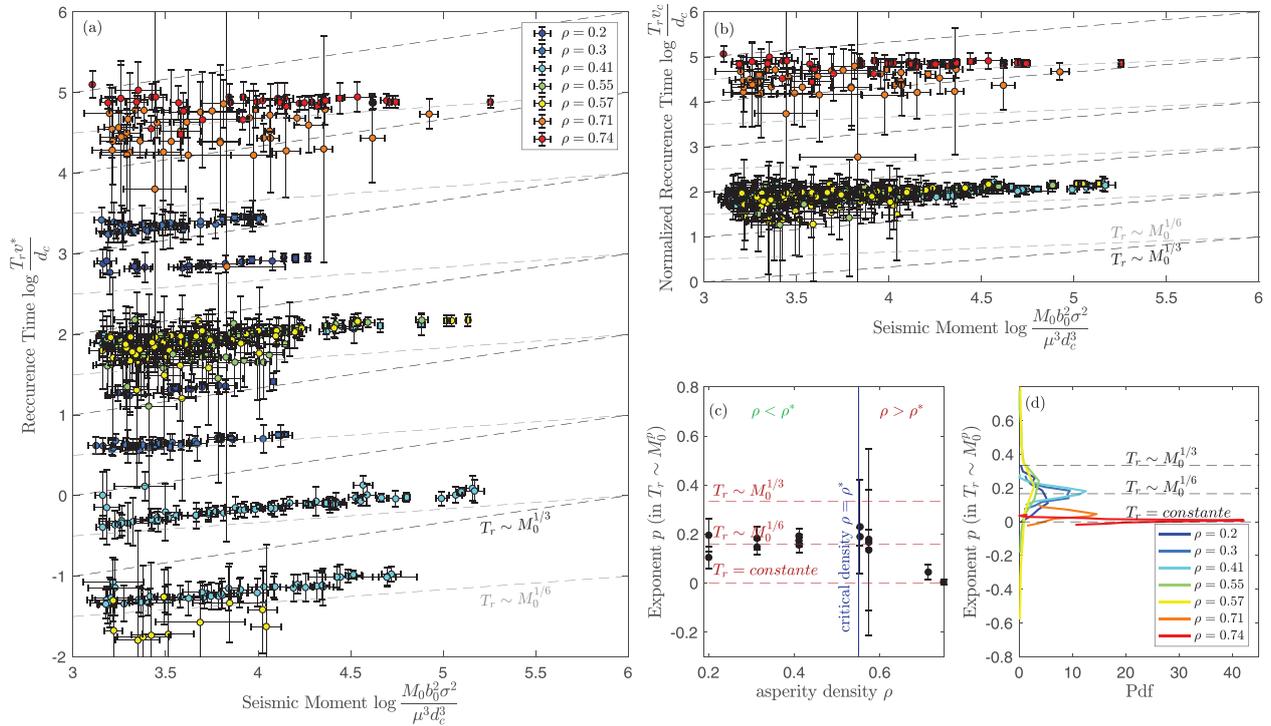
Figure 1. (a) Recurrence times T_r versus seismic moment M_0 for all the repeating earthquake sequences considered. Colors indicate the asperity density ρ. Gray dashed lines indicate the observed scaling $T_r \sim M_0^{1/6}$, black dashed lines the scaling expected for constant stress drop and no aseismic slip on the asperities $T_r \sim M_0^{1/3}$. T_r and M_0 are normalized by the typical time d_c/v^* and $\mu^3 d_c^3/b_0^2\sigma^2$, respectively, where v^* is the remote imposed displacement rate, d_c is the critical slip of the rate-and-state friction law, b_0 is the reference rate-and-state b parameter used in Dublanchet (2018), μ is the shear modulus of the medium, and σ the normal stress acting on the fault. (b) Normalized recurrence time V_cT_r/d_c versus seismic moment. The variables are here again normalized as in (a). V_c is the average slip rate on the fault. (c) Mean value and standard deviation of the best p parameter explaining data in (a) and (b) (assuming $T_r \sim M_0^p$). Red dashed lines indicate particular scalings discussed in the main text ($p = 0, 1/3$ or $1/6$). The blue vertical line indicates the critical asperity density ρ^* defined by Dublanchet et al. (2013b). (d) Probability density function of the inverted p parameter for different asperity densities. Black dashed lines indicate the same scalings as red dashed lines in (c).

−4 approximately corresponds to the rupture of the smallest patch R_1 (Dublanchet, 2018). Doing so, I eliminate most of the partial ruptures. Magnitudes larger than −4 are approximately power-law distributed (Dublanchet, 2018).

3. Results

The relationship between recurrence time T_r and seismic moment M_0 for the different repeating earthquake sequences is represented in Figure 1a. The error bars indicate that all of the repeating earthquake sequences slightly deviate from the perfect repeating earthquake model. For low enough asperity density ($\rho \leq 0.55$), T_r tends to increase as $M_0^{1/6}$ and not as $M_0^{1/3}$ as expected from a constant stress drop crack model (Nadeau & McEvilly, 1999). However, for higher asperity densities ($\rho = 0.71$ or $\rho = 0.74$), we get approximately the same T_r at any value of the seismic moment M_0.

Furthermore, different fault scenarios lead to different intercepts of the T_r, M_0 relationship (Figure 1a). All the fault scenarios are characterized by different average slip rates V_c on the fault (Dublanchet, 2018). As illustrated in Figures S2, S4, S6, S8, S10, S12, S14, S16, S18, S20, S22, S24, S26, and S28, V_c is approximately constant during the time period considered.. Following Chen et al. (2007), I interpret the different intercepts observed in Figure 1a as being due to different average slip rates V_c and define the normalized recurrence time T_r^* as

$$T_r^* = \frac{V_c}{v^*} T_r. \tag{1}$$

Doing so, all the results obtained for small enough asperity density collapse to the same tendency (Figure 1b). In this case, the different sequences follow the observed $T_r \sim V_c^{-1} M_0^{1/6}$ scaling. This suggests that the

dynamics of repeating earthquakes is primarily controlled by creep. Higher densities of asperities still do not follow this trend.

To better quantify the T_r, M_0 relationship obtained, I fit my results with a law of the form

$$T_r = kM_0^p \qquad (2)$$

and analyze the resulting exponent p. The uncertainty about the parameter p is obtained by resampling the data 100 times within the error bars. The results are represented in Figures 1c and 1d. Here again, most of the p values are in the vicinity of 1/6 for low enough density of asperity. As ρ increases to 0.55, the distribution of p is still centered in the vicinity of 1/6, but the scatter increases significantly. For higher densities $\rho > 0.57$, the p values are clustered around 0. This statistical analysis confirms that the $T_r \sim M_0^{1/6}$ scaling is replaced by a moment-independent recurrence as the asperity density increases.

The different dynamics observed for small and large asperity densities could be interpreted from the critical density of asperity defined by Dublanchet et al. (2013b). The critical density of asperity ρ^* corresponds to the minimum density allowing the different asperities to be connected in large ruptures. It is shown in Dublanchet et al. (2013b) that ρ^* depends on the distribution of rate-and-state frictional properties a and b, in a way that ρ^* makes the spatial average of $a - b$ vanish. Considering the a and b values used in Dublanchet (2018), I have here $\rho^* \simeq 0.55$. In my results, the $T_r \sim M_0^{1/6}$ is obtained under subcritical asperity density ($\rho < \rho^*$) while the $T_r = constante$ regime characterizes supercritical densities ($\rho > \rho^*$). In the vicinity of the critical density (for $\rho = 0.55$ and $\rho = 0.57$), the scatter of the possible p values could possibly be interpreted as a progressive transition between the two regimes (Figures S18, S20, S22, S26, and S28).

When $\rho < \rho^*$, asperities are either far from each other or separated by strong velocity strengthening barriers, so that they could be considered as isolated. The behavior of asperities is then similar to what is analyzed by T. Chen & Lapusta (2009, 2019) and Cattania and Segall (2019); some amount of aseismic slip occurs on the velocity weakening patches during interseismic periods, due to the penetration of a slow slip front from the edges of the patches. When $\rho > \rho^*$, it is shown in Figure S6 and S8, that the seismic activity is highly clustered in time around a mainshock that ruptures the entire fault. It consists of a foreshock sequence accelerating to the main event, as detailed in Dublanchet (2017). The mainshock releases all the accumulated stress, so that no immediate aftershocks are observed and the mean slip (creep) decreases and remains negligible until the next foreshock sequence starts (see average slip history in Figures S6 and S8). Here the absence of aftershocks is similar to the quiescence of microseismicity following large stress release in the model by Jiang and Lapusta (2016). The recurrence of all the events is to the first order the recurrence T_0 of the mainshock. Dimensionally, T_0 is of the order of $T_0 \sim \Delta\tau H/\mu v^*$, $\Delta\tau$ being the stress drop of the mainshock. $\Delta\tau$ and therefore T_0 are independent of the seismic moment released (Dublanchet, 2018). With my choice of parameters, $T_0 \simeq 3$ to $6.10^4 d_c/v^*$ for the two supercritical scenarios shown here (see Dublanchet (2018) for the values of stress drop). These values are a correct estimate of the mainshock periodicity (Figures 1a, S6, and S8). The important scatter observed for some sequences (Figures 1a and 1b) is associated with asperities rupturing more than once during the foreshock sequences of the main events, leading to punctual very small recurrences times. The two scalings shown in Figure 1a therefore reflect a creep control of the seismicity at $\rho < \rho^*$, which disappears at $\rho > \rho^*$.

For each repeating earthquake sequence, I also computed the covariance COV for the recurrence time T_r (standard deviation divided by the mean of T_r (Chen et al., 2013; Lengliné & Marsan, 2009). Recall that $COV = 0$ indicates perfect periodicity, while $COV = 1$ corresponds to Poissonian behavior, and $COV > 1$ to clustering. Results are shown in Figure 2 for different asperity densities. Overall, the COV in Figure 2 are within the range of observations (K. H. Chen et al., 2007; K. H. Chen et al., 2009, 2013; Lengliné & Marsan, 2009). Here again, I observe a slight increase of the covariance when approaching the critical density from below (Figure 2h). For asperity densities close to critical, I observe an important scatter of the COV. This result could be interpreted as follows. The deviation from the perfect repeating earthquake model (measured by the covariance) could be attributed to the mechanical interaction between asperities: the stress perturbations associated by nearby ruptures either hasten or delay the next rupture on a particular asperity. Such stress perturbations could either emanate from a direct static triggering effect (which is more pronounced as the interasperity distance decreases, i.e. as the asperity density increases) or from accelerated creep events generated by a nearby rupture (here again, the effect is more pronounced if velocity strengthening areas are more sensitive to stress perturbations, which corresponds to asperity densities closer to critical
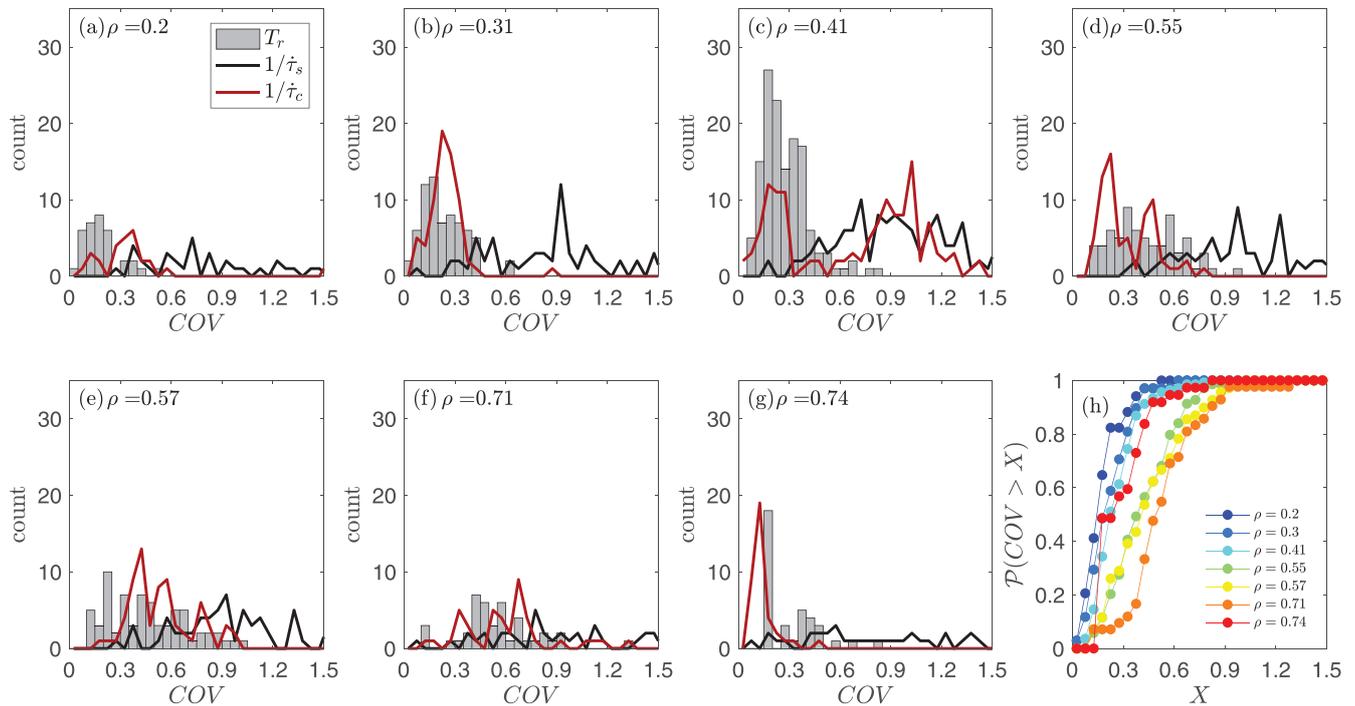
Figure 2. (a–g) Distribution of the covariance COV for the recurrence time T_r, the inverse static stressing rate $1/\dot{\tau}_s$, and the inverse stressing rate related to creep $1/\dot{\tau}_c$ versus asperity density for all the repeating earthquake sequences shown in Figure 1a. (h) Cumulative distribution function $\mathcal{P}$ for the covariance on T_r.

Dublanchet et al., 2013b). At higher densities, the covariance decreases again (see peak of COV distribution around 0.2 in Figure 2g); because of the synchronization operated by the mainshock rupture, the scatter in T_r becomes less important. The COV and thus the variability of T_r within repeating earthquake sequences are therefore controlled in these simulations by the asperity density. Very low densities lead to more regular repeating earthquakes. Note that different fault scenarios correspond to the same asperity density, so that the variations in COV for the same ρ likely reflects different mechanical environment of the repeating earthquake sequences (distance to nearest asperities, extent of the creeping surroundings).

In order to discriminate between the effect of static stress redistribution and the effect of stress changes mediated by creep in the deviations from periodicity, I compared the statistics of stressing rates (stressing rate due to static effects $\dot{\tau}_s$ and due to creep $\dot{\tau}_c$) to my statistics of recurrence times. The underlying assumption is that interevent time delay scales as the inverse stressing rate: $\Delta\tau/\dot{\tau}$, $\Delta\tau$ being the constant stress drop of the events. For each interevent period in a given sequence (on the source i), I computed an approximate stressing rate related to static stress transfers following Chen et al. (2013). For that, I identify all the events j occuring during the interevent period and estimate the static shear stress perturbation dS_{ij} on the repeating source as

$$dS_{ij} = \frac{1}{6\pi}\frac{M_{0j}}{r_{ij}^3}, \tag{3}$$

where M_{0j} is the seismic moment released by the earthquake j and r_{ij} is the distance between the source of j and the source of the sequence i. The total static stress perturbation dS acting on the source of sequence i is the sum of dS_{ij} over j, and the static stressing rate on i (τ_s) is then given by dS divided by the interevent time. For the same interevent period, I estimate the creep related stressing rate $\dot{\tau}_c$ from the average stress history on the fault. $\dot{\tau}_c$ is computed as the average absolute value of stressing rate prevailing during interseismic periods (coseismic periods contain also the static effects).

I therefore end up with a value of $\dot{\tau}_s$ and $\dot{\tau}_c$ for each T_r in our dataset. $\dot{\tau}_s$ and $\dot{\tau}_c$ are estimates of the stressing rates due to static stress transfers and creep, respectively. T_r is compared to $1/\dot{\tau}_s$ and $1/\dot{\tau}_c$ in Figure 3. We immediately see that T_r increases approximately as $1/\dot{\tau}_c$, while there is no clear relationship between T_r and $1/\dot{\tau}_s$ (the same T_r could be obtained for a wide range of different $1/\dot{\tau}_s$). Furthermore, it is shown in
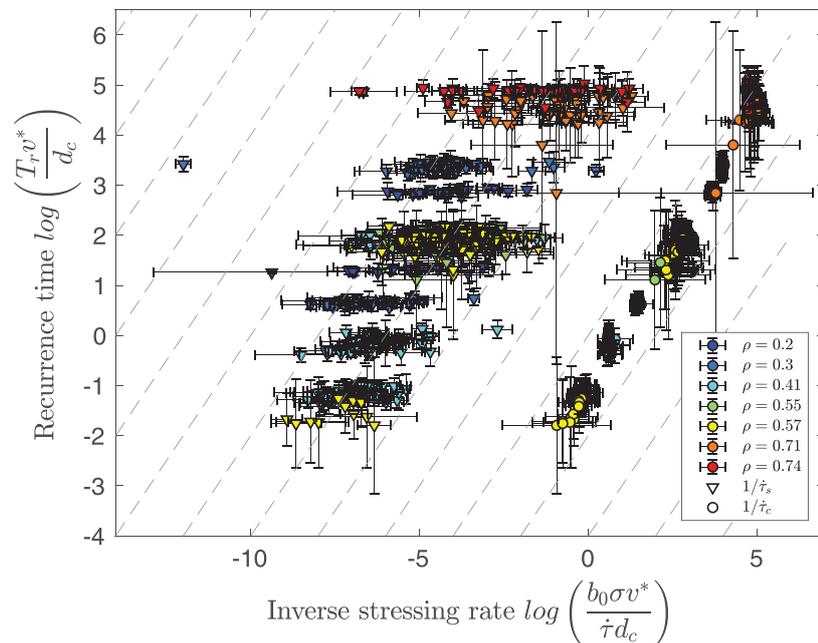
Figure 3. Recurrence times T_r versus inverse stressing rate $1/\dot{\tau}$. Triangles correspond to the inverse static stressing rates $1/\dot{\tau}_s$, circles indicate the inverse stressing rate related to creep $1/\dot{\tau}_c$. Gray dashed lines correspond to linear scaling $T_r \sim 1/\dot{\tau}$ (constant stress drop). Recurrence times and stressing rates are normalized using the mechanical parameters defined in Figure 1.

Figure 2 that the distribution of the covariance of $1/\dot{\tau}_c$ follows the covariances of T_r more closely than the distribution of the covariance of $1/\dot{\tau}_s$ does. In other words, the fluctuations in T_r within one sequence tracks the fluctuations in $1/\dot{\tau}_c$. The mechanical interactions between the repeating earthquake sources (at the origin of the fluctuations of T_r) seem therefore to being dominated by creep mediated stress transfers rather than by direct static stress perturbations. The increase of the covariance (and the variability) of T_r as the fault gets closer to the critical density of asperities is therefore not dominated by the decrease of the distances between asperities but by an increase of the sensitivity of fault creep to seismic ruptures.

4. Discussion

One of the main conclusion of this analysis concerns the scaling between recurrence time T_r and moment rate M_0 in the context of interacting repeating earthquake sequences. The scaling in the model reproduces the observed scaling $T_r \sim V_c^{-1} M_0^{1/6}$ if the density of asperities is smaller than the critical density allowing large ruptures to connect a group of asperities. One could conclude that tectonic faults where such a scaling has been observed are characterized by a subcritical density of asperities. Repeating earthquakes have been reported within the coseismic rupture zones of the Tohoku and Izmit earthquake (Bouchon et al., 2011; Uchida, 2019) where we would expect supercritical asperity densities. It is however unclear whether they obey the classical scaling since T_r decreases during the nucleation process. These events are usually interpreted as being triggered by the acceleration of slow slip within the nucleation zone (Dublanchet, 2017). We therefore expect the $M_0^{1/6}$ to be locally possible but over the limited duration of the seismic cycle involving significant creep. Identifying supercritical asperity regions based on repeating earthquakes dynamics would therefore require to observe over the entire cycle of the mainshock, which is currently not possible for mega earthquakes.

An important issue regarding interacting repeating earthquake sequences is whether such sequences could be used to monitor slip rate on the fault. Because of the inverse dependence of T_r on slip rate V_c, the distribution of T_r could thus be used as a measure of the average slip rate. Here again, a subcritical density of asperities could be interpreted as asperities being mechanically isolated from each other so that they behave as in the models by Beeler et al. (2001) and T. Chen and Lapusta (2009).

It has been shown here that the variability of recurrence time in a particular sequence (covariance on T_r) increases with the asperity density (low density leads to more regular repeating earthquakes than higher densities). Based on Figure 2g, an increase of ρ from 0.2 to 0.57 corresponds to an increase of mean COV from 0.15 to 0.45, which indicates that COV increases approximately linearly with asperity density in the subcritical regime. This result is similar to the observations reporting more regular repeating earthquake sequences when sources are far from each other on the Longitudinal Valley Fault in Taiwan (K. H. Chen et al., 2009), and on Parkfield segment on the San Andreas Fault (Chen et al., 2013). K. H. Chen et al. (2013) and K. H. Chen et al. (2009) report an increase of COV from $0.05 - 0.2$ to $0.7 - 0.9$ as the number of larger earthquakes in the vicinity of the repeating source increase by a factor of 5 to 10 in the Parkfield area and on the Longitudinal Valley Fault in Taiwan. This is compatible with a linear dependance of the COV on the number of neighbors. My results thus provide a reasonable order of magnitude and more importantly a mechanical interpretation for COV differences in terms of seismogenic asperity density.

In my model, the scatter in T_r within individual sequences is the consequence of mechanical interaction dominated by creep mediated stress transfers. It has been shown that static stress transfers may explain the variability of repeating earthquake sequences in Parkfield mainly after and in the direct vicinity of significant earthquakes (magnitude 4 to 5) (K. H. Chen et al., 2010, 2013). Such conditions may not be achieved in my model because of the limited source size range considered. However, accelerated creep is also frequently associated with variations in recurrence intervals of repeating earthquake sequences (K. H. Chen et al., 2010; Lui & Lapusta, 2016; Schaff et al., 1998), which is similar to my results.

This conclusion was furthermore based on a very simple estimation of the stressing rate associated with static effects, and on the assumption that interevent time depends linearly on the inverse of the stressing rate. Under rate-and-state friction, the interevent time delay is a non linear function of the stressing history (J. Dieterich, 1994; J. H. Dieterich 1992). I did not consider such non linear response here. Furthermore, I used an oversimplified estimation of the shear stress redistribution (equation (3)). Nevertheless, the dominance of creep related stress transfers is also supported by the strong dependence of T_r on the average creep rate V_c.

My results suggest that the distance to critical asperity density is the relevant mechanical parameter controlling the dynamics of repeating earthquake sequences on a creeping fault. Here I have only considered fault scenarios with different asperity densities but with the same values of velocity weakening and velocity strengthening a and b rate-and-state parameters. These parameters do play a role in the interaction processes between asperities leading to variability in recurrence and moment (Lui & Lapusta, 2018). However, since the critical asperity density depends on a and b distribution (Dublanchet et al., 2013b), I expect that the only effect of varying these parameters would be to shift the transition between the different regimes observed. However, this issue requires more attention.

In this analysis, I should mention that our model being quasi-dynamic, it does not produce any dynamic (wave mediated) stress perturbations. Such dynamic stresses may play a role in the interaction between different repeating earthquake sequences and in the scatter in the observed T_r. This issue still needs to be investigated.

Note also that we have not discussed the scatter in the moments characterizing a particular repeating earthquake sequence. This scatter is usually less important than the scatter in T_r (Figures 1a and 1b). Among possible origins for the variability in seismic moment are slight changes in stress drop caused by different stressing conditions (Dublanchet et al., 2013a) or a trade-off between changes in T_r and M_0 so that the seismic moment is released at an average constant rate. This latter explanation would require the same scatter in T_r and M_0.

5. Conclusion

Based on the analyses of synthetic repeating earthquake sequences, I have shown that the observed relationship between recurrence time, seismic moment, and long-term slip rate on faults $T_r \sim V_c^{-1} M_0^{1/6}$ could emerge even under mechanical interaction between repeating earthquake sources (asperities) as long as the density of sources is smaller than a critical threshold allowing large ruptures to develop. The inverse dependence of T_r with slip rate V_c in this model supports the use of complex interacting repeating earthquake sequences to monitor fault slip rate. I also provide a mechanical interpretation of the variability of

recurrence time in a particular sequence in terms of asperity density and enhanced creep mediated stress transfers. However, I can not fully rule out contribution from static and dynamic stress transfers in the transient changes of the recurrence time.

References

Bürgmann, R., Schmidt, D., Nadeau, R., d'Alessio, M., Fielding, E., Manaker, D., et al. (2000). Earthquake potential along the northern Hayward fault, California. *Science*, *289*(5482), 1178–1182.

Beeler, N., Lockner, D., & Hickman, S. (2001). A simple stick-slip and creep-slip model for repeating earthquakes and its implication for microearthquakes at Parkfield. *Bulletin of the Seismological Society of America*, *91*(6), 1797–1804.

Bouchon, M., Karabulut, H., Aktar, M., Özalaybey, S., Schmittbuhl, J., & Bouin, M. P. (2011). Extended nucleation of the 1999 mw 7.6 izmit earthquake. *Science*, *331*(6019), 877.

Cattania, C., & Segall, P. (2019). Crack models of repeating earthquakes predict observed moment-recurrence scaling. *Journal of Geophysical Research: Solid Earth*, *124*, 476–503. https://doi.org/10.1029/2018JB016056

Chen, K. H., Bürgmann, R., & Nadeau, R. M. (2010). Triggering effect of m 45 earthquakes on the earthquake cycle of repeating events at Parkfield, California. *Bulletin of the Seismological Society of America*, *100*(2), 522–531.

Chen, K. H., Bürgmann, R., & Nadeau, R. M. (2013). Do earthquakes talk to each other? Triggering and interaction of repeating sequences at Parkfield. *Journal of Geophysical Research: Solid Earth*, *118*, 165–182. https://doi.org/10.1029/2012JB009486

Chen, T., & Lapusta, N. (2009). Scaling of small repeating earthquakes explained by interaction of seismic and aseismic slip in a rate and state fault model. *Journal of Geophysical Research*, *114*, B01311. https://doi.org/10.1029/2008JB005749

Chen, T., & Lapusta, N. (2019). On behaviour and scaling of small repeating earthquakes in rate and state fault models. *Geophysical Journal International*, *218*(3), 2001–2018.

Chen, K. H., Nadeau, R. M., & Rau, R.-J. (2007). Towards a universal rule on the recurrence interval scaling of repeating earthquakes? *Geophysical Research Letters*, *34*, L16308. https://doi.org/10.1029/2007GL030554

Chen, K. H., Nadeau, R. M., & Rau, R.-J. (2008). Characteristic repeating earthquakes in an arc-continent collision boundary zone: The Chihshang fault of Eastern Taiwan. *Earth and Planetary Science Letters*, *276*(3-4), 262–272.

Chen, K. H., Rau, R.-J., & Hu, J.-C. (2009). Variability of repeating earthquake behavior along the Longitudinal Valley fault zone of Eastern Taiwan. *Journal of Geophysical Research*, *114*, B05306. https://doi.org/10.1029/2007JB005518

Dieterich, J. H. (1979). Modeling of rock friction-1. Experimental results and constitutive equations. *Journal of Geophysical Research*, *84*, 2161–2168.

Dieterich, J. H. (1992). Earthquake nucleation on faults with rate-and state-dependent strength. *Tectonophysics*, *211*(1-4), 115–134.

Dieterich, J. (1994). A constitutive law for rate of earthquake production and its application to earthquake clustering. *Journal of Geophysical Research*, *99*(B2), 2601–2618.

Dublanchet, P. (2017). The dynamics of earthquake precursors controlled by effective friction. *Geophysical Journal International*, *212*(2), 853–871.

Dublanchet, P. (2018). Inferring fault slip rates from cumulative seismic moment in a multiple asperity context. *Geophysical Journal International*, *216*(1), 395–413.

Dublanchet, P., Bernard, P., & Favreau, P. (2013a). Creep modulation of Omori law generated by a coulomb stress perturbation in a 3-d rate-and-state asperity model. *Journal of Geophysical Research: Solid Earth*, *118*, 4774–4793. https://doi.org/10.1002/jgrb.50311

Dublanchet, P., Bernard, P., & Favreau, P. (2013b). Interactions and triggering in a 3-d rate-and-state asperity model. *Journal of Geophysical Research: Solid Earth*, *118*, 2225–2245. https://doi.org/10.1002/jgrb.50187

Dublanchet, P., Godano, M., & Bernard, P. (2015). Inferring fault mechanical conditions from the source parameters of a complex microseismic multiplet in the Corinth rift, Greece. *Journal of Geophysical Research: Solid Earth*, *120*, 7655–7682. https://doi.org/10.1002/2015JB012259

Ellsworth, W. L., & Bulut, F. (2018). Nucleation of the 1999 izmit earthquake by a triggered cascade of foreshocks. *Nature Geoscience*, *11*(7), 531.

Gardonio, B., Marsan, D., Lengliné, O., Enescu, B., Bouchon, M., & Got, J.-L. (2015). Changes in seismicity and stress loading on subduction faults in the Kanto region, Japan, 2011–2014. *Journal of Geophysical Research: Solid Earth*, *120*, 2616–2626. https://doi.org/10.1002/2014JB011798

Gardonio, B., Marsan, D., Socquet, A., Bouchon, M., Jara, J., Sun, Q., et al. (2018). Revisiting slow slip events occurrence in Boso Peninsula, Japan, combining GPS data and repeating earthquakes analysis. *Journal of Geophysical Research: Solid Earth*, *123*, 1502–1515. https://doi.org/10.1002/2017JB014469

Godano, M., Bernard, P., & Dublanchet, P. (2015). Bayesian inversion of seismic spectral ratio for source scaling: Application to a persistent multiplet in the western Corinth rift. *Journal of Geophysical Research: Solid Earth*, *120*, 7683–7712. https://doi.org/10.1002/2015JB012217

Igarashi, T., Matsuzawa, T., & Hasegawa, A. (2003). Repeating earthquakes and interplate aseismic slip in the northeastern Japan subduction zone. *Journal of Geophysical Research*, *108*(B5), 2249. https://doi.org/10.1029/2002JB001920

Jiang, J., & Lapusta, N. (2016). Deeper penetration of large earthquakes on seismically quiescent faults. *Science*, *352*(6291), 1293–1297.

Lengliné, O., & Marsan, D. (2009). Inferring the coseismic and postseismic stress changes caused by the 2004 mw= 6 Parkfield earthquake from variations of recurrence times of microearthquakes. *Journal of Geophysical Research*, *114*, B10303. https://doi.org/10.1029/2008JB006118

Lui, S. K., & Lapusta, N. (2016). Repeating microearthquake sequences interact predominantly through postseismic slip. *Nature Communications*, *7*, 13020.

Lui, S. K., & Lapusta, N. (2018). Modeling high stress drops, scaling, interaction, and irregularity of repeating earthquake sequences near Parkfield. *Journal of Geophysical Research: Solid Earth*, *123*, 10,854–10,879. https://doi.org/10.1029/2018JB016472

Nadeau, R., Foxall, W., & McEvilly, T. V. (1995). Clustering and periodic recurrence of microearthquakes on the San Andreas fault at Parkfield, California. *Science*, *267*(5197), 503–507.

Nadeau, R. M., & Johnson, L. R. (1998). Seismological studies at Parkfield vi: Moment release rates and estimates of source parameters for small repeating earthquakes. *Bulletin of the Seismological Society of America*, *88*(3), 790–814.

Nadeau, R., & McEvilly, T. (1997). Seimological studies at parkfield v: Characteristic microearthquake sequences as fault-zone drilling targets. *Bulletin of the Seismological Society of America*, *87*(6), 1463–1472.

Nadeau, R. M., & McEvilly, T. V. (1999). Fault slip rates at depth from recurrence intervals of repeating microearthquakes. *Science*, *285*(5428), 718–721.

Poupinet, G., Ellsworth, W., & Frechet, J. (1984). Monitoring velocity variations in the crust using earthquake doublets: An application to the Calaveras fault, California. *Journal of Geophysical Research*, *89*(B7), 5719–5731.

Rice, J. R. (1993). Spatio-temporal complexity of slip on a fault. *Journal of Geophysical Research*, *98*, 9885–9907.

Rubin, A. M., & Ampuero, J. P. (2005). Earthquake nucleation on (aging) rate and state faults. *Journal of Geophysical Research*, *110*, B11312. https://doi.org/10.1029/2005JB003686

Ruina, A. L. (1983). Slip instability and state variable friction laws. *Journal of Geophysical Research*, *88*, 10,359–10,370.

Sammis, C. G., & Rice, J. R. (2001). Repeating earthquakes as low-stress-drop events at a border between locked and creeping fault patches. *Bulletin of the Seismological Society of America*, *91*(3), 532–537.

Schaff, D. P., Beroza, G. C., & Shaw, B. E. (1998). Postseismic response of repeating aftershocks. *Geophysical Research Letters*, *25*(24), 4549–4552.

Schmidt, D., Bürgmann, R., Nadeau, R., & d'Alessio, M. (2005). Distribution of aseismic slip rate on the Hayward fault inferred from seismic and geodetic data. *Journal of Geophysical Research*, *110*, B08406. https://doi.org/10.1029/2004JB003397

Templeton, D. C., Nadeau, R. M., & Bürgmann, R. (2008). Behavior of repeating earthquake sequences in central California and the implications for subsurface fault creep. *Bulletin of the Seismological Society of America*, *98*(1), 52–65.

Uchida, N. (2019). Detection of repeating earthquakes and their application in characterizing slow fault slip. *Progress in Earth and Planetary Science*, *6*(1), 40.

Uchida, N., & Matsuzawa, T. (2011). Coupling coefficient, hierarchical structure, and earthquake cycle for the source area of the 2011 off the Pacific coast of Tohoku earthquake inferred from small repeating earthquake data. *Earth, planets and space*, *63*(7), 30.

Uchida, N., Matsuzawa, T., Hasegawa, A., & Igarashi, T. (2003). Interplate quasi-static slip off Sanriku, NE Japan, estimated from repeating earthquakes. *Geophysical Research Letters*, *30*(15), 1801. https://doi.org/10.1029/2003GL017452

Uchida, N., Matsuzawa, T., Hirahara, S., & Hasegawa, A. (2006). Small repeating earthquakes and interplate creep around the 2005 Miyagi-Oki earthquake (m= 7.2). *Earth, Planets and Space*, *58*(12), 1577–1580.

Uchida, N., Nakajima, J., Hasegawa, A., & Matsuzawa, T. (2009). What controls interplate coupling?: Evidence for abrupt change in coupling across a border between two overlying plates in the NE Japan subduction zone. *Earth and Planetary Science Letters*, *283*(1-4), 111–121.